

PLACE IN RETURN BOX to remove this checkout from your record.
TO AVOID FINES return on or before date due.

DATE DUE	DATE DUE	DATE DUE
_____	_____	_____
_____	_____	_____
_____	_____	_____
_____	_____	_____
_____	_____	_____
_____	_____	_____
_____	_____	_____

MSU Is An Affirmative Action/Equal Opportunity Institution

**A STUDY OF CALCIUM OXALATE CRYSTALLIZATION
IN KIDNEY STONE FORMATION**

By

Carol ShuhuiLin Hsu

A DISSERTATION

Submitted to
Michigan State University
in partial fulfillment of the requirements
for the degree of

DOCTOR OF PHILOSOPHY

Department of Chemical Engineering

1989

003603X

ABSTRACT

A STUDY OF CALCIUM OXALATE CRYSTALLIZATION IN KIDNEY STONE FORMATION

By

Carol ShuhuiLin Hsu

This work was undertaken to gain a fundamental understanding of the physical and chemical mechanisms involved in the formation of kidney stones. Calcium oxalate is the major component of kidney stones and was chosen as the representative of stone minerals. Experiments were performed in a mixed-suspension, mixed-product-removal (MSMPR) crystallizer and in a flow chamber crystallizer.

Previous work has shown the significant influence of urinary macromolecules on calcium oxalate crystallization. Both inhibition and promotion of crystal growth and crystal aggregation by these biopolymers has been reported; however, crystal growth and crystal aggregation mechanisms were not isolated in these studies. In work conducted with the MSMPR crystallizer, the linear population density model has been used to describe nonlinear data; crystal growth rates were obtained but crystal aggregation was neglected. Crystal aggregation has been suspected as being important in stone formation.

In this work, experiments with the MSMPR crystallizer were conducted to characterize calcium oxalate crystallization. The entire MSMPR crystallization process was characterized by unsteady state, quasi-steady state, and steady state periods. At unsteady state, nucleation, crystal growth, and crystal aggregation all occurred in the system. In passing from the unsteady to the steady state, the crystallization process progressed with reduced nucleation and crystal

aggregation . At steady state, only crystal growth was important. The unsteady state operation of the MSMPR crystallizer was of interest due to the presence of crystal aggregation; however, a clear understanding of the crystal aggregation mechanism depends upon knowing crystal growth kinetics.

An approach was developed to obtain crystal growth rate for the entire process, including unsteady and steady states, by identifying the shifts of particle size distributions along the x-axis with time. The growth rates obtained from this method correlated well with the results of the linear population density model and the experiments with a flow chamber crystallizer. With this method, a model urinary biopolymer, poly-L-glutamate (PGA), was identified as a growth rate inhibitor.

The flow chamber crystallizer experiments were conducted to investigate the effects of healthy and injured cultured epithelium (Maden Darby Canine Kidney (MDCK) cells) on the growth of single calcium oxalate crystals in the presence of flow shear. Healthy MDCK cells were found to inhibit crystal nucleation. The crystal growth rate of calcium oxalate monohydrate (COM) decreased in the order of crystal growth on glass > MDCK cells treated with HCl > MDCK cells treated with papain > healthy MDCK cells. The biopolymer additive, heparin, inhibited COM crystal growth on healthy MDCK cells.

Copyright by

CAROL SHUHUILIN HSU

1989

DEDICATION

This work is dedicated to
the author's parents, Mr. and Mrs. Lin-Kou Lin,
the author's parents-in-law, Mr. and Mrs. Chin-Ann Hsu,
Cheazone, Victoria, and Eleanor.

ACKNOWLEDGMENTS

I am greatly grateful to my research advisor, Dr. Daina M. Briedis, for her patience, encouragement, and financial support. Her guidance in the preparation of this dissertation and her friendship and encouragement make this work possible. Many thanks are due to Dr. William S. Spielman in the Department of Physiology for his kind help in the preparation of MDCK cells, to Dr. Mackenzie L. Davis in the Department of Civil and Environmental Engineering for lending the AA spectrophotometer, to Dr. Kalinath Mukherjee in the Department of Metallurgy, Mechanics, and Materials Science and Dr. Duncan F. Sibley in the Department of Geological Science for their lending of X-ray diffractometers. I also want to thank Dr. Donald K. Anderson and Dr. Charles A. Petty in the Department of Chemical Engineering and Dr. Paul Kindel in the Department of Biochemistry for their work on my guidance committee. Appreciation is also due the other faculty and staff of the Chemical Engineering Department. Special thanks are due to my parents and my parents-in-law for their care of my children and constant support, to my sisters and brothers (-in-law) for their love, and to many friends for their great concerns and their prayers. I thank my husband, Cheazone, for his understanding and encouragement. Finally, I thank the Creator for His everlasting care and love, especially for allowing me to know His great name, who is also my Father through Jesus Christ.

TABLE OF CONTENTS

CHAPTER 1 INTRODUCTION AND BACKGROUND

1-1. Introduction	1
1-2. Causes of Renal Stone Disease	2
1-2-1. <u>Stone Compositions</u>	2
1-2-2. <u>Theories of Stone Formation</u>	4
1-3. Stone Formation and Crystallization Mechanisms	6
1-3-1. <u>Supersaturation</u>	7
1-3-2. <u>Nucleation</u>	8
1-3-3. <u>Crystal Growth</u>	10
1-3-4. <u>Crystal Aggregation</u>	13
1-3-4-1. Diffuse Double Layer of A Single Particle in Solution	16
1-3-4-2. Repulsive Force of Two Approaching Particles	18
1-3-4-3. Attractive Force Between Two Particles	19
1-3-4-4. Total Energy of Two Interacting Particles and Stability of Particle Aggregation and Dispersion	21
1-3-4-5. Kinetics of Aggregation	23
1-4. Review of Experimental Methods	26
1-4-1. <u>Batch Experiments</u>	26
1-4-2. <u>Constant Composition Method</u>	29
1-4-3. <u>MSMPR Crystallizer</u>	30
1-4-4. <u>Single Crystal Growth</u>	37
1-5. Scope of Research	37

CHAPTER 2 SUPERSATURATION IN ELECTROLYTE SOLUTIONS

2-1. Saturation	40
2-2. Definition of Supersaturation	41
2-3. Formation of Complexes	44
2-4. Calculation of Supersaturations	47
2-5. Accuracy of the Calculated Supersaturations	51

CHAPTER 3 PARTICLE SIZE DISTRIBUTIONS, POPULATION BALANCE EQUATIONS AND DETERMINATION OF PARTICLE SIZE DISTRIBUTIONS

3-1. Introduction	54
3-2. Particle Size Distributions and Population Balance Equations	54
3-3. Determination of Particle Size Distributions	58
3-3-1. <u>Basic Operating Principles of the ELZONE^(R) System</u>	60
3-3-2. <u>Correlating Particle Size Distributions with the Instrument Counted Data</u>	60
3-3-3. <u>Comments on the ELZONE^(R) Analysis Program</u>	62
3-3-3-1. "Histogram" Display	63
3-3-3-2. Scaling Factor in Volume Data	63
3-3-3-3. Blending of Volume Data	65
3-3-3-4. Sampling Volume	67
3-4. Calibration Procedure and the "Normalize" Function	68
3-4-1. <u>Original Calibration Procedure</u>	69
3-4-2. <u>Modified Calibration Procedure</u>	71
3-4-3. <u>Calibrations with Known-Size Standard Particles</u>	73
3-5. Modification of ELZONE's Data Analysis	74
3-5-1. <u>An Alternate Procedure for Sampling Volume</u>	75
3-5-2. <u>Data Manipulation</u>	76

CHAPTER 4 MIXED-SUSPENSION, MIXED-PRODUCT-REMOVAL CRYSTALLIZATION SYSTEM

4-1. Introduction	78
4-2. Experimental Methods	80
4-2-1. <u>Apparatus and Materials</u>	80
4-2-2. <u>Experimental Scheme</u>	84
4-2-3. <u>Measurement of Particle Size Distributions</u>	85
4-2-4. <u>Measurement of Calcium Concentrations</u>	86
4-2-5. <u>Determination of Crystal Habit and Crystal Hydrate Phases</u>	87
4-3. Characterization of Calcium Oxalate Crystallization in MSMPR System	87
4-3-1. <u>Calcium Oxalate Hydrates and Crystal Habit</u>	87
4-3-2. <u>Particle Size Distributions</u>	88
4-3-3. <u>Calcium Concentrations in the Crystallizer</u>	95
4-3-4. <u>Crystallization Mechanisms</u>	98
4-3-5. <u>Effect of PGA Additive on Calcium Oxalate Crystallization</u>	100
4-4. Crystal Growth Rate	104
4-4-1. <u>Approach A: Growth Rate by Comparison of PSD Curves</u>	105
4-4-2. <u>Approach B: Growth Rate at Quasi-Steady State</u>	117
4-4-3. <u>Comparison of Growth Rates</u>	120
4-5. Discussion	123

CHAPTER 5 THE EFFECT OF MDCK CELLS ON CALCIUM OXALATE GROWTH IN A FLOW CHAMBER

5-1. Introduction	125
5-2. Precipitator Design and Assembly	128

5-3. Fluid Mechanics Properties in Upper Chamber	134
5-3-1. <u>Reynolds Number</u>	134
5-3-2. <u>Transition Length</u>	136
5-3-3. <u>Velocity Profile</u>	136
5-3-4. <u>Shear Stress</u>	139
5-4. Experimental Materials and Methods	141
5-4-1. <u>Maden Darby Canine Kidney Cells</u>	141
5-4-2. <u>Solution Preparation</u>	142
5-4-3. <u>Experimental Set-Up</u>	146
5-4-4. <u>Experimental Scheme</u>	149
5-4-4-1. Viability Tests on MDCK Cells	149
5-4-4-2. Growth Rate Experiments:	
Effects of Additives and Tissues Surfaces	150
5-4-4-3. Induction Period in Closed Vessels	154
5-5. Results and Discussion	154
5-5-1. <u>Cell Viability</u>	154
5-5-2. <u>Observations on Formation of Single Crystals</u>	155
5-5-2-1. Nucleation	155
5-5-2-2. Heterogeneous Nucleation	158
5-5-2-3. Nucleation on Glass and on MDCK Cells	158
5-5-2-4. Crystal Habit	163
5-5-3. <u>Supersaturation Level in Flow Chamber</u>	164
5-5-4. <u>Growth Rate under Effects of Additive</u>	
<u>and Tissue Surfaces</u>	167
5-5-4-1. Effects of Tissue Surfaces	167
5-5-4-2. Effects of Heparin	167
5-5-5. <u>Experimental Results and Stone Formation Hypothesis</u>	174

CHAPTER 6 SUMMARY, CONCLUSIONS, AND RECOMMENDATION

6-1. Summary and Conclusion	178
6-2. Recommendations for Future Research	182

APPENDICES

APPENDIX A EQUIL COMPUTER PROGRAMS	183
APPENDIX B CALIBRATION DATA OF THE ELZONE^(R) SYSTEM AND THEIR APPLICATIONS	191
APPENDIX C COMPUTER PROGRAM 80XYABCV.BAS	199
APPENDIX D PHYSICAL PROPERTIES OF SOLUTIONS	202
APPENDIX E COMPUTER PROGRAM NTM3.FOR	203
APPENDIX F SHIFTS OF THE $v(L, t)$ CURVES	209
APPENDIX G COMPUTER PROGRAM GSMMPR	216

BIBLIOGRAPHY	221
-------------------------------	------------

LIST OF TABLES

1-1	Growth rate correlations of calcium oxalate crystals at 30°C	14
1-2	Values for α	25
2-1	Thermodynamic solubility products of calcium oxalate hydrates at 37°C	41
2-2	Stability constants	48
2-3	$S_{COM,i}$ calculated with different stability constants for solutions containing $CaCl_2$, $K_2C_2O_4$, and KCl (ionic strength buffer); ionic strength = 0.15 M	52
3-1	F factors calculated from comparison of reported and calculated differential volume data. (abbreviated version)	64
4-1	Geometrical parameters of the crystallizer	83
4-2	Experimental scheme	85
4-3	Crystal hydrates	88
4-4	Correlations of growth rates with supersaturations	116
4-5	Growth rates at quasi-steady state	120
4-6	Comparison of growth rates with previous work	121
4-7	Growth rates at steady state	122
5-1	Reynolds number, transition length, and maximum shear stress for flow chamber precipitator	135
5-2	Original Earle's medium recipe (1X)	143
5-3	A typical solution composition for $[Ca^{2+}] = [C_2O_4^{2-}] = 0.001\text{ M}$	145
5-4	MDCK cell viability with shear stress	155
5-5	Calculated induction periods at the reactant concentrations used in single crystal experiments	156

5-6	Calcium concentrations of some effluent samples	165
5-7	Rate constants of COM growth	168

LIST OF FIGURES

1-1	Screw dislocation on crystal surface and incorporation of solute molecules into crystal lattices	12
1-2	The diffuse-double layer and potential profile around a particle	17
1-3	Interaction energy of particles at distance H	22
1-4	Semi-log population density plot; linear and curved distributions	36
3-1	Blending of a simulated v_{ch} and $v(L)$ data; (a) linear population density plot, (b) volume density, (c) differential volume per channel, (d) v_{ch} by blending routine. The thicker dash lines represent the data from the 76 μm aperture tube; the thinner solid lines represent the data from the 300 μm aperture tube. Sampling volume is 1 ml for both data sets	66
4-1	Repeating unit of polyglutamate	80
4-2	MSMPR experimental set-up	81
4-3	400 ml hybrid tank	82
4-4	Photomicrograph of a sample taken from the experiment with 3 mM calcium and oxalate concentrations	89
4-5	Population density plot A; $[\text{Ca}^{2+}] = [\text{C}_2\text{O}_4^{2-}] = 3 \text{ mM}$, without PGA, $\tau = 8 \text{ min}$, sampling time = 74 min	90
4-6	Population density plot B; $[\text{Ca}^{2+}] = [\text{C}_2\text{O}_4^{2-}] = 2 \text{ mM}$, PGA = 100 ppm, $\tau = 8 \text{ min}$, sampling time = 68 min	91
4-7	$v(L,t)$ particle size distribution; $[\text{Ca}^{2+}] = [\text{C}_2\text{O}_4^{2-}] = 2 \text{ mM}$, PGA = 100 ppm, $\tau = 8 \text{ min}$, sampling time = 68 min	92
4-8	$v(L,t)$ with extrapolated small size range	93

4-9	Total particle numbers and the third moments for the base run;	
(a)	total particle numbers, N_T ,	
(b)	the third moments, M_3	96
4-10	Calcium concentrations in the filtrates and in the suspensions;	
	$[Ca^{2+}] = [C_2O_4^{2-}] = 2 \text{ mM}$, PGA = 10 ppm	97
4-11	Effects of PGA additive on total particle numbers,	
	the third moments, and the maximum particle sizes;	
(a)	effect of PGA on total particle numbers, N_T ,	
(b)	effect of PGA on the third moments, M_3 ,	
(c)	effect of PGA on the maximum particle sizes, L_{max}	101
4-12	Effect of PGA additive on total calcium concentrations in	
	suspensions; $[Ca^{2+}] = [C_2O_4^{2-}] = 2 \text{ mM}$, $\tau = 8 \text{ min}$	102
4-13	Effect of PGA additive on calcium concentrations in	
	filtrates; $[Ca^{2+}] = [C_2O_4^{2-}] = 2 \text{ mM}$, $\tau = 8 \text{ min}$	103
4-14	Shift of $v(L,t)$ curve and calculation of growth rate;	
	PGA = 100 ppm	107
4-15	$S_{COT,c}$ in the crystallizer in experiments with varied	
	residence time	108
4-16	Growth rates and supersaturations for the experiment with	
	1 mM calcium and oxalate concentrations	110
4-17	Growth rates and supersaturations for the base run	111
4-18	Growth rates in experiments with varied residence time	112
4-19	Growth rates in experiments with various levels of PGA	
	additive	113
4-20	Growth rates in experiments with varied calcium and	
	oxalate concentrations	114
4-21	Langmuir isotherm of PGA adsorption on calcium oxalate	
	crystals	118
5-1	Repeating unit of heparin	126
5-2	Top view of growth chamber	129
5-3	Exploded side view of the growth chamber	130
5-4	Upper chamber holder	131
5-5	Lower chamber holder	132

5-6	Modeling coordinates of the flow chamber precipitator	133
5-7	Illustrative velocity profiles; flow rate at 40 ml/min . . .	138
5-8	Shear stress at interface surface; flow rate at 40 ml/min . .	140
5-9	Crystal growth flow system	147
5-10	Induction period for the formation of CaC_2O_4	157
5-11	COM crystals on MDCK cells; Run 1102087, $T_{\text{Ca}} = T_{\text{Ox}} = 1.5 \text{ mM}$, taken after experiment	160
5-12	COM crystals on glass in an experiment with MDCK cells, a spot with cells detached; Run 1102087, $T_{\text{Ca}} = T_{\text{Ox}} = 1.5 \text{ mM}$, taken after experiment	160
5-13	COM crystals on MDCK cells treated with papain; Run 2110487, $T_{\text{Ca}} = T_{\text{Ox}} = 1.25 \text{ mM}$, $t = 15 \text{ min}$	161
5-14	COM crystals on MDCK cells treated with HCl; Run 2102087, $T_{\text{Ca}} = T_{\text{Ox}} = 1.5 \text{ mM}$, $t = 27 \text{ min}$	161
5-15	COM crystals on glass; Run 2092387, $T_{\text{Ca}} = T_{\text{Ox}} = 1.25 \text{ mM}$, $t = 35 \text{ min}$	162
5-16	COM crystals on MDCK cells with 100 mg/l heparin; Run 1082587, $T_{\text{Ca}} = T_{\text{Ox}} = 1.0 \text{ mM}$, $t = 40 \text{ min}$	162
5-17	Effluent calcium concentrations	166
5-18	Growth rate versus $(S_{\text{COM},c})_b$; (a) crystal growth on glass and on healthy MDCK cells, (b) crystal growth on HCl treated MDCK cells, (c) crystal growth on papain treated MDCK cells	169
5-19	Growth rate versus $(S_{\text{COM},i})_b$; (a) crystal growth on glass and on healthy MDCK cells, (b) crystal growth on HCl treated MDCK cells, (c) crystal growth on papain treated MDCK cells	170
5-20	Comparison of growth rates at any constant $(S_{\text{COM},c})_b$	172
5-21	Inhibition of COM crystal growth on MDCK cells by heparin; $T_{\text{Ca}} = T_{\text{Ox}} = 1.0 \text{ mM}$	173
5-22	Inhibitory effect of heparin on COM crystal growth follows Langmuir adsorption isotherm	175
F-1	Shifts of $v(L,t)$ for the experiment with $\text{PGA} = 100 \text{ ppm}$;	

	sampling time: 3 to 51.6 min. Arrows and "*" identify points compared among the PSD curves	210
F-2	Shifts of $v(L,t)$ for the experiment with PGA = 100 ppm; sampling time: 51.6 to 131 min	211
F-3	Shifts of $v(L,t)$ for the experiment with PGA = 100 ppm; sampling time: 131 to 206 min	212
F-4	Shifts of $v(L,t)$ for the base run; sampling time: 2.5 to 42.5 min	213
F-5	Shifts of $v(L,t)$ for the base run; sampling time: 42.5 to 98.5 min	214
F-6	Shifts of $v(L,t)$ for the base run; sampling time: 98.5 to 194.5 min	215

CHAPTER 1

INTRODUCTION AND BACKGROUND

1-1. Introduction

The objective of the work described in this dissertation was to gain a fundamental understanding of the physical and chemical mechanisms involved in the formation of kidney or renal stones (calculi). Renal calculus formation is one of the oldest diseases known to man. A bladder stone found in an Egyptian mummy was estimated to have been formed five thousand years ago (Kraljevich, 1981). While the vesical calculus (bladder stones, mostly uratic in composition and found in boys) is more common in undeveloped and developing countries, renal calculus (mainly calcium oxalate, with or without apatite, found in adults) is more common in developed countries (Pyrah, 1979). In the U.S., hospital admissions for the treatment of kidney stones were about every one to four persons per 2,000 of the population (ibid.); \$47 million was spent annually for the treatment of these patients (Finlayson, 1974). Besides the economic consumption, the patients also suffer emotional and physical trauma due to the extreme pain experienced when a sharp stone passes through the urinary tract.

Research in nephrolithiasis (kidney stones) has often focused on metabolic and occupational causes of the disease. It has been suggested that a richer diet--a higher intake of calcium-containing foods and animal protein--might be one of the factors which causes renal calculus formation. It was also found statistically that people with relatively sedentary occupations or individual working in high temperature environments have higher incidence of stones (Pyrah, 1979). Yet, consensus on the mechanisms of the formation of kidney stone has

not been achieved. Because kidney stone formation is a crystallization-precipitation process as considered from the chemical engineer's point of view, this research is motivated by the desire for an understanding the physical and chemical mechanisms of kidney stone formation and crystallization phenomena.

1-2. Causes of Renal Stone Disease

Formation of renal stone must be initiated from the molecular level at which nuclei of calculi are formed in urine. The small nuclei may attach to the surfaces of the urinary tract and grow to larger stones or more than one nuclei may combine to form larger stones that threaten a person's health. Composition of stones will be reviewed to gain preliminary understanding of the disease since the composition and morphology of kidney stones gives some information on the possible etiology of stone formation.

1-2-1. Stone Compositions

Most urinary stones usually contain about 97.5% of one or more crystalline substances and 2.5% colloidal matrix (Kraljevich, 1981; Pyrah, 1979). Matrix calculi, a separate class of stones, contain 65-85% matrix (macromolecular compounds) by weight. Sixty-three to 88 percent of stone-forming patients pass stones composed entirely or predominantly of calcium oxalate (Pyrah, 1979; Pak, 1987). It was for this reason that calcium oxalate was chosen for this study.

Calcium oxalate itself is an interesting crystal for study. There are three hydrates of calcium oxalate crystals:

calcium oxalate monohydrate (COM), or whewellite, $\text{CaC}_2\text{O}_4 \cdot \text{H}_2\text{O}$, which forms as monoclinic crystals;

calcium oxalate dihydrate (COD), or weddellite, $\text{CaC}_2\text{O}_4 \cdot (2+x)\text{H}_2\text{O}$, $x \leq 0.5$, forming as tetragonal crystals; and

calcium oxalate trihydrate (COT); $\text{CaC}_2\text{O}_4 \cdot (2+x)\text{H}_2\text{O}$, $0.5 \leq x \leq 1$, which appears as triclinic crystals.

Because COM is thermodynamically the most stable phase, COT and COD may precipitate first but transform to COM gradually. COT has been suggested as the precursor in stone formation (Gardner, 1976; Tomazic and Nancollas, 1976), but is a rare component in urinary stones (Pyrah, 1979). Heijnen et al. (1985), however, found that COT was common in the outermost layer (up to a few hundred microns thick) of one third of the largely whewellite stones they examined.

Phosphate is another component subordinate to calcium oxalate. The phosphates are identified as apatite (hydroxyapatite, $\text{Ca}_{10}(\text{PO}_4)_6(\text{OH})_2$, carbonate-apatite, $\text{Ca}_{10}(\text{PO}_4 \cdot \text{CO}_3\text{OH})_6 \cdot \text{OH}_2$), struvite ($\text{MgNH}_4\text{PO}_4 \cdot 6\text{H}_2\text{O}$), brushite ($\text{CaHPO}_4 \cdot 2\text{H}_2\text{O}$), whitlockite ($\beta\text{-Ca}_3(\text{PO}_4)_2$), and octacalcium phosphate ($\text{Ca}_8\text{H}_2(\text{PO}_4)_6 \cdot 6\text{H}_2\text{O}$). Other urinary stone components are uric acid, uric acid dihydrate, cystine, and xanthine (Pyrah, 1979; Pak, 1987). These minor components were not considered in the work.

Although the matrix content in stones is small, it is believed to have a complicated involvement in stone formation and composition. Cross-sections of the stones or of the decalcified stones (stones immersed in EDTA solution for about 40 days) show a concentrically laminated structure of the organic matrix, giving an indication of the possible "glue-like" involvement of the matrix in stone formation. The organic matrix is composed of two thirds mucoproteins and one third mucopolysaccharides by weight--mainly high molecular weight substances found in urine. Some of the proteins in the mucoprotein fraction are

hexosamine, hexuronic acid, sialic acid, and glucosamine. About half of the mucoprotein contains aspartic and glutamic acids (Kraljevich, 1981). The mucopolysaccharides may be chondroitin sulphates or may contain sugars, such as glucose and mannose. A urinary mucoprotein discovered by Tamm and Horsfall was found at elevated levels in patients with renal stone disease. Another mucoprotein, matrix substance A, has been present in the matrix of infective stones (Pyrah, 1979).

1-2-2. Theories of Stone Formation

Several theories concerning stone formation have been prevalent--the matrix theory, supersaturation theory, and inhibitor or promoter theory. These will be discussed in the following paragraphs.

Because of the special structure of the colloid matrix in urinary stones (described above), the "matrix theory" of stone formation has been suggested. Boyce (1969, 1973) studied the relationship of the crystals to the laminar organic matrix and concluded that stones are formed by inclusion of the crystalline matter in a preformed organic matrix. Others suggested that aggregation of the small crystalline particles is the initial step and urinary macromolecules are then adsorbed onto the particle aggregates (Leal and Finlayson, 1977).

With the exception of matrix stones (stones without crystalline matter), most stones contain crystalline material. Calcification of the crystalline material requires the urine to be supersaturated with the crystalline mineral. This forms the basis of supersaturation theory of stone formation. For example, calcium oxalate stones are found in patients with hypercalciuria or with hyperoxaluria, the symptoms of excess calcium or oxalate in urine. Since the urine from

both the stone-formers and non-stone-formers are usually supersaturated with calcium oxalate and calcium phosphate (Coe, 1978), supersaturation of urine with respect to crystalline minerals is a necessary but insufficient condition for stone formation.

Either the matrix theory or the supersaturation theory alone cannot explain the stone formation. Yet, these two theories are not contradictory to each other when considered in the context of the inhibitor (promoter) theory. The inhibitor theory suggests that some substances in the urine of non-stone-formers inhibit stone formation even though the urine is supersaturated with respect to calcium oxalate or calcium phosphate. These inhibitors may be absent or present in smaller amounts in the urine of stone-formers. The deficiency in the concentration of inhibitors results in the formation of stones. The converse to this may be that the presence of some promoter materials in the urine of stone-former results in stones. Both the inhibitor and the promoter theories always emphasize the relationship of the urinary colloid (organic matrix) with the calcifying process.

Although inorganic substances such as pyrophosphate, citrate, and magnesium have been reported as being inhibitors of calcium oxalate crystallization, only five to 20 percent of the inhibition by urine is due to the presence of these inorganic substances (Gardner and Doremus, 1978). Studies of urinary mucopolysaccharide and mucoprotein inhibitors have been more prevalent. Among the substances studied are hyaluronic acid, chondroitin sulfate, heparin, ribonucleotides, and the acidic peptides containing aspartic or glutamic acid residues (Vermooten, 1956; Ito and Coe, 1977; Gjaldbaek, 1982; Drach et al., 1982). The Tamm-Horsfall mucoprotein and matrix substance A which were suggested as possible promoters to the formation of urinary stone were

found to behave as inhibitors of the growth of calcium oxalate crystals (Robertson et al., 1981).

The "free particle" theory describes one possible physical mechanism of stone formation. This theory suggests that small crystals are aggregated in the urinary tract to become large particles that become kidney stones. In studies of the urine of stone-formers and of normal persons both supersaturated with calcium oxalate, the crystals found in the urine of stone-formers were greater in number, larger in size, and included a larger fraction of aggregates (Rose, 1982; Pyrah, 1979).

Contrary to the free particle theory, evidence of the possibility of a nidus for stone formation--a fixed nuclei on the walls of renal system--supports the "fixed particle theory". In the fixed particle theory, a nidus may be formed on the tissue surface through heterogeneous nucleation or may be formed in the urinary system as free particles and then adsorbed or "glued" to the tissue possibly through the interaction of crystals and high molecular weight urinary materials (possibly the matrix type material or biopolymers) (Robertson, Scurr, and Bridge, 1981).

In vitro studies of the effects of these macromolecular substances on the chemical and physical mechanisms of the mineralization process may provide a clear understanding of the involvement of biopolymers in the etiology of kidney stone formation.

1-3. Stone Formation and Crystallization Mechanisms

The physicochemical study of urinary calculi formation, a biological mineralization process, is best described by crystallization theories. Supersaturation of the calculus mineral in the renal fluid

is required for the process to take place. In this work the process is envisioned as one in which nuclei are formed, and they grow and/or aggregate to form particles of the sizes which cause physiological problems.

In crystallization processes, supersaturation of the solute substances may be generated by cooling the saturated or undersaturated solution, by evaporating the solvent, or by mixing of two reactants to increase the solute concentration in solution. In this study, supersaturation of calcium oxalate was generated by mixing of calcium and oxalate solutions. By convention, such a process is called a precipitation process; however, the term crystallization has been used commonly in calcium oxalate urolithiasis studies. Crystallization and precipitation will be used interchangeably in this study.

Supersaturation is the necessary pre-condition for the crystallization process; therefore, a broad overview of supersaturation will be introduced followed by a review of nucleation, crystal growth, and crystal aggregation, the three major mechanisms of crystallization potentially important in kidney stone formation. A definition and calculation of supersaturation suitable for the calcium oxalate system will be discussed in Chapter 2.

1-3-1. Supersaturation

A saturated solution is the solution in equilibrium with the solid phase of the solute, which is the sparingly soluble salt, calcium oxalate, in this study. Solutions may be undersaturated or supersaturated with the solute depending on the amount of solute contained in the liquid phase. The supersaturated solution contains more solute than the amount of solute at equilibrium, and the

undersaturated solution contains less solute. Thermodynamically, this is described in terms of the activity and chemical potential.

The chemical potential of the solute in the liquid phase, μ , is related to the activity of the solute, a , by

$$\mu = \mu^* + RT \ln a \quad (1-1)$$

where R is the universal gas constant, T is the absolute temperature, and μ^* is the chemical potential at the reference state where the activity is 1.

At saturation, the chemical potential of the solute, μ_0 , is also related to its activity, a_0 , such that

$$\mu_0 = \mu^* + RT \ln a_0 \quad (1-2)$$

The activity of a solute in a supersaturated solution is higher than the activity at saturation, which is higher than the activity of the solute in an undersaturated solution. The same relationships pertain to the chemical potential. The chemical potential of the solute in an undersaturated solution will be increased by dissolving the solute from the solid phase. On the other hand, the higher value of the chemical potential in the supersaturated solution may be lowered by transferring solute from liquid phase to solid phase. In the latter process, solid phase is formed through either nucleation or chemical deposition, i.e., crystal growth.

1-3-2. Nucleation

Nucleation is the formation of new small particles from the solution phase. The chemical potential of a solute in a supersaturated solution provides the driving force for the formation of such a solid phase. The nucleation process results in a negative chemical potential

change. Because of the looser and weaker bonding of the ions or molecules at the surface of a solid phase compared to ions in the bulk solid volume, formation of a solid surface requires a positive free energy change; this excess energy is the surface tension of a macroscopic body. As a result, the total free energy change of a system due to formation of a solid phase is comprised of two parts: the free energy change resulting from transfer of solute from the liquid to solid phase and the surface free energy change. This may be written as (Nielsen, 1964)

$$\Delta G = (\mu_s - \mu)\Delta n + \sigma A \quad (1-3)$$

where ΔG is the total free energy change of the system, Δn is the number of solute molecules or ion pairs transferred from the liquid phase to the solid phase, σ is the surface energy per unit surface area, and A is the surface area of the newly formed particle. The process will occur spontaneously if the total free energy change is negative. Because of the positive surface energy term on the right hand side of Equation (1-3), nucleation may not necessarily occur in a supersaturated solution, i.e., the solution may be metastable. The region between saturation and the supersaturation where nucleation finally does occur is termed the metastable region (Finlayson, 1977).

When considered on a microscopic scale, ion or molecular clusters are formed and may be redissolved in a supersaturated solution under the following conditions. The smaller the cluster, the larger is the surface energy per unit mass. For the clusters having a size that possesses a surface energy resulting in a negative total free energy in Equation (1-3), the cluster will survive and grow in the supersaturated

solution. The size of the surviving clusters is called critical size, and such clusters are called nuclei.

Formation of nuclei may be termed as primary or secondary. Homogeneous and heterogeneous nucleation are primary. Formation of nuclei in a solution as the result of supersaturation alone is defined as homogeneous, and formation of nuclei in the presence of foreign particles is heterogeneous nucleation. Secondary nucleation requires the existence of crystals and is induced by small embryos generated by attrition from existing crystals either under the influence of fluid shear or from collision with other crystals, reactor wall, or propeller (McCabe, Smith and Harriott, 1985).

In the consideration of the energetics of the nucleation process, formation of nuclei from homogeneous nucleation requires a high supersaturation to compensate for the free energy required for the formation of a new surface. In heterogeneous or secondary nucleation, because of existing surfaces provided by the foreign particles or small embryos from attrition from crystals, nuclei may be formed in a solution of a relatively lower supersaturation, usually in the metastable region.

1-3-3. Crystal Growth

Supersaturation in a solution may also be relieved by the addition of solute to crystals existing in solution, a surface reaction that incorporates solute molecules or ion pairs into the crystal lattice. This is commonly referred to as crystal growth. The consumption of the solute material at the crystal surface due to the surface reaction results in a concentration difference between the bulk solution and the solid-liquid interface. This concentration difference provides a

driving force for mass transfer across the concentration gradient towards the crystal surface. This description of crystal growth is modelled as a two-step mechanism, a mass diffusion step and a surface reaction step. The process is diffusion-controlled if the growth rate is limited by the diffusion step; the process is surface-reaction controlled if the growth rate is limited by the lattice integration step (McCabe et al., 1985).

When the growth process is surface-reaction controlled, mass transfer resistance in the solution is negligible. Several theories describe the surface-reaction controlled crystal growth as reviewed by Ohara and Reid (1973) include the mononuclear, polynuclear, and birth and spread two-dimensional nucleation theories and the Burton-Cabrera-Frank (BCF) surface diffusion and dislocation model.

Two-dimensional nucleation theories suggest integration of crystals through surface formation of critical-sized embryos (surface nucleation) with assumption of zero, infinite, or intermediate growth velocity on the subsequent lateral spreading across crystal surfaces. However, growth rates predicted from these theories have been much too low in comparison to experimental data (ibid).

The widely used BCF surface diffusion and dislocation model suggests formation of crystals through growth spirals which originate at a screw or edge dislocation as shown in Figure 1-1. First, solute molecules are adsorbed on the flats between steps of the growth spirals. After migration to the steps under a surface concentration gradient, the molecules are then incorporated into kinks on the spiral steps (lattice incorporation). The physical reasoning and mathematical derivation of this theory has been carefully examined by Ohara and

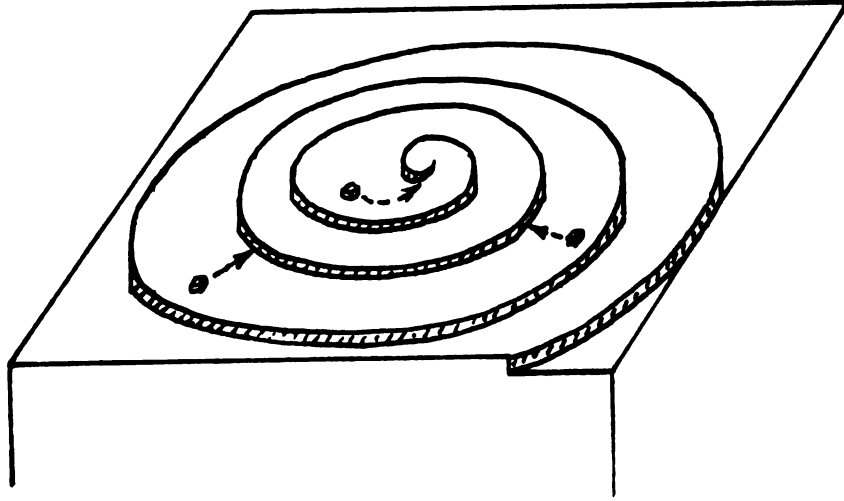


Figure 1-1 Screw dislocation on crystal surface and incorporation of solute molecules into crystal lattices.

Reid (ibid), and the linear growth rate normal to the crystal surface is expressed as:

$$G = C_6 T S_B \ln(1+S_B) \tanh[C_7 / T \ln(1+S_B)] \quad (1-4)$$

$$\text{where } C_6 = 2D_S C_{SE} k \beta \gamma_0 / 19 x_s \sigma \quad (1-5)$$

$$\text{and } C_7 = 19 \sigma V_m / 2 k x_s \quad (1-6)$$

The symbols used in the above equations are summarized below:

- T absolute temperature;
- S_B bulk supersaturation, $= (C_B - C_{BE}) / C_{BE}$;
- C_{BE} equilibrium concentration in the bulk solution;
- D_S surface diffusivity;
- C_{SE} equilibrium concentration of surface adsorbed molecules if the bulk supersaturation were unity;
- k Boltzmann constant;
- β a retardation factor relating bulk supersaturation and surface supersaturation;
- γ_0 kink retardation factor, related to ledge diffusion rates;

- x_s mean distance traveled by an adsorbed molecule before it desorbs;
- σ interfacial tension;
- V_m effective volume of a molecule.

When S_B is very low so that $\tanh(C_7/TS_B) \approx 1$, the growth rate model of Equation (1-4) predicts a second power dependence of growth rate to the bulk supersaturation, S_B . At larger S_B where $\tanh(C_7/TS_B) \approx C_7/TS_B$, the growth rate is linearly dependent on the bulk supersaturation.

In calcium oxalate crystallization studies, growth rate results have been reported in the form

$$\text{growth rate} = k_g s^b \quad (1-7)$$

where k_g is a proportional constant, and the growth rate and the independent variable, s , have several diverse definitions as shown in Table 1-1. Table 1-1 also shows the b values for each individual growth rate correlation and the growth rate predictions by the BCF theory.

1-3-4. Crystal Aggregation

Because of the excess energy confined within surface tension, a suspension containing many fine crystals is not thermodynamically stable. Particle size redistribution may take place by Ostwald ripening or by crystal aggregation. In the ripening process, smaller crystals dissolve to provide the solute concentration for larger ones to grow; in aggregation, smaller crystals aggregate to form larger ones. Both of these mechanisms result in changes of size distributions of crystal suspensions with respect to time (Nielsen, 1964). Crystal aggregation is more prevalent in the calcium oxalate crystallization process and is the focus of this section.

Table 1-1 Growth rate correlations of calcium oxalate crystals at 37°C.

[Growth rate, s, b]	
<u>BCF model</u> (Ohara and Reid, 1973)	
[G, S_B , Equation (1-4)]	for high S_B
[G, S_B , 2]	for $\tanh(C_7/TS_B) \approx 1$
[G, S_B , 1]	for $\tanh(C_7/TS_B) \approx C_7/TS_B$
G, S_B : described in context.	
<u>Meyer and Smith, 1975</u>	
$\left[\left(-\frac{d[Ca^{2+}]}{dt} \right), \left[[Ca^{2+}] - [Ca^{2+}]_0 \right], 2 \right]$	
$[Ca^{2+}]_0$: $[Ca^{2+}]$ at equilibrium.	
<u>Drach et al., 1978*</u>	
[G_L , $C-C_s$, 2.55]	
G_L : linear growth rate from MSMRP experiments (Section 1-4-3), $\approx 2G$;	
C : COD solubility concentration in the MSMRP process at steady state operation;	
C_s : COD solubility concentration at equilibrium.	
<u>Sheehan and Nancollas, 1980</u>	
$\left[\left(-\frac{dm}{dt} \right), (m-m_0), 2 \right]$	
m = $[CaC_2O_4]$;	
m_0 : m at equilibrium.	
<u>Tomazic and Nancollas, 1980</u>	
$\left[\left(-\frac{dT_{Ca}}{dt} \right), \left[\left([Ca^{2+}][C_2O_4^{2-}]y_2^2 \right)^{1/2} - K_{sp,COM} \right], 2 \right]$	
y_2 : activity coefficient of $[Ca^{2+}]$ and $[C_2O_4^{2-}]$;	
$K_{sp,COM}$: thermodynamic solubility product of COM.	
<u>Garside et. al., 1982</u>	
$\left[G_L, \left(\frac{([Ca^{2+}][C_2O_4^{2-}]y_2^2 - K_{sp})}{K_{sp}} \right), 2 \right]$	
G_L : linear growth rate from MSMRP experiments (Section 1-4-3), $\approx 2G$;	
K_{sp} : thermodynamic solubility product of COM or of COT.	
(cont'd.)	

Table 1-1 (cont'd.).

DeLong, 1988

$$\left[G, \left(\frac{[Ca^{2+}][C_2O_4^{2-}]y_2^2}{K_{sp,COM}} - K_{sp,COM}^{1/2} \right), \begin{matrix} (b-110, b-010, b-\underline{1}01) \\ (2.15, 2.20, 2.47) \end{matrix} \right]$$

The three b values are for COM growth on the respective crystal faces, 110, 010, and 101.

*: Temperature unknown.

In the discussion of biological crystallization, the terms aggregation and agglomeration are usually used interchangeably. A standardized nomenclature, however, was proposed by Randolph and Drach (1980) as follows: agglomerates are particles held by weak cohesive forces, such as electrostatic forces, and aggregates are held by strong intermolecular bondings. Agglomerates can be broken up by flow shear whereas aggregates cannot. The characteristics of aggregates were deemed to be more appropriate for this study.

According to the International Union of Pure and Applied Chemistry, colloids are defined as particles having sizes ranging from 1 to 1000 nanometers (1 μm) (Hirtzel and Rajagopalan, 1985). Although the primary calcium oxalate particles may be about 10 μm in size and the aggregates may be over 50 μm , the theories underlying both aggregation and colloid coagulation phenomena are fundamentally and physically the same and have been applied in this work.

The Deryaguin-Landau-Verwey-Overbeek (DLVO) theory describes coagulation of particles by considering repulsive and attractive forces of two interacting particles and explains the stability of particle aggregation or dispersion by the resultant total energy of the repulsive and attractive forces. The repulsive force of two approaching particles is due to the electrical charges surrounding each

single particle. The electrical environment of a particle in solution is discussed in the next section.

1-3-4-1. Diffuse Double-Layer of A Single Particle in Solution

The electrical environment of particles in electrolytic media has been described by the theory of diffuse double-layer (Sonntag and Streng, 1972; Hirtzel and Rajagopalan, 1985). In an electrolytic medium, the crystal surface may be positively or negatively charged depending on the concentration of potential determining ions, the ions that make up the crystal lattice. The "double-layer" is envisioned as two layers of charge localization-- one on the surface of the crystal and the other in a diffuse region spreading into the solution. For a negatively charged particle surface, the diffuse double layer is pictured in Figure 1-2.

Potential determining ions and other ions may be adsorbed on the particle surface to form an "inner Helmholtz layer". These specifically adsorbed ions in the inner Helmholtz layer are dehydrated or dehydrated at least in the direction closest to the particle. Counter ions, ions of charges opposite to the specifically adsorbed ions, surround the inner Helmholtz layer to form the Stern layer or outer Helmholtz layer. Outside the Stern layer is the Gouy layer, a diffuse electrical layer containing counter ions, specifically adsorbed ions, and indifferent ions. The density of counter ions is higher close to the Stern layer and decreases gradually until electroneutrality is established at some distance from the particle surface.

The potential energy profile of the diffuse double-layer is also shown in Figure 1-2, where ψ_0 is the surface potential and ψ_d is the Stern potential, the potential at the Stern layer (Shaw, 1980). The

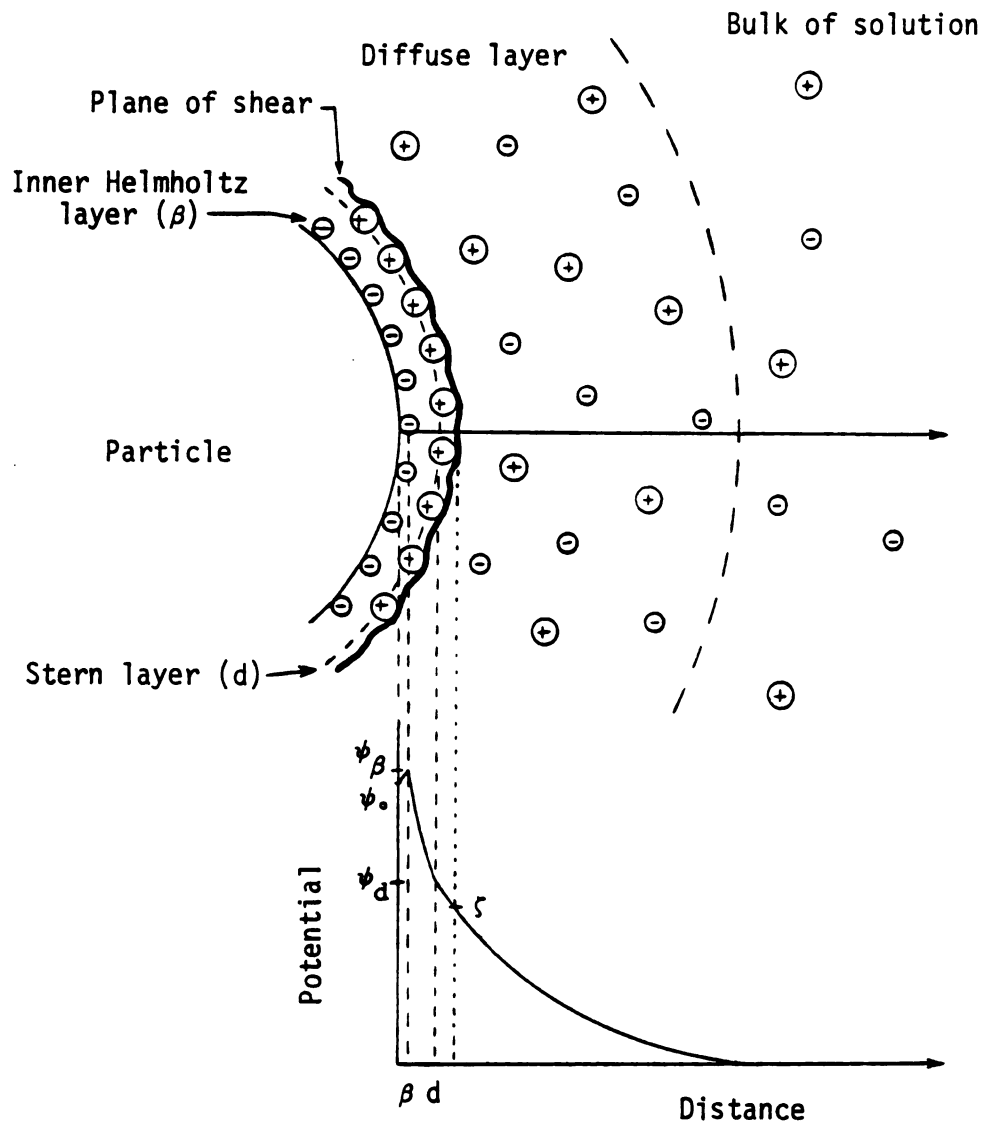


Figure 1-2 The diffuse-double layer and potential profile around a particle.

electrokinetic ζ (zeta) potential, the potential at the surface of shear, is experimentally obtainable from electrophoresis measurement. The Stern potential may be estimated by the ζ potential with small errors (ibid; Adair, 1981).

1-3-4-2. Repulsive Force of Two Approaching Particles

Because the crystal particles are surrounded by electrical charges, repulsive forces arise as a consequence of overlapping of the double layers when two particles approach each other. The interaction energy for two approaching particles may be described by the Poisson equation which relates net volume charge density to electrostatic potential and by the Boltzmann distribution which relates point charge density to electrical potential. The combined Poisson-Boltzmann equation has no exact analytical solution. Approximate solutions have been developed assuming two extreme cases for this interaction, maintenance of constant surface potential during the interaction and constant surface charge density. For two spherical particles with radii r_1 and r_2 , κr_1 and κr_2 (κ defined in Equation (1-11)) much greater than one, and ψ_d less than 50 mV, the repulsion potential for the constant charge case, V_R^σ , and for the constant potential case, V_R^ψ , are obtained (Shaw, 1980; Harnby et al., 1985; Hiemenz, 1986) from the following equations:

$$V_R^\sigma = -4\pi\epsilon \frac{r_1 r_2}{r_1 + r_2} \psi_d^2 \ln[1 - \exp(-\kappa H)] \quad (1-8)$$

$$V_R^\psi = 4\pi\epsilon \frac{r_1 r_2}{r_1 + r_2} \psi_d^2 \ln[1 + \exp(-\kappa H)] \quad (1-9)$$

where ϵ is the permittivity of the dispersion medium and H is the shortest distance between Stern layers. Since the dielectric constant

of a material, ϵ_r , is the ratio of its permittivity to the permittivity of vacuum, ϵ_0 , the permittivity ϵ may be expressed as

$$\epsilon = \epsilon_r \epsilon_0 \quad (1-10)$$

The parameter κ may be related to the concentration of ions in the solution according to (Hiemenz, 1986):

$$\kappa = \left(\frac{1000e^2 N_A}{\epsilon kT} \sum_i z_i^2 C_i \right)^{1/2} \quad (1-11)$$

where e is the unit electric charge, 1.6×10^{-19} Coulombs, N_A is the Avogadro's number, 6.02×10^{23} , and z_i and C_i are the charge and concentration of the ionic species i , respectively. The summation term in Equation (1-11) is twice the ionic strength, I , and may be replaced with $2I$.

The parameter κ in Equations (1-8) and (1-9) has the unit of reciprocal length; therefore, κ^{-1} has units of length and is a measure of the thickness of the double layer. Since κ is proportional to \sqrt{I} , the thickness of double layer decreases with increase of ionic strength in solution.

1-3-4-3. Attractive Force Between Two Particles

Particles are attracted to each other under the influence of van der Waals force. The van der Waals force, or London dispersion force, is the interaction of the induced dipoles from the molecules of each particle. At large particle separations, due to the propagation of the electromagnetic interaction by the speed of light, the van der Waals attraction is retarded. For spherical particles at the separation, H , smaller than ca. 10 nm, the potential energy of the non-retarded van der Waals force are (Vold and Vold, 1983; Hiemenz, 1986)

$$V_A = - \frac{A}{6} \left[\frac{2 r_1 r_2}{R^2 - (r_1 + r_2)^2} + \frac{2 r_1 r_2}{R^2 - (r_1 - r_2)^2} + \ln \frac{R^2 - (r_1 + r_2)^2}{R^2 - (r_1 - r_2)^2} \right] \quad (1-12)$$

where A is the van der Waals-Hamaker constant and R is the separation distance between the centers of the spheres.

For two slab-shaped particles of the same size, the energy of van der Waals forces (Vold, 1954) shows a preferred approach between particles--with the wide sides facing each other and the long axes parallel rather than perpendicular to each other. For the particles with width w, thickness $c_t w$, and length $c_l w$ and the long axes parallel to each other, this attraction energy is (ibid)

$$V_A = - \frac{A c_l w}{12\pi} \left[\frac{(w^2 + H^2)^{3/2}}{w^2 H^2} + \frac{(w^2 + (H + 2c_t w)^2)^{3/2}}{w^2 (H + 2c_t w)^2} - \frac{2(w^2 + (H + c_t w)^2)^{3/2}}{w^2 (H + c_t w)^2} \right] + \frac{A c_l w}{8\pi} \left[\frac{1}{H} + \frac{1}{H + 2c_t w} - \frac{2}{H + c_t w} \right] \quad (1-13)$$

This equation is valid for the distances H smaller than the length of particles. H is the shortest distance between the Stern layers of two approaching particles.

For particles of the same volume, particles of slab shapes exhibit greater attraction energy than spherical particles. At large distances of separation, there is no difference between Equations (1-12) and (1-13), and both equations approach the attraction law for atoms, which is

proportional to the inverse of particle separation to the sixth power (ibid).

1-3-4-4. Total Energy of Two Interacting Particles and Stability of Particle Aggregation and Dispersion

The total energy of interaction of two approaching particles is the sum of the repulsion and attraction energies:

$$V_T = V_A + V_R \quad (1-14)$$

Figure 1-3 illustrates the energy distribution as a function of H . The total energy curve as shown in Figure 1-3 helps explain the formation and stability of aggregates or the stability of a dispersed system.

A positive potential energy is a repulsive force, and a negative potential energy is an attractive force. A system tends to lower its total energy. From the illustration in Figure 1-3, two particles may form strong aggregates at a small interparticle distance, the "primary minimum", after overcoming the energy barrier of the positive maximum of the total energy. The higher the energy maximum, the greater the energy barrier. On the other hand, reversible flocculation may occur at a larger interparticle distance at the secondary minimum as seen on the total energy curve.

In a system without shear, aggregates or flocs are formed under the influence of the thermal energy, kT . If the positive energy maximum is higher than the thermal energy, the dispersed system stays stable, i.e., no aggregation takes place, or vice versa. The stability of the floc structure also depends on the depth of the secondary minimum compared to the thermal energy. Since the van der Waals forces are greater for larger particles, flocculation may be dominant as a consequence of a deeper secondary minimum for the larger particles.

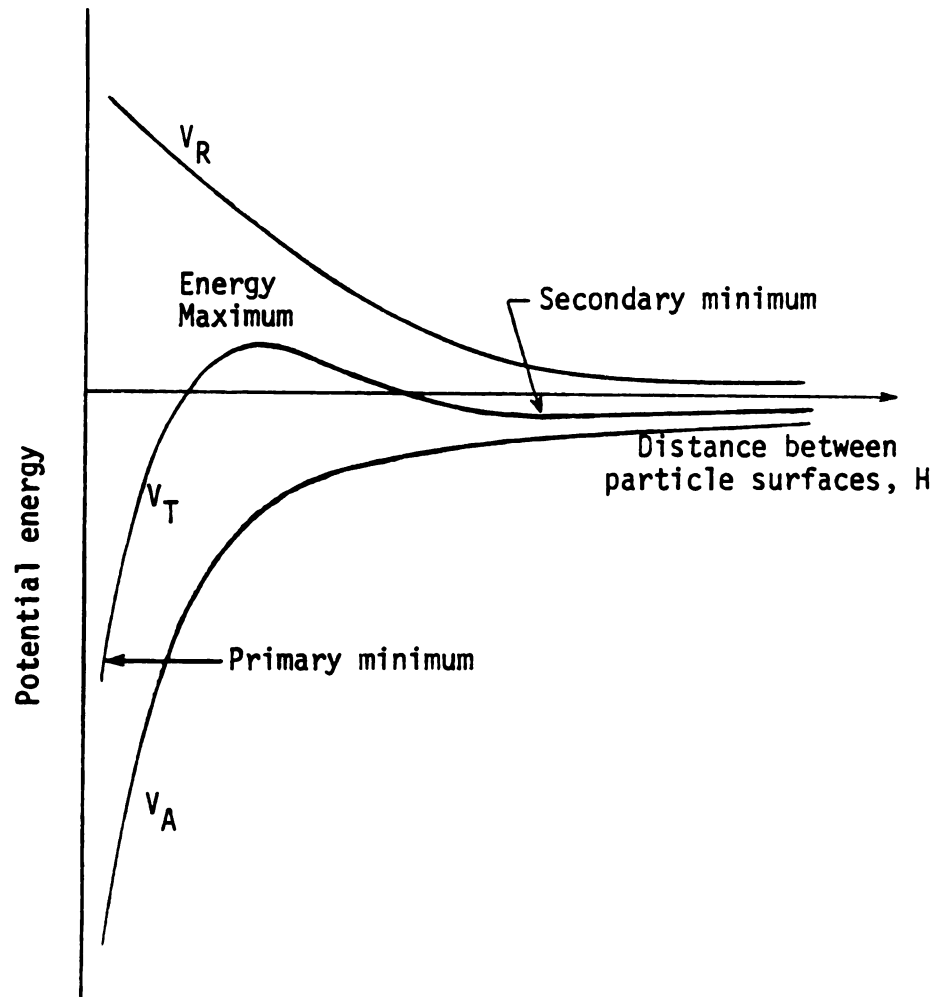


Figure 1-3 Interaction energy of particles at distance H .

However, in systems under shear, floc structures are not likely to persist against the flow shear. Formation of strongly bonded aggregates is the main concern in the crystallization system of this study where flow shear is present.

1-3-4-5. Kinetics of Aggregation

The energy status of the particles determines thermodynamically the possibility of forming aggregates; the kinetic aspect--how quickly aggregates are formed--is determined by the collision rate of particles. By assuming that aggregates are formed by binary collisions, the kinetics of particle aggregation may be modelled similarly to the bimolecular reaction (Hansen, 1975).

The rate of aggregation is proportional to the frequency of particle collisions which is proportional to the concentration of particle numbers. The aggregation rate $B(v_1, v_2)$, is therefore expressed as

$$B(v_1, v_2) = \beta(v_1, v_2) n(v_1) n(v_2) \quad (1-15)$$

where $\beta(v_1, v_2)$ is the collision frequency factor and $n(v_1)$ and $n(v_2)$ are the number concentrations of particles of volumes v_1 and v_2 , respectively. The particles may be brought together by Brownian diffusion, known as perikinetic (non-agitated) aggregation, or by orthokinetic (agitated) aggregation.

For Brownian motion, the collision frequency factor, the kernel, has been derived by von Smoluchowski for spherical particles as (Drake, 1972):

$$\beta_B(v_1, v_2) = \frac{2kT}{3\mu} \left(v_1^{1/3} + v_2^{1/3} \right) \left(v_1^{-1/3} + v_2^{-1/3} \right) \quad (1-16)$$

where μ is the fluid viscosity.

In a turbulent flow, collision of particles due to the dissipation rate of turbulence and particle inertia causes orthokinetic aggregation. For colloids aggregating in an agitated tank reactor, it may be assumed that particles follow the fluid flow fairly well. As a result, aggregation due to particle inertia is not significant (Hartel and Randolph, 1986).

For particles smaller than the length scale of the small turbulent eddies, the collision frequency factor for particles aggregating in isotropic turbulence is given as

$$\beta_T(r_1, r_2) = \alpha (r_1 + r_2)^3 \bar{G} \quad (1-17)$$

where \bar{G} is the mean velocity gradient in the turbulent fluid and is related to the average turbulent energy dissipation rate per unit mass, $\bar{\epsilon}$, and the kinematic viscosity of the fluid, ν , according to

$$\bar{G} = \left(\frac{\bar{\epsilon}}{\nu} \right)^{1/2} \quad (1-18)$$

The kinematic viscosity is $\nu = (\mu/\rho)^{1/2}$, and ρ is the density of the fluid.

The turbulent collision frequency factor in terms of particle volume becomes

$$\beta_T(v_1, v_2) = \alpha \left(\frac{3}{4\pi} \right)^{1/3} \left[v_1^{1/3} + v_2^{1/3} \right]^3 \left(\frac{\bar{\epsilon}}{\nu} \right)^{1/2} \quad (1-19)$$

Several different values of the leading coefficient α in Equations (1-17) and (1-19) found in the literature are summarized in Table 1-2.

Equations (1-17) and (1-19) are valid for isotropic turbulent flow with particles smaller than the small eddies of the turbulence. In an agitated tank, the flow becomes isotropically turbulent when a modified Reynolds number is higher than 10^4 (Shinnar, 1961; Perry and Chilton,

Table 1-2 Values for α .

α value	Reference
$\frac{4}{3}$	(Camp and Stein, 1943)
1.67	(Saffman and Turner, 1956)
1.25	(Beal, 1972)
$\left(\frac{1}{15}\right)^{\frac{1}{2}} \pi$ (= 0.811)	(Delichatsios and Probstein, 1975)
1.67	(Yuu, 1985)

1973). The dimensionless modified Reynolds number for an agitated tank is defined as

$$Re_T = \frac{ND_a^2 \rho}{\mu} \quad (1-20)$$

where N is the propeller speed in revolutions per second and D_a is the diameter of the propeller.

The length scale of small eddies is described by the Kolmogorov microscale, λ , given as (Delichatsios and Probstein, 1975; Shinnar, 1961)

$$\lambda = \left(\frac{\nu^3}{\epsilon} \right)^{\frac{1}{4}} \quad (1-21)$$

Considering Brownian diffusion and turbulent diffusion in addition to the total potential energy of two interacting particles, the rate constant for aggregation is expressed as (Shaw, 1980; Voigt 1986; Hunter 1987)

$$\beta(v_1, v_2) = \frac{\beta_B(v_1, v_2) + \beta_T(v_1, v_2)}{W(r_1, r_2)} \quad (1-22)$$

where $W(r_1, r_2)$, the stability factor, is

$$W(r_1, r_2) = 2 \int_2^{\infty} \frac{\exp(V_T/kT)}{s^2} ds \quad (1-23)$$

and $s = 2 [1 + H/(r_1 + r_2)]$.

The aggregation rate constant described by Equation (1-22) can be estimated numerically. With the particle size distributions experimentally observed in a crystallization system, changes (increases or decreases) in number density of particles at certain sizes may be characterized by Equation (1-15). These may be used with the population balance equation to simulate the particle size distribution in a crystallization system. The relevant population balance equation and functions describing particle density will be discussed in Chapter 3.

1-4. Review of Experimental Methods

This section will review briefly several experimental methods used in the study of stone formation and the effects of inhibitor substances (mostly organic macromolecules) on calcium oxalate crystallization. In these methods, studies were carried out with either batch or continuous experiments. Crystallization mechanisms were characterized by measuring turbidity, calcium or oxalate depletion (concentration), or particle size distribution.

1-4-1. Batch Experiments

Robertson and Peacock (1972) studied calcium oxalate crystal growth and aggregation by observing the changes of particle size distributions of calcium oxalate crystals with time. The crystals were incubated in metastable calcium oxalate solutions with or without the

addition of 5% urine. The metastable solution was prepared to allow the seeded COM crystals to grow but to avoid spontaneous nucleation. During 4 hours of incubation, the seed particles grew and aggregated. This was seen in an increase in particle numbers at a larger particle size, e.g., 20 μm . A fractional rate of growth and aggregation was calculated from the increase of numbers of particles at 20 μm in the solution containing 5% urine compared to the increase in solution containing 5% NaCl, such that

$$\text{fractional rate of growth and aggregation} = \frac{(N_{20 \mu\text{m}, 4 \text{ hr.}} - N_{20 \mu\text{m}, 0 \text{ hr.}})_{5\% \text{ urine}}}{(N_{20 \mu\text{m}, 4 \text{ hr.}} - N_{20 \mu\text{m}, 0 \text{ hr.}})_{5\% \text{ NaCl sol'n}}} \quad (1-24)$$

The tests with urine from stone-formers showed higher fractional rates of growth and aggregation than with normal urine.

Felix and his coworkers (1977) produced calcium oxalate aggregates following the method of Robertson and Peacock except that the crystals were incubated for 2 hours to evaluate the inhibiting activity of urine. Aggregation was tested by filtering suspensions through an "agglomerator", a filter of 20 μm pore size operated under a constant pressure 100 mm Hg. The volumes of suspension filtered in 2 seconds were recorded to evaluate the percentage of aggregation relative to the inhibiting activity of urine according to

$$\% \text{ aggregation} = \frac{V_0 - V_u}{V_0 - V_c} \quad (1-25)$$

where V_0 is the volume filtered in 2 seconds for a suspension before incubation, V_u is the volume filtered for the suspension incubated in the solution with inhibiting substances, and V_c is the volume filtered for a suspension incubated in the solution absent of inhibiting compounds (control). Their results show that the inhibition of

aggregation by 10% urine was close to the inhibition by 100% urine. Orthophosphate and magnesium at concentrations found in urine, citrate at 10^{-4} M, pentanemonophosphonate, and uromucoid had no effect in inhibiting aggregation. Through a series of ultrafiltration, fractionation, and gel-filtration steps, the inhibitor in urine was isolated and tested; the inhibitory activity of urine was attributed to the macromolecules in urine larger than 10,000 daltons.

Bowyer, Brockis, and McCulloch (1979) also used the same technique as Robertson and Peacock (1972) to measure the rate of crystal growth and aggregation. A mixture of glycosaminoglycans was isolated from urine and showed the same inhibitory effect as a 1% urine solution. The glycosaminoglycans were identified as chondroitin 6-sulphate and chondroitin 4-sulphate by infra-red spectroscopy studies. Further tests of the crystal growth and aggregation rate with the commercially available chondroitin 6-sulphate and chondroitin 4-sulphate gave inhibition identical to the glycosaminoglycans and 1% urine solutions.

This batch reactor scheme with seeded COM crystals was also adopted by Nakagawa et al. (1983) to measure the growth rate of COM crystals by the depletion rate of 14 C-labeled oxalate. The oxalate depletion rate was found to be proportional to the second power of the concentration difference of oxalate at the reaction time and at equilibrium. A highly acidic glycoprotein with molecular weight 1.4×10^4 was found to inhibit the growth rate of COM crystals. The change in the rate constant for crystal growth with the inhibitor concentration followed a Langmuir adsorption isotherm. This suggests that the inhibition effect is due to the adsorption of inhibitor on crystal surfaces which prevents further crystal growth. An assay of amino acid content of the isolated glycoprotein inhibitor was found to

be rich in aspartic acid, threonine, serine, glutamic acid, and glycine and contained about two γ -carboxyglutamic acid residues.

1-4-2. Constant Composition Method

Sheehan and Nancollas (1980) suggested a constant composition method for studying the kinetics of crystal growth by measuring the amounts of calcium and oxalate solutions added to a slurry of growing calcium oxalate crystals. The calcium and oxalate solutions were added to maintain constant calcium and oxalate concentration levels in a seeded reaction vessel. Calcium concentrations in the reaction vessel were monitored by a calcium selective electrode in the reaction vessel and an automatic titrator was activated to add calcium and oxalate solutions to return the calcium concentration to its set point. The crystal growth rate, determined from the amount of solution added, was found to be proportional to the second power of the excess calcium oxalate concentration in the solution.

With the constant composition method, Lanzalaco et al. (1988) investigated the effect of urinary macromolecules on COM crystal growth. The macromolecular additives tested include pre-bladder urine, normal urine, the macromolecular fractions of these urines, and macromolecules extracted from the matrix of both kidney stones and bladder stones. The inhibitory activity of the additives was defined in terms of growth rate in the absence of additive, R_0 , and the growth rate in the presence of additive, R_i , according to

$$\% \text{ inhibition} = 100 (R_0 - R_i)/R_0 \quad (1-26)$$

Their results show that pre-bladder urine and normal urine have equal inhibitory effects on COM growth. The macromolecular components

fractionated from urine and from stone matrix also inhibited the growth of COM.

1-4-3. MSMPR Crystallizer

One of the major areas of study in understanding the physicochemical etiology of urolithiasis is the use of the continuous mixed-suspension mixed-product removal (MSMPR) crystallizer for simulating the kidney. Finlayson (1977) initiated this approach due to the similarity between the operation of kidney and the continuous crystallizer system. Since the MSMPR crystallizer has been widely used in crystallization industry, the theories of crystallization mechanisms and crystal characterization as related to this system have been well documented (Randolph and Larson, 1971).

For the study of calcium oxalate crystallization, the MSMPR crystallizer system is a continuously stirred crystallization vessel with two feed streams, one stream for calcium and the other for oxalate. The concentrations in the feed streams are prepared such that the mixed solution is supersaturated with calcium oxalate. The two streams of reactants are fed continuously to the reactor vessel where calcium oxalate crystals are precipitated. The crystals and mother liquor are well mixed and withdrawn continuously from the reactor to maintain a constant suspension volume in the reactor. It is assumed that calcium oxalate crystallization does not change the total volume of suspension; therefore, the total flow rate of the inlet streams is equal to the flow rate of outlet stream. The suspension has an constant average retention time in the reactor, or residence time (τ), which is calculated as the reactor volume divided by the flow rate (in or out). In steady-state operation, temperature, flow rates, volume of

suspension in the crystallizer, chemical composition, pH, and crystal size distribution are all constant with respect to time and position in the reactor.

The crystal size distribution (CSD) or particle size distribution (PSD) of the crystals generated in the MSMPR crystallizer system may be described by the population balance equation (Randolph and Larson, 1971):

$$\frac{\partial n(L,t)}{\partial t} + \frac{\partial(G_L n(L,t))}{\partial L} + \frac{n(L,t)}{\tau} = 0 \quad (1-27)$$

where $n(L,t)$ is the particle (crystal) population density as a function of particle size, L , and time t . G_L is the crystal growth rate, $\frac{dL}{dt}$. The growth rate, G_L , is the increase of particle diameter, or equivalent spherical diameter, with respect to time. This should be distinguished from the growth rate defined as the increase of total precipitate mass or volume with time or the increase in moles of calcium oxalate precipitate per unit area of seed surface with time. The latter definitions are usually used in the studies in which crystal "growth rate" is determined from the depletion of reactants in solution with time.

If the growth rate, G_L , is independent of crystal size, L , the population balance equation describing the steady state MSMPR operation becomes

$$G_L \frac{dn(L)}{dL} + \frac{n}{\tau} = 0 \quad (1-28)$$

After integration, this becomes

$$\ln n(L) = \ln n(0) - \frac{L}{G_L \tau} \quad (1-29)$$

where $n(0)$ is the population density at zero size. The population density, $n(L)$, is usually obtained experimentally from counting

crystals or particles with an electronic sizing instrument. Typical sizing instruments allow acquisition of $n(L)$ data within a limited size range. Linear regression of the acquired $n(L)$ data on a natural log scale results in a straight line with slope $\left(-\frac{1}{G_L \tau}\right)$ and intercept $[\ln n(0)]$. With known τ , the growth rate, G_L , may be calculated from the slope. This type of representation, $\ln n(L)$ or $\log n(L)$ data versus L , is called the population density plot. It should be noted, however, that the growth rate obtained in this analysis is the actual growth rate of crystals only if no other competing phenomena (e.g. aggregation, crystal breakage) exist in the crystallizer.

The intercept of the population density plot or the population density at zero size, is the nucleation rate, B_0 . It may be calculated according to (Randolph and Larson, 1971):

$$B_0 = n(0) G_L \quad (1-30)$$

This technique of using the MSMPR crystallizer to estimate linear crystal growth rate and nucleation rate has been adopted by many researchers in studying modifiers of calcium oxalate crystallization. Drach and his coworkers (1978) were among the pioneers of this technique in their work with COD crystallization. COD crystals were formed in the synthetic urine supersaturated with calcium oxalate (the control), and two modifiers, pyrophosphate and methylene blue, were tested for their effect on nucleation rate, growth rate, and total crystal mass generated. The total crystal mass is the total calcium oxalate precipitated per time, including the crystals in suspension and the crystals fouling the reactor walls. Both modifiers were found to have significant inhibitory effect on nucleation rate and total crystal mass; COD growth rates with the modifiers were higher than the control.

It was also suggested that the inhibition of nucleation rate might be correlated to the inhibition of crystal aggregation, although aggregation was not measured.

Drach, Thorson, and Randolph (1980) then investigated COD crystallization under the effects of urinary macromolecules, including urine from calcium oxalate stone-formers and from healthy persons. For these experiments, the MSMPR crystallizer system was run with 95% synthetic urine (a solution prepared to mimic urine) plus 5% natural urine. Their results show that addition of both normal (Nl) and stone-former (SF) urines inhibited linear growth rate and enhanced nucleation rate of COD. Both urines had equally significant inhibition on the total crystal mass. Crystal growth rate was lower with SF urine, but nucleation rate was higher. The addition of uromucoid, a high molecular weight mucopolysaccharide, also inhibited growth rate and enhanced nucleation rate, though there was no effect on the total crystal mass. It was hypothesized that uromucoid may contribute to the difference between Nl urine and SF urine.

To focus on the differences between the urine of Nl and of SF, Drach, Kraljevich, and Randolph (1982) separated urinary macromolecules into low molecular weight macromolecules (LMWMM, <30,000 daltons) and high molecular weight macromolecules (HMWMM, >50,000 daltons). Macromolecules between 30,000 and 50,000 daltons were not recovered from either SF or Nl urine. The urine of SF contained much more HMWMM than Nl urine, but SF urine had no LMWMM. Experiments with COD crystallization in synthetic urine showed that the LMWMM from Nl had no effect on COD nucleation rate and growth rate. Both SF and Nl HMWMM had equal effects on nucleation rate and growth rate, but SF HMWMM reduced significantly the total solid concentration produced in the

crystallizer (total crystal mass). It was decided that the higher concentration of HMWMM in the SF urine must play an important role in decreasing the linear crystal growth rate and increasing the nucleation rate when compared to the control for which urinary macromolecules were not added.

Randolph and Drach (1981) extended the MSMPR technique to observe the effects of osmolarity, calcium and oxalate concentrations, urea, and magnesium on COD crystallization in synthetic urine. The crystal growth rate, nucleation rate, and the total solids produced in the crystallizer were found to be reduced by decreases in calcium and oxalate concentrations. However, changes in osmolarity and urea and magnesium additives did not affect COD crystallization significantly as had been observed with the addition of urinary macromolecules.

In further investigations of the urinary inhibitors using an MSMPR crystallizer, Drach, Sarig, and their coworkers (1982) found that the addition of polylysine did not have a significant effect on COD crystallization. The addition of both heparin and polyglutamate, however, increased nucleation rate and decreased linear growth rate, average crystal size, and the total mass of the COD crystals formed in synthetic urine; polyglutamate had a more marked effect. Addition of polyglutamate also decreased the deposition of calcium oxalate precipitates on the wall of the crystallizer, which is a common problem in calcium oxalate crystallization in an MSMPR crystallizer (Drach, Randolph, and Miller, 1978; Randolph and Drach, 1981; Drach, Sarig, et al., 1982; Garside et al., 1982).

In the MSMPR crystallizer studies described above, linear population density distributions were assumed in analyzing steady state particle size distributions, where crystal aggregation or agglomeration

was neglected. However, curved population density distributions obtained from steady state calcium oxalate crystallization (illustrated in Figure 1-4) were observed (Garside et al., 1982; Brecevic and Garside, 1982; Robertson and Scurr, 1986). Robertson and Scurr considered the curved population density plots to be an indication of particle agglomeration. Based on the binary collision theory, a linear population density distribution of the predicted nonagglomerated crystals, n_{pred} , was calculated from the curved distribution, n_{obs} , by computer simulation. The degree of agglomeration, A , was defined as:

$$A = \frac{(\sum n_{pred} - \sum n_{obs})}{(\sum n_{pred} - 1)} \quad (1-31)$$

The inhibition of agglomeration, $IN(A)$, was then calculated from A_c and A_t , the degree of agglomeration for the control and for the tested additive, respectively, such that

$$IN(A) = \frac{(A_c - A_t)}{A_c} \quad (1-32)$$

For the evaluation of nucleation rate, linear growth rate, and total crystal mass, Robertson and Scurr followed the analyses for the steady state linear population distribution. Several modifiers of calcium oxalate crystallization were tested with synthetic urine. For additives within their urinary concentration range, the results are summarized as follows: magnesium and citrate slightly inhibited linear growth rate and crystal mass. Pyrophosphate only inhibited crystal growth rate but to an insignificant degree. Chondroitin sulphate, ribonucleic acid, and heparin inhibited crystal growth, degree of agglomeration, and crystal mass production. Among these modifiers, ribonucleic acid acted most strongly.

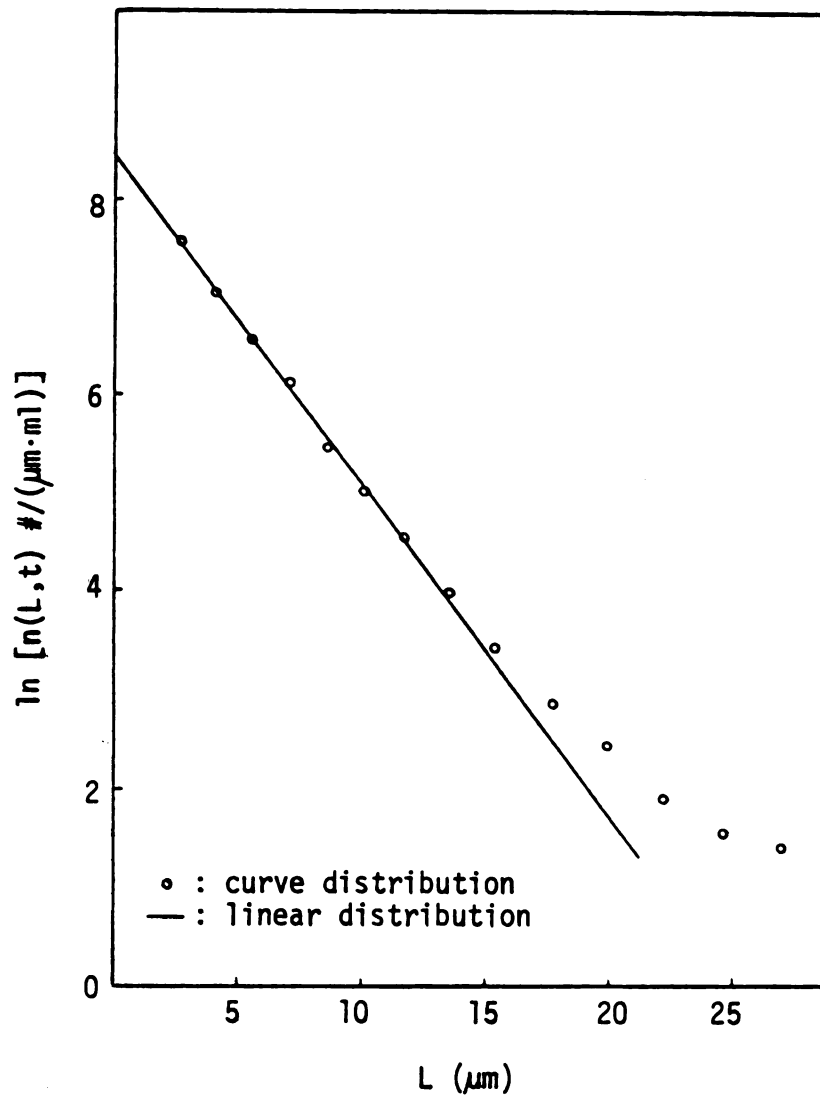


Figure 1-4 Semi-log population density plot;
linear and curved distributions.

1-4-4. Single Crystal Growth

Special attempts have been successfully made to study the growth of calcium oxalate crystals without interference from other types of crystallization phenomena. DeLong (1988) used a growth cell to measure the facial linear growth rates of single calcium oxalate crystals. The growth cell is a small (≈ 5 ml) isothermal chamber in which single crystals can be observed and photographed with a light microscope. Calcium and oxalate solutions were mixed in a T-junction and then introduced into the cell chamber. The mixed solution was supersaturated with calcium oxalate, so that crystal nuclei formed on the observation platform (a glass cover slip) installed in the chamber. The nuclei then grew in the supersaturated solution. Photographs were taken in a time sequence, and the growth rates of crystals were calculated from changes in linear dimensions of the photographed crystal sizes with respect to time. COM was the major crystal phase studied. The results showed that presence of the macromolecular additives, polyglutamate and heparin, inhibit single COM crystal growth. The advantage of this technique is that it allows the effects of macromolecular modifiers on crystal growth to be evaluated separately from their effects on nucleation or on aggregation.

1-5. Scope of Research

The research conducted in this study had the ultimate goal of understanding the physical and chemical formation of kidney stones. Since urinary macromolecules have been shown to be important in modifying calcium oxalate crystallization, the purpose of the work was to elucidate the effects of these macromolecules on each step of the stone formation mechanisms. To this end, the MSMPR crystallization

system was chosen for its similarity to crystallization in the human kidney--i.e. that the stone constituents are supplied continuously to the reacting volume, that crystals are formed through nucleation, crystal growth, and/or crystal aggregation, and that the mixture of crystals and mother liquor are continuously withdrawn from the reacting volume.

The MSMPR crystallizer system also has some advantages over the batch system. Because of the continuous supply of calcium and oxalate solutions from the feed streams, supersaturation and, subsequently, growth rate in the crystallizer do not decrease as rapidly as in a batch reactor. Besides, the prolonged process of MSMPR operation makes possible the observation of crystallization mechanisms with several samplings, while sampling from batch reactors is limited by the total reacting volume and by the relatively brief reaction time for calcium oxalate precipitation. Because of the problem of crystal fouling on the calcium electrode, the constant composition method was not considered the method of choice either.

The MSMPR crystallization system was adopted to characterize calcium oxalate crystallization. A complete population balance equation including an aggregation term was chosen to model the crystal size distributions instead of the simple steady state model leading to the linear population density distribution. The crystal growth rate was isolated from the particle distribution data in which both crystal growth and crystal aggregation were superimposed.

The effects of tissue surface on crystal growth were also investigated due to the attention drawn to this interaction by the fixed particle theory of stone formation. It was hypothesized that injured kidney cells may provide the attachment site for a stone nidus

or that injured cells or healthy cells may have promotive or inhibitory effects on nucleation and crystal growth. To provide insight to these questions, experiments were conducted using Maden Darby Canine Kidney (MDCK) cells and the photomicroscopic technique for observation of single crystal growth. The growth cell from the photomicroscopic technique was modified to allow observation of calcium oxalate crystals and the kidney cells under a fully developed laminar flow. Several chemical methods of injury to MDCK cells were evaluated for their resultant effects on nucleation and growth of calcium oxalate crystals.

Because of the importance of supersaturation in the crystallization process, calculation of supersaturation for the systems used in this work is addressed in Chapter 2. The MSMPR crystallization is best described by the population balance equation which requires particle size distribution data, accurate measurement of particle size is needed. The particle size distributions and population balance equation pertinent to describing the MSMPR crystallizer system and accurate determination of particle size distributions will be discussed in Chapter 3. Experiments using the MSMPR crystallizer system are the main issue of Chapter 4; the effects of MDCK cells on calcium oxalate growth is addressed in Chapter 5. The summary of this work and recommendations for future research are described in Chapter 6.

CHAPTER 2

SUPERSATURATION IN ELECTROLYTE SOLUTIONS

Supersaturation is a quantity of importance in the study of calcium oxalate crystallization. It is the driving force for nucleation and for crystal growth. Calcium oxalate supersaturations must be known to quantify and understand the precipitation phenomena observed in this study. Because solution saturation is a reference state for supersaturation, saturation of calcium oxalate will be discussed first followed by a discussion of supersaturation and ion complexation.

2-1. Saturation

Calcium oxalate, the sparingly soluble salt of interest in this work, forms three hydrates depending on solution concentrations, temperature, and pH. The three hydrates are calcium oxalate monohydrate (COM), calcium oxalate dihydrate (COD), and calcium oxalate trihydrate (COT) (Garside et al, 1982; Tomazic and Nancollas, 1979; Gardner, 1975). When any of these calcium oxalate hydrates is in equilibrium in solution, the solution is considered to be saturated with that hydrate. Thermodynamic solubility products of the phases in the saturated solutions are defined as

$$K_{sp,hydrates} = (Ca^{2+})_{eq} (C_2O_4^{2-})_{eq} \quad (2-1)$$

where $(Ca^{2+})_{eq}$ and $(C_2O_4^{2-})_{eq}$ are the activities of calcium and oxalate free ions in the saturated solutions, respectively. The K_{sp} values at human body temperature (37°C) are listed in Table 2-1.

Table 2-1 Thermodynamic solubility products of calcium oxalate hydrates at 37°C.

Hydrate	$K_{sp} \times 10^9$	Reference
$\text{CaC}_2\text{O}_4 \cdot \text{H}_2\text{O}$ (COM)	2.51	Garside et al., 1982
$\text{CaC}_2\text{O}_4 \cdot 2\text{H}_2\text{O}$ (COD)	5.01	Nancollas and Gardner, 1974 Gardner, 1975
$\text{CaC}_2\text{O}_4 \cdot 3\text{H}_2\text{O}$ (COT)	7.88 (8.2)	Tomazic and Nancollas, 1982 (Garside et al., 1982)

2-2. Definition of Supersaturation

For solutions having higher calcium oxalate activity products than K_{sp} , the solutions are supersaturated with respect to calcium oxalate. Formation of calcium oxalate crystals occurs through nucleation and crystal growth to reduce the solution activity product to the equilibrium value. To quantify the driving force for nucleation and crystal growth in the solutions supersaturated with the electrolytic calcium oxalate solute, conventional definitions of supersaturation will be reviewed and re-evaluated for the specific case of calcium oxalate crystallization.

The conventional supersaturation ratio for molecular solutes is expressed in terms of the activities of solute in the supersaturated solution and at equilibrium, a and a_0 , which is

$$\text{supersaturation ratio} = \frac{a}{a_0} \quad (2-2)$$

Finlayson (1977) defined a relative supersaturation as the ratio of activities of the associated calcium oxalate ion pairs similar to Equation (2-2), i.e.,

$$\text{relative supersaturation} = \frac{(\text{CaC}_2\text{O}_4)}{(\text{CaC}_2\text{O}_4)_{\text{eq}}} \quad (2-3)$$

where (CaC_2O_4) and $(\text{CaC}_2\text{O}_4)_{\text{eq}}$ are the activities of calcium oxalate ion pair in supersaturated and in saturated solution, respectively. A value of 6.16×10^{-6} M for $(\text{CaC}_2\text{O}_4)_{\text{eq}}$ was used by Finlayson.

Garside et al. (1982) defined the supersaturation in terms of the activity products of calcium oxalate as

$$\text{supersaturation} = \frac{(\text{Ca}^{2+})(\text{C}_2\text{O}_4^{2-}) - K_{\text{sp,hydrate}}}{K_{\text{sp,hydrate}}} \quad (2-4)$$

Gardner (1978) and Gardner and Doremus (1978) defined a relative supersaturation according to

$$\text{relative supersaturation} = \frac{([\text{Ca}^{2+}][\text{C}_2\text{O}_4^{2-}])^{1/2} - \frac{(K_{\text{sp,hydrate}})^{1/2}}{y_2}}{\frac{(K_{\text{sp,hydrate}})^{1/2}}{y_2}} \quad (2-5)$$

where $[\text{Ca}^{2+}]$ and $[\text{C}_2\text{O}_4^{2-}]$ are the concentrations of free calcium and free oxalate ions, respectively, and y_2 is the activity coefficient for divalent ions in the solution.

While the activity of complexed calcium oxalate in Equation (2-3) or the activity product of calcium and oxalate in Equation (2-4) stresses the contribution of either the complex species or the resultant contribution of calcium and oxalate ions to the driving force of crystallization, Equation (2-5) stresses the contribution of the individual calcium and oxalate ions. The mechanisms of electrolyte crystal growth and nucleation are not understood well enough to distinguish whether crystals grow and nucleate by integration of calcium oxalate ion pairs or individual calcium and oxalate ions.

Therefore, two definitions of supersaturation have been adopted for this study.

The first definition is the relative supersaturation in terms of the activity of the calcium oxalate complex ion, i.e.,

$$S_{\text{hydrate},c} = \frac{(\text{CaC}_2\text{O}_4) - (\text{CaC}_2\text{O}_4)_{\text{eq}}}{(\text{CaC}_2\text{O}_4)_{\text{eq}}} = \frac{(\text{CaC}_2\text{O}_4)}{(\text{CaC}_2\text{O}_4)_{\text{eq}}} - 1 \quad (2-6)$$

The relative supersaturation in terms of activities of free calcium and free oxalate ions is defined as

$$S_{\text{hydrate},i} = \frac{[(\text{Ca}^{2+})(\text{C}_2\text{O}_4^{2-})]^{\frac{1}{2}} - (K_{\text{sp,hydrate}})^{\frac{1}{2}}}{(K_{\text{sp,hydrate}})^{\frac{1}{2}}} \quad (2-7)$$

Several features of and justifications for the use of these two definitions of supersaturation are as follows:

1. Activities of participating species are used instead of concentrations because activities are thermodynamically directly related to the free energy driving force of the forward precipitation processes.
2. Since there is no nucleation or crystal growth at saturation, the supersaturation driving force for nucleation and crystal growth must be defined such that the processes do not proceed at zero driving force.
3. Dimensionless forms of supersaturation are chosen so that comparisons of data among different systems are feasible.

Equations (2-6) and (2-7) may be related to definitions of supersaturations given in Equations (2-4) and (2-5), respectively. As will be discussed in the next section, association of calcium and oxalate ions forms a calcium oxalate ion pair, such that



The activity of calcium oxalate ion pair is related to activities of free calcium and free oxalate ions according to

$$(\text{CaC}_2\text{O}_4) = K_{\text{CaOx}} (\text{Ca}^{2+})(\text{C}_2\text{O}_4^{2-}) \quad (2-9)$$

where K_{CaOx} is the stability constant of this association reaction. Using Equation (2-9), Equations (2-4) and (2-6) may be rearranged to show that $S_{\text{hydrate},c}$ defined in Equation (2-6) is identical to the supersaturation defined in Equation (2-4). Likewise, $S_{\text{hydrate},i}$ defined in Equation (2-7) may be shown to be identical to the relative supersaturation defined in Equation (2-5).

2-3. Formation of Complexes

In experimentation, supersaturated solutions of calcium oxalate are usually generated by mixing solutions containing salts of calcium and of oxalate. Indifferent ions, such as sodium, potassium, chlorine, and/or nitrate ions, are added unavoidably as the oppositely charged ions of the salts of calcium and of oxalate. They may also be added directly in the form of salts of indifferent ions to buffer ionic strength of the solutions. In such electrolytic solutions, some of the constituents, including calcium and oxalate ions, form complexes; supersaturation of calcium oxalate is consequently affected by the formation of complexes in solution.

Ion complexations are association reactions--associations between simple ions, ion pairs, or associated ions. These reactions may be expressed as (Sillén and Martell, 1964):



where ML_{n-1} is a metal ion (when $n=1$) or complex ion, and L is the ligand of the complex.

The stability constant associated with this reaction is the thermodynamic association constant, K_{ML_n} , which is expressed as

$$K_{ML_n} = \frac{y_{ML_n} [ML_n]}{y_{ML_{n-1}} [ML_{n-1}] y_L [L]} \quad (2-11)$$

where the square brackets denote the concentrations and y is the molar activity coefficient of the indicated species.

There are usually several associated species existing in a solution depending on the chemicals added to generate supersaturation. For experiments conducted in the MSMPR system, $Ca(NO_3)_2$, $K_2C_2O_4$, and KNO_3 were used. Solutions contained the simple ions Ca^{2+} , $C_2O_4^{2-}$, K^+ , NO_3^- , H^+ , and OH^- , and the associated species H_2O , HNO_3 , $HC_2O_4^-$, $H_2C_2O_4$, $CaOH^+$, $CaNO_3^+$, CaC_2O_4 , $Ca(C_2O_4)_2^{2-}$, $Ca_2C_2O_4^{2+}$, $CaHC_2O_4^+$, $Ca(HC_2O_4)_2$, KNO_3 , and $KC_2O_4^-$. For experiments conducted in the flow chamber precipitator that will be discussed in Chapter 5, the modified medium solutions contained $CaCl_2$, $Na_2C_2O_4$, KCl , $NaCl$, and glucose. Therefore, the simple ion are Ca^{2+} , $C_2O_4^{2-}$, Na^+ , K^+ , Cl^- , H^+ , and OH^- . The associated species considered were H_2O , $HC_2O_4^-$, $H_2C_2O_4$, $CaOH^+$, CaC_2O_4 , $Ca(C_2O_4)_2^{2-}$, $Ca_2C_2O_4^{2+}$, $CaHC_2O_4^+$, $Ca(HC_2O_4)_2$, $NaC_2O_4^-$, $NaCl$, $KC_2O_4^-$, and KCl . Although some of the complex species were not present in significant amounts, they were included for completeness.

The calculation for solution supersaturations for the MSMPR crystallizer system and for the flow chamber precipitation system are similar. To avoid redundancy, only the formulation for the modified medium solutions that were used in the flow chamber system are illustrated in detail in this chapter.

For the modified medium solution, the association reactions and the rearranged expressions for the corresponding stability constants are shown with "Ox" representing oxalate in the stability constants:



$$[\text{HC}_2\text{O}_4^-] = K_{\text{HOx}}[\text{H}^+][\text{C}_2\text{O}_4^{2-}]y_2 \quad (2-13)$$

$$\text{H}^+ + \text{HC}_2\text{O}_4^- = \text{H}_2\text{C}_2\text{O}_4 \quad (2-14)$$

$$[\text{H}_2\text{C}_2\text{O}_4] = K_{\text{H}_2\text{Ox}}[\text{H}^+][\text{HC}_2\text{O}_4^-]y_1^2/y_0 \quad (2-15)$$

$$\text{Ca}^{2+} + \text{OH}^- = \text{CaOH}^+ \quad (2-16)$$

$$[\text{CaOH}^+] = K_{\text{CaOH}}[\text{Ca}^{2+}][\text{OH}^-]y_2 \quad (2-17)$$

$$\text{Ca}^{2+} + \text{C}_2\text{O}_4^{2-} = \text{CaC}_2\text{O}_4 \quad (2-18)$$

$$[\text{CaC}_2\text{O}_4] = K_{\text{CaOx}}[\text{Ca}^{2+}][\text{C}_2\text{O}_4^{2-}]y_2^2/y_0 \quad (2-19)$$

$$\text{Ca}^{2+} + \text{HC}_2\text{O}_4^- = \text{CaHC}_2\text{O}_4 \quad (2-20)$$

$$[\text{CaHC}_2\text{O}_4^+] = K_{\text{CaHOx}}[\text{Ca}^{2+}][\text{HC}_2\text{O}_4^-]y_2 \quad (2-21)$$

$$\text{Ca}^{2+} + 2\text{HC}_2\text{O}_4^- = \text{Ca}(\text{HC}_2\text{O}_4)_2 \quad (2-22)$$

$$[\text{Ca}(\text{HC}_2\text{O}_4)_2] = K_{\text{CaHOx}_2}[\text{Ca}^{2+}][\text{HC}_2\text{O}_4^-]^2 y_1^2 y_2 / y_0 \quad (2-23)$$

$$\text{Ca}^{2+} + \text{CaC}_2\text{O}_4 = \text{Ca}_2\text{C}_2\text{O}_4^{2+} \quad (2-24)$$

$$[\text{Ca}_2\text{C}_2\text{O}_4^{2+}] = K_{\text{Ca}_2\text{Ox}}[\text{Ca}^{2+}][\text{CaC}_2\text{O}_4]y_0 \quad (2-25)$$

$$\text{C}_2\text{O}_4^{2-} + \text{CaC}_2\text{O}_4 = \text{Ca}(\text{C}_2\text{O}_4)_2^{2-} \quad (2-26)$$

$$[\text{Ca}(\text{C}_2\text{O}_4)_2^{2-}] = K_{\text{CaOx}_2}[\text{C}_2\text{O}_4^{2-}][\text{CaC}_2\text{O}_4]y_0 \quad (2-27)$$

$$\text{K}^+ + \text{C}_2\text{O}_4^{2-} = \text{KC}_2\text{O}_4^- \quad (2-28)$$

$$[\text{KC}_2\text{O}_4^-] = K_{\text{KOx}}[\text{K}^+][\text{C}_2\text{O}_4^{2-}]y_2 \quad (2-29)$$

$$\text{Na}^+ + \text{C}_2\text{O}_4^{2-} = \text{NaC}_2\text{O}_4^- \quad (2-30)$$

$$[\text{NaC}_2\text{O}_4^-] = K_{\text{NaOx}}[\text{Na}^+][\text{C}_2\text{O}_4^{2-}]y_2 \quad (2-31)$$

$$\text{H}^+ + \text{OH}^- = \text{H}_2\text{O} \quad (2-32)$$

$$[\text{H}_2\text{O}] = K_{\text{H}_2\text{O}}[\text{H}^+][\text{OH}^-]y_1^2/y_0 \quad (2-33)$$

$$\text{Na}^+ + \text{Cl}^- = \text{NaCl} \quad (2-34)$$

$$[\text{NaCl}] = K_{\text{NaCl}}[\text{Na}^+][\text{Cl}^-]y_1^2/y_0 \quad (2-35)$$

$$\text{K}^+ + \text{Cl}^- = \text{KCl} \quad (2-36)$$

$$[\text{KCl}] = K_{\text{KCl}}[\text{K}^+][\text{Cl}^-]y_1^2/y_0 \quad (2-37)$$

where K 's are the stability constants of the indicated species and y_i is the molar activity coefficient of the zero charged ($i=0$), monovalent ($i=1$), or divalent ($i=2$) species. It may be assumed that $y_0 = 1$ (Finlayson, 1977), and an extended form of Debye-Hückel equation proposed by Davies (Tomazic and Nancollas, *ibid*; Davies, 1962) may be used to calculate y_1 and y_2 . It is given by

$$-\log y_z = -D z^2 [I^{1/2}/(1+I^{1/2}) - 0.3I] \quad (2-38)$$

where z is the valence of ionic species, D is the Debye-Hückel parameter, and I is the ionic strength of solution. A D value at 37°C of 0.523 (Tomazic and Nancollas, *ibid*) was used. Table 2-2 lists the stability constants used in the calculation of supersaturations in this work.

2-4. Calculation of Supersaturations

In calculating supersaturations for calcium oxalate hydrates in this work, the computer program EQUIL described by Finlayson (*ibid*) has been followed, but some modifications have been added.

The supersaturation was calculated by assuming that there is no precipitation taking place and that all the reactions between the free ions and associated species are in equilibrium. Due to the assumption of equilibrium, stability constants of the complexations may quantitatively relate the activities of the free and associated species in the solution. With known total amounts of chemical species and known solution pH, the concentration of each free or associated species may be calculated by iterative computer algorithms using material balances on the the constituent atoms or ions in solution. Once the concentrations of all species are known, supersaturation of calcium

Table 2-2 Stability constants.

Stability constant		Temperature (°C)	Reference
K_{H_2O}	3.89e13	37	a
K_{HOx}	21008.7	37	a
K_{H_2Ox}	19.12	37	b
K_{CaOx}	1869	37	c
K_{CaHOx}	64.59	25	d
$K_{Ca(HOx)_2}$	312.8	25	d
K_{CaOH}	29.5	37	a, e
K_{CaOx_2}	17.3	38	f
K_{Ca_2Ox}	71.6	38	g
K_{CaNO_3}	4.786	25	h
K_{NaNO_3}	0.2692	25	h
K_{KNO_3}	0.4786	37	a, b, h
K_{HNO_3}	0.04939	37	a, h
K_{NaCl}	0.3981	25	h
K_{KCl}	0.1738	25	h
K_{KOx}	13.3		c
K_{NaOx}	13.3	38	g

a: Sillén and Martell, 1964.

b: Sillén and Martell, 1971.

c: Tomazic and Nancollas, 1979.

d: Perrin, 1979.

e: Curreri, Onoda, and Finlayson, 1979.

f: Burns, Finlayson, and Smith, 1981.

g: Finlayson, Roth, and Dubois, 1972.

h: Högfeltdt, 1982.

oxalate may be estimated from the calculated concentrations of free calcium and oxalate ions or from the concentration of calcium oxalate ion pairs (Finlayson, *ibid*).

For the modified medium solution, the species balances were written as:

$$T_{Ca} = [Ca^{2+}] + [CaOH^+] + [CaC_2O_4] + [CaHC_2O_4^+] + [Ca(HC_2O_4)_2] \\ + [Ca(C_2O_4)_2^{2-}] + 2 [Ca_2C_2O_4^{2+}] \quad (2-39)$$

$$T_{Ox} = [C_2O_4^{2-}] + [HC_2O_4^-] + [H_2C_2O_4] + [CaC_2O_4] + [CaHC_2O_4^+] \\ + 2 [Ca(HC_2O_4)_2] + 2 [Ca(C_2O_4)_2^{2-}] + [Ca_2C_2O_4^{2+}] \\ + [KC_2O_4^-] + [NaC_2O_4^-] \quad (2-40)$$

$$T_{Na} = [Na^+] + [NaCl] + [NaC_2O_4^-] \quad (2-41)$$

$$T_K = [K^+] + [KCl] + [KC_2O_4^-] \quad (2-42)$$

$$T_{Cl} = [Cl^-] + [KCl] + [NaCl] \quad (2-43)$$

where T_{Ca} , T_{Ox} , T_{Na} , T_K , and T_{Cl} are the total concentrations of calcium, oxalate, sodium, potassium, and chlorine in the solution.

Substituting the appropriate stability constant equations (Equations (2-13) and (2-15) through (2-37)) into Equations (2-39) through (2-43), after rearrangement, the expressions for free ion concentrations are as follows:

$$[Ca^{2+}] = T_{Ca} / \left[1 + K_{CaOx} [C_2O_4^{2-}] y_2^2 + K_{CaOH} [OH^-] y_2 \right. \\ + K_{CaHOx} K_{HOx} [H^+] [C_2O_4^{2-}] y_2^2 + K_{CaHOx_2} (K_{HOx} [H^+] [C_2O_4^{2-}] y_1 y_2)^2 y_2 \\ \left. + K_{CaOx_2} K_{CaOx} [C_2O_4^{2-}]^2 y_2^2 + 2 K_{Ca_2Ox} K_{CaOx} [Ca^{2+}] [C_2O_4^{2-}] y_2^2 \right]$$

(2-44)

$$\begin{aligned}
[C_2O_4^{2-}] = T_{Ox} / & \left[1 + K_{HOx}[H^+]y_2 + K_{H_2Ox}K_{HOx}[H^+]^2y_1^2y_2 \right. \\
& + K_{CaOx}[Ca^{2+}]y_2^2 + K_{CaHOx}K_{HOx}[Ca^{2+}][H^+]y_2^2 \\
& + 2 K_{CaHOx_2}(K_{HOx}[H^+]y_1y_2)^2[Ca^{2+}][C_2O_4^{2-}]y_2 \\
& + 2 K_{CaOx_2}K_{CaOx}[Ca^{2+}][C_2O_4^{2-}]y_2^2 + K_{Ca_2Ox}K_{CaOx}[Ca^{2+}]^2y_2^2 \\
& \left. + K_{KOx}[K^+]y_2 + K_{NaOx}[Na^+]y_2 \right] \quad (2-45)
\end{aligned}$$

$$[Na^+] = T_{Na} / \left[1 + K_{NaCl}[Cl^-]y_1^2 + K_{NaOx}[C_2O_4^{2-}]y_2 \right] \quad (2-46)$$

$$[K^+] = T_K / \left[1 + K_{KCl}[Cl^-]y_1^2 + K_{KOx}[C_2O_4^{2-}]y_2 \right] \quad (2-47)$$

$$[Cl^-] = T_{Cl} / \left[1 + K_{NaCl}[Na^+]y_1^2 + K_{KCl}[K^+]y_1^2 \right] \quad (2-48)$$

As will be discussed in Chapters 4 and 5, COM and COT were the most frequently encountered hydrates in this work. Supersaturations of these two hydrates may be calculated according to Equations (2-6) and (2-7). The calculations were implemented with computer programs written in BASICA for the IBM AT, IBM XT, or IBM compatible systems.

The program was developed according to the following logic:

1. define stability constants and K_{sp} s;
2. input solution pH and values of T_{Ca} , T_{Ox} , T_{Na} , T_K , and T_{Cl} in solution;
3. calculate $[H^+]$ and $[OH^-]$ from the input pH value;
4. guess concentrations for free ions, $[Ca^{2+}]$, $[C_2O_4^{2-}]$, $[Na^+]$, $[K^+]$, and $[Cl^-]$; guess activity coefficients, y_1 and y_2 ;
5. calculate new values of free-ion concentrations by Equations (2-44) to (2-48);
6. compare the guessed concentrations and the calculated values to see whether the relative difference of the concentrations of each free ions is within a preset tolerance;

- a) if it is not, use the new calculated concentrations for the guessed values to calculate ionic strength, I , use this I value to calculate y_1 and y_2 by Equation (2-38), and then repeat calculations from step 5;
 - b) if tolerance satisfied, go to step 7;
7. calculate supersaturations according to Equations (2-6) and (2-7).

Listings of programs are shown in Appendix A. The supersaturations thus calculated are for solutions without solid calcium oxalate precipitate. In that sense they are the initial driving forces for nucleation or for crystal growth before any precipitation takes place.

2-5. Accuracy of the Calculated Supersaturations

In calculating supersaturations as described above, some unavoidable uncertainties in the parameters were noticed. The stability constants used in the modified EQUIL programs were obtained from the literature. It was assumed that stability constants corrected for infinitely dilute solutions or for the asymptotic values at zero concentrations are independent of composition but depend only on temperature. In order to obtain stability constants for infinite dilute solutions at 37°C, extrapolation or interpolation was used whenever necessary. For the stability constants without information on the dependence on temperature, values at 25°C or at 38°C were also used. For some data, different references reported different values of stability constants for similar solution conditions. The effect of using different values for stability constants on calculated supersaturations may be seen in Table 2-3, where supersaturations of COM, $(S_{\text{COM},i})_A$ and $(S_{\text{COM},i})_B$, are calculated from a modified EQUIL program for systems containing Ca^{2+} , Ox^{2-} , and KCl using different

Table 2-3 $S_{\text{COM},i}$ calculated with different stability constants for solutions containing CaCl_2 , $\text{K}_2\text{C}_2\text{O}_4$, and KCl (ionic strength buffer); ionic strength = 0.15 M.

$T_{\text{Ca}} - T_{\text{Ox}}$ (mM)	Supersaturation		Difference in $(S_{\text{COM},i})_{\text{A}}$ and $(S_{\text{COM},i})_{\text{B}}$ (%)
	$(S_{\text{COM},i})_{\text{A}}$	$(S_{\text{COM},i})_{\text{B}}$	
0.5	1.484	1.365	8.62
0.75	2.616	2.452	6.66
1.0	3.685	3.482	5.80
1.25	4.699	4.462	5.28
1.5	5.661	5.396	4.90

Stability constants and $K_{\text{sp},\text{COM}}$ used in calculation			
	for $(S_{\text{COM},i})_{\text{A}}$		$(S_{\text{COM},i})_{\text{B}}$
K_{HOx}	21141.6		21008.7
K_{KOx}	10.0		13.3
K_{CaOx}	1871.03		1869
$K_{\text{Ca}_2\text{Ox}^{2+}}$	71.4		71.6
$K_{\text{H}_2\text{O}}$	1.0e-14		2.57e-14
$K_{\text{sp},\text{COM}}$	2.493e-9		2.514e-9

stability constants. The stability constants used in the calculations for $(S_{\text{COM},i})_A$, and for $(S_{\text{COM},i})_B$ are also listed. The differences between these two values are listed in the last column of Table 2-3. As an example, the difference between these two supersaturations is 6.66% for the lowest experimental concentrations, $T_{\text{Ca}} = T_{\text{Ox}} = 0.75 \text{ mM}$, used in this work.

Another source of uncertainty in calculating supersaturation is from the activity coefficients from Equation (2-38). This equation has the advantage of representing activity coefficients of several types of single electrolytes-- uni-univalent, bi-univalent, or uni-bivalent-- in a single equation. The average deviation of values predicted by the equation was 1.6-2.2% from the true activity coefficient values for the solutions containing the single electrolytes (Davies, *ibid*). When the equation is applied to systems containing multiple components, the accuracy is unknown. Because of the minor deviations for the single electrolyte solutions, the equation is used in dilute systems containing multiple components. It offers reasonable approximations for the activity coefficients, but with unavoidable uncertainty.

The methods described in this chapter allow calculation of supersaturation driving force for calcium oxalate crystallization for a variety of solution conditions. They are important for the quantification of crystal growth in this work.

CHAPTER 3
PARTICLE SIZE DISTRIBUTIONS, POPULATION BALANCE EQUATIONS
AND DETERMINATION OF PARTICLE SIZE DISTRIBUTIONS

3-1. Introduction

Particle size distributions (PSD) or crystal size distributions (CSD) are of value in crystallization studies; they offer both qualitative and quantitative information which characterize crystallizing and precipitating systems. Randolph and Larson (1971) did some of the first work in the use of PSD to characterize crystallizing systems through the use of population balance equations. As a preamble to Chapter 4, this chapter will discuss the theoretical aspects of particle size distributions and population balance equations, as well as the practical aspects of acquisition of particle size distributions. Portions of this chapter are excerpted from two papers published as part of this work (Lin and Briedis, 1988a, 1988b).

3-2. Particle Size Distributions and Population Balance Equations

There are several ways of presenting particle size distributions. One of the most popular particle size distributions used is differential population density, $n(L,t)$ or $n(L)$, representing number of particles per differential length per sample volume. This PSD representation uses a characteristic length of the particles, L , as the independent variable and may or may not be a function of time t . For particles of irregular shapes, the equivalent spherical diameter is usually used for the characteristic length.

Assuming L_c is the smallest particles in the sample, the total particle number, N_T (no./ml), may be calculated according to (Randolph

and Larson, 1971):

$$N_T(t) = \int_{L_c}^{\infty} n(L,t) dL \quad (3-1)$$

The upper limit of this integration can also be the largest particle size of the sample instead of ∞ .

The differential volume density, $v(L,t)$, may be obtained from the number density by:

$$v(L,t) = \frac{\pi L^3}{6} n(L,t) \quad (3-2)$$

The third moment of the number density, M_3 , is expressed as (ibid):

$$M_3(t) = \int_{L_c}^{\infty} n(L,t) L^3 dL \quad (3-3)$$

This moment is also related to the total particle volume in the sample, $v_T(t)$ ($\mu\text{m}^3/\text{ml}$), according to:

$$M_3(t) = \frac{6}{\pi} v_T(t) \quad (3-4)$$

The total suspension mass expressed in terms of the third moment is

$$M_T(t) = \frac{\pi \rho}{6} M_3(t) \quad (3-5)$$

where ρ is the density of the suspended particles.

For the MSMPR continuous crystallization system with nucleation, crystal growth, and aggregation involved, the unsteady state population balance equation may be written as (ibid):

$$\frac{\partial n(L,t)}{\partial t} + \frac{\partial (G_L n(L,t))}{\partial L} + \frac{n(L,t)}{\tau} = B_a - D_a \quad (3-6)$$

where G_L is the particle growth rate, or $\frac{dL}{dt}$, in units of $\mu\text{m}/\text{min}$, and τ is the residence time in the MSMPR crystallizer. The first term on the left hand side of the equation accounts for changes in particle

numbers in the system with time, the second term accounts for particle growth by transfer of material from the solution phase to the particles, also called the condensation term, and the third represents removal of particles by constant outlet withdrawal. Since L is the equivalent spherical diameter of particles, G_L is twice the value of the growth rate defined as the procession of a surface with time as used in Chapter 5. B_a and D_a are particle birth and death into and from a given size resulting from particle collisions and aggregations.

Aggregation of particles may result in conservation of particle volume instead of particle diameter; that is, the volume of aggregates is the sum of the volume of the aggregate-forming particles. The population balance equation written in terms of $n(x,t)$ is more suited for representing the aggregation terms, where x is the volume of particles of size L . The PSD $n(x,t)$ is related to $n(L,t)$ by

$$n(x,t) dx = n(L,t) dL \quad (3-7)$$

and

$$x = \frac{\pi}{6} L^3 \quad (3-8)$$

If it is assumed that aggregates are formed by collision of only two particles at a time (Hansen, 1975), the whole population balance can be written as (Swift and Friedlander, 1964; Drake, 1972)

$$\begin{aligned} \frac{\partial n(x,t)}{\partial t} + \frac{\partial (G_v n(x,t))}{\partial x} + \frac{n(x,t)}{\tau} \\ - \frac{1}{2} \int_{x_c}^x \kappa(y, x-y) n(y,t) n(x-y,t) dy \\ - n(x,t) \int_{x_c}^{\infty} \kappa(x,y) n(y,t) dy \end{aligned} \quad (3-9)$$

where G_v is $\frac{dx}{dt}$, the increase of particle volume with respect to time, x_c is the particle volume at size L_c , and $\kappa(x,y)$ is the aggregation kernel for particles of volumes x and y , similar to the kinetic rate constant in bimolecular reactions.

Because volume is proportional to the third power of L , the $n(x,t)$ distribution tends to be weighted more heavily to larger sizes than a $n(L,t)$ distribution. A compromise between length and volume-based distributions is to define another size distribution, $m(w,t)$, such that (Gelbard and Seinfeld, 1978)

$$m(w,t) = x n(x,t) \ln \left(\frac{x_b}{x_c} \right) \quad (3-10)$$

and

$$w = \frac{\ln \left(\frac{x}{x_c} \right)}{\ln \left(\frac{x_b}{x_c} \right)} \quad (3-11)$$

where x_c and x_b are the lower and upper limits on particle volume. Let

$$m(w_x,t) = x n(x,t) \ln \left(\frac{x_b}{x_c} \right) \quad (3-12)$$

$$m(w_y,t) = y n(y,t) \ln \left(\frac{x_b}{x_c} \right) \quad (3-13)$$

and

$$w_{x-y} = \frac{\ln \left(\frac{x-y}{x_c} \right)}{\ln \left(\frac{x_b}{x_c} \right)} \quad (3-14)$$

Applying the chain rule in changing the coordinate from x to w , the population balance equation becomes

$$\begin{aligned}
& \frac{\partial m(w,t)}{\partial t} + \frac{\partial (G_w m(w,t))}{\partial w} + \frac{m(w,t)}{\tau} \\
& - \frac{1}{2} \int_{w_c}^{w-x_c} \frac{x}{x-y} \kappa(y, x-y) m(w_y, t) m(w_{x-y}, t) dw_y \\
& - m(w,t) \int_{w_c}^{w_b} \kappa(x,y) m(w_y, t) dw_y \quad (3-15)
\end{aligned}$$

where $G_w = \frac{dw}{dt}$, and, according to Equation (3-11), w_b and w_c are equal to 1 and 0, respectively.

For an unsteady state continuous crystallization process in which the total particle number is small, there may be no aggregation taking place in the system. For such a case, the population balance equations describing the system may be rewritten by omitting the aggregation terms. Using the PSD $n(L,t)$ as an example, the population balance equation for such a process may be described as:

$$\frac{\partial \ln n(L,t)}{\partial t} + G_L \frac{\partial \ln n(L,t)}{\partial L} + \frac{\partial G_L}{\partial L} + \frac{1}{\tau} = 0 \quad (3-16)$$

If the growth rate G_L is independent of particle sizes, Equation (3-16) may be rearranged to result in an equation to be used in Chapter 4 to calculate the growth rate, i.e.,

$$G_L = - \frac{\frac{\partial \ln n(L,t)}{\partial t} + \frac{1}{\tau}}{\frac{\partial \ln n(L,t)}{\partial L}} \quad (3-17)$$

For the time-independent case, this formulation reduces to Equation (1-28).

3-3. Determination of Particle Size Distributions

Particle size distributions modelled with the use of population balance equations are of great importance in characterizing

crystallization system; however, an accurate and time-economic particle sizing method is required to obtain representative CSD or PSD data.

Several techniques such as sieving, sedimentation, and electronic sizing may provide particle size distribution data. In this work, because the particles generated from the MSMPR system were below 100 μm in sizes, they were below the sieve-sizing range. On the other hand, sedimentation methods require long times for particle size differentiation due to long particle settling times. Sedimentation method is not suited for the rapid analysis required for the time-dependent study of the MSMPR crystallizer system. The electronic sizing method was chosen for its capability of analyzing data with high resolution (100 or 128 sizing channels), good reproducibility (Allen, 1981), and its ability to size without altering the physical state of the suspension samples generated from the MSMPR crystallizer.

The particle sizing instruments operating on the electrical sensing zone principle typically used to determine PSDs are the Coulter Counter (Coulter Electronics, Inc., Hialeah, Florida) and the ELZONE^(R) system (Particle Data, Inc., Elmhurst, Illinois). The latter was available for this work.

The Particle Data ELZONE^(R) Particle Analyzer provides a well established technique for particle counting and particle size distribution determination for liquid suspension samples. It has inherent value as an analytical tool in several of its unique features which include its normalization capability, the 128 channel analysis, and the option of installing an additional sample stand. Therefore, the computerized ELZONE^(R) Particle Data Analyzer (model 112 LSGD/ADC/SSA-SGS/80XY/VM5/TP50) was adapted for sizing the crystals formed from the MSMPR continuous crystallization system to be discussed

in Chapter 4. The practical aspects concerning the use of this instrument will be discussed in the sections that follow and were published as two papers (Lin and Briedis, 1988a, 1988b).

3-3-1. Basic Operating Principles of the ELZONE^(R) System

The electronic sizing instruments count particles of suspension samples in solutions with electrical conductance. The sensor parts are an orifice tube and two electrodes, one inside the orifice tube, the other outside the tube. The instrument generates vacuum to draw a sample of known volume into the orifice tube for particle counting. The electrodes sense the resistance changes of the solution caused by the passing particles when suspension solution is drawn through the orifice. With constant electric current passing through the orifice, the resistance change due to a passing particle generates a voltage pulse proportional to the particle volume (Kachel, 1979). The instrument collects the signals of the voltage pulses, discriminates the signals into size channels, and then reports the particle counts in each channel and/or other particle counting information based on these particle count data. The representative sizes of these sizing channels are obtained by calibrating the instrument with particles of known sizes called standard particles.

3-3-2. Correlating Particle Size Distributions with the Instrument Counted Data

Based on the operating principles stated above, the population density, $n(L)$, is related to the counted particle data, n_{ch} , or particle number in the sampling volume in each channel, by

$$n(L) = \frac{n_{ch}}{\Delta L_{ch} V_s} DF \quad (3-18)$$

where ΔL_{ch} is the channel width in units of $\mu\text{m}/\text{channel}$, V_s is the sampling volume for which the particle data are counted, and DF is the dilution factor used in sample preparation for particle counting. Since time is an independent variable with respect to data processing, the time independent form of PSDs or counted particle data will be used here for simplicity.

A quantity useful in data manipulation, $n_{ch,c}$, the corrected count in a given channel ch , in units of $\text{no.}/(\text{channel} \cdot \text{unit sample volume})$, may be defined as

$$n_{ch,c} = \frac{n_{ch}}{V_s} DF \quad (3-19)$$

The volume density, $v(L)$, may be related to differential volume data, v_{ch} , according to

$$v(L) = \frac{v_{ch}}{\Delta L_{ch} V_s} DF \quad (3-20)$$

where v_{ch} is the total volume of particles in each channel in the sampling volume analyzed and may be calculated from differential population data according to

$$v_{ch} = k_v L_{ch}^3 n_{ch} \quad (3-21)$$

where k_v is the geometric shape factor of particles (Randolph and Larson, 1971, McCabe and Smith, 1976) and L_{ch} , the representative length of channel ch , is equivalent to particle size L . In the case where L is the equivalent spherical diameter, the geometric shape factor is $\frac{\pi}{6}$.

3-3-3. Comments on the ELZONE^(R) Analysis Program

During the course of this work with the computerized ELZONE^(R) system, several limitations were discovered in its "firmware" (a program stored permanently in Read Only Memory) for quantitative volume and numbers distribution analysis.

The ELZONE^(R) system used in this work consists of the primary particle sensor and counter which is interfaced to the minicomputer (Model ADC-80-XY-VMS) of the secondary instrumentation for data acquisition and processing. The data processing program stored in the ROM offers several optional functions which include reporting of data on either a population (numbers) or volume basis and in differential or cumulative display, blending of multi-orifice data for particulate systems of broad size distributions, and extrapolation of the blended or single orifice data.

In analyses where only relative volumes and relative population distributions are necessary, as with the ELZONE^(R) "histogram" display or for percentile presentation, the existing firmware calculations are adequate. However, some characteristics of the ELZONE^(R) firmware limit its application for quantitative volume or numbers distribution analyses which are needed for modeling of number-dependent phenomena (Halfon and Kaliaguine, 1976; Swift and Friedlander, 1964; Gelbard and Seinfeld, 1978; Delichatsios and Probstein, 1975; Hartel and Randolph, 1986). Such details have been neglected in descriptions of the operation and data analysis package of the ELZONE^(R) system (Particle Data, (b); Karuhn and Berg, 1984). It is the purpose of this section to address these limitations. The comments and discussion herein are specific to the software version described in OXY007.R01 80XY User's

Manual - REX 710, and may not apply to other versions distributed by Particle Data, Inc.

3-3-3-1. "Histogram" Display

The population or volume data reported from the ELZONE^(R) system are given in a "histogram" representation (Particle Data, (b)); i.e., the data presented are in some proportion to the quantitatively correct data. For example, the differential population data, n_{ch} , are given in a computer printout of the differential population display from the 80XY program. In normal instrument operation, the channel widths of each set of data counted vary with the aperture tube, size span, and current and gain settings chosen. Therefore, the reported "histogram" cannot be quantitatively compared for data sets that have been acquired at different size span, current, and gain settings or with different aperture tubes, sampling volumes, and dilution factors. For further quantitative analyses, these data sets require modifications that will be discussed in Section 3-5.

3-3-3-2. Scaling Factor in Volume Data

It was noticed that the differential volume histogram data, v_{rep} , reported by the ELZONE^(R) firmware are not equivalent to the differential volume data, v_{ch} . Table 3-1 presents a channel-by-channel comparison of the v_{rep} data with the volume data, v_{cal} , calculated from Equation (3-21) using $k_v = \frac{\pi}{6}$. The results show that the actual conversion equation implemented by the firmware must include an additional factor, F , such that v_{cal} and v_{rep} are related according to:

$$v_{cal} = v_{rep} F \quad (3-22)$$

where F is approximately constant for each individual sample. However,

Table 3-1 F factors calculated from comparison of reported and calculated differential volume data.
(abbreviated version)

Sample Parameters:

76 micron Orifice Tube, serial # 179

Volumetric: 498.4 μl

True Log: 10.0 (10)

Dia. Ch 1: 1.902 (μm)

Dia. Ch 128: 19.22 (μm)

Low Cal.: ch.1 (1.902 μm)

Current: 5.5

Gain: 3.5

Preset Time: 21.7 (sec)

Elapsed Time: 21.7 (sec)

High Cal.: ch.128 (19.252 μm)

Total Count = 10870

Total Volume = 47373

ch	L _{ch}	n _{ch}	v _{rep}	v _{cal}	F	ch	L _{ch}	n _{ch}	v _{rep}	v _{cal}	F
24	2.892	50	3	633.23	211.1	57	5.278	77	31	5927.9	191.2
25	2.946	52	4	696.15	174.0	58	5.375	77	33	6260.7	189.7
26	3.000	51	4	721.00	180.2	59	5.474	78	35	6699.0	191.4
27	3.055	52	4	776.31	194.1	--					
28	3.111	52	4	819.79	204.9	--					
29	3.168	49	4	815.74	203.9	--					
30	3.227	48	4	844.57	211.1	--					
--						123	17.55	94	1413	2.660e5	188.3
--						124	17.88	88	1397	2.634e5	188.5
--						125	18.28	84	1408	2.687e5	190.8
54	4.997	66	23	4311.9	187.5	126	18.53	81	1434	2.698e5	188.2
55	5.089	70	26	4830.5	185.8	127	18.94	74	1384	2.633e5	190.2
56	5.183	72	28	5249.0	187.5	128	19.22	324	6400	1.204e6	188.2

Average value of F: 189.7

between several sample data sets analyzed, F has been found to vary anywhere from 189 to 1516.

Information concerning this factor provided upon request from Particle Data, Inc., shows that the scaling factor F of the 80XY program is a relative value. The scaling process is designed to avoid overflows in the microprocessor memory. As a result, the volume data in every channel are normalized to a peak height of 6400 counts by the scaling factor and are then rounded off to integer values. This methodology is valid when relative volume distribution are required, but precludes quantitative comparisons of volume distributions from one sample to another.

3-3-3-3. Blending of Volume Data

The blending routine in the ELZONE^(R) firmware manipulates multiple orifice data to give a complete histogram across the size range of importance. It uses data represented on a volume basis (Karuhn and Berg, 1984; Particle data, (b)). It is herein that questions about the correctness of the routine arise as the volume representation generated by the ELZONE^(R) firmware as described in paragraphs above is not quantitatively correct.

It is important to take into account differences between v_{ch} data and $v(L)$ data. As an example, suppose a suspension sample is observed to have a linear population density given by the expression, $\ln n(L) = -0.2L + 12.5$ (Figure 3-1(a)), and is to be analyzed with two aperture tubes of 76 μm and 300 μm . These sample data are then to be blended. Identical dilutions in sample preparation and equal sampling volumes (1 ml) in data acquisition are assumed. Figures 3-1(b) and 3-1(c) show the simulated quantitatively correct $v(L)$ data and v_{ch} data, respectively. The discontinuity seen in the v_{ch} distribution curve

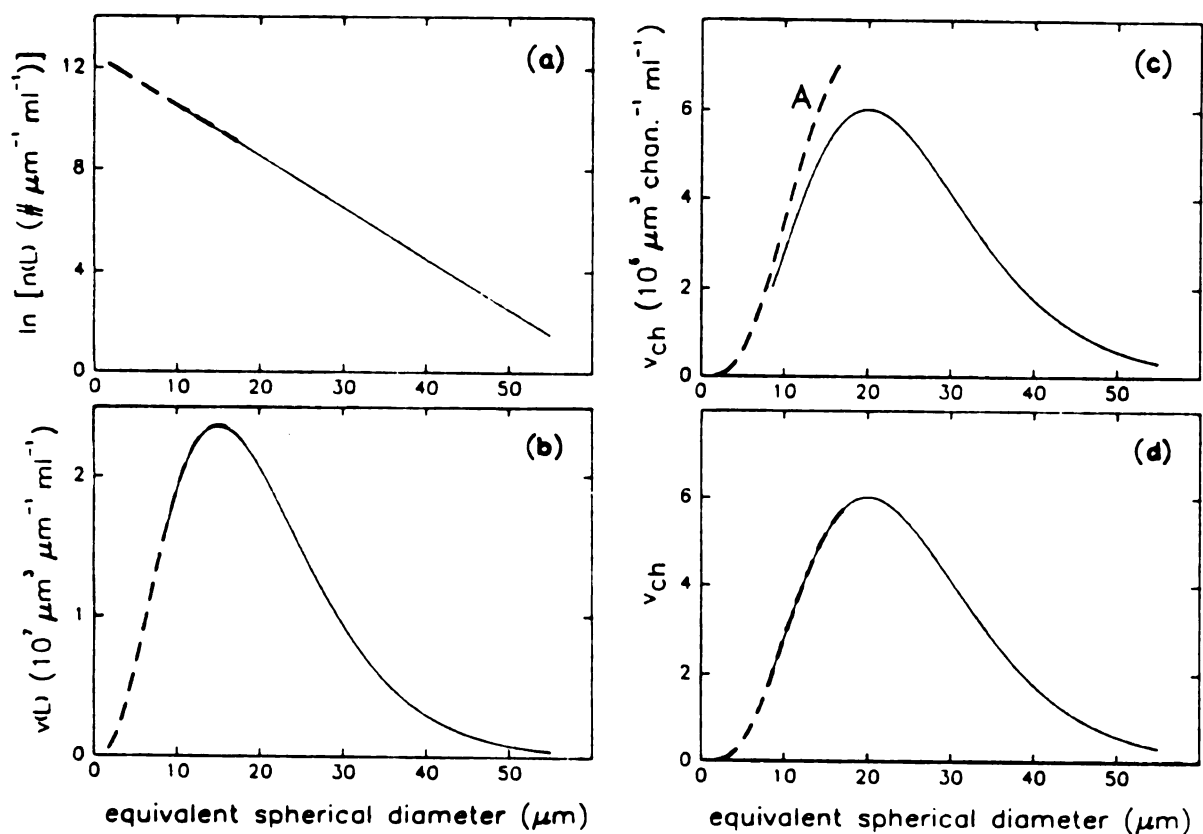


Figure 3-1 Blending of a simulated v_{ch} and $v(L)$ data;

- (a) linear population density plot,
- (b) volume density,
- (c) differential volume per channel,
- (d) v_{ch} by blending routine.

The thicker dash lines represent the data from the $76 \mu\text{m}$ aperture tube; the thinner solid lines represent the data from the $300 \mu\text{m}$ aperture tube. Sampling volume is 1 ml for both data sets.

arises due to the inherently smaller channel widths for the 76 μm orifice tube than for the 300 μm orifice tube. The program performs its routine simply by adjusting the two v_{ch} curves based on matching "the same or most nearly same" (Particle Data, (b)) slopes of the curves enclosed by the low and high markers in the region where data of several channels overlap. In order to simulate the procedure, curve A in Figure 3-1(c) must be scaled down by a factor of 0.8006 (based on most nearly the same slopes between 9 to 12 μm) to yield a continuous curve as shown in

Figure 3-1(d). Additionally, the blending routine in the ELZONE^(R) system rescales the curve to yield a peak value of 6400.

The results of this routine cannot be used quantitatively with confidence. The above assumption of equal sampling volumes in data acquisition is usually not realizable. In the analysis of populations of broad size distributions, two mercury volumetric sections are often used in acquiring data with different size aperture tubes. Such data sets are necessarily each on a different volume basis and should not be blended without correction.

3-3-3-4. Sampling Volume

It has also been discovered that in its present design the instrument has no way of directly coordinating the start of sample analysis (counting of particles in each channel) with the start of intake of the calibrated sample volume, V_v , in the system's ANALYZE or TIMED ANALYZE data acquisition mode. Therefore, even when the same aperture tube and mercury section are used for different samples, the lack of automatic coordination between intake and counting causes uncertainty in the values of v_{ch} obtained. For generating quantitative

number or volume distribution data, $n(L)$ and $v(L)$, respectively, a true sampling volume is required.

To estimate the true sampling volume for each data set, Particle Data, Inc., offers an approach based on the total counts in two successive sample analyses. Analysis of a sample in the ANALYZE mode yields a distribution of particle numbers and the total count, $N_{T,s}$. For the same suspension sample, another analysis is performed for a sample volume equal to the calibrated volume of mercury section, V_v , by moving the vacuum/flush control toggle from VACUUM to COUNT. This is done in the ANALYZE mode and so does not generate the particle numbers distribution in the system's memory. The total count thus obtained is $N_{T,v}$. The true sampling volume, V_s , for the analysis of known particle number distribution is then calculated as

$$V_s = V_v \left(\frac{N_{T,s}}{N_{T,v}} \right) \quad (3-23)$$

However, this method is not valid in systems having particle size distributions varying with time. In order to obtain reliable data for the crystallization system as will be described in Chapter 4, an alternate approach for sampling volume as well as modification of data manipulation was used and will be described in Section 3-5.

3-4. Calibration Procedure and the "Normalize" Function

The "normalize" function, one of the unique features of the ELZONE^(R) system, is available on all the ELZONE^(R) instruments manufactured since 1970 (Particle Data, (a)). It provides a null check of calibration against any property changes in electrolyte and circuits (Particle Data, (b)). As described by Particle Data, Inc., the normalizing procedure serves to adjust the calibration for either a)

any electrolyte conductivity changes due to changes in electrolyte composition or temperature, or b) any circuit drift caused by aging or temperature changes. Questions have arisen as to the correctness of the normalize function and the calibration procedure. Because the operating procedure of the instrument relies greatly on the application of the normalize function for accurate data and because the calibration procedure is required for correlating the sizes of counting channels with the switch settings of the instrument, efforts were taken to verify the normalize function and the calibration technique in question. A modified calibration procedure was developed and verified to be analogous to the original calibration procedure, but it offers a much clearer understanding of the basis for the calibration procedure and a more straightforward determination of calibration constants than the original technique. In this section, the original calibration procedure will be reviewed, and the modified calibration procedure will be discussed and verified with calibration experiments.

3-4-1. Original Calibration Procedure (Particle Data, (a))

The logarithmic span mode in the ELZONE^(R) system provides a relatively broad sizing span for particle counting. In the logarithmic mode, for a given orifice tube and a given log span setting, the calibration equation as provided by the manufacturer is

$$V_{Tr} = Kc \frac{2^{L_s(Tr-1)}}{(I \cdot G)} \quad (3-24)$$

where V_{Tr} is the particle volume at trigger level Tr , Kc is the calibration constant, L_s is the true log span, I and G are the current and gain switch settings on the instrument respectively, and $(I \cdot G)$ is the IG product, or $2^{(I+G)}$. The trigger level Tr , which has a value

from 0 to 1, controls the discrimination between the electric pulses, which are related to particle sizes as described in Equation (3-24). The log span settings on the front panel of the instrument are only nominal values of the true log span, L_s .

The original graphical calibration method is summarized as follows. For a given orifice tube and a log span switch setting, the instrument is calibrated with one size of standard particles at several current and gain switch settings. The trigger levels corresponding to the median (half count) or modal (peak) size are recorded. The technique then requires plotting of the logarithm of a pseudo-volume versus the trigger level or "instrument scale" (dial setting, channel number, ...) at several current and gain switch settings to generate a linear calibration line. From this line, a ratio, R , is calculated from the volume at "full scale", V_f , and at "zero reading", V_z :

$$R = \frac{V_f}{V_z} \quad (3-25)$$

The "full scale" and "zero reading" correspond to channel 128 and channel 1, respectively (see Equation (3-29)).

The calibration constants, K_c and L_s in Equation (3-24), are given as

$$K_c = I \cdot G \cdot V_f \quad (3-26)$$

and

$$L_s = \frac{\log R}{\log 2} \quad (3-27)$$

K_c and L_s are used in Equation (3-24) to calculate particle volume versus trigger level or channel.

Based on the understanding of the instrument's function and design, some modifications to the original graphical procedure have been proposed. These are described in the following sections.

3-4-2. Modified Calibration Procedure

For instruments manufactured after January 1978, the IG product is internally set as $2^{(I+G)}$ (Particle Data, (a)); therefore, Equation (3-26) is rewritten as

$$K_c = 2^{(I+G)} V_f \quad (3-28)$$

A modified approach to calibration is suggested as follows. The channel numbers, ch, are related to trigger levels by

$$ch = 127 Tr + 1 \quad (3-29)$$

This equation is based on the understanding that as Tr is varied from 0 to 1 the instrument analyzes data from channel 1 to channel 128.

As described in the Operator's Manual (Particle Data, (a)) the ELZONE^(R) system is designed such that the particle-pulse amplitude for a given orifice is directly proportional to current, gain, and particle volume. In other words, if the particle-pulse amplitude, which is proportional to particle volume, is to be proportional to $2^{(I+G)}$, then varying I and G values to vary $2^{(I+G)}$ has the same effect as varying particle volumes; this is defined as the pseudo-volume, V_p . If the standard particles with volume V_{std} yield a certain particle-pulse amplitude at set I_1 and G_1 , then for different (I+G) values, the same standard particles would show particle-pulse amplitudes of particles with volume V_p different from V_{std} . The proportionality between particle-pulse amplitude and the quantity $2^{(I+G)}$ yields

$$\frac{V_p}{V_{std}} = \frac{2^{(I+G)}}{2^{(I_1+G_1)}} \quad (3-30)$$

or

$$\log V_p = \log V_{std} + [(I+G)-(I_1+G_1)] \log 2 \quad (3-31)$$

If the quantity ($\log V_p$) is a linear function of trigger level (as described in the original graphical procedure), and since trigger level is proportional to channel number (Equation (3-29)), then from Equation (3-31) the variable ($I+G$) is a linear function of channel number.

Instead of the original graphical method, a linear regression method is used to correlate the ($I+G$) values and ch directly such that

$$(I+G) = (\text{slope}) \cdot \text{ch} + \text{intercept} \quad (3-32)$$

where ($I+G$) is the sum of the current and gain switch settings, ch is the recorded median channel (half count) of standard particles corresponding to ($I+G$), "slope" is the slope of the linear regression line, and "intercept" is the intercept of the linear regression line.

Using Equations (3-29) and (3-32), Equation (3-30) is rewritten as

$$V_p = V_{std} 2^{\left[\frac{(I+G)_{128}}{2} \right]} \frac{2^{[127 \cdot (\text{slope}) \cdot (\text{Tr}-1)]}}{2^{(I_1+G_1)}} \quad (3-33)$$

where $(I+G)_{128} = (I+G)$ value at $\text{ch} = 128$ from Equation (3-32).

Since the pseudo-volume, V_p , and (I_1+G_1) are arbitrarily chosen values, for general cases, the pseudo-volume should be equal to the volume at trigger level, V_{Tr} , and the subscripts in (I_1+G_1) may be omitted. Comparing Equation (3-33) with Equation (3-24), the calibration constants, K_c and L_s , may be expressed as

$$K_c = V_{std} 2^{\left[\frac{(I+G)_{128}}{2} \right]} \quad (3-34)$$

$$\text{and } L_s = (\text{slope}) \cdot 127 \quad (3-35)$$

Since it can be shown that Equations (3-34) and (3-35) are equivalent to Equations (3-28) and (3-27), respectively, the proposed modified method is consistent with the original graphical procedure.

In summary, the calibration is performed by a correlation of particle volume, V_{Tr} , or more specifically, standard particle volume, V_{std} , with channel number, ch , at selected current and gain values for a particular log span setting. Mathematically, this is expressed as Equation (3-24) with constants Kc and L_s defined by Equations (3-34) and (3-35), and Equation (3-29) providing the proportionality between ch and Tr . For the equivalent spherical diameter being used in determining the sizes of particulate particles from the calibration data, the representative length of the particles counted in each channel, L , is determined directly from the calibration equations as:

$$L = D_{std} \frac{1}{2} \left[(I+G)_{128} + \frac{L_s}{127} (ch-128) - (I+G) \right] \quad (3-36)$$

Here D_{std} is the diameter of calibration standard particles with $V_{std} = \frac{\pi}{6} D_{std}^3$. The channel width ΔL_{ch} for channel ch , an important quantity in the calculation of quantitative data for the MSMPR crystallizer system, was estimated as the difference of L at $ch+0.5$ and L at $ch-0.5$ according to Equation (3-36).

3-4-3. Calibrations with Known-Size Standard Particles

Experiments described in this section were conducted to confirm the validity of the modified calibration procedure and the null checking of the instrument against changes in electrolytes.

With 0.15 M KNO_3 as the electrolyte in all cases, a 150 μ m orifice tube was used with 10.00 μ m, 20.27 μ m and 41.1 μ m standard particles to

check the calibration data at log span 10. The 300 μm orifice tube was used at log span 8 with 20.27 μm , 41.1 μm and 87.3 μm standard particles. Median channels were determined with varying (I+G) values, and data were fit according to Equation (3-32). Correlation coefficients from individual linear regression were all greater than .9998 which shows the validity of the proposed linear correlation of (I+G) versus ch. For a given orifice tube at one log span setting, the standard deviations of calculated channel sizes were between 1.14 and 5.50% for the three different calibration standards when compared at the same current and gain switch settings for all channels. Since the results may include deviations of the nominal size of the standard particles used, the results of this method are satisfactory.

For the 300 μm orifice tube at log span 8, calibrations were also conducted with two other electrolytes, 0.05 M KNO_3 and 0.15 M KCl . Comparing the data at the same I and G values, the mean channel sizes resulting from calibrations of three standard particles showed only a 0.2% standard deviation for the different electrolytes. Since all the above calibrations were conducted with application of the "normalize" function, these results demonstrate the validity of the "normalize" function in compensating for electrolyte changes and illustrate its convenience in the conservation of operator's time and improvement of operation efficiency. Examples of calibration data and the modified calibration procedure are shown in Appendix B.

3-5. Modification of ELZONE's Data Analysis

Since quantitative data were needed for this research, complimentary data analysis procedures were developed through the use of the data transmission capability of the ELZONE^(R) system.

Instrument operation techniques were revised to obtain a representative sampling volume, and further data manipulation was made available both with user-written programs and marketed spreadsheet software for the IBM PC.

3-5-1. An Alternate Procedure for Sampling Volume

This technique utilizes the built-in TIMED ANALYZE mode (Particle Data, (b)) of the ELZONE^(R) system.

In the "time" mode, the timer in the instrument measures the time span for the intake of volume V_v . The measured time span may be entered as the "preset time", T_{ps} . "Time remaining", one of the variables shown in the transmitted data, is equivalent to the "elapsed time", T_e , the sampling time elapsed in data acquisition and particle counting. When the vacuum of the system is steady, the orifice is clean, and no blockage occurs, it may be assumed that the sampling volume is proportional to the sampling time. The true sampling volume of the data set may be estimated according to:

$$V_s = V_v \left(\frac{T_e}{T_{ps}} \right) \quad (3-37)$$

This time-corrected estimation of sampling volume requires proper operating conditions as well as a representative counting time. Some conditions need to be observed for proper implementation of this method:

a. The flow rate of the analyzed suspension changes during analysis since the differential pressure drop of the vacuum-mercury system may vary by five to fifteen percent from start to stop. Consequently, the sampling volume is not exactly proportional to the sampling time. The resulting error may be practically minimized by operating the TIMED

ANALYZE mode immediately after closing the vacuum (moving the vacuum/flush control toggle to COUNT) and by allowing data acquisition to be halted by the mercury stop contact and not by the "CTRL stop" key.

b. "Preset peak" and "preset total", two of the "status variables" entered by the operator into the "status" screen before data acquisition, stop the data acquisition whenever the counted number in the "peak" or "total" of the measured sample reaches the "preset peak" or "preset total". Because the interruption of data acquisition by these two set points is not registered into the timer to influence the T_e reading, the "preset peak" and the "preset total" should be set large enough so as to avoid their activation and the subsequent interruption of data acquisition.

3-5-2. Data Manipulation

Based on the discussion presented in Section 3-3, use of the ELZONE^(R) system for quantitative data representation requires data manipulation separate from the ELZONE^(R) firmware. This may be readily accomplished by transmission of data from the ELZONE^(R) to a remote device. For the data processing practice in this work, a communication program, 80XYABCV.BAS, written in BASICA, was used to transmit T_e , T_{ps} , and n_{ch} for 128 channels from the ELZONE^(R) system to an IBM PC. With dilution factor, DF, and the calibrated sample volume, V_v , as inputs, the program calculated sample volume, V_s , as per Equation (3-37) and the corrected count in channel, $n_{ch,c}$, as per Equation (3-19). The $n_{ch,c}$ data were then stored onto floppy diskettes for further data processing. The population density was calculated using spreadsheets (SuperCalc4 (tm) or Lotus 1-2-3) by dividing $n_{ch,c}$ by the appropriate

ΔL_{ch} discussed in Section 3-4-2. These techniques were used to gather and manipulate the data presented in Chapter 4.

The communication and data analysis program 80XYABCV.BAS is listed in Appendix C.

CHAPTER 4

MIXED-SUSPENSION, MIXED-PRODUCT-REMOVAL CRYSTALLIZATION SYSTEM

4-1. Introduction

The objective of the work described in this chapter was to characterize the calcium oxalate crystallization in the MSMPR crystallizer system and to extract crystal growth rate data from the simultaneous crystal growth and crystal aggregation phenomena occurring in the system. As a result, the effects of biopolymers on crystal growth were well defined. The isolation of growth rate results offers the possibility of investigating the effect of biopolymers on crystal aggregation for future research.

The continuous mixed suspension, mixed product removal (MSMPR) crystallization system has been widely used in industry (Randolph and Larson, 1971). Because an MSMPR crystallizer provides a continuous supersaturated inlet stream and continuous removal of the precipitated particles and solution, it has been used to simulate the function of the kidney in the study of nephrolithiasis (Drach et al., 1978, 1980, 1982; Garside et al., 1982; Robertson and Scurr, 1986). As discussed in the first chapter, much research has been done in this area; steady state experimental results have been reported in which linear population density models have been used to describe nonlinear data (Garside et al., 1982). Besides nonlinear population density data, scaling of calcium oxalate crystals on the wall of reaction vessel was also observed in the operation of the MSMPR crystallizer (Drach, Randolph, and Miller, 1978; Randolph and Drach, 1981; Drach, Sarig, et al., 1982; Garside et al., 1982).

Our preliminary experiments also showed heavy deposition of calcium oxalate in the crystallizer and demonstrated calcium oxalate aggregation. Because of the involvement of aggregation phenomenon in the system, the simple population balance equation with only crystal nucleation and crystal growth considered could not be valid. In addition, the scaling effect is an indication of the unsteady-state nature of the system based on the definition of steady state described in Chapter 1. The main focus of this work, therefore, was to first characterize the calcium oxalate crystallization process by evaluating chemical compositions and particle size distributions of the system with respect to time in order to test the steady state assumption.

Secondly, this study was highly motivated by the need to differentiate the effects of the two superimposed crystallization mechanisms, crystal growth and crystal aggregation, in the continuous process. Two approaches were developed to calculate the linear crystal growth rate, G_L , for the unsteady state process in which aggregation was present. With these methods, the effects of a biopolymer additive, polyglutamate, on crystal growth were examined.

Studies on the inhibitors of calcium oxalate crystallization have demonstrated the significant inhibitory effects of anionic urinary macromolecules (Ito and Coe, 1977; Nakagawa et al., 1983). Glutamate and aspartate are the two amino acids having acidic side chains. The repeating unit of poly-L-glutamic acid is glutamate shown in Figure 4-1; poly-L-glutamic acid was chosen as the model biopolymer in this study.

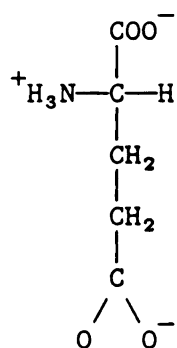


Figure 4-1 Repeating unit of polyglutamate.

4-2. Experimental Methods

4-2-1. Apparatus and Materials

The MSMPR crystallizer or precipitator is a continuously stirred tank reactor (CSTR) system; Figure 4-2 shows its experimental configuration. Calcium and oxalate solutions were pumped through filters, flowmeters, and heating coils and were mixed in the crystallizer. Calcium oxalate crystals were formed in the reactor, and the suspension was withdrawn continuously from the reactor.

The crystallizer used in the system was constructed by the Glass Shop of the Department of Chemistry of Michigan State University. The reactor was designed with a hybrid-type bottom for effective mixing as per Chudacek (1984) (shown in Figure 4-3). The diameter of the propeller and the geometrical parameters of the tank with four symmetrical baffles are listed in Table 4-1.

The three-blade propeller and the motor were controlled by a constant-speed power supply (Cole-Parmer Master Servodyne drive system) for constant stirring rate. The Servodyne drive system offers the option of turning the propeller either clockwise or counter-clockwise. Because the blades of the propeller have a 1:1 pitch, rotating the

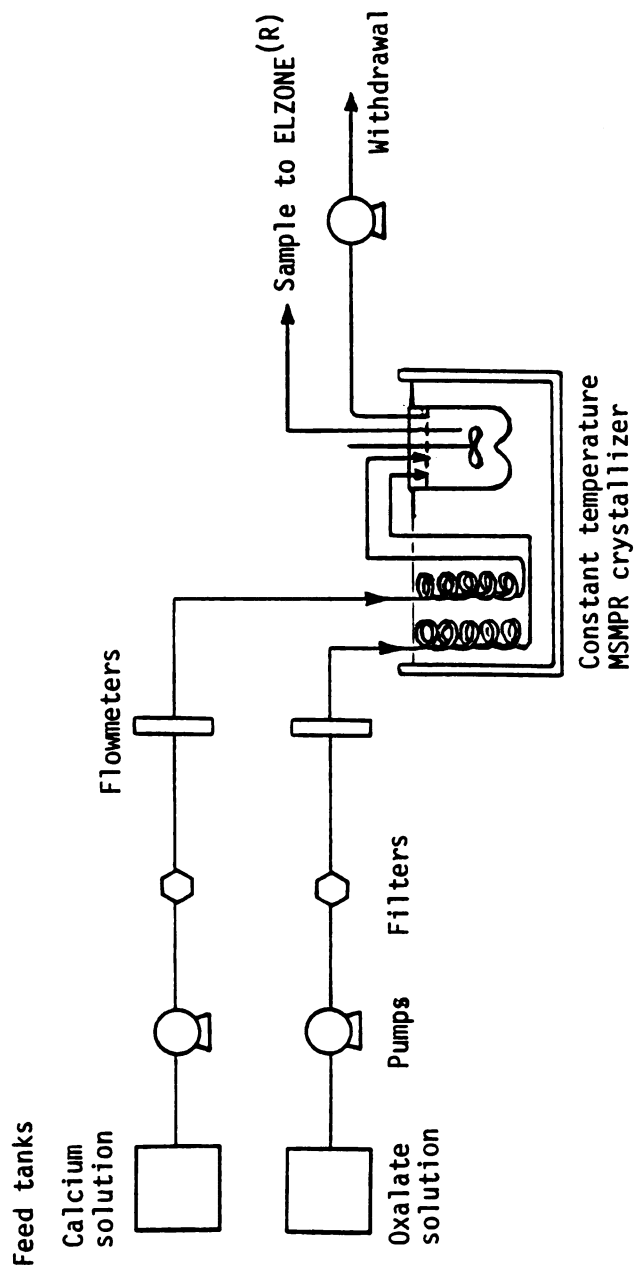


Figure 4-2 MSMPR experimental set-up.

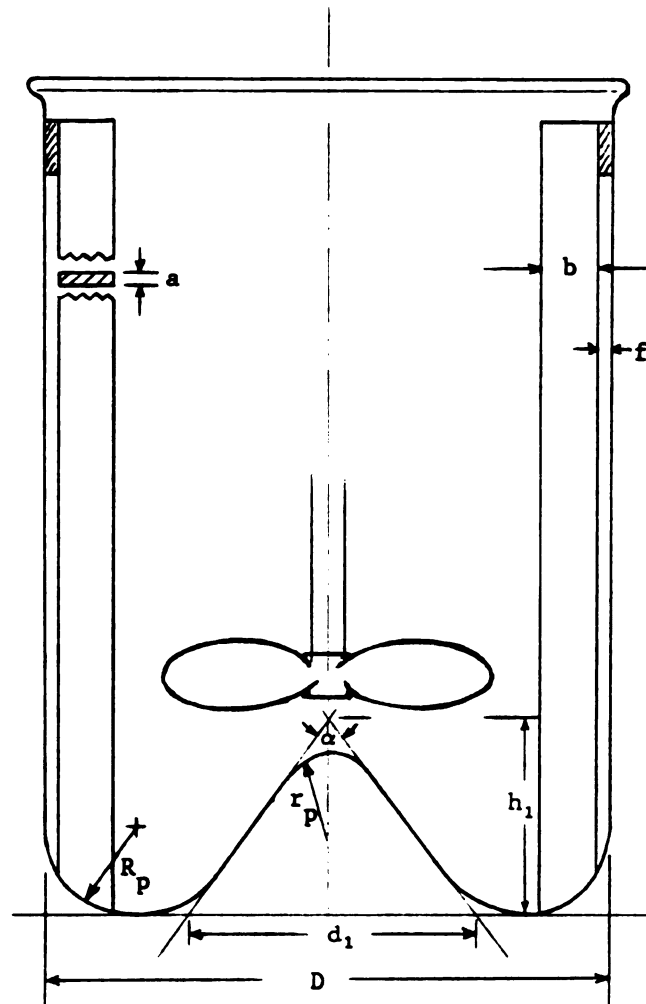


Figure 4-3 400 ml hybrid tank.

Table 4-1 Geometrical parameters of the crystallizer.

Propeller diameter, D_a	4.7 cm
Tank diameter, D	8 cm
Profiled-bottom radius, R_p	1.28 cm
Central-cone height, h_1	2.8 cm
Central-cone angle, α	72.5°
Central-profile radius, r_p	1.2 cm
Central-cone diameter, d_1	4.16 cm
Baffle thickness, a	0.2 cm
Baffle width, b	0.8 cm
Baffle clearance, f	0.2 cm

propeller clockwise or counter-clockwise directed the main stream of fluid either 45° upward or downward in the crystallizer. Since calcium oxalate crystals (density 2.2 g/cm³ (CRC Handbook)) are more dense than the fluid (with density close to water), the propeller was rotated so as to push the suspension upward to compensate for gravity and to ensure homogeneous mixing. Vigorous turbulent mixing with trapped air bubbles was seen when the stirring rate was higher than 500 rpm. Therefore, the stirring rate was set at 500 rpm for homogeneous mixing and to minimize particle breakage. The modified Reynolds number for the agitated tank was calculated according to Equation (1-20):

$$Re_T = \frac{ND_a^2 \rho}{\mu} \quad (1-20)$$

A value of 26750 was obtained, which ensures turbulent flow ($Re_T > 10^4$) in the reactor. The fluid viscosity and fluid density used for the calculation of Reynolds number are shown in Appendix D.

Flow rate in each stream of the inlet solutions was monitored with flowmeters (Cole-Parmer) to ensure the required residence time of the

solution in reactor. The on-line filters used were 0.2 μm ULTIPOR^(TM) disposable filter assemblies (Pall Corporation). Reaction temperature was kept at 37°C by a water bath with an immersion circulator (Haake, model E3).

Solutions were prepared using reagent grade chemicals and doubly distilled deionized water. $\text{Ca}(\text{NO}_3)_2 \cdot 4\text{H}_2\text{O}$ (from J. T. Baker) and $\text{K}_2\text{C}_2\text{O}_4 \cdot \text{H}_2\text{O}$ (from Sigma) were used as the sources of calcium and oxalate respectively. The biopolymer additive was polyglutamate (poly-L glutamic acid, sodium salt, (PGA), from Sigma) of molecular weight 26,500. pH values of the feed solutions were adjusted to 6.00 ± 0.01 with HNO_3 and KOH ; KNO_3 (J. T. Baker Chemical) was added to maintain ionic strength at 0.15 molal. Equal molar concentrations of calcium and oxalate ranging from 1 to 4 mM (based on the total volume of the mixed solution) were used. Supersaturation of calcium oxalate, pH, and ionic strength were chosen to simulate the physiological conditions of urine.

4-2-2. Experimental Scheme

The experiment with calcium and oxalate concentration at 2 mM without polyglutamate additive and a residence time of eight minutes was chosen as the base case to compare directly with physiological conditions. Other experimental runs were carried out by varying calcium and oxalate concentration level, residence time, and PGA concentration. Residence time, τ , was varied from 6 to 16 minutes, and the PGA concentration levels used were 1 ppm, 10 ppm, and 100 ppm. The experimental scheme is summarized in Table 4-2.

Table 4-2 Experimental scheme.

Run number	<u>Experimental conditions</u>		
	τ (min)	$[\text{Ca}^{2+}] - [\text{C}_2\text{O}_4^{2-}]$ (mM)	PGA (ppm)
4	8	1	0
8	8	2	0
7	8	3	0
6	8	4	0
9	6	2	0
10	16	2	0
14	8	2	1
12	8	2	10
13	8	2	100

Each experiment was initiated with 400 ml of a saturated calcium oxalate solution in the reactor. Throughout the run, suspension solution was sampled from the crystallizer every 1 to 2 residence times for the determination of particle size distributions, total calcium concentration in the suspensions, and calcium concentration in the filtrates of suspensions. Each run was carried out for a period of about 24 residence times.

4-2-3. Measurement of Particle Size Distributions

The ELZONE^(R) Particle Data Analyzer (Particle Data, Inc.) described in Chapter 3 was used to determine the size distributions of crystals and aggregates. The ELZONE^(R) was calibrated with standard microspheres (10.00 and 41.1 μm) and latex particles (20.27 μm). Diameters of the aperture tubes used were 76 μm , 95 μm , 150 μm , or 300 μm depending on the particle sizes of the samples. Generally, the

higher the calcium and oxalate concentrations or the longer the residence time, the larger the particles formed.

A 0.15 molal KNO_3 solution saturated with calcium oxalate crystals was prepared as the electrolytic solution used for particle counting with the ELZONE^(R). Immediately before use, the electrolytic solution was filtered through a 0.45 μm membrane filter and a 0.2 μm ULTIPOR^(TM) disposable filter assembly (Pall Corporation) in series. Samples were diluted one to three or one to six by volume with the prepared electrolytic solution before particles were counted with the ELZONE^(R) system. Dilution was necessary because too many particles in the samples could cause clogging at the orifice during particle counting.

The particle sizing data were transmitted to an IBM PC and stored on floppy diskettes as described in Chapter 3. For further data manipulation, particle data were imported to SuperCalc 4 (tm) or Lotus 1-2-3 spreadsheets. Particle size distributions, $n(L,t)$ or $v(L,t)$ versus particle size, L , or $m(w,t)$ versus w (defined in Chapter 3) were calculated and presented as figures. The distributions in the form of tabulated data or figures were printed out as needed.

4-2-4. Measurement of Calcium Concentrations

Calcium concentrations in the filtrates and in the suspensions (10 ml of each) were determined using atomic absorption (AA) spectrophotometry. The AA spectrophotometer (Varian AA-375) was made available by Dr. Mackenzie L. Davis in the Department of Civil and Environmental Engineering. The filtrates were prepared from suspension samples drawn with a syringe and filtered with 0.2 μm membrane filters assembled in the syringe filter holder. For the determination of total calcium concentration in the suspension samples, the calcium oxalate

crystals or precipitates in the solution were dissolved by the addition of concentrated sulphuric acid for AA analyses.

4-2-5. Determination of Crystal Habit and Crystal Hydrate Phases

Crystal hydrates were identified from microscopy (One-Ten Microstar^(R), AO Scientific Instruments) and X-ray diffractometry. Powder samples were collected at between 6 to 12 °C and filtered through 0.8 µm membrane filters for X-ray identification. Two X-ray diffractometers were used in this work-- one made available by Dr. Kalinath Mukherjee in the Department of Metallurgy, Mechanics, and Materials Science, and the other by Dr. Duncan F. Sibley in the Department of Geological Sciences. The radiation used in both diffractometers was CuKα filtered with Ni filters.

4-3. **Characterization of Calcium Oxalate Crystallization in MSMR System**

4-3-1. Calcium Oxalate Hydrates and Crystal Habit

Aggregates of calcium oxalate crystals were formed in the precipitation processes as confirmed with the optical microscope. Figure 4-4 shows a photograph taken from the experiment with calcium and oxalate concentrations at 3 mM. A COM (DeLong, 1988) crystal was seen as marked. The other crystals are most likely COT (Gardner, 1975).

Crystal hydrates were identified by comparison of the X-ray diffractograms to the crystallography data for COM, COD (Sutor and Scheidt, 1968), and COT (Brindley, 1957). Table 4-3 summarizes the major hydrates formed for each set of experimental conditions. Because of the limits of sensitivity of the X-ray diffractometer, minor crystal

hydrates present in less than 5% were not shown in the diffractograms. For example, the COM seen in Figure 4-4 was not observed by X-ray diffraction.

Table 4-3 Crystal hydrates.

Experiment with	<u>Hydrates</u>
$[\text{Ca}^{2+}] - [\text{C}_2\text{O}_4^{2-}]$:	
1 mM	COM
2 mM	COT
3 mM	COT
4 mM	COT
Residence time:	
6 min	COT
16 min	COT
PGA additive:	
1 ppm	COM and COT
10 ppm	COM and COD
100 ppm	COM and COD

4-3-2. Particle Size Distributions

The time-dependent particle size distributions of each experimental run may be presented in the form of $n(L,t)$, $v(L,t)$, or $w(m,t)$ as per the equations shown in Chapter 3. Figures 4-5 and 4-6 are typical population density plots of the samples taken between eight to ten residence times. Figure 4-5 data are without PGA additive, and Figure 4-6 data are with PGA additive. With PGA additive, the particle size distribution exhibits a wave-like shape. The wave shape of population distribution is more pronounced in the $v(L,t)$ PSD representation (Figure 4-7).

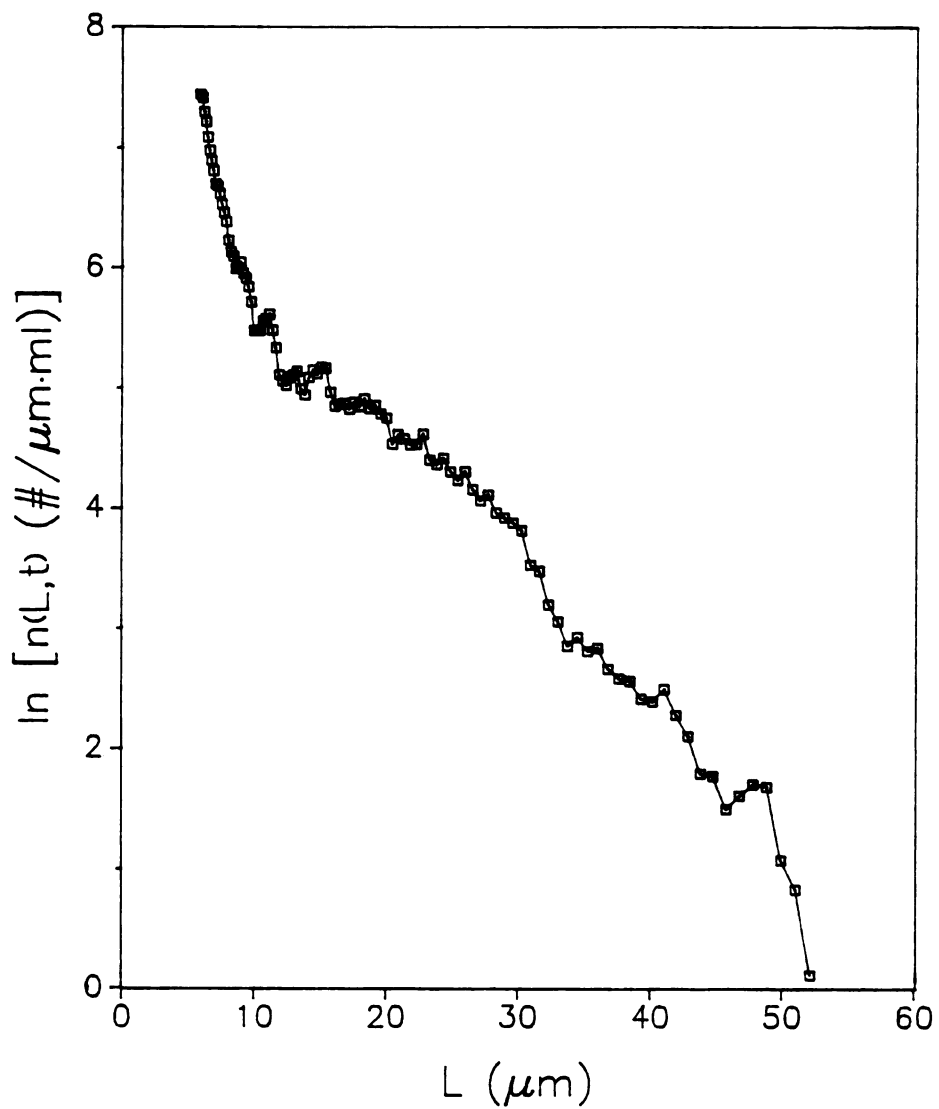


Figure 4-5 Population density plot A;

$[\text{Ca}^{2+}] = [\text{C}_2\text{O}_4^{2-}] = 3 \text{ mM}$, without PGA,

$r = 8 \text{ min}$, sampling time = 74 min.

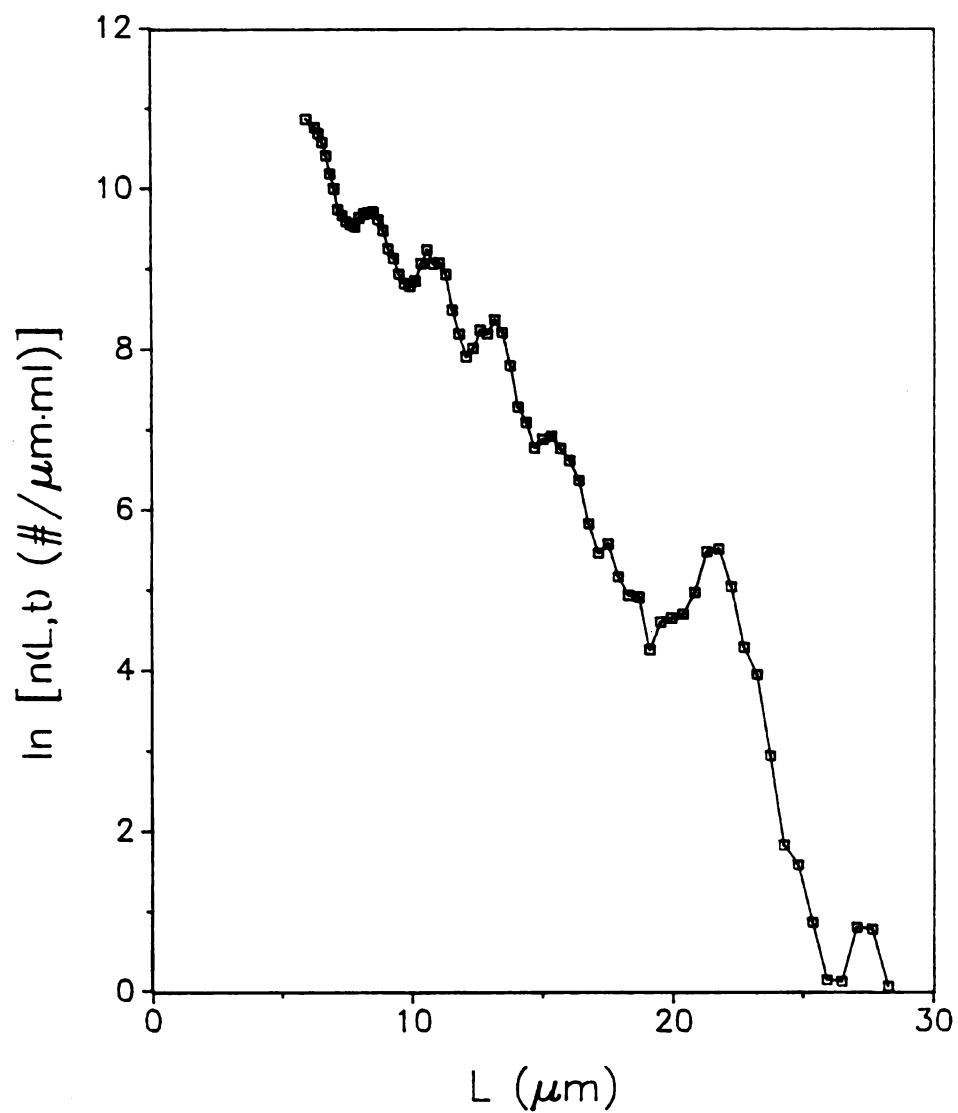


Figure 4-6 Population density plot B;

$[\text{Ca}^{2+}] - [\text{C}_2\text{O}_4^{2-}] = 2 \text{ mM}$, PGA = 100 ppm,
 $\tau = 8 \text{ min}$, sampling time = 68 min.

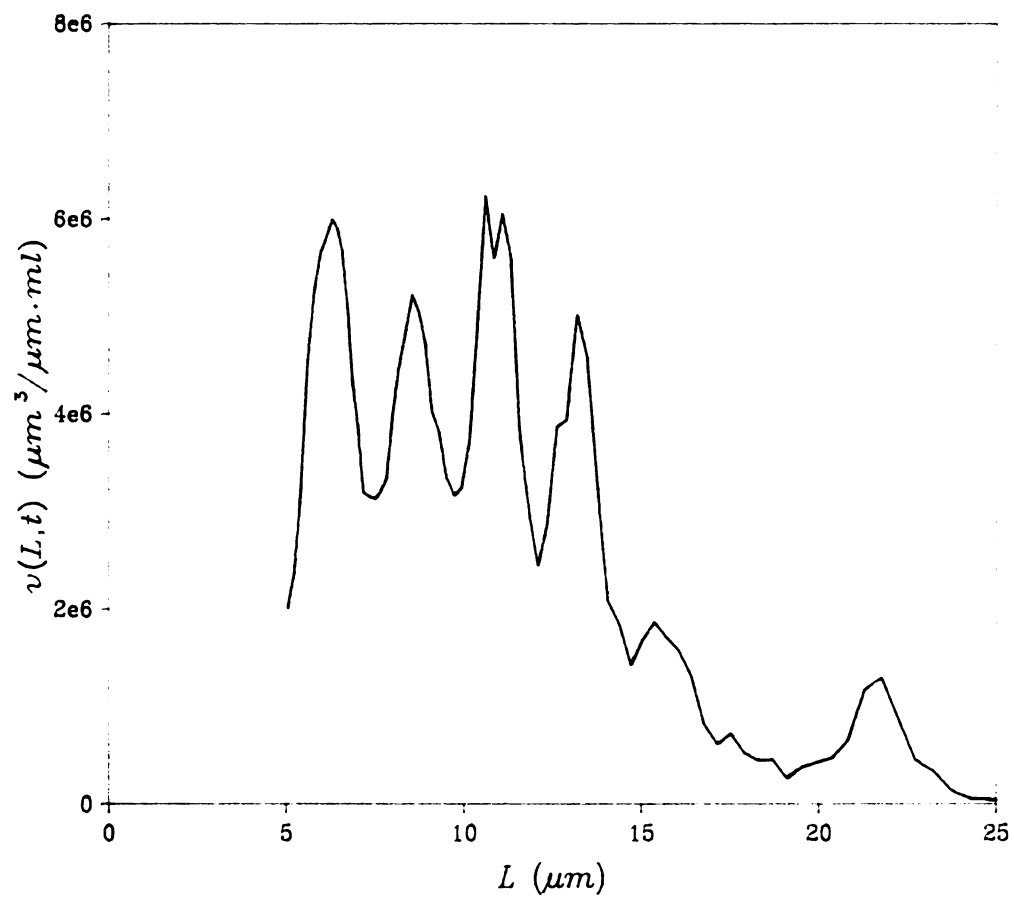


Figure 4-7 $v(L,t)$ particle size distribution;

$[Ca^{2+}] = [C_2O_4^{2-}] = 2 \text{ mM}$, PGA = 100 ppm,

$\tau = 8 \text{ min}$, sampling time = 68 min.

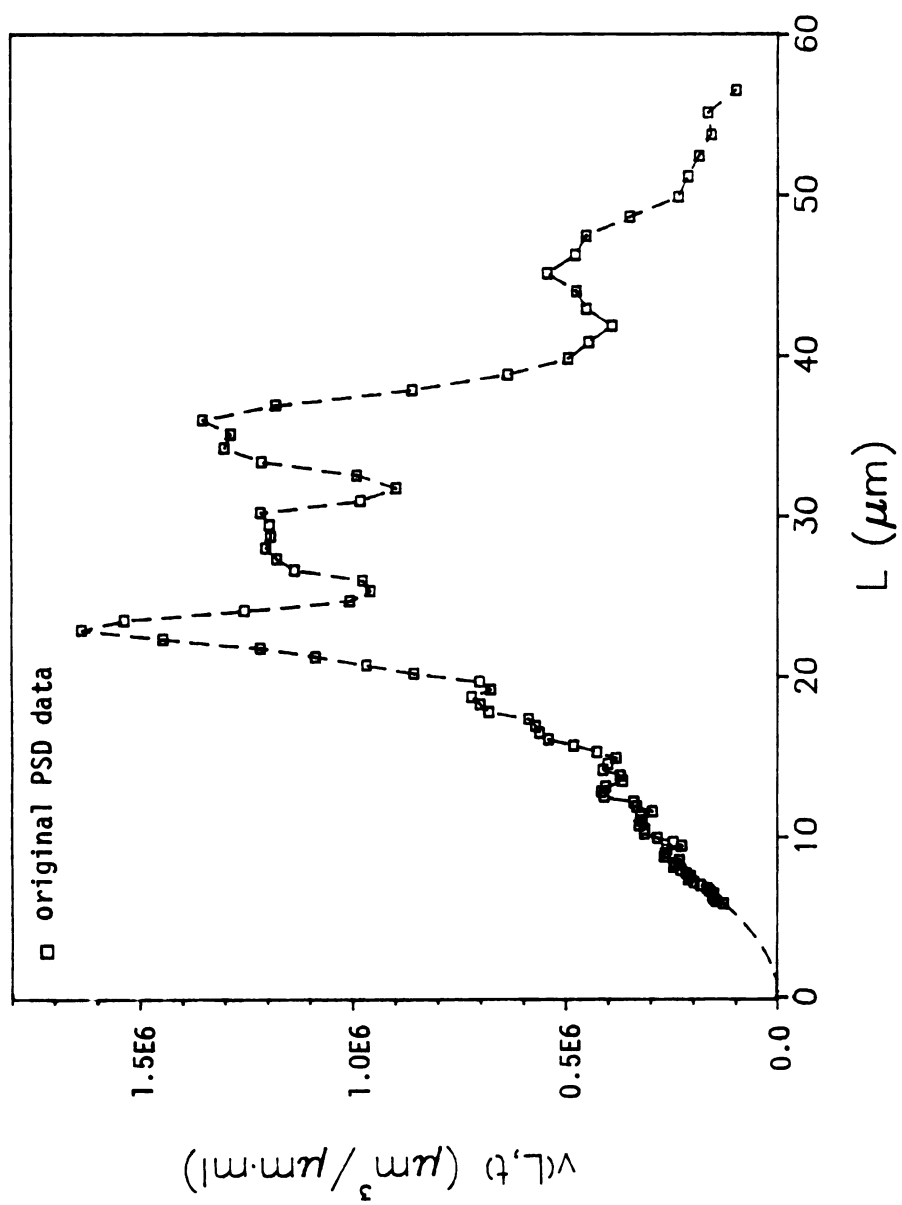


Figure 4-8 $v(L,t)$ with extrapolated small size range.

Figure 4-8 also illustrates a $v(L,t)$ PSD. The original PSD is shown with the square symbol. Because of the nature of the particle sizing instrument, particles below certain size limits were not counted; Figure 4-8 shows the size distribution above $5.5 \mu\text{m}$. In this $v(L,t)$ data, the size distribution follows a general trend of decreasing volume with decreasing particle sizes ranging from $5.5 \mu\text{m}$ to $23 \mu\text{m}$. Because of this general trend over a relatively wide range of the existing particle sizes, it may be assumed that the size distribution is a monotonically smooth curve below the lower sizing limit. If a curve of the second power of particle sizes is assumed for this small size range, the whole particle size distribution is shown as the dashed curve in Figure 4-8, where the distribution above the lower counting limit is presented by straight lines connecting the data points.

This fitted complete size distribution provides a feasible way to calculate the total particle number, N_T , the third moment, M_3 , the total mass, M_T , or total volume, V_T , in suspension. In this work, the computer program NTM3.FOR was written in FORTRAN to calculate N_T and M_3 according to Equations (3-1) and (3-3):

$$N_T(t) = \int_{L_c}^{\infty} n(L,t) dL \quad (3-1)$$

$$M_3(t) = \int_{L_c}^{\infty} n(L,t) L^3 dL \quad (3-3)$$

The $n(L,t)$'s used in the calculations were calculated from the fitted $v(L,t)$ distributions input to the program. The theoretically calculated critical cluster size, L_c , from homogeneous nucleation data is $0.0013 \mu\text{m}$ for calcium oxalate crystals (Walton, 1967). This value

was the lower bound of the integration used in calculation. IMSL spline and integration routines were used as shown in the flow chart and in the listing of the NTM3.FOR program (see Appendix E).

For the base case, the N_T and M_3 results are shown in Figure 4-9. Figure 4-9(a) shows a maximum in N_T at 36 min ($= 4.5 \tau$) and Figure 4-9(b) shows a maximum in M_3 at 24 min ($\approx 8.1 \tau$). Since the third moment is proportional to the total crystal mass (Equation (3-5)), both the total crystal number and total crystal mass decrease gradually after reaching their maximum values. After eight to ten residence times (64 to 80 min), the rates of decrease of N_T and M_T slowed.

4-3-3. Calcium Concentration in the Crystallizer

Figure 4-10 presents typical results from the calcium concentration measurements. The calcium concentration in the filtrate measured by AA spectrophotometry is the total calcium content in the liquid phase and is related to the solution supersaturation in the crystallizer. The total calcium concentration of the suspension is the sum of the calcium content in the crystal phase and in the liquid phase. The difference between these two concentrations is the calcium content of the crystal mass and should be proportional to M_T or M_3 (the shaded region).

In Figure 4-10, both the filtrate calcium concentration and the suspension calcium concentration show the same trend as the N_T and M_3 results-- an initial increase and a subsequent decrease with respect to time. These concentrations leveled off after eight to ten residence times.

The solid line in Figure 4-10 (marked theoretical) is the maximum

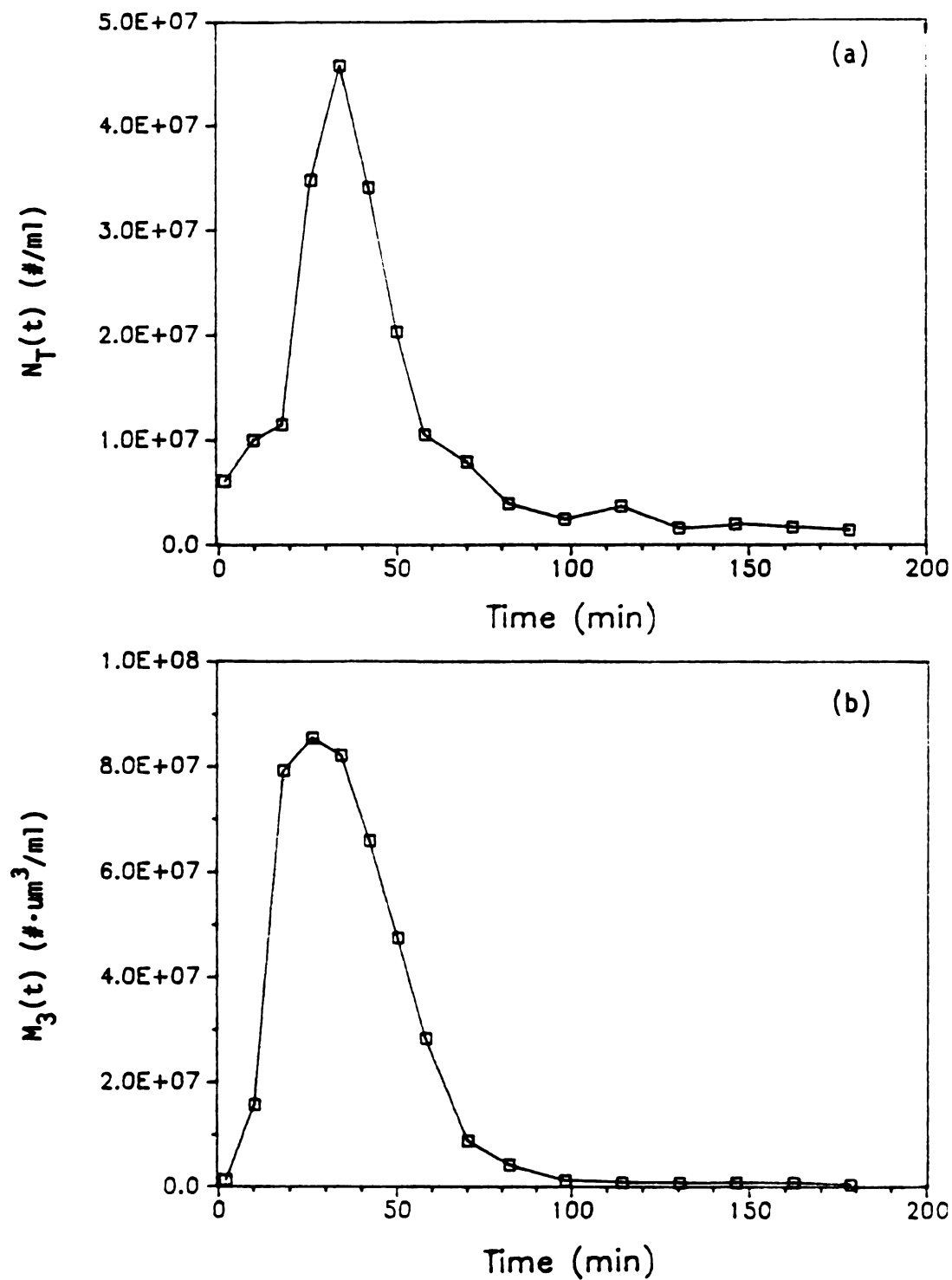


Figure 4-9 Total particle numbers and the third moments for the base run;
 (a) total particle numbers, N_T ,
 (b) the third moments, M_3 .

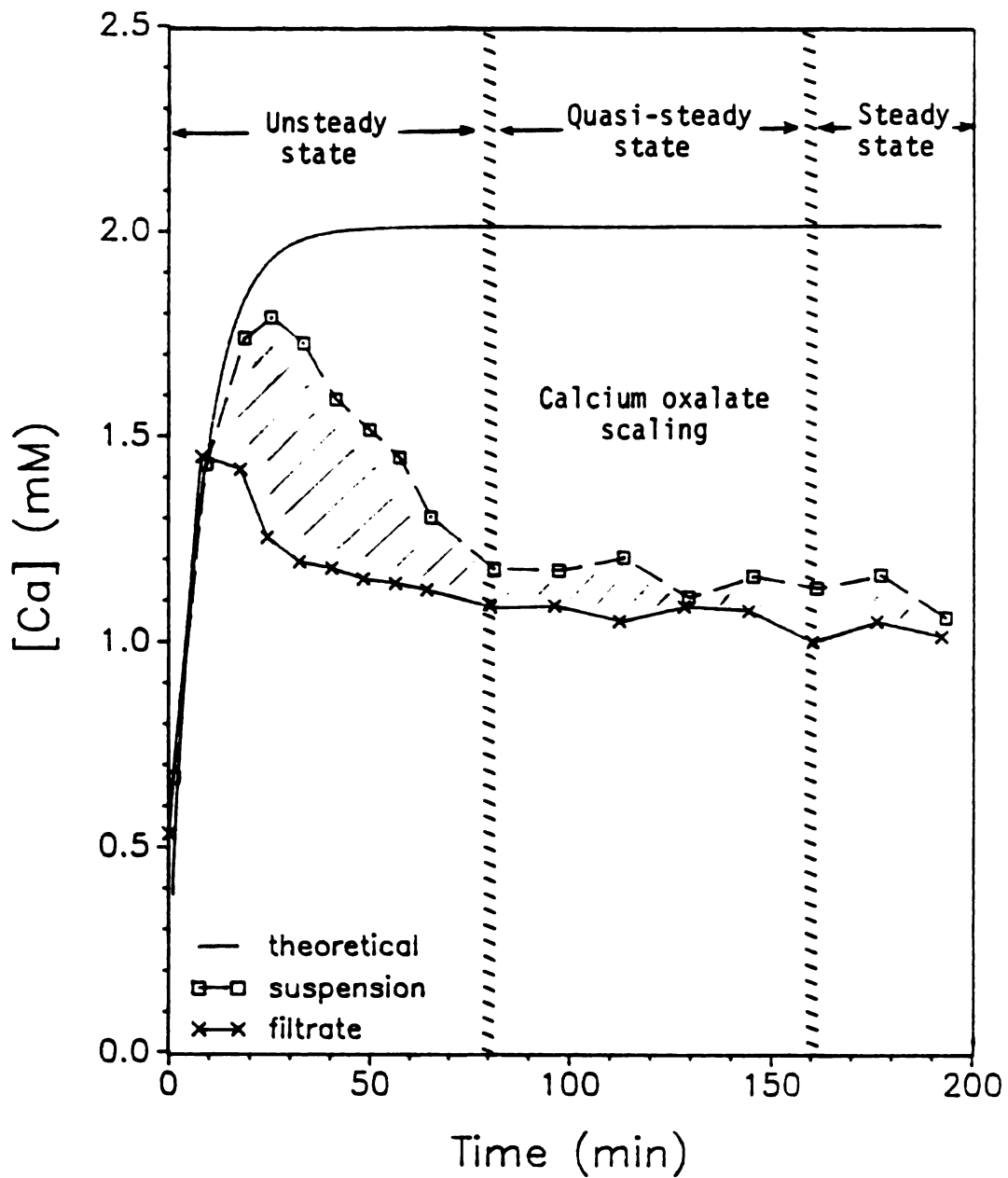


Figure 4-10 Calcium concentrations in the filtrates and in the suspensions;

$$[Ca^{2+}] = [C_2O_4^{2-}] = 2 \text{ mM}, \text{ PGA} = 10 \text{ ppm}.$$

calcium concentration calculated to show the upper limit of the total calcium concentration in the suspension. It was calculated from species balance for a CSTR system (Levenspiel, 1972):

$$[Ca]_t = [Ca]_i \left[1 + \left(\frac{[Ca]_0}{[Ca]_i} - 1 \right) \exp \left(- \frac{t}{\tau} \right) \right] \quad (4-1)$$

where $[Ca]_t$ is the calcium concentration in the crystallizer as a function of time t , $[Ca]_i$ is the inlet calcium concentration, and $[Ca]_0$ is the initial calcium concentration in the crystallizer. Since saturated calcium oxalate solution was used in the crystallizer to initiate the operation of the MSMMPR crystallizer, $[Ca]_0$ was calculated from the COM solubility product assuming equal calcium and oxalate concentrations; an approximated value of 0.31 for the activity coefficients of calcium and of oxalate as calculated from the EQUIL-NA.BAS program (Appendix A) was used.

The deviations from the theoretically calculated and the observed total calcium concentrations are due to the severe scaling effect. Because of the scale formed on the walls of the reactor, baffles, and the propeller, particle numbers and total crystal mass in suspension decreased during a run (Figures 4-9).

4-3-4. Crystallization Mechanisms

The distributions of calcium concentrations, the total number, and the third moment as presented in Figures 4-9 and 4-10 give an indication of the mechanisms involved in the crystallization process.

The literature generally reports that steady state may be achieved in a calcium oxalate MSMMPR crystallizer after eight to ten residence times (Garside, Brecevic, and Mullin 1982; Drach, Thorson and Randolph, 1980). In Figures 4-9 and 4-10, the unsteady-state nature of the

process is seen before 8 to 10 τ as expected. After about 10 τ , the concentrations level off, and the process begins to approach a steady state after at least 12 τ at which point there are fewer particles in the solution (in Figure 4-9(a) the peak $N_T = 4.48E7$ at $t = 4.3 \tau$, $N_T = 2.38E6$ at $t = 12.3 \tau$, and $N_T = 1.35E6$ at 22.3τ).

The process may be divided into three regions, unsteady state, quasi-steady state, and steady state as shown in Figure 4-10. In this figure, three regions are divided at 8 τ and at 20 τ . However, this delimitation is conceptual especially at the division between the quasi-steady state and steady state. The quasi-steady state is characterized by the continuous but gradual decrease of particle numbers with time.

At unsteady state, because of the presence of a high supersaturation and a large amount of crystal mass, formation of crystal nuclei may be via heterogeneous nucleation and secondary nucleation. In the early stage of the MSMPR crystallization process when there were no crystals in the system, the initial nucleation in the system is most likely heterogenous nucleation, one of the primary nucleation mechanisms, since homogeneous nucleation is rare. After a large number of nuclei formed, the presence of existing crystals suggests the occurrence of secondary nucleation.

High supersaturations also ensured crystal growth, and a large number of crystals provided a high collision frequency for the formation of aggregates. Therefore, nucleation, crystal growth, and aggregation were all involved in the precipitation process.

At quasi-steady to steady state, the total particle numbers decreased. Low total particle numbers may greatly reduce both secondary nucleation and particle aggregation with time. Eventually,

crystal growth is the only significant crystallization phenomenon in the system.

4-3-5. Effect of PGA Additive on Calcium Oxalate Crystallization

It was observed that addition of PGA in the experimental solutions decreased the scaling effect. The total particle numbers and the third moments were higher but the maximum particle sizes observed from the PSDs were lower with the addition of PGA (Figure 4-11). Adding PGA also increased the total calcium concentrations in suspension and the calcium concentrations in filtrates (Figures 4-12 and 4-13). Because the third moment is proportional to the total crystal mass, the higher values of the third moment indicate higher total crystal mass due to addition of PGA to the solution. The higher the calcium concentration in the filtrate, the higher the supersaturation in solution. Therefore, addition of PGA increases the total crystal number, crystal retention (crystal mass), and supersaturation in the reactor, but decreases the crystal size formed in the crystallization process.

These results suggest that addition of PGA may inhibit crystal growth by reducing the generation of active sites for crystal growth. As a result, a smaller number of the growth sites on the wall of the reactor reduced scaling effect. The lower growth rate also indicates a lower calcium oxalate consumption due to crystallization, which in turn results in higher supersaturation. The higher supersaturations are relieved by the formation of more but smaller crystals.

PGA may inhibit crystal nucleation by providing a protective layer on the crystal debris which generate new particles since secondary nucleation is the most likely nucleation mechanism in the system. But high supersaturation results in a burst of nucleation. This may be the

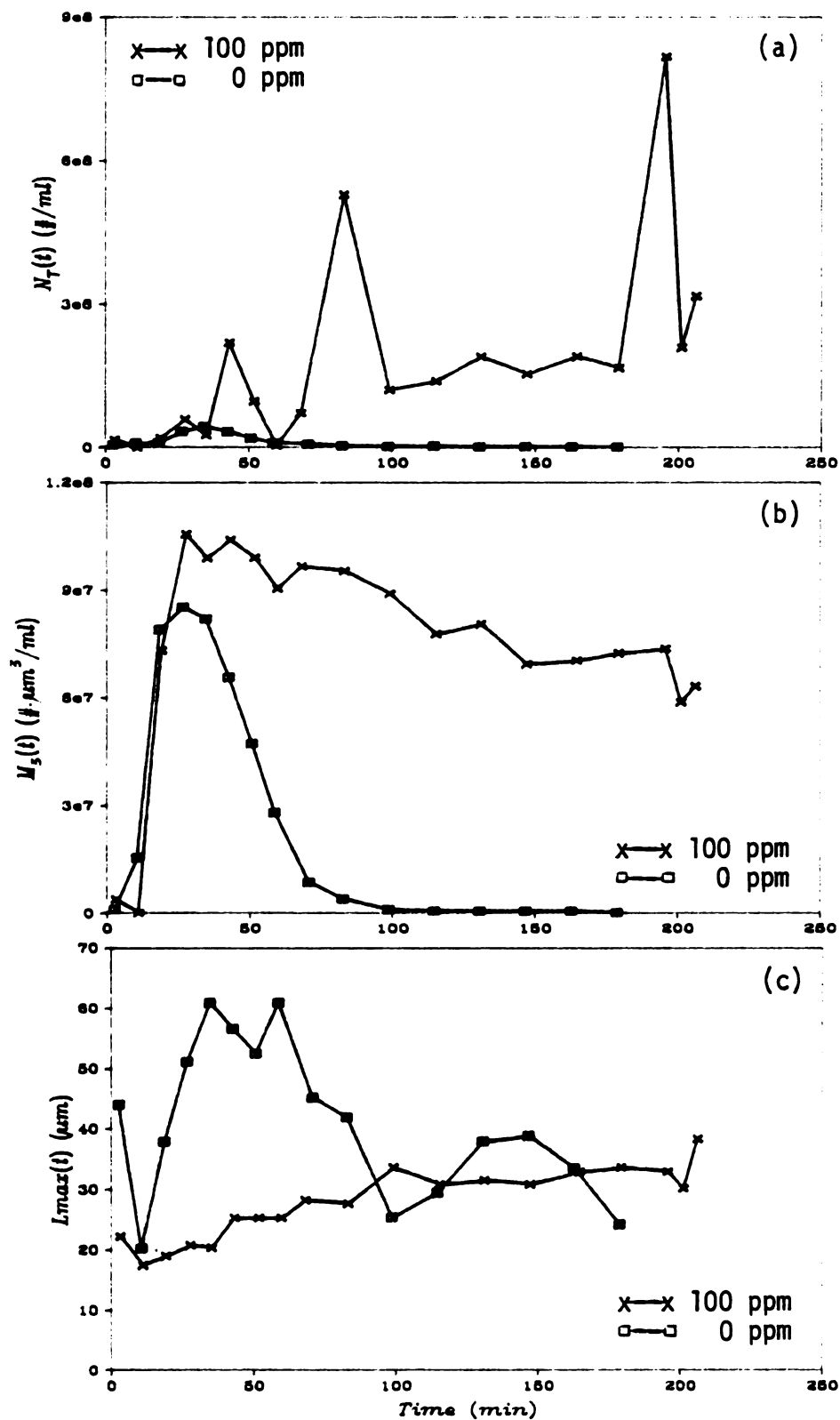


Figure 4-11 Effects of PGA additive on total particle numbers, the third moments, and maximum particle sizes;
 (a) effect of PGA on total particle numbers, N_T ,
 (b) effect of PGA on the third moments, M_3 ,
 (c) effect of PGA on maximum particle sizes, L_{max} .

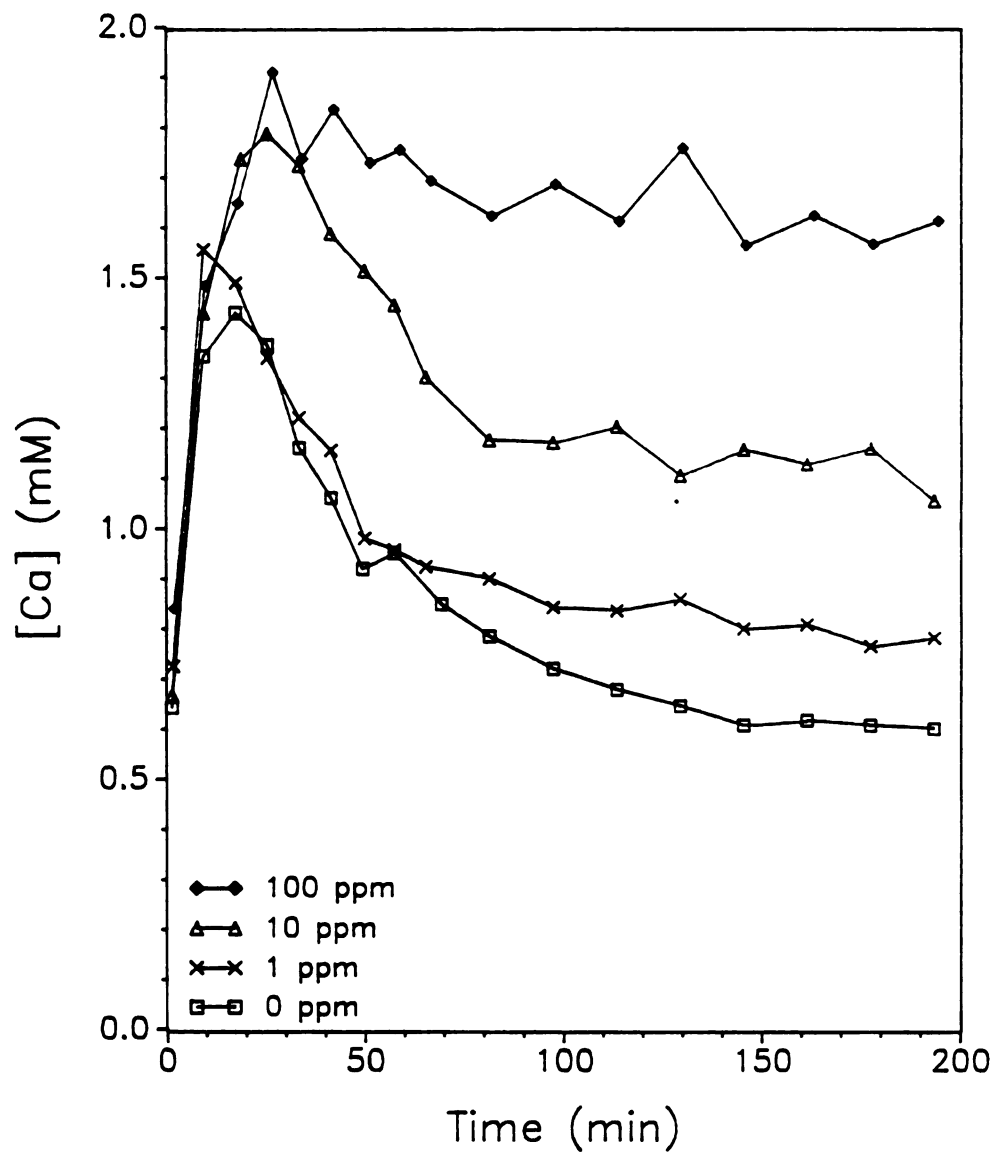


Figure 4-12 Effect of PGA additive on total calcium concentrations in suspensions;

$[Ca^{2+}] = [C_2O_4^{2-}] = 2 \text{ mM}$, $\tau = 8 \text{ min}$.

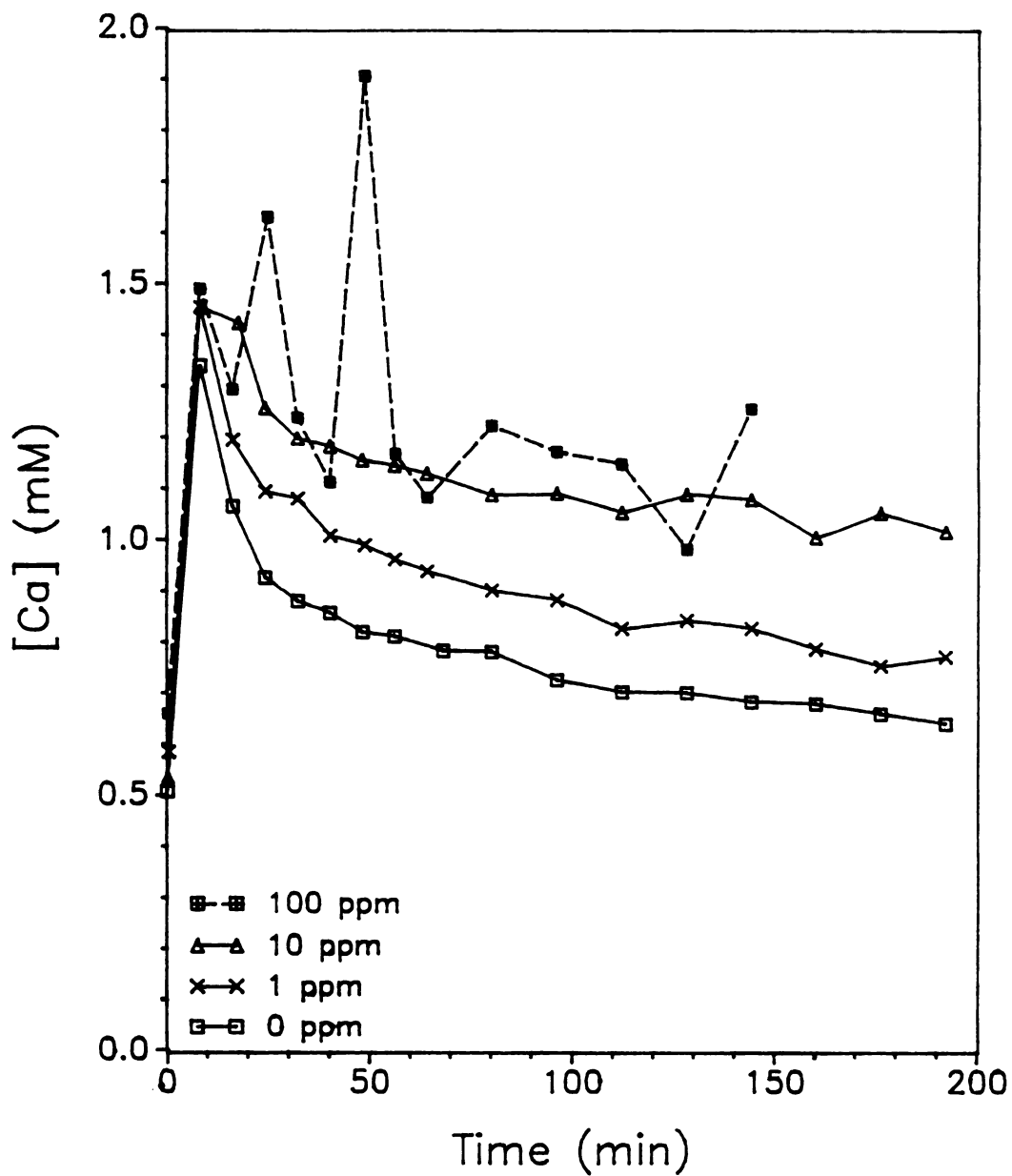


Figure 4-13 Effect of PGA additive on calcium concentrations in filtrates;

$$[\text{Ca}^{2+}] = [\text{C}_2\text{O}_4^{2-}] = 2 \text{ mM}, \tau = 8 \text{ min.}$$

reason for the wave curve observed in the PSDs with PGA additive. When crystal growth is size independent and crystal aggregation does not significantly affect the PSDs, the wave curve is sustained to fairly large sizes.

The filtrate calcium concentrations for the experiment with 100 ppm PGA addition (Figure 4-13) were not accurate because filtration of the suspensions for this experiment was difficult. It is probable that the large molecules of PGA clogged the pores of the filters.

4-4. Growth rate

The discussion in Section 4-3-4 shows that crystal aggregation occurs predominantly during the unsteady state operation of the MSMPR crystallization system. Since an ultimate goal of this work was to gain an understanding of the role of crystal aggregation in kidney stone formation and the effects of biopolymers on crystal aggregation, the unsteady state period in MSMPR operation is of interest. Because crystal growth and crystal aggregation occurred simultaneously in the unsteady-state MSMPR crystallizer operation, understanding of aggregation phenomenon relies upon knowing growth rate kinetics of crystals. Two approaches were developed to find the growth rate of calcium oxalate crystals in the MSMPR crystallizer: Approach A is for the growth rate of the whole process, unsteady state through steady state, and Approach B is for the growth rate at the quasi-steady state. In these approaches, growth rate dispersion and size dependent growth were not considered based on results of single crystal growth experiments conducted in this lab (DeLong and Briedis, 1985) that showed neither phenomenon occurring.

4-4-1. Approach A: Growth Rate by Comparison of PSD Curves

From the experiments described earlier, time dependent particle size distributions were obtained. Careful observation of time-sequenced PSDs from the experiment with 100 ppm PGA additive showed that the wave curves as seen in Figure 4-7 appeared to shift along the L axis when one PSD was compared to the next. This observation led to an understanding of the changes in PSDs for the MSMPR crystallizer as described in the following paragraphs.

For an MSMPR crystallizer operating at unsteady state, the particle size distribution in the crystallizer changes with time due to the constant withdrawal of suspension from the reactor and due to crystal growth and aggregation. The constant withdrawal of suspension from the reaction vessel results in an exponential decay both of particle number of each size and total particle number. In this case, the shape (the characteristic peaks and valleys) of the PSD curves remain the same. Adding the effect of crystal growth to the exponentially decaying PSD results in a shift of the PSD to right on the size axis, L. The crystal growth rate may be calculated from the shifted length, ΔL , and the time interval of data samplings, Δt , according to

$$G_L = \frac{\Delta L}{\Delta t} \quad (4-2)$$

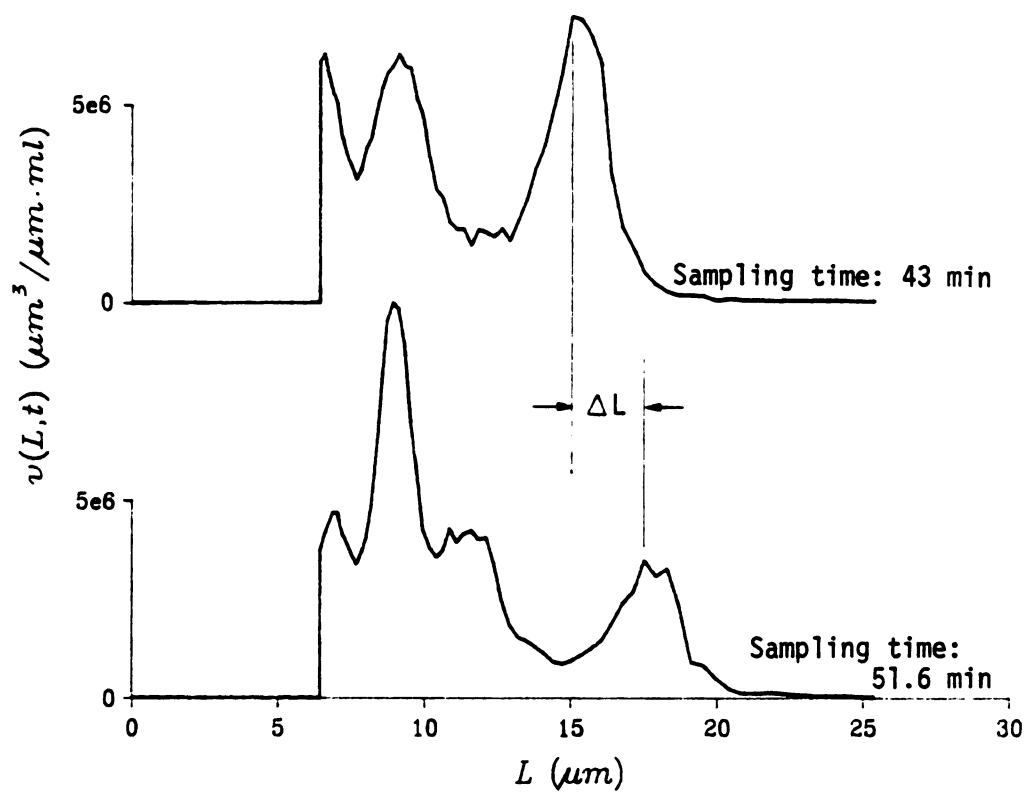
For the case of simultaneous crystal growth and crystal aggregation superimposed on the constant particle withdrawal, this growth rate equation also holds true when the changes of particle size distribution due to crystal aggregation are described by a smooth curve superimposed on the changes of PSD due to crystal growth.

Based on this argument, every two $v(L,t)$ data sampled at consecutive times were compared. The $\ln n(L,t)$ or $m(L,t)$ ($m(w(L),t)$ as a function of L) curves were also compared to confirm the shifting of PSD based on matching of the characteristic shape of the PSD curves. The crystal growth rates between every two consecutive PSDs were calculated from the shifted x-axis and the time interval of the two samplings according to Equation (4-2). Figure 4-14 shows the shift of the $v(L,t)$ curve between two sampling times, 43 min and 51.6 min, and the calculation of growth rate from the curve shifting.

In order to correlate growth rate and supersaturation, supersaturations for each run were calculated from the measured calcium concentrations of the filtrates by EQUIL-NA.BAS, a modified EQUIL program (described in Chapter 2). As an example, Figure 4-15 shows the supersaturations of COT in terms of the calcium oxalate complex, $S_{COT,c}$, for the experiments with varied residence times.

Since the experiments were all conducted with the same stirring rate, identical correlation between supersaturation and growth rate may be assumed for the growth conditions under which the same calcium oxalate phases were generated. This was applied to the experiments in which residence time was varied for the same inlet concentration. Therefore, growth rates were determined by measuring the shifts of curves for several types of PSDs, correlating growth rate with supersaturation, assuming consistent growth rate and supersaturation correlations for varied residence times, and by observing a consistent trend of the growth rate and supersaturation correlations for varied inlet concentrations and for various PGA additives. These procedures for finding growth rates are described in the following.

First, growth rates were obtained by matching the characteristic



$$G_L = \frac{\Delta L}{(51.6 - 43) \text{ min}} \frac{\mu\text{m}}{\text{min}}$$

Figure 4-14 Shift of $v(L,t)$ curve and calculation of growth rate; PGA = 100 ppm.

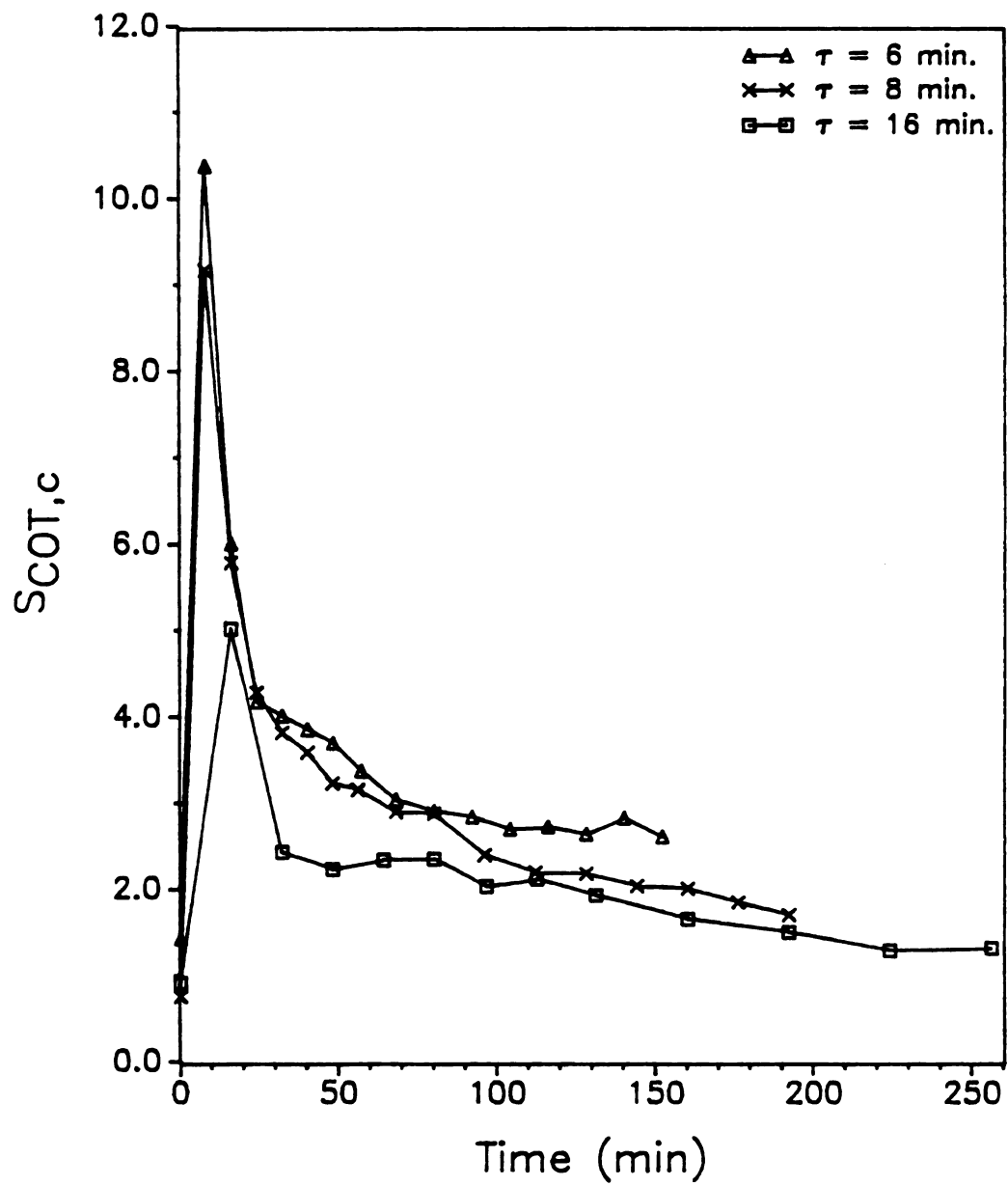


Figure 4-15 $S_{COT,c}$ in the crystallizer in experiments with varied residence times.

shapes of the PSD curves. These growth rate versus time data were used to find a growth rate-supersaturation correlation for each experiment. For some of the growth rate data showing large errors in the correlations, suggested growth rates for better correlation were given. The shifting of curves corresponding to the suggested growth rate was checked again for matches of the PSD curves. The growth rates with reasonable matches of the characteristic shapes of curves were accepted. Otherwise, comparisons of the curves for the growth rates were repeated until the growth rate data correlated well with the supersaturations.

The next step was checking the growth rate-supersaturation correlations for a consistent trend with respect to the varied experimental conditions. For example, the growth rate-supersaturation correlations for various PGA additions should consistently decrease or increase parallel to PGA concentrations. This checking was conducted similarly for the growth rate data with varied residence time and with varied calcium and oxalate inlet concentrations.

The shifts of the $v(L,t)$ curves from the procedures described above for the run with 100 ppm PGA and for the base run are shown in Appendix F. Figures 4-16 and 4-17 show the correlations between the growth rates and supersaturations for the experiments with calcium and oxalate concentrations at 1 mM and 2 mM. The growth rates thus obtained for the experiments with varied residence times, PGA additives, and calcium and oxalate concentrations are presented in Figures 4-18, 4-19, and 4-20. The growth rates were correlated linearly with supersaturations for several experimental conditions according to:

$$G_L = k \times \text{supersaturation} \quad (4-3)$$

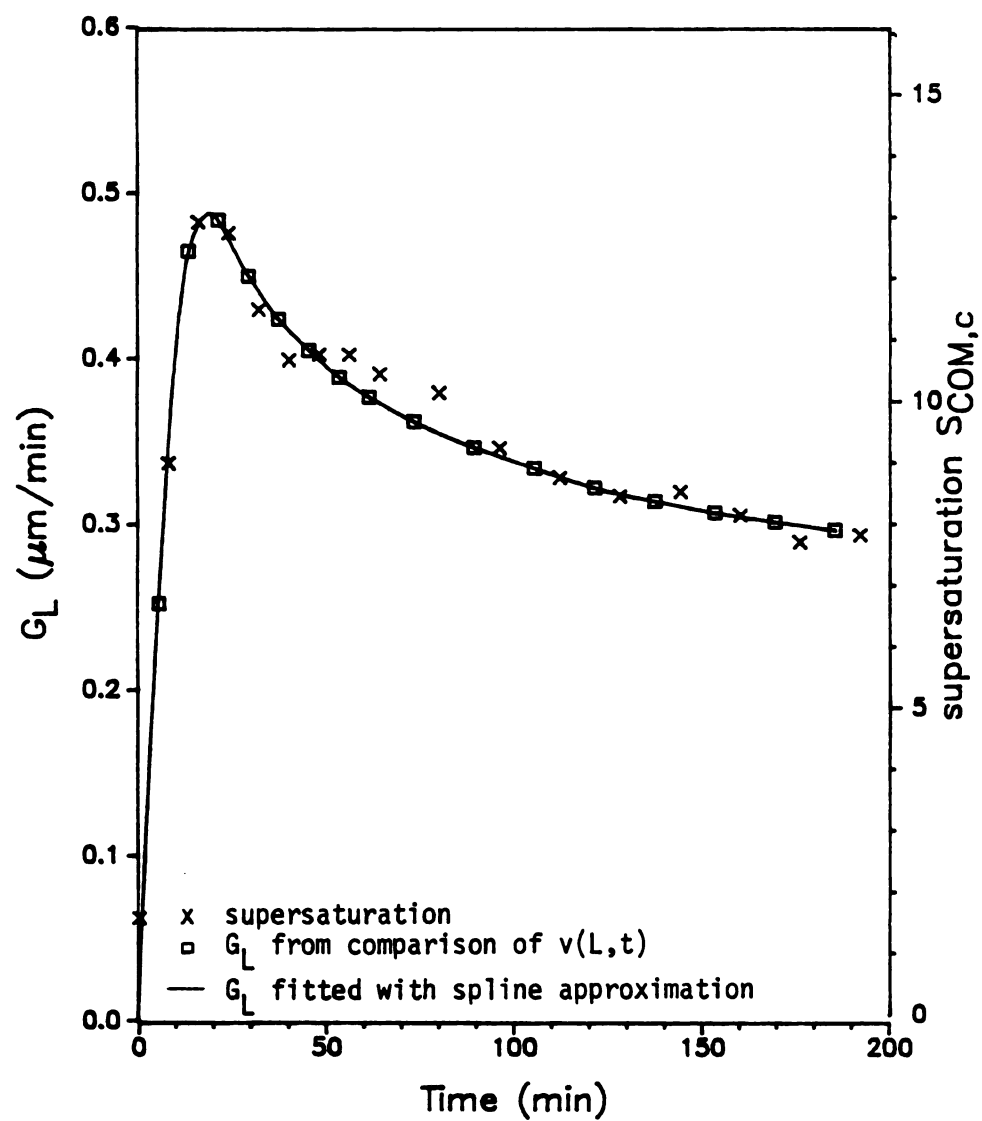


Figure 4-16 Growth rates and supersaturations for the experiment with 1 mM calcium and oxalate concentrations.

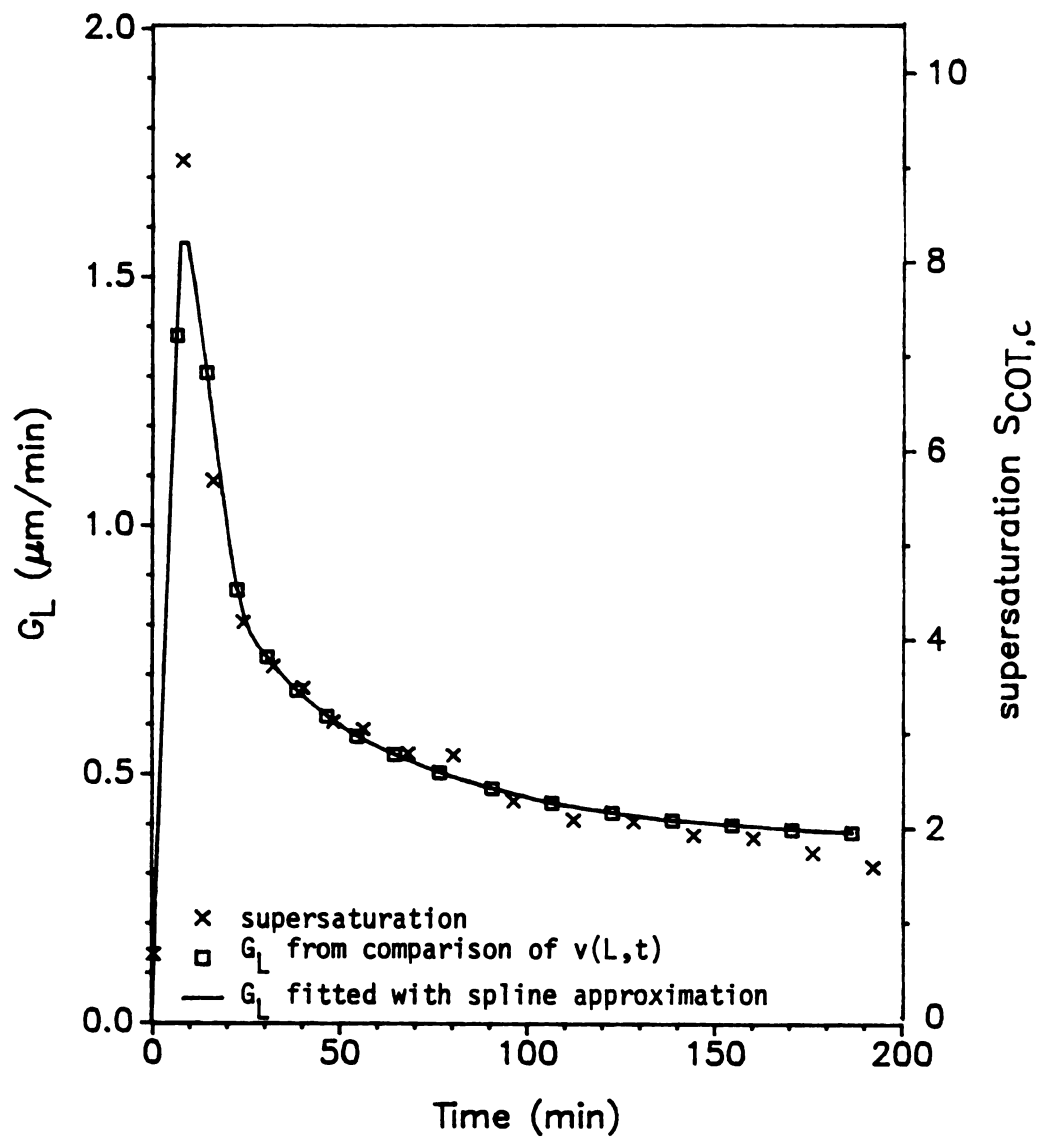


Figure 4-17 Growth rates and supersaturations for the base run.

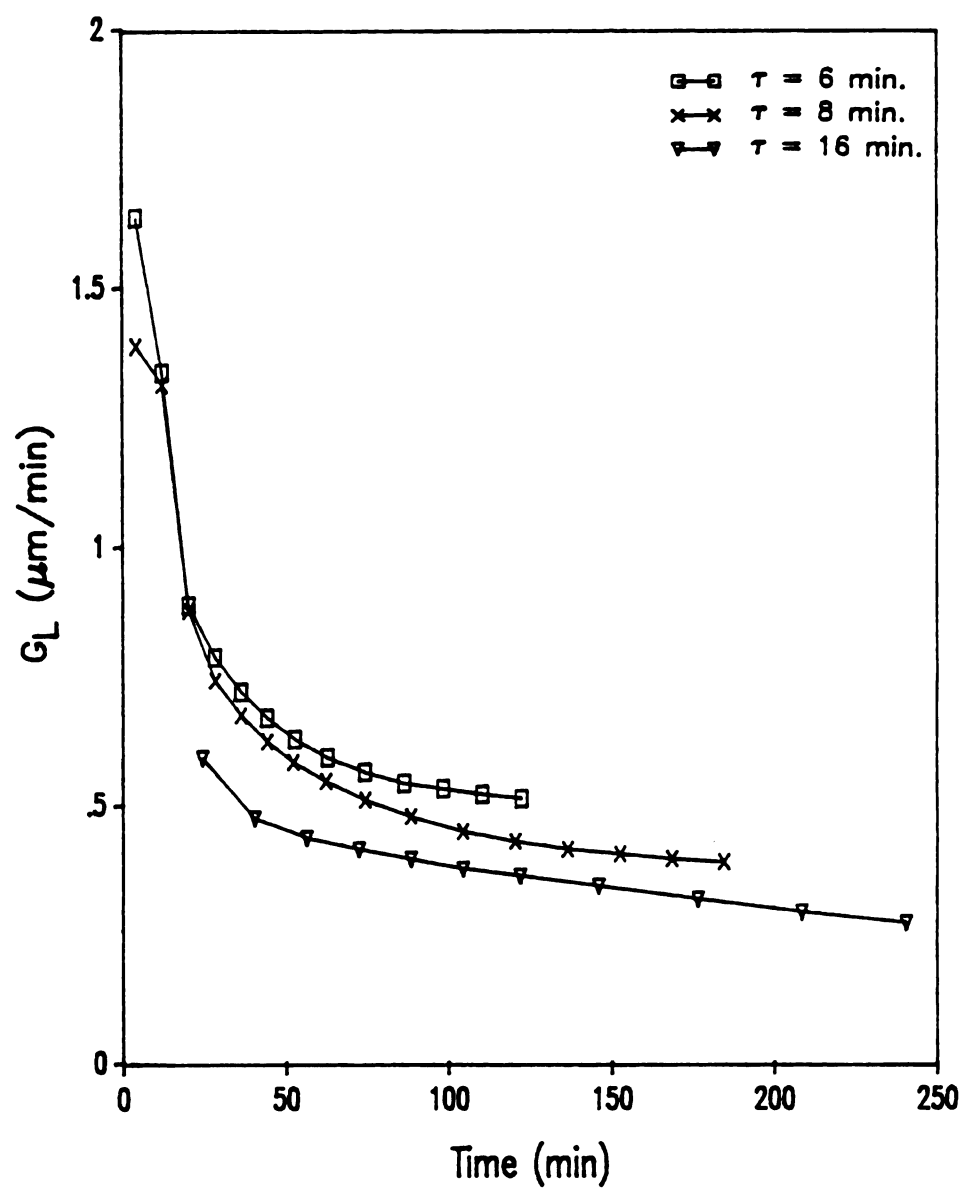


Figure 4-18 Growth rates in experiments with varied residence time.

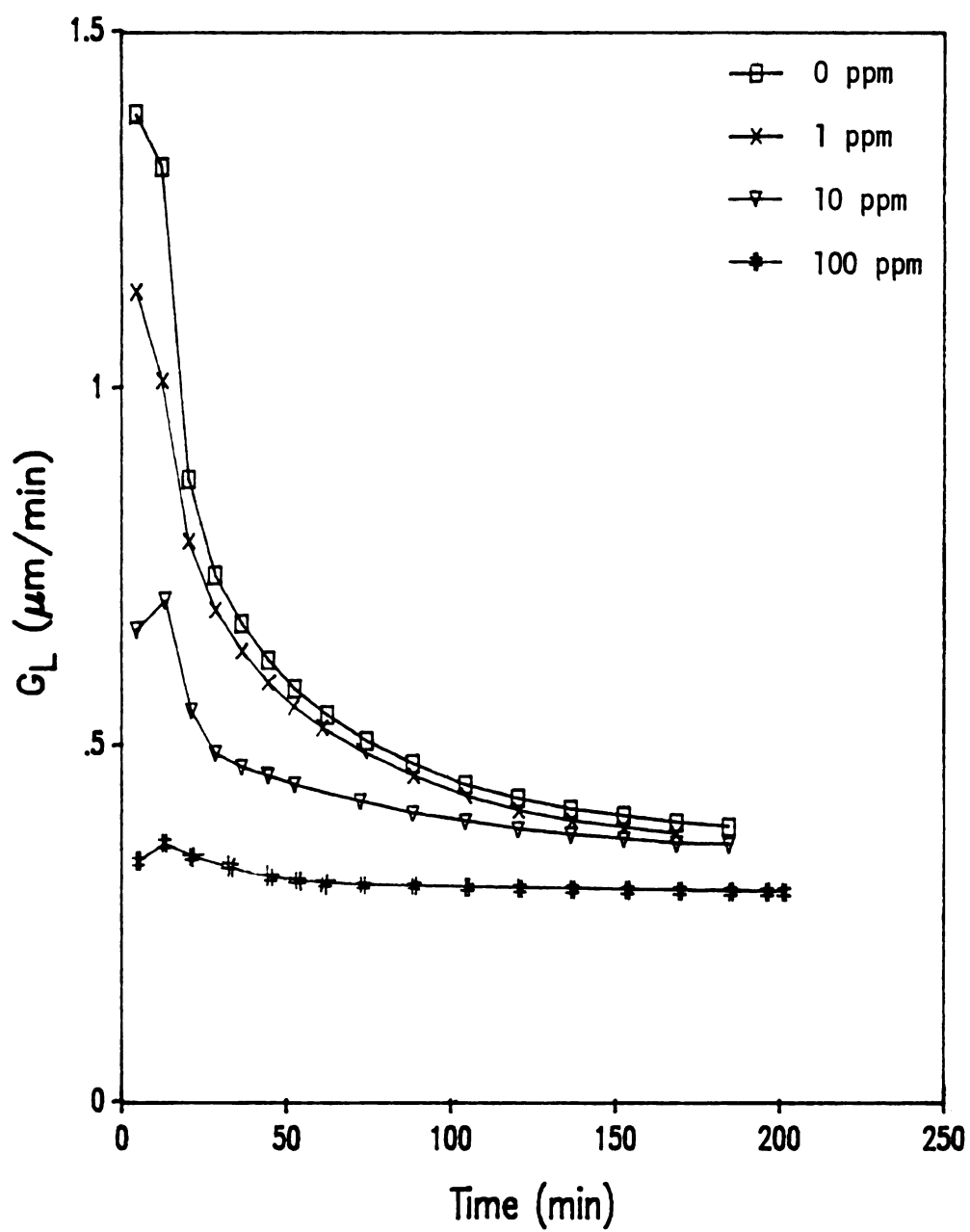


Figure 4-19 Growth rates in experiments with various levels of PGA additive.

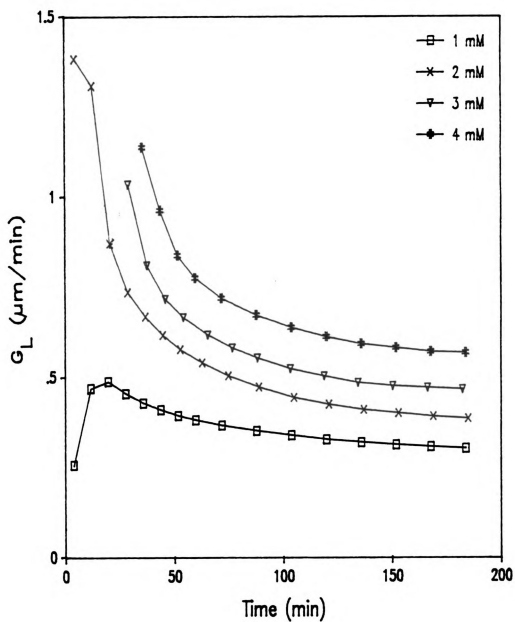


Figure 4-20 Growth rates in experiments with varied calcium and oxalate concentrations.

where k is the growth rate constant. The correlations are summarized in Table 4-4. As shown in this table, for the experiments generating the same crystal phase, i.e. for the runs with calcium and oxalate concentrations equal to 2 mM, 3 mM, and 4 mM and for the runs with varied residence times, the growth rate constants are the same. These consistent growth rate correlations are important in verifying the validity of this growth rate determination method.

The results from measurement of calcium concentrations in filtrates are unsatisfactory in the experiments marked with an asterisk as shown in Table 4-5. Supersaturations for these runs were obtained by extrapolation from the supersaturations for the series of runs in which the same experimental parameters were varied. For example, the supersaturations for the run with 100 ppm PGA were extrapolated from the supersaturations for the runs with the addition of zero (base run), one, and 10 ppm PGA additive. Therefore, growth rates for these experiments were obtained only by comparing the PSD curves for the shift of curves between two samplings; these supersaturation-growth rate correlations are estimated only.

Correlations of growth rates with the supersaturations in terms of ionic species, $S_{\text{COT},i}$ and $S_{\text{COM},i}$, were also implemented similarly to the correlations with the supersaturations in terms of complex species, $S_{\text{COT},c}$ and $S_{\text{COM},c}$. It may be more plausible that growth rate is a linear function of the square of supersaturation in terms of ionic species, since both calcium and oxalate ions contribute to crystal growth. It was found that growth rates fit better linearly with the supersaturations, $S_{\text{COT},c}$ and $S_{\text{COM},c}$. The growth rates obtained from the best fit of the linear relationship with each supersaturation

Table 4-4 Correlations of growth rates with supersaturations.

Experiment with [Ca ²⁺]-[C ₂ O ₄ ²⁻]:	<u>Correlations</u> (G _L = k x supersaturation)	
1 mM	0.037 x S _{COM,c}	0.15 x S _{COM,i}
2 mM	0.19 x S _{COT,c}	0.57 x S _{COT,i}
3 mM*	0.19 x S _{COT,c}	0.57 x S _{COT,i}
4 mM*	0.19 x S _{COT,c}	0.57 x S _{COT,i}
Residence time:		
6 min	0.19 x S _{COT,c}	0.57 x S _{COT,i}
16 min	0.19 x S _{COT,c}	0.57 x S _{COT,i}
PGA additive:		
1 ppm	0.12 x S _{COT,c}	0.392 x S _{COT,i}
10 ppm	0.065 x S _{COT,c}	0.25 x S _{COT,i}
100 ppm*	0.029 x S _{COT,c}	0.15 x S _{COT,i}

*: estimated correlations for these experimental conditions.

definition are slightly different. However, due to the accuracy of growth rates obtained from this approach, one correlation cannot be differentiated from the other.

Although COT was not the main hydrate formed in the experiments with PGA additive, growth rates were correlated with the supersaturation of COT, the main hydrate formed in the base run experiment, for the purpose of illustrating the effect of the addition of PGA. Inhibition of PGA on the growth rate was seen from the decrease of the correlation constants with increase in PGA concentration as shown in Table 4-5. If the inhibition by PGA of calcium oxalate crystal growth is due to PGA adsorption on the crystal surface, the growth rate constants at various PGA concentrations, $[PGA]$, should follow the Langmuir isotherm. That is, for the growth rate constant without PGA additive, k_0 , and the rate constants with PGA additive, k_{PGA} , the plot of $k_0/(k_0 - k_{PGA})$ versus $1/[PGA]$ should be linear. Figure 4-21 shows the Langmuir isotherm behavior for PGA adsorption and the linear regression line with a 0.992 correlation coefficient.

4-4-2. Approach B: Growth Rate at Quasi-Steady State

In the operation of the MSMPR crystallizer at quasi-steady state, crystal growth was the predominant crystallization mechanism. Because of the constant withdrawal of the suspension, the total particle numbers in the reactor decayed with time. Crystal growth rates at the quasi-steady state were calculated according to Equation (3-17);

$$G_L = - \frac{\frac{\partial \ln n(L,t)}{\partial t} + \frac{1}{r}}{\frac{\partial \ln n(L,t)}{\partial L}} \quad (3-17)$$

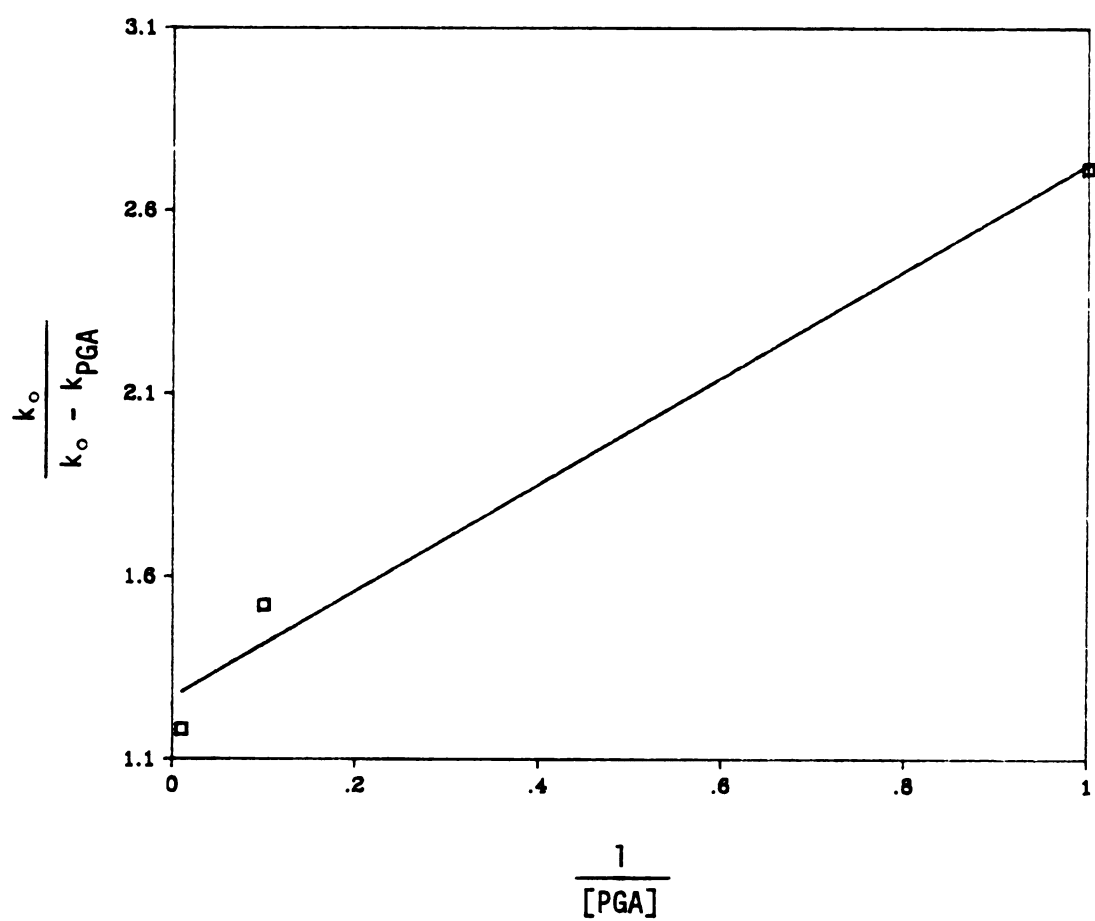


Figure 4-21 Langmuir isotherm of PGA adsorption on calcium oxalate crystals.

The semi-log population density plots of the PSDs at quasi-steady state were printed out from the spreadsheet program and were smoothed by hand-fitting. Coordinates of points on the smoothed curves were digitized using the digitizer in the Case Center of the College of Engineering. A FORTRAN program, GMSMPR, was written using Equation (3-17) to calculate growth rates, G_L , from the digitized $\ln n(L,t)$ data. Every two consecutively sampled PSDs were used to generate one growth rate datum; the differentiation of $\ln n(L,t)$ with time was estimated as the difference of two $\ln n(L,t)$ points over time. The differentiation of $\ln n(L,t)$ with size was calculated from the splined $\ln n(L,t)$ data using IMSL routines. The computer program is shown in Appendix G.

The average growth rates for the data between eight to 16 τ are representative of the quasi-steady state and are shown in Table 4-5 for various experimental conditions. The growth rate extracted from the time-dependent growth rate results from Approach A for $t = 12 \tau$ are also reported in the second column in Table 4-5. In comparing the results from these two approaches, growth rates of the same order of magnitude are obtained. The higher values obtained from Approach B might be due to the smaller slopes of the $\ln n(L,t)$ data due to the hand-fitting of the $\ln n(L,t)$ PSDs, especially where only few particles were observed in the quasi-steady and steady state periods. As seen from Equation (3-17), smaller slopes result in higher calculated crystal growth rates. This hand-fitting of the PSDs was less difficult for the samples containing more crystal particles. Because crystal numbers increase with increased calcium and oxalate inlet concentrations, the calculation error from Approach B due to underestimated slopes may be reduced. This may be the reason why identical growth rates are calculated from Approach B for the

experiments with 2 mM, 3 mM, and 4 mM calcium and oxalate concentrations. With increased calcium and oxalate concentrations, the calculation error decreases; therefore, the growth rate calculated from Approach B approaches the value obtained from Approach A.

Table 4-5 Growth rates at quasi-steady state.

Experiment with	G_L ($\mu\text{m}/\text{min}$)	
	<u>Approach A</u>	<u>Approach B</u>
$[\text{Ca}^{2+}] = [\text{Ox}^{2-}]$:		
1 mM	0.344	0.42
2 mM	0.466	0.67
3 mM	0.538	0.67
4 mM	0.653	0.67
Residence time:		
6 min	0.571	0.80
16 min	0.308	0.54
PGA additive:		
1 ppm	0.445	0.635
10 ppm	0.401	0.40
100 ppm	0.304	0.315

4-4-3. Comparison of Growth Rates

The growth rate results for calcium oxalate crystallization under the effect of PGA additive may be compared with previous growth rate data. Drach, Sarig, et al. (1982) measured calcium oxalate growth rate in urine-like solutions with added PGA. The steady-state linear population density model was adopted, and the growth rate data were reported as shown in the third column of Table 4-6. The second column of this table shows the growth rates extracted from time-dependent results of this work for time equal to 12 residence times. It is seen

that these two sets of growth rates are of the same order of magnitude. The higher growth rates of this work may be due to the higher inlet concentrations of calcium and oxalate used in this work. The urine-like solutions may exhibit an inhibitory effect on crystal growth. The molecular weight of PGA used by Drach and associates were 14,000; the PGA molecular weight is 26,500 in this work. DeLong (1988) found that PGAs of different molecule weights show identical inhibitory effect on COM crystal growth at the same molar concentration. The higher growth rates of this work may be also due to the lower PGA molar concentrations at the same weight concentration of PGA addition due to the difference in molecular weight.

Table 4-6 Comparison of growth rates with previous work.

PGA concentration	G_L ($\mu\text{m}/\text{min}$)	
	This work	Previous work (Drach et al., 1982)
0 ppm	0.466	0.391
1 ppm	0.445	---
2 ppm	---	0.125
10 ppm	0.401	0.136
100 ppm	0.304	---

For an MSMPR crystallizer operating at steady state, the linear growth rate may be obtained from the slope of the semi-log population density distribution as described by

$$\ln n(L) - \ln n(0) = -\frac{L}{G_L \tau} \quad (1-29)$$

Average growth rates obtained from the PSDs after 20 τ for various experimental conditions are shown in Table 4-7. The steady state growth rate extracted from Approach A are also presented in the second

column in this table. When considering the uncertainty in the determination of a linear curve fit to the curved distribution, the steady state growth rates from Approach A and from the linear population density model are fairly consistent.

Table 4-7 Growth rates at steady state.

Experiment with	G_L ($\mu\text{m}/\text{min}$)	
	<u>Approach A</u>	<u>Linear population density model</u>
$[\text{Ca}^{2+}] = [\text{Ox}^{2-}]$:		
1 mM	0.308	0.321
2 mM	0.394	0.395
3 mM	0.472	0.408
4 mM	0.572	0.543
Residence time:		
6 min	0.518	0.504
16 min	0.296	0.330
PGA additive:		
1 ppm	0.379	0.377
10 ppm	0.365	0.315
100 ppm	0.298	0.326

The steady state growth rate for the experiment with 1 mM calcium and oxalate concentrations may be compared with the MSMPR crystallizer study of Garside et al. (1982). Garside et al. obtained a value of $0.18 \mu\text{m}/\text{min}$ for the COM crystal growth rate at $S_{\text{COM},c}$ equal to 10 at 37°C . In this work, the COM growth rate of $0.308 \mu\text{m}/\text{min}$ was obtained at $S_{\text{COM},c}$ equal to 7.92. The higher value obtained in this work may be due to the higher degree of turbulence generated by the propeller type of stirrer compared to the stirrer with flat blades used by Garside et al. For the same total calcium concentration in the

filtrate, the supersaturation calculated in this work may be lower than the value calculated by Garside et al., since Garside only considered the complexation of $\text{H}_2\text{C}_2\text{O}_4$, HC_2O_4^- , and CaC_2O_4 . Many more complex species were considered in this work, thus giving a more realistic measure of the driving force for crystal growth.

Garside et al. (ibid) correlated growth rate to a second order dependence on calcium oxalate supersaturation-- a supersaturation based on the activity of the associated calcium oxalate species (as per Equation (2-4)). As seen in Table 4-4, the growth rates in this work are correlated to first power of supersaturation $S_{\text{COM},c}$. Since the associated calcium oxalate species is large relative to free ions, it is reasonable that growth rate would show a first order dependence on $S_{\text{COM},c}$ similar to the growth rate correlations observed for molecular crystal growth with higher supersaturations. The second order growth rate observed by Garside et al. may also have been due to crystal aggregation effects which are unaccounted for in the linear population density model.

4-5. Discussion

The two approaches for the calculation of crystal growth rate described in this chapter show consistent results between each method and with previous work. Approach A described was to obtain growth rates by comparing PSD curves for time-dependent growth rates for the unsteady state, quasi-steady state, and steady state periods. With this method, the effects of biopolymers on crystal growth may be isolated from their effects on crystal aggregation.

In the study of the effect of PGA additive, growth rate inhibition by PGA was observed. The inhibition is most likely due to the adsorption of PGA on the growing calcium oxalate crystals.

The growth rate data for the entire duration of MSMPR crystallizer operation may be further used in the studies of crystal aggregation with or without biopolymer additives. The integro-differential population balance equations which describe the crystal aggregation phenomenon (Chapter 3) may be solved by numerical methods with the input of the known crystal growth data obtained by the methods described in this chapter.

CHAPTER 5

THE EFFECT OF MDCK CELLS ON CALCIUM OXALATE GROWTH IN A FLOW CHAMBER

5-1. Introduction

The objectives of the work described in this chapter have been to investigate the effect of kidney tissue on calcium oxalate crystal growth and to relate the inhibition or promotion of crystal growth to tissue injury and to the presence of a biopolymer additive.

The observation of the crystal growth in an isothermal growth chamber was first adopted by Valcic in the study of the growth rate of saccharose crystals (Valcic, 1975). This type of controlled constant-temperature growth chamber has been used in the growth rate study of crystals formed from secondary nucleation (Garside and Larson, 1978; Berglund, 1981; Shiau and Berglund, 1987). In nephrolithiasis research, DeLong and Briedis (1985) and DeLong (1988) used a chamber of similar design in a continuous-flow system to observe growth rate of single calcium oxalate crystals. This work has contributed significantly to the investigation of the effects of solution chemistry and biopolymeric additives on the formation of renal stones.

Gill et al. (1980) have been pioneers in using catheterized rat bladders to study the effect of living tissue on the crystallization of calcium oxalate. Their results show that the nature of the container surface in which crystal growth experiments are preformed, whether it is glass, normal urothelium, or chemically injured urothelium, has marked effects on the adhesion of crystals and on the metastable concentration limit of calcium oxalate. The healthy urothelial surface exhibited a protective action against calcium oxalate nucleation and

adhesion. This protective property was destroyed by injurious agents such as dilute hydrochloric acid, Triton X100 (a nonionic detergent), or papain (a proteolytic enzyme).

Gill and associates (1982) found that heparin was the only saccharide they tested that restored the protective effect of urolithial cells injured by HCl or by Triton X100. The saccharides they examined were two sulfated glycosaminoglycans (heparin and chondroitin sulfate C), a sulfated glucose polysaccharide (dextran sulfate), a nonsulfated polysaccharide with repeating subunits similar to heparin (hyaluronic acid), and the nonsulfated monosaccharide subunits of heparin (D-glucuronic acid and N-acetyl-D-glucosamine). It was also found that heparin bound to the HCl- and Triton X100- injured urothelium but not to the normal urothelium. The special effect of heparin in restoring the anticrystal adhesion may have been due to the negatively charged carboxylate and sulfate groups on heparin (Figure 5-1). The negatively charged groups may preferentially adsorb on the Ca^{2+} ions on the crystal surface and may chemically or sterically prevent crystal adhesion.

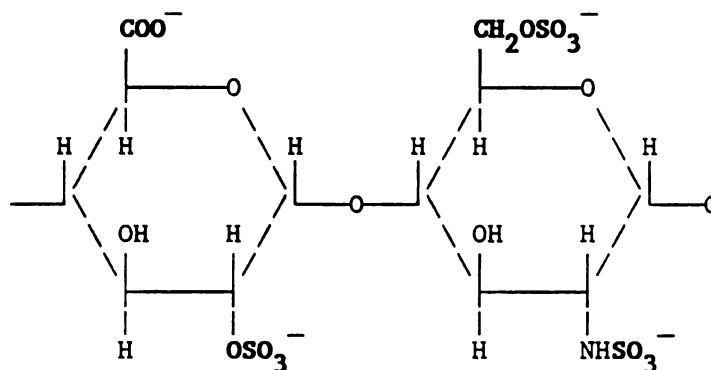


Figure 5-1 Repeating unit of heparin.

Wiessner et al. (1987) isolated the rat renal inner papillary collecting tubule (RPCT) cells and studied the interaction of the cells with preformed COM and COD crystals. Cultured RPCT cells were exposed to media containing COM or COD crystals, which were rinsed off after 15 minutes. The crystals, especially small ones, were found adhering on or around the rounded-up cells. This suggests a possible interaction between crystals and unhealthy cells.

In further work, Mandel et al. (1987) studied the crystal-membrane interactions by measuring the red blood cell hemolysis induced by crystals. The results showed that the several known inhibitors of calcium oxalate crystal growth and aggregation inhibited the potential for COM and COD crystals to interact with membranes. The methods used in the studies of Wiessner et al. and Mandel et al. were done in a batch, stagnant condition and did not take into account the fluid dynamics of renal flows. The work described in this chapter considers both crystal-membrane interactions and flow dynamics.

In this work, the integration of the photomicroscopic technique and experimentation on living cells will be addressed. A monolayer culture of Maden Darby Canine Kidney (MDCK) cells was incorporated in a modified growth chamber to study the effect of epithelium on the growth of single calcium oxalate crystals. The original cylindrical growth chamber described earlier was redesigned to a rectangular configuration so that the flow pattern in the chamber was well characterized. This permitted quantitative analyses of the mechanistic effect of the flow on epithelium.

The rectangular growth chamber maintains the advantage of the original growth chamber for direct microscopic observation of crystal

nucleation and growth. Its design and assembly are discussed in the following section.

5-2. Precipitator Design and Assembly

The flow chamber precipitator is a multi-layer assembly held tight with screws (Figures 5-2 and 5-3). The chamber was designed by Alan L. Powell and was constructed in the Machine Shop of the College of Engineering. It contains two main chambers divided by transparent plastic; the upper chamber is for the flow of solutions, and the lower chamber is for the circulation of water for temperature regulation. The diagrams for upper and lower chamber pieces are shown in Figures 5-4 and 5-5. When the growth cell is fully assembled, the experimental solution is introduced into the cell laterally as shown in Figure 5-2. It then flows upward to the upper chamber. The upper chamber is of a rectangular cross section with width, b , of 1.27 cm and height, a , of 0.397 cm (Figure 5-6). The total volume of the upper fluid pathway, including the horizontal flow chamber and the inlet and outlet portions of the chamber, is 5.5 ml. A thermistor is located at the downstream end of the cell in the solution side for monitoring of temperature.

A cover glass is positioned on the plastic divider and provides a surface of glass or of cultured MDCK cells for growing crystals. The monolayer of cultured epithelial cells may be treated chemically or enzymatically to simulate tissue damage. This configuration allows the chemical effect of the presence of living cells (normal or injured) on crystal formation or the flow mechanistic effect on the cells to be observed by photomicroscopy.

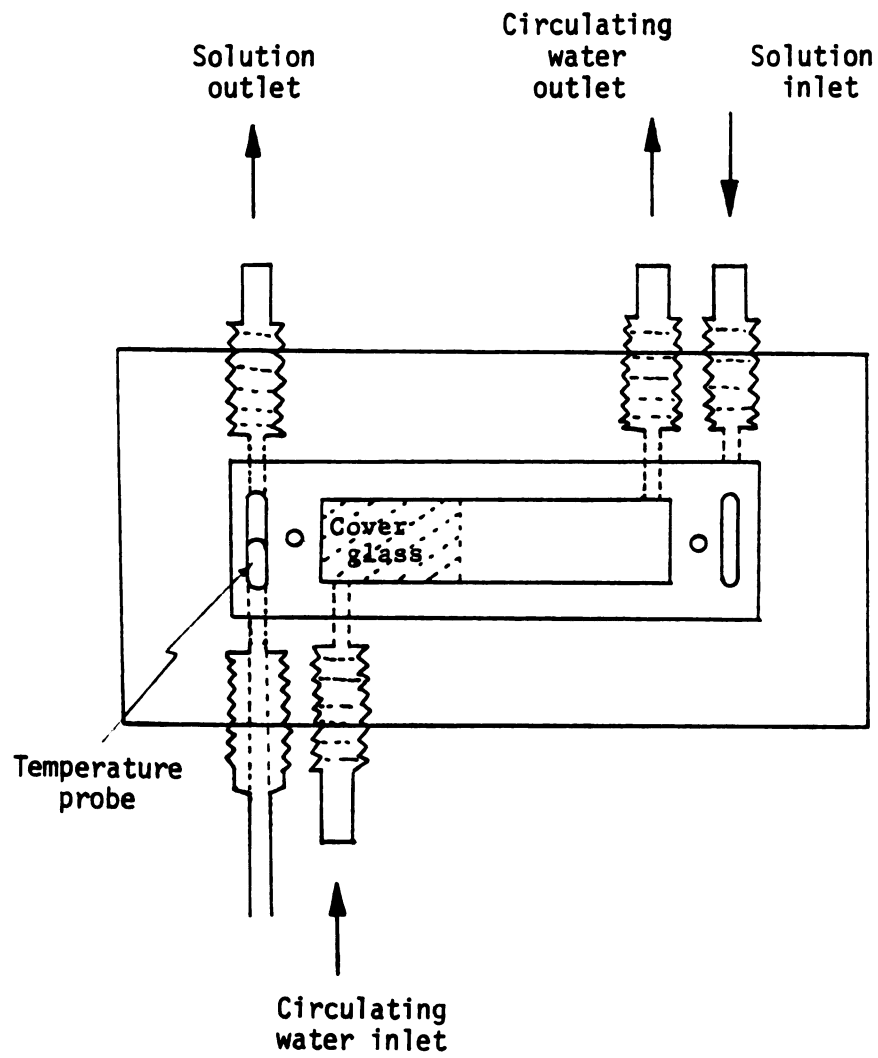
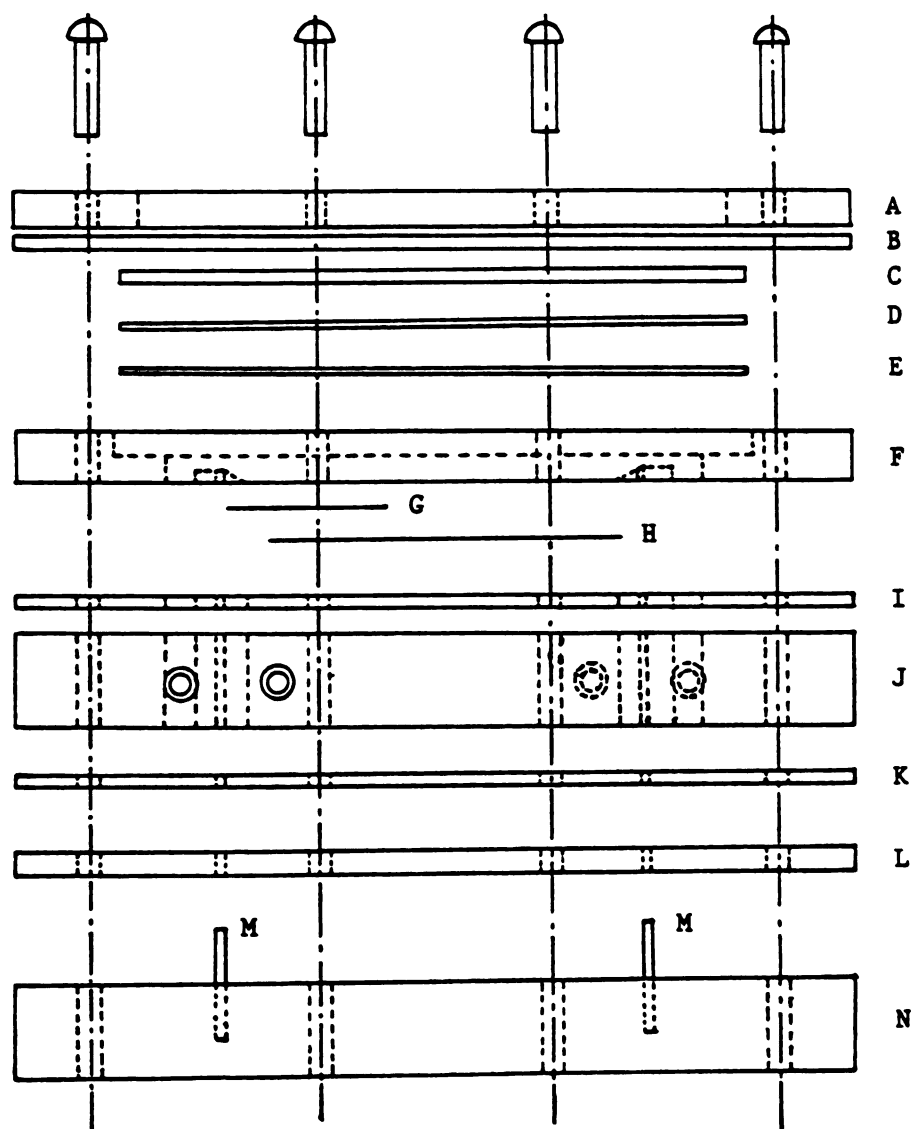


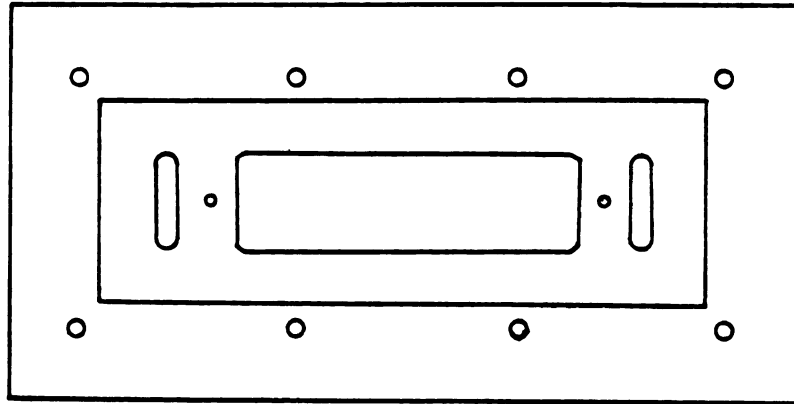
Figure 5-2 Top view of the growth chamber.



- | | |
|------------------------------|---|
| A: Upper retainer | I: Divider gasket |
| B: Spacer 1 | J: Lower chamber holder |
| C: Spacer 2 | K: Bottom gasket |
| D: Microscopic slide | L: Base plate |
| E: Cover gasket, 1/32" thick | M: 2 stainless steel pins
(1 7/32" long) |
| F: Upper chamber holder | N: Lower retainer |
| G: Cover glass | |
| H: Plastic divider | |

Figure 5-3 Exploded side view of the growth chamber.

Top view



Side view (2X)

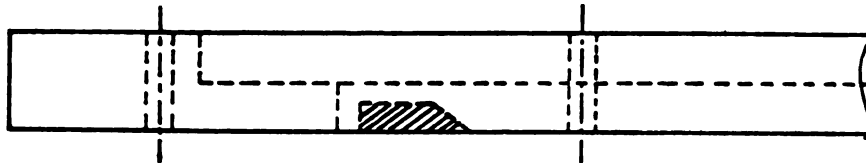
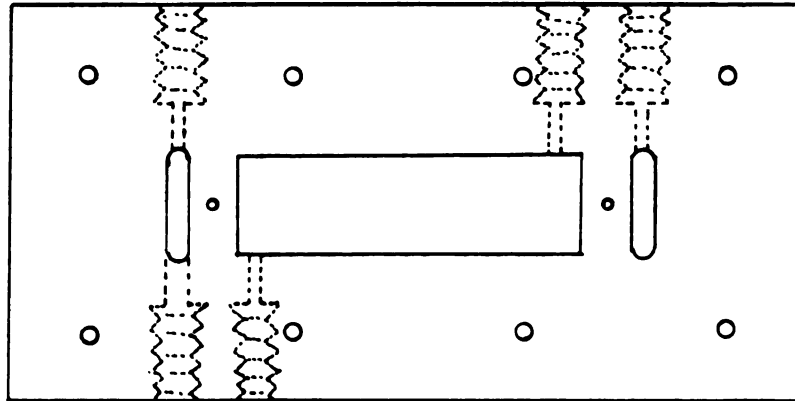


Figure 5-4 Upper chamber holder.

Top view



Side view

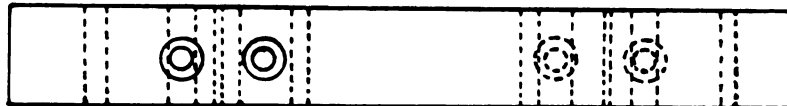


Figure 5-5 Lower chamber holder.

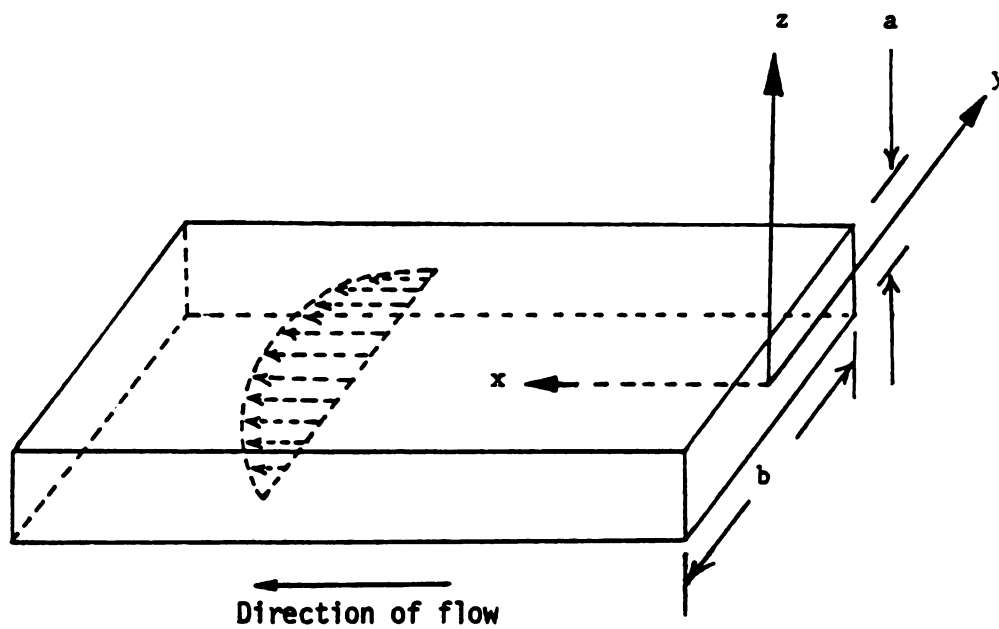


Figure 5-6 Modeling coordinates of the flow chamber precipitator.

5-3. Fluid Mechanics Properties in Upper Chamber

In order to quantify the mechanistic effect of flow on cells, calculation of some of the flow characteristics in the upper chamber is necessary. These are average velocity of the flow, Reynolds number, transition length, velocity profile, and shear stress. Calculations were done based on the geometric dimensions of the solution chamber and the physical properties of the test fluid. The physical properties of the model renal fluid used in experiments are shown in Appendix D.

According to the design, the flow chamber precipitator may be modeled as a rectangular slit with dimensions and defined coordinates shown in Figure 5-6. The horizontal x-axis is the direction of flow. Excluding two discontinuities in the chamber floor (Figure 5-4), the total length in the x-direction is 4.5 cm.

The average velocity of the flow, \bar{V} (cm/s), is related to the volumetric flow rate, Q (cm³/s), according to

$$\bar{V} = Q/A \quad (5-1)$$

where A is the cross-sectional area of the flow (cm²). For the chamber of rectangular cross section,

$$A = ab \quad (5-2)$$

where a and b are the thickness and width of the upper chamber.

5-3-1. Reynolds Number

The characteristic dimensionless number for flow, the Reynolds number, Re , is the ratio of inertial forces to viscous forces and is expressed as

$$Re = \frac{d_e \bar{V} \rho}{\mu} \quad (5-3)$$

where ρ is the fluid density, g/cm^3 , and μ is the fluid viscosity, $\text{g/cm}\cdot\text{s}$. The equivalent diameter of this noncircular conduit, d_e , cm, is calculated as

$$d_e = \frac{4 ab}{2(a+b)} \quad (5-4)$$

a definition related to cross-sectional area and wetted perimeter of the conduit (McCabe et al., 1985).

The magnitude of Re determines whether the flow pattern is laminar or turbulent. For Re below 2100, the flow is laminar; above about 4000, the flow is turbulent. The transition region lies between 2100 and 4000 where the flow depends on roughness of conduit surface and configuration of the conduit entrance.

Reynolds number for the flow chamber designed in this work was calculated for various flow rates shown in Table 5-1. In all cases flow was laminar. The transition length and maximum shear stress shown in Table 5-1 are discussed in Section 5-3-2 and 5-3-4, respectively.

Table 5-1 Reynolds number, transition length, and maximum shear stress for flow chamber precipitator.

Flow Rate (ml/min)	Re	x_t (cm)	τ_{\max} ($\text{g/cm}\cdot\text{s}^2$)
10	28.4	0.859	0.0403
20	56.8	1.718	0.0807
25	71.0	2.147	0.1008
30	85.2	2.577	0.1210
40	113.6	3.436	0.1613
50	142.0	4.295	0.2017
99	281.2	8.503	0.3993

5-3-2. Transition Length

Transition length is the length required in the entrance region for the boundary layer to reach the center of the flow and the velocity profile to become fully developed. In laminar flow, it is empirically formulated as (McCabe et al., 1985):

$$\frac{x_t}{D} = 0.05 \text{ Re} \quad (5-5)$$

where x_t is the transition length and D is the diameter of the flow pipe. For the flow chamber precipitator of noncircular cross section, equivalent diameter was used for D to calculate transition lengths as shown in Table 5-1. To assure a well developed, well characterized flow field over the region where crystal growth was photomicroscopically observed, Table 5-1 shows that the flow rate for experiments was limited to 50 ml/min or below because of the length of the chamber.

5-3-3. Velocity Profile

In laminar flow, no lateral mixing is assumed. For a fully developed laminar flow in rectangular conduits, the velocity profile in x-direction has been given by Timoshenko and Goodier (see Knudsen and Katz, 1958):

$$u_x(y,z) = \frac{-4a^2 g_c}{\pi^3 \mu} \frac{dP}{dx} \sum_{n=1,3,5} \frac{1}{n^3} (-1)^{(n-1)/2} x \left[1 - \frac{\cosh(n\pi y/a)}{\cosh(n\pi b/2a)} \right] \cos(n\pi z/a) \quad (5-6)$$

where P is the hydraulic pressure of the steady flow fluid. The pressure gradient due to friction, dP/dx , is related to the friction factor, f , according to (ibid):

$$\frac{dP}{dx} = - \frac{2\rho\bar{V}^2}{d_e g_c} f \quad (5-7)$$

where the Fanning friction factor, f , has been derived theoretically (ibid):

$$f \left(\frac{a}{d_e} \right)^2 \left(1 - \frac{192a}{\pi^5 b} \tanh\left(\frac{\pi b}{2a}\right) - \frac{1}{3^5} \tanh\left(\frac{3\pi b}{2a}\right) + \dots \right) = \frac{6}{Re} \quad (5-8)$$

With known a , b , and d_e , the friction factor was calculated for the flow chamber to give

$$f = \frac{17.312}{Re} \quad (5-9)$$

The expression describing the velocity profile in the chamber may be derived from Equation (5-6) and is expressed as

$$u_x(y,z) = \frac{138.5a^2}{\pi^3 d_e^2 b} \sum_{n=1,3,5} \frac{1}{n^3} (-1)^{(n-1)/2} x \left[1 - \frac{\cosh(n\pi y/a)}{\cosh(n\pi b/2a)} \right] \cos(n\pi z/a) \quad (5-10)$$

Figure 5-7 illustrates the velocity profiles calculated from Equation (5-10) for z at $H \mu\text{m}$ above the bottom wall of the chamber for a flow rate of 40 ml/min. Since hyperbolic cosine is an even function, $u_x(y,z)$ is an even function of y ; i.e., velocity profile is symmetrical with respect to y . Figure 5-7 shows only the curves for $y \geq 0$.

From Equation (5-10), it is seen that velocities at constant z or constant H are each the same function of y , i.e., a summation consisting of $[1 - \cosh(n\pi y/a)/\cosh(n\pi b/2a)]$. Therefore, curves in Figure 5-7 have the same profile when they are presented in terms of percentages of the maximum value of each curve. The vertical lines in this figure mark the percentages of the values in terms of their

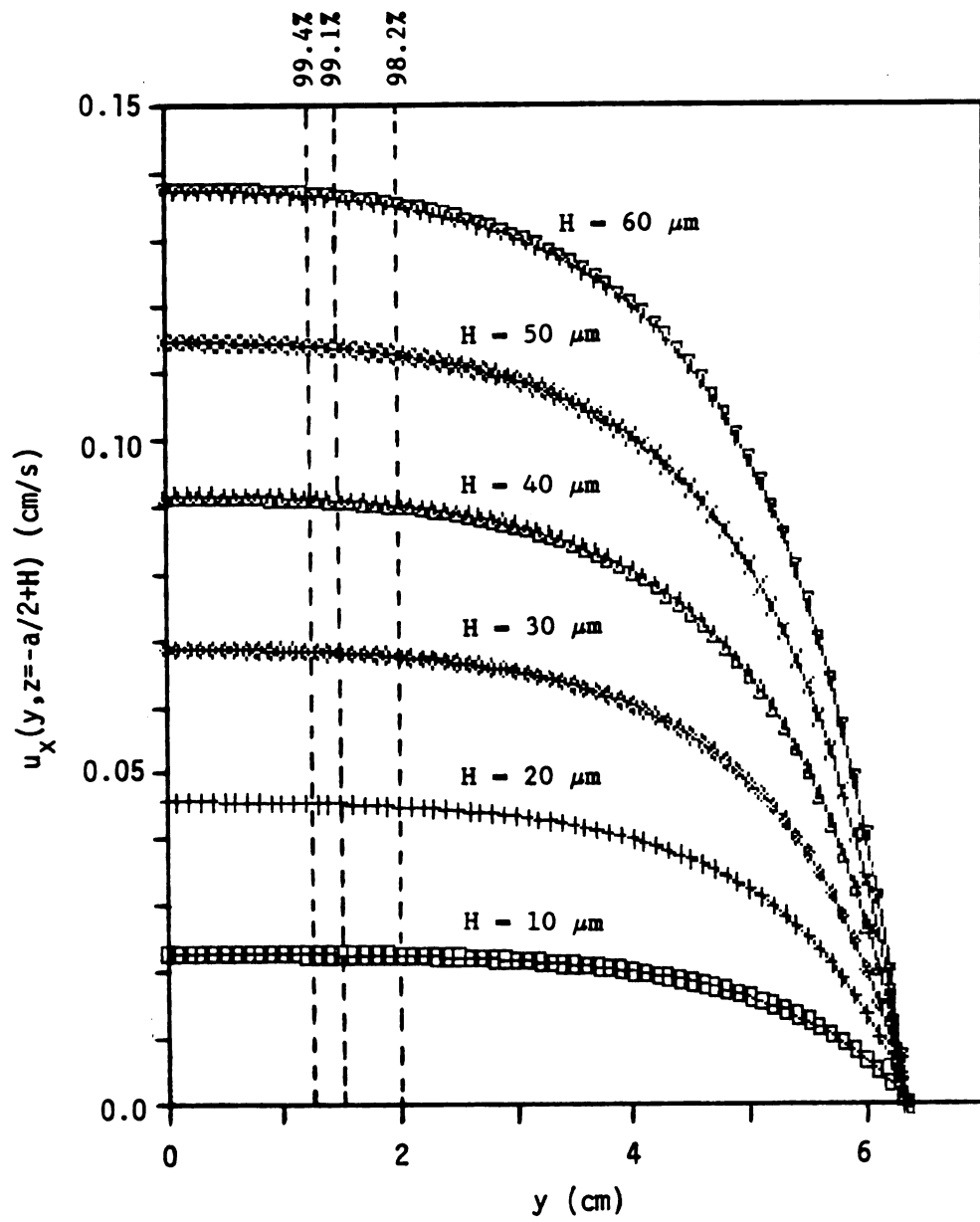


Figure 5-7 Illustrative velocity profiles; flow rate at 40 ml/min.

maximum values, which occur at $y = 0$. Nearly constant velocities are found within $y = \pm 0.2$ cm.

5-3-4. Shear Stress

The shear stress at the interface between the flow and epithelial cells is a quantity of importance in observing the mechanistic effect of flow on living cells. It is defined as (Bird et al., 1960)

$$\tau_{zx}(y, z=-a/2) = -\mu \left. \frac{\partial u_x(y, z)}{\partial z} \right|_{z=-a/2} \quad (5-11)$$

Substituting Equation (5-10) into Equation (5-11) for $u_x(y, z)$ and taking the derivative with respect to z gives:

$$\tau_{zx}(y, z=-a/2) = -\frac{138.5\mu Q}{\pi d_e^2 b} \sum_{n=1,3,5} \frac{1}{n^2} (-1)^{(n-1)/2} \left[1 - \frac{\cosh(n\pi y/a)}{\cosh(n\pi b/2a)} \right] \sin(-n\pi/2) \quad (5-12)$$

Figure 5-8 shows the shear stress calculated from Equation (5-12).

Since shear stress in laminar flow also represents a flux of momentum, negative values of shear stress in Figure 5-8 denote that the momentum is transferred towards the direction of negative z . Since Equation (5-12) contains the same function of y as that in Equation (5-10), shear stress at the surface may also be presented in terms of percentages of the maximum shear stress, the maximum absolute value of shear stress, which also occurs at $y = 0$.

Let $\left| \tau_{zx}(y=0, z=-a/2) \right| = \tau_{\max}(Q)$, then

$$\tau_{\max}(Q) = \frac{138.5\mu Q}{\pi d_e^2 b} \sum_{n=1,3,5} \frac{1}{n^2} \left[1 - \frac{1}{\cosh(n\pi b/2a)} \right] \quad (5-13)$$

Table 5-1 shows the calculated maximum absolute shear stress at several flow rates.

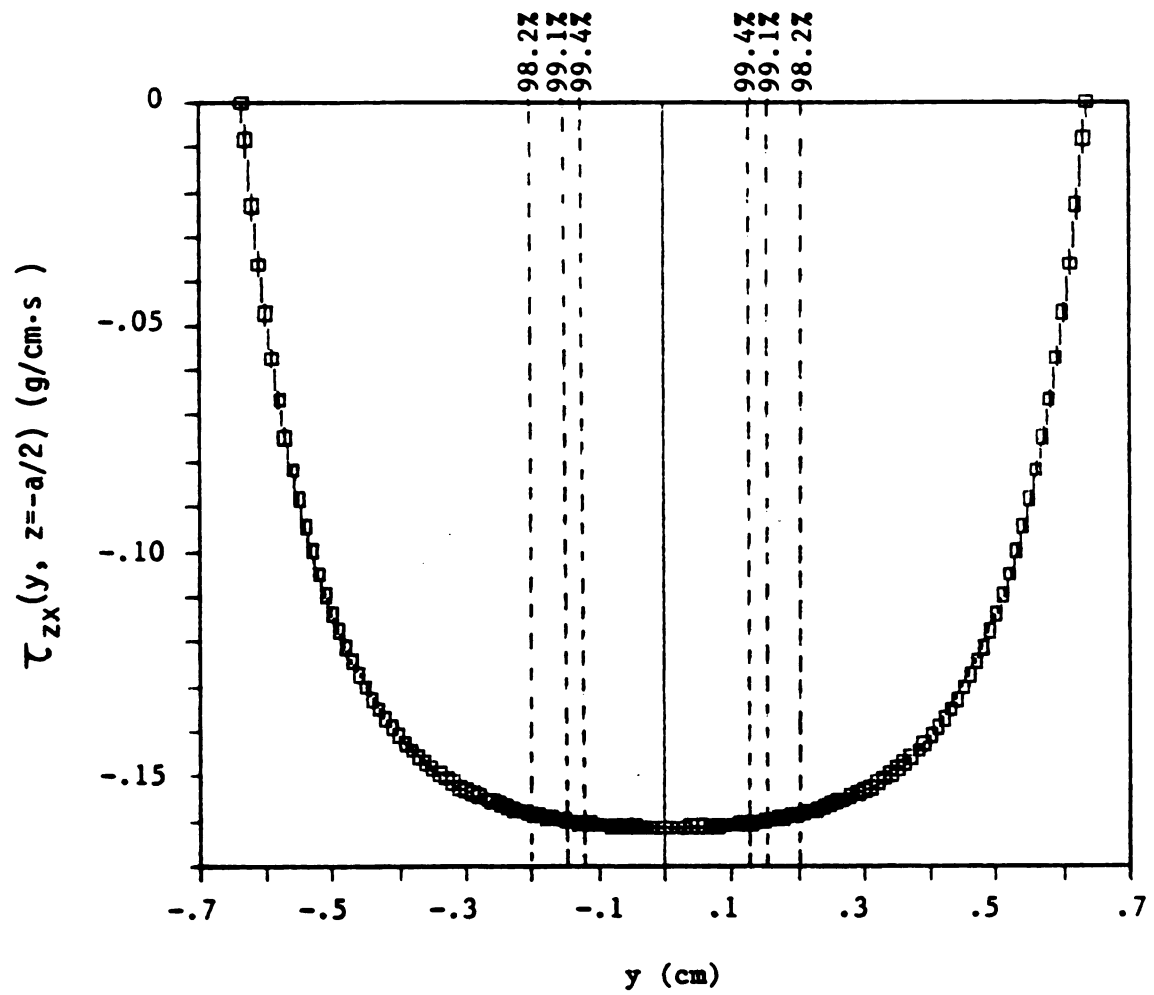


Figure 5-8 Shear stress at interface surface; flow rate at 40 ml/min.

5-4. Experimental Materials and Methods

The experimental technique and procedures were developed and implemented to test the hydrodynamic effects on cell viability and to observe the effects of cell presence on crystal growth.

5-4-1. Maden Darby Canine Kidney Cells

The Maden Darby Canine Kidney (MDCK) cell line was chosen for use as it is one of the best characterized epithelial cell lines available for study (Taub and Suier, 1979). The cells present the morphological and enzymatic properties of the epithelium from the distal tubule of the kidney. In this work, facilities for culturing MDCK cells were provided by Dr. William S. Spielman of the Department of Physiology. Monolayer cell cultures were successfully grown on an ordinary cover glass. The cells were cuboidal in shape. For consistency in experimental runs, the cell samples were used four days after culturing; at that time, they were confluent and multicellular blisters or domes were always observed. Formation of multicellular blisters in confluent MDCK cultures is an indication of healthy cells that are ready for water and solute transport (ibid). The culturing technique used is briefly described below.

Dr. Spielman provided the starter culture of MDCK cells in a 100x15 mm culture dish. For these cells, 5 ml of phosphate buffered saline (PBS) was added to remove calcium ion from the original medium residue. Three ml of 0.1% trypsin in a 0.05% EDTA solution was used to disaggregate the cells. After 10 to 15 minutes, the cell dish was tapped gently to ensure the detachment of the cells. They were then washed twice each with 5 ml DulBecco Modified Eagle's medium (DMEM) and collected in a centrifuge tube. After centrifuging at 1500 rev./min

for 5 minutes, the supernatant in the tube was removed, and 5 ml of 10% fetal bovin serum (FBM) in DMEM was added. Three drops of the well-mixed cell medium mixture were then transferred onto a cover glass (briefly sterilized with a flame) and put in a 35x10 mm culture dish. With careful addition of 1.5 ml 10% FBS in DMEM to the culture dishes, the cut cells were placed in an incubator to achieve confluency.

5-4-2. Solution Preparation

For the MSMPR crystallizer system described in Chapter 4, calcium oxalate was chosen as the model urinary precipitating agent; equal concentrations of calcium and of oxalate were used. Likewise, equal molal concentrations of calcium and of oxalate were also used in this study.

In order to prepare solutions for the experiments with cultured MDCK cells, a modified Earle's medium containing compounds necessary both for cell maintenance and for calcium oxalate precipitation was required. Table 5-2 lists components of the unmodified Earle's medium (Gibco Laboratories), the calculated ionic strength, sodium to potassium ratio, and total species concentrations. These values were calculated by assuming that all the ingredients were completely dissociated in solution and no complex formation among ion species occurred.

Using Earle's medium as a basis, the compositions of experimental solutions were determined to accommodate several criteria:

1. adjustment of Earle's medium to include equal calcium and oxalate concentration in each preparation of solutions;
2. adjustment of medium osmolarity to prevent water loss from the intracellular compartment via osmotic flux (Cooney, 1976);
3. control of medium Na/K ratio and Na concentration to prevent significant nonequilibrium distribution of ions via cells' sodium-potassium pump (Berne and Levy, 1983);
4. addition of fewest ingredient species possible to avoid

Table 5-2 Original Earle's medium recipe (1X).

	Molecular Weight	Concentration (g/l)	(M)
INORGANIC SALTS:			
CaCl ₂	110.99	.2	.0018020
Na ₂ C ₂ O ₄	134.		
KCl	74.56	.4	.0053648
MgSO ₄ ·7H ₂ O	246.48	.2	.0008114
NaCl	58.44	6.8	.1163587
NaHCO ₃	84.	2.2	.0261905
NaH ₂ PO ₄ ·H ₂ O	137.99	.14	.0010146
Na ₂ HPO ₄ ·7H ₂ O	268.07		
OTHER COMPONENTS:			
D-Glucose	180.16	1.	.0055506
Phenol red	354.38	.01	.0000282
AMINO ACIDS:			
L-Arginine·HCl	210.67	.126	.0005981
L-Cystine	240.3	.024	.0000999
L-Glutamine	146.15	.292	.0019979
L-Histidine HCl·H ₂ O	209.63	.042	.0002004
L-Isoleucine	131.18	.052	.0003964
L-Leucine	131.18	.052	.0003964
L-Lysine HCl	182.65	.0725	.0003969
L-Methionine	149.21	.015	.0001005
L-Phenylalanine	165.19	.032	.0001937
L-Threonine	119.12	.048	.0004030
L-Tryptophane	204.23	.01	.0000490
L-Tyrosine	181.19	.036	.0001987
L-Valine	117.15	.046	.0003927
VITAMINS:			
D-Ca pantothenate	476.54	.001	.0000021
Choline chloride	139.63	.001	.0000072
Folic acid	441.41	.001	.0000023
i-Inositol	180.16	.002	.0000111
Nicotinamide	122.13	.001	.0000082
Pyridoxal HCl	203.63	.001	.0000049
Riboflavin	376.37	.0001	.0000003
Thiamine HCl	337.27	.001	.0000030
CALCULATIONS:			
Sum(Cj)			.3441467
Ionic strength			.2150339
Na/K			26.76027

complicating the experimental results due to the presence of multiple ionic species while still maintaining MDCK cell viability.

Many species used in the original Earle's medium are present to provide for cell growth and multiplication; the objective herein was only to maintain the cells in a viable state for the duration of the experiments (one to two hours). Therefore, the inorganic salts chosen for the solution were $\text{CaCl}_2 \cdot 2\text{H}_2\text{O}$, $\text{Na}_2\text{C}_2\text{O}_4$, KCl , and NaCl , and the only organic species was D-glucose.

Table 5-3 shows the composition of solutions prepared for experiments with $[\text{Ca}^{2+}] = [\text{C}_2\text{O}_4^{2-}] = 0.001 \text{ M}$ and its derivation from the original Earle's medium. In the table, recipe A excludes all organic components from the medium except D-glucose. Recipe B shows a recipe with dihydrous calcium chloride replacing anhydrous calcium chloride and with $\text{MgSO}_4 \cdot 7\text{H}_2\text{O}$, NaHCO_3 , and $\text{NaHPO}_4 \cdot 7\text{H}_2\text{O}$ omitted to avoid effects of these ingredients on experimental results. The amount of NaCl was increased to maintain identical total Na concentration. The column for recipe C shows that the concentrations of KCl and NaCl were increased proportionally by multiplying the ratio of $\text{Sum}(C_j)$ in the column of recipe A to that of recipe B. Since single crystal experiments require mixing of the cationic (containing Ca^{2+}) and anionic (containing $\text{C}_2\text{O}_4^{2-}$) solutions, these two solutions were prepared separately but each contained equal concentrations of KCl , NaCl and D-glucose. Upon mixing of the two solutions, the total Na concentrations and Na/K ratio were the same as those in recipe C. Weights of chemicals for solution preparation are also shown in Table 5-3.

For experiments with calcium and oxalate concentrations other than 0.001 M, weights of $\text{CaCl}_2 \cdot 2\text{H}_2\text{O}$ and $\text{Na}_2\text{C}_2\text{O}_4$ were changed according to

Table 5-3 A typical solution composition for
 $[\text{Ca}^{2+}] = [\text{C}_2\text{O}_4^{2-}] = 0.001 \text{ M.}$

Inorganic Salts M.W.	Recipes			Experimental Conc., after Mixing (M)	Weight in Solutions		
	A (M)	B (M)	C (M)		g/2 ℓ	g/4 ℓ	g/6 ℓ
$\text{CaCl}_2 \cdot 2\text{H}_2\text{O}$ 147.	---	.00180	---	0.001	.5881	1.1762	1.7643
CaCl_2 111.	.00180	---	---	---	---	---	---
$\text{Na}_2\text{C}_2\text{O}_4$ 134.	---	---	---	.001	.5360	1.0720	1.608
KCl 74.55	.00536	.00536	.00588	.00588	.8773	1.7546	2.6319
$\text{MgSO}_4 \cdot 7\text{H}_2\text{O}$ 246.5	.00081	---	---	---	---	---	---
NaCl 58.45	.11634	.14354	.15742	.15542	18.1683	36.3365	54.5048
NaHCO_3 84.	.02619	---	---	---	---	---	---
$\text{NaH}_2\text{PO}_4 \cdot \text{H}_2\text{O}$ 138.	.00101	---	---	---	---	---	---
D-glucose 180.2	.00555	.00555		.00555	2.	4.	6.
Sum(Cj)*	.3386	.3089	---	.3342			
Ionic Strength*	.2150	.1543	---	.1673			
Na/K	26.756	26.756	26.756	26.7565			
pH					7.2	7.2	7.2
Ionic Strength**		.1489		.1613			

*: Assuming all ions were dissociated and no reaction took place.

**: Assuming all ions were dissociated and reaction consumed all Ca^{2+}
and $\text{C}_2\text{O}_4^{2-}$.

the required concentrations, but the amount of NaCl was reduced to maintain the same total Na concentrations and Na/K ratio as those in recipe C.

All the chemicals used in this study were of reagent grade. $\text{CaCl}_2 \cdot 2\text{H}_2\text{O}$ was obtained from J. T. Baker Chemical, $\text{Na}_2\text{C}_2\text{O}_4$ from Fisher Scientific, and KCl, NaCl, and D-glucose were from Mallinckrodt Chemical. Solutions were prepared with doubly distilled deionized water. The solution pH was adjusted to 7.2, an optimum pH for living cells, immediately before use. The Metrohm E632 pH-meter and a Metrohm combined pH glass electrode were used in monitoring pH values in solution.

5-4-3. Experimental Set-Up

Figure 5-9 shows the experimental set-up for the crystal growth flow system. Calcium and oxalate solutions were pumped separately through filters, flowmeters, heating coils, and then into the flow cell. There growth of single crystals and mechanistic effects of the flow on living cells or on crystals were observed microscopically. The microscope used was the 110 Microstar^(R) microscope manufactured by AO Scientific Instruments.

A 10X objective with a 9.1 mm working distance was used to accommodate the design of the flow chamber precipitator. When the microscope was in use with the flow chamber precipitator, the objective extended into the rectangular opening of the upper retainer of the precipitator. This configuration and the dimensions of the opening and the objective allowed the microscope to focus on objects only within a range of approximately $y = \pm 1.25$ mm in the flow chamber. From Figures 5-7 and 5-8, it can be seen that both the fluid velocity and shear

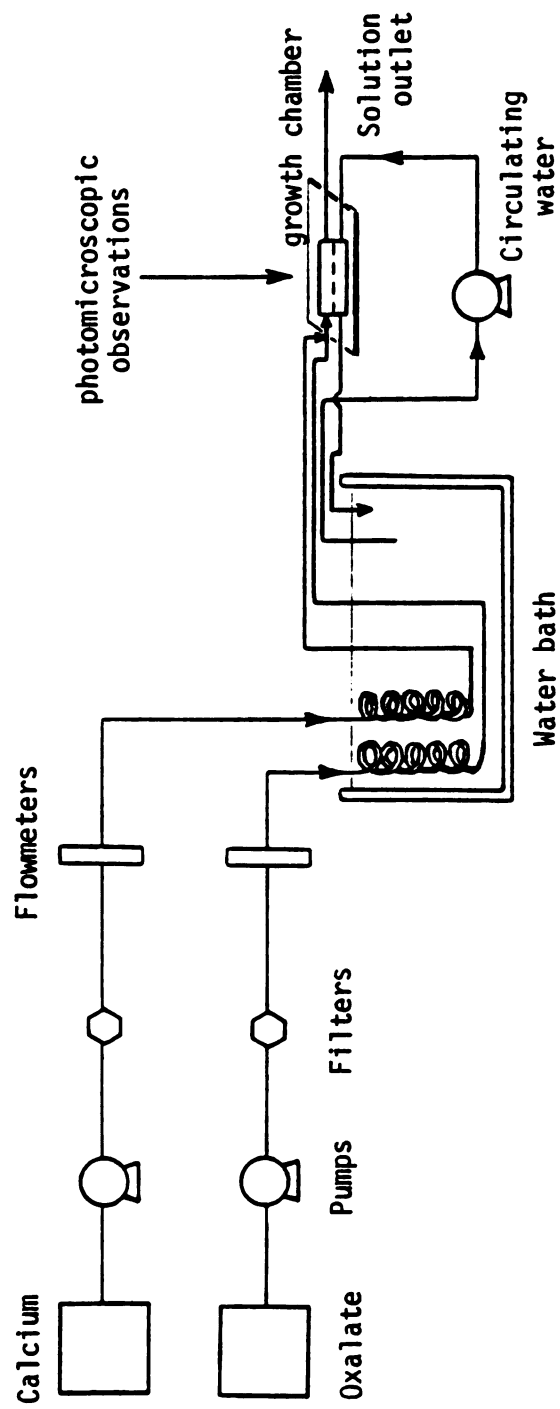


Figure 5-9 Crystal growth flow system.

stress are within 99% of their maximum values within this range of $y = \pm 1.25$ mm. It is therefore reasonable to assume that the experimental observations were implemented under a fairly constant flow field. An Olympus OM-G camera and an automatic winder, Olympus Motor-Winder 2, were mounted on the microscope for photomicroscopic observation. Photography was automated by the coupling of a timer with the automatic winder.

The pumps used in this work were Cole-Parmer Masterflex variable speed peristaltic pumps. The flowmeters were Cole-Parmer variable-area flowmeters. For the filters, 0.2 μ m cellulose acetate membrane of 25 mm in diameter, manufactured by Micro Filtration Systems, were used with in-line holders. The glass heating coils were made in glass shop of the Department of Chemistry. An E-3 Haake circulator was used to control the temperature in the water bath.

A stainless steel thermistor probe (YSI series 400) of 1/8 inch in diameter was inserted into the flow chamber and connected to a multimeter (Keithley Instruments, Model 179 A TRMS). The temperature of the solution in the flow chamber was indicated by converting the resistance reading of the multimeter to temperature. The desired solution temperature was 37°C to simulate human body temperature. Because of the heat loss from the liquid flowing out of the water bath to the flow chamber, the temperature in constant temperature water bath was usually several degrees higher than 37°C.

A T-connector, placed immediately upstream of the growth chamber, allowed the mixing of the calcium and oxalate streams and introduced the mixed solution into the cell. The flow configuration of such a T-junction was believed to provide thorough mixing of two solutions based on the kinetics of ion complexation (DeLong and Briedis, 1985).

Tygon^(R) tubing was used for the connecting lines throughout this experimental set-up.

5-4-4. Experimental Scheme

Experiments in this work included testing the viability of MDCK cells under flow shear stress and observation of single crystal growth on MDCK cells. Monolayer MDCK cells grown on a piece of cover glass, 18 mm square, were installed in the flow chamber to simulate a physiologically realistic interface between the model renal fluid and renal epithelial tissue. For observations of crystal growth on glass, a plain cover glass was used. The cover glass, with or without MDCK cells, was placed in the chamber so that the observed single crystals were in a fully developed flow field according to the transition lengths calculated.

5-4-4-1. Viability Tests on MDCK Cells

Testing of MDCK cell viability was studied using three flow rates, 25, 49.5, and 99 ml/min. At the flow rate of 99 ml/min, the transition length (Table 5-1) was longer than the length of the chamber, i.e., the velocity profile within the chamber was not fully developed. However, the boundary layer effects could be considered to be similar to fully developed flow, especially at a region close to the wall where boundary layers develop. The flow shear stress on MDCK cells is an effect of the boundary layer at the wall; its value may be calculated from the equation for flow of a developed velocity distribution, i.e., from Equation (5-13).

Solutions for the shear tests were prepared with low calcium and oxalate concentrations, 0.0002 M, to avoid crystallization of calcium oxalate from the solution. Therefore, only one solution stream was

necessary. After testing the cells under shear stress for several hours, the solution pump was turned off, and 1 to 1.5 ml of 0.4% trypan blue stain (Sigma Chemical Company, Catalog number T 9520) was injected from upstream of the solution chamber. The blue dye was allowed to flow into the chamber and was left in the chamber for about 10 min. Dead cells with ruptured cell membranes would take up the dye. After replacing the blue dye with clear solution, dead MDCK cells were easily distinguished from the living ones.

Specific results of the viability tests are discussed in Section 5-5. Satisfactory viability tests of the MDCK cells made possible the growth rate study of calcium oxalate crystals on MDCK epithelium.

5-4-4-2. Growth Rate Experiments: Effects of Additive and Tissue Surfaces

The objective of studying the growth rate of single calcium oxalate crystals was to observe the interaction of kidney epithelial cells and COM crystals as a possible precursor to the formation of urinary stones. These studies were performed under controllable conditions through a simulated renal flow system while previous work had been done only in a static environment (Mandel et al., 1987; Wiessner et al., 1987).

For the requirement of fully developed flow, flow rate for experiments was also limited by the length of the flow chamber according to the transition length calculated. The flow rate for this study was set constant at 40 ml/min, almost the maximum flow rate attainable for a well characterized flow field. Before beginning an experiment, solutions were prepared and connected to solution pumps. The circulator for the water bath was turned on. Air bubbles in solution lines, mostly trapped in the filters and flowmeters, were

purged out of the system while the growth chamber was not in line. After the chamber precipitator was assembled, it was placed on the microscope stage and connected to the solutions and to the circulation water. The pumps for solutions and for heating water were turned on, and the flow rates were increased gradually using the pump controllers. Both the upper and the lower chambers of the precipitator were filled so that there were no gas bubbles trapped in the chambers. Tilting and tapping the chamber accomplished this. The flow chamber was then observed under the microscope with the objective focused on the solution-surface (glass or cells) interface. While waiting for the formation of crystal nuclei to occur, the solution flow rates and the precipitator temperature were monitored.

After the induction time, nuclei of single crystals were formed and observed. Timed-sequenced photomicrographs of crystals were taken to follow the course of crystal growth. The photographic slides were developed and images of the crystals were transferred to paper. Equivalent circular diameters, L_{eq} (μm), of the crystal images were then calculated from the area of crystals measured with an image-analyzer (the HipadTM Digitizer, Houston Instrument), i.e.,

$$L_{eq} = \sqrt{4A/\pi} \quad (5-14)$$

Growth rate G , $\mu\text{m}/\text{min}$, of each crystal was then calculated:

$$G = \frac{\Delta L_{eq}}{2\Delta t} \quad (5-15)$$

where Δt is the time interval between photographs (in min).

To test the effects of solution chemistry on the growth rate of crystals growing on MDCK cells, experiments with various concentrations of equimolar calcium and oxalate were conducted to observe the effects of supersaturation. Values of supersaturation were calculated

according to the equations in Chapter 2. For comparison, experiments with crystals growing on plain glass were performed with the same solution conditions as for the crystal growth experiments on MDCK epithelium.

One of the other significant effects of solution composition is the inhibition or promotion of crystal growth on MDCK cells in the presence of biopolymers. This could provide evidence for kidney stone etiology in terms of the concentration or species of the constituents in renal fluid. Each individual candidate biopolymer may be added into experimental solutions to examine its effect on the rate of crystal formation. In this work, heparin was chosen to model the effects of biopolymer additives in experimentation. The sodium salt of heparin from Sigma Chemical Company (H 3125) was added to the anionic solution to prevent interactions of calcium cations and the anionic heparin. Since heparin would have been filtered out by the in-line filters, preparation of the anionic testing solution was altered. The solution was filtered in batch before addition of heparin, and the solution pH was adjusted afterwards. The in-line filter for the anionic stream was then removed from the system. Concentrations of heparin from 2 mg/l up to 100 mg/l, in terms of the total volume of mixed solution, were tested.

In order to understand the effect of damaged tissue surface on the possible mechanism of renal calculi formation, MDCK epithelium injured with HCl and with papain were included in the photomicroscopic crystal growth study. Papain is a proteolytic enzyme, which hydrolyses a variety of peptides, amides, and esters (Barman, 1969) and is used in tissue disaggregation (Schwartz and Azar, 1981). Although the specific

action of HCl is not known, it was suspected of denaturing cellular surface proteins.

The chemical concentration and length of time of MDCK cell exposure for chemical injury were tested to assure cell viability during the time period of an experimental run. Appropriate procedures were identified for HCl and for papain injured cells; healthy MDCK cells on a cover glass were soaked in 0.1 N HCl solution for 4 minutes and in a prepared papain solution for 35 seconds. The papain soaking solution was prepared as follows: 0.0333 g crude papain powder (Sigma Chemical Company, type II, Catalog number P 3375) was added to 100 ml H₂O, then shaken occasionally for 30 minutes. One ml of the papain decantant, 1 ml 83.3 ppm EDTA solution (as an activator), and 0.666 ml of 0.5 M acetate buffer solution, pH 6.5, were mixed with H₂O to a total volume 50 ml.

To test the system's performance and to understand the mass transfer phenomena in the system, growth rates of crystal grown on glass surface were also investigated in comparison with DeLong's work which was conducted with a cylindrical flow chamber (DeLong and Briedis, 1985; DeLong, 1988). The ionic strength of solutions were kept at 0.15 M by addition of KCl instead of the compositions used to prepare the modified Earle's media. Potassium oxalate was used in place of sodium oxalate, and solution pH was adjusted to 6.0. For some of the runs, effluent samples from the flow chamber were collected and diluted 1:10. Total calcium concentrations were then analyzed with an atomic absorption spectrophotometer (Varian AA-375). The concentrations of free calcium ions were measured with a calcium electrode (Orion, Model 93-20) on the Fisher Accumet^(R) pH meter (Model

825 MP). The reference electrode used was a single-junction electrode (Orion, Model 90-01).

5-4-4-3. Induction Period in Closed Vessels

For calcium and oxalate solutions mixing in a closed vessel, an induction or incubation period is usually observed before occurrence of nucleation of crystals (Walton, 1967; Nielsen, 1955). In order to understand the nucleation phenomena in the flow chamber system, auxiliary experiments on induction period were performed by direct mixing of calcium and oxalate (potassium salt) solutions in beakers. The ionic strength of solutions were kept at 0.15 M by adding KCl. D-glucose and NaCl were not added. The induction period was defined as the time period between mixing of solutions and occurrence of visible turbidity.

5-5. Results and Discussion

5-5-1. Cell Viability

After the live epithelia were exposed to the flow shear, some of the cells became rounded and eventually detached from the supporting surface. Stathopoulos and Hellums (1985) studied the effects of shear stress on human embryonic kidney cells and suggested an argument that the cells remaining attached are all viable. This was also assumed for the discussion that follows.

At the three flow rates used to test for cell viability, the results show significant effects of the flow shear stress on MDCK cells (Table 5-4). After the application of trypan blue stain after each experimental run, no intake of the blue dye was observed for the cells remaining attached, though they were rounded to some extent. It was

also discovered that the length of time that cells were outside of the incubator also played an important role in cell viability.

As a result of these observations, the conservative conclusion made was that, with careful handling, MDCK cells remained viable through the time period for experimental runs in the study of single crystal growth, which took 1 to 2 hrs at a solution flow rate of 40 ml/min.

Table 5-4 MDCK cell viability with shear stress.

Flow Rate (ml/min)	τ_{\max} (g/cm \cdot s ²)	Cell Viability
25.0	.1008	intact for 7 hrs.
49.5	.1997	some cells detached after 2 hrs, the rest are fine for 6 hrs.
99.0	.3993	some cells detached at the onset of the run, the rest are fine for 6 hrs.

5-5-2. Observations on Formation of Single Crystals

During the experiments of single crystal growth, observations on crystal nucleation and crystal habit were made and are discussed in this section.

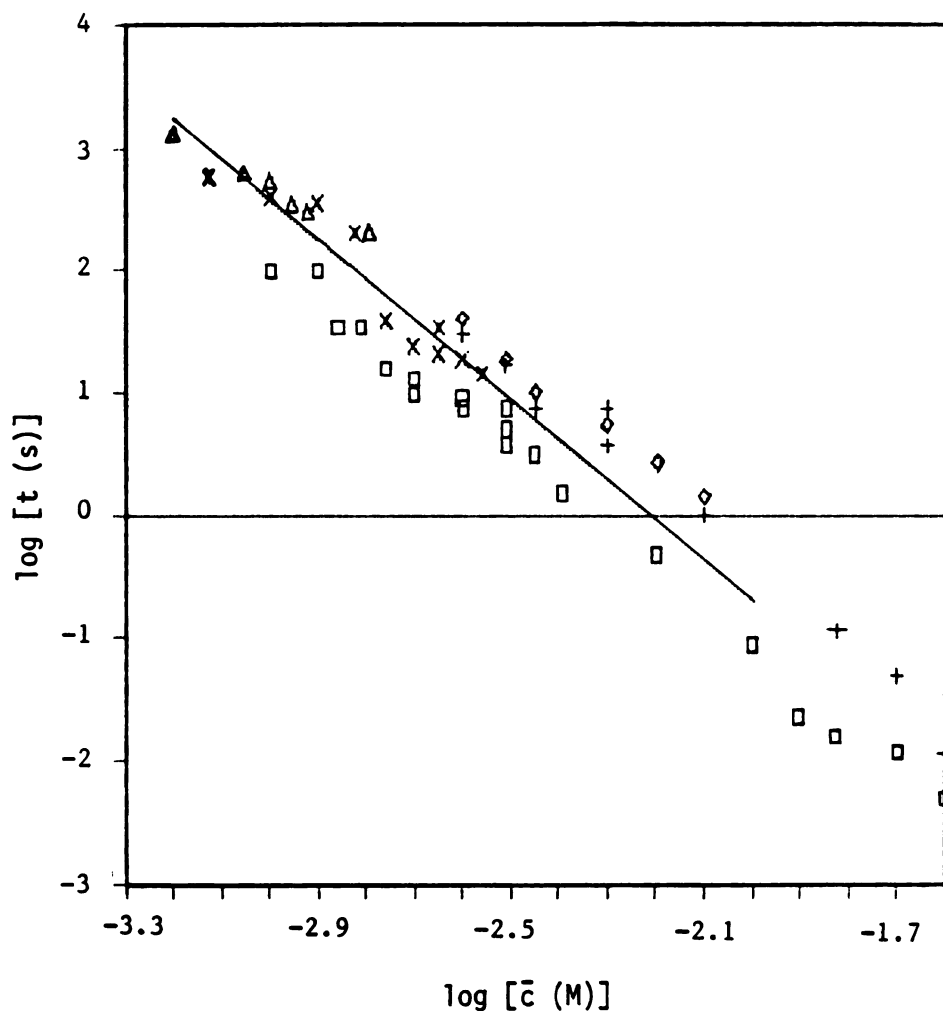
5-5-2-1. Nucleation

It was found that single crystals grew all over the surface of the upper flow chamber, from the T-junction, where solutions were mixed, to the tubing that leads solution out of the flow chamber. It is interesting to compare the nucleation observed in the flow chamber with

the homogeneous nucleation in a closed vessel which occurs after an induction period after mixing of calcium and oxalate solutions. Figure 5-10 shows induction period data for the formation of calcium oxalate from the literature (Nielsen, 1955; Skrtic et al., 1984) and from experiments conducted in this work, in which \bar{c} is the initial reactant concentration or the geometric mean concentration of the mixed solution. Although the data were obtained by mixing calcium and oxalate from different salt sources with diverse experimental conditions (temperature, ionic strength, stirring condition), the data exhibit a consistent monotonic decrease of induction time with increasing concentration and a fairly consistent increase of induction time with increasing ionic strength. The experimental data for ionic strength of 0.15 M were fit to yield a linear regression line shown in the figure. From this regression line, the induction periods calculated for concentrations used in the single crystal experiments are tabulated in Table 5-5. These induction period data could be used to help identify the nucleation mechanism occurring in the flow chamber precipitator.

Table 5-5 Calculated induction periods at the reactant concentrations used in single crystal experiments.

Reactant Concentration, \bar{c} (mM)	Induction Period, t (s)
0.5	3630
0.75	965
1.0	377
1.25	182
1.4	126
1.5	100



- : $\text{Ca}(\text{CH}_3\text{COO})_2 + (\text{NH}_4)_2\text{C}_2\text{O}_4$, 23°C, no salt added (Nielsen, 1955)
 +: $\text{Ca}(\text{CH}_3\text{COO})_2 + (\text{NH}_4)_2\text{C}_2\text{O}_4$, 23°C, ionic strength 0.5 M by adding NaCl (ibid)
 ◊: $\text{CaCl}_2 + \text{Na}_2\text{C}_2\text{O}_4$, 6°C, ionic strength 0.5 M by adding NaCl (ibid)
 Δ: $\text{CaCl}_2 + \text{Na}_2\text{C}_2\text{O}_4$, 25°C, ionic strength 0.3 M by adding NaCl, constantly stirring (Skrtec et al., 1984)
 x: $\text{CaCl}_2 + \text{K}_2\text{C}_2\text{O}_4$, room temperature, ionic strength 0.15 M by adding KCl, without stirring (experimental data of this work)

Figure 5-10 Induction period for the formation of CaC_2O_4 .

5-5-2-2. Heterogeneous Nucleation

If homogeneous nucleation was the only mechanism of crystal nucleation in the growth cell no nucleation should have been observed in the chamber, because the induction period for homogeneous nucleation (Table 5-5) was significantly longer than the solution residence time in the chamber (9 seconds at a flow of 40 ml/min). The nearly instantaneous nucleation observed at the inner surface of T-junction may have been due to a nucleation mechanism entirely different from the homogeneous, or near-homogeneous, nucleation in a closed vessel.

Two effects probably played important roles in affecting crystal nucleation in the growth cell. The first is the turbulent agitation resulting from the mixing of two solution streams at 180 degrees in a small contact space in the T-junction (inside diameter of approximately 3/32 to 1/8 inches). The second effect is heterogeneous nucleation that occurred in the flow chamber due to the presence of good nucleation surfaces.

Experimental evidence and theory show that heterogeneous nucleation occurs at a lower supersaturation level than that for homogeneous nucleation (Walton, 1967). In the flow chamber system, the relatively high surface area to solution volume ratio compared with other precipitator systems (e.g., a stirred tank reactor) may provide abundant sites for surface nucleation. Surface nucleation on the wall of the chamber, one route of heterogeneous nucleation, probably prevailed in this system.

5-5-2-3. Nucleation on Glass and on MDCK Cells

Nucleation of calcium oxalate on MDCK cells was somehow inhibited. The inhibition of nucleation on MDCK cells, healthy or injured, was observed as 1) a prolonged "induction period" for the first appearance

of calcium oxalate crystals on the MDCK cell surface and 2) from the low number density of single crystals formed on the MDCK cell surface. The "induction period" lasted over an hour in some cases; therefore, in experiments with live cells, nucleation had to be initiated by initial use of solutions of higher supersaturation (usually a concentration of 1.5 mM) or had to be enhanced by using elevated solution flow rates. This was never necessary in experiments in which a glass surface was used as the nucleating surface nor where crystals were grown directly on the plastic divider.

Single crystals were found to preferentially nucleate on glass and on the plastic chamber divider than on MDCK cells. Figures 5-11 and 5-12 are photographs taken at the end of an experimental run with healthy MDCK cells in which several spots of bare glass were observed by photomicroscopy in the same run. These figures show the comparison of nucleation on the spots with and without MDCK cells. It is seen that more crystals are evenly dispersed on the glass surface without MDCK cells than with MDCK cells (Figure 5-12).

The enhancement of nucleation by flow might suggest a secondary nucleation mechanism on the epithelial cells. That is, new nuclei may have been formed by sweeping away the nuclei or embryos on the crystals that grew on an upstream portion of the chamber surface (McCabe et al., 1985). The delayed nucleation, enhanced nucleation in the presence of elevated flow rates, and the likelihood of nuclei being generated from the turbulent flow at the T-junction all support the possibility of a secondary nucleation mechanism.

After the first stage of nucleation, new crystals were observed occasionally throughout the experiments, except in the experiments with HCl injured cells. For the untreated (Figure 5-11) and papain injured

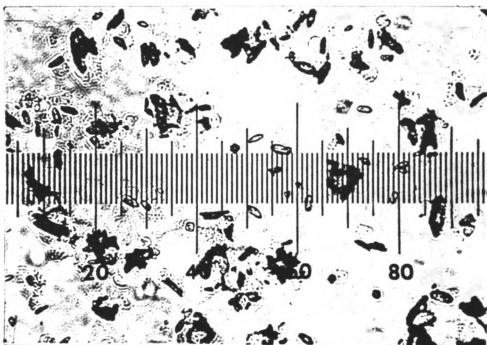


Figure 5-11 COM crystals on MDCK cells; Run 1102087,
 $T_{Ca} - T_{Ox} = 1.5$ mM, taken after experiment.

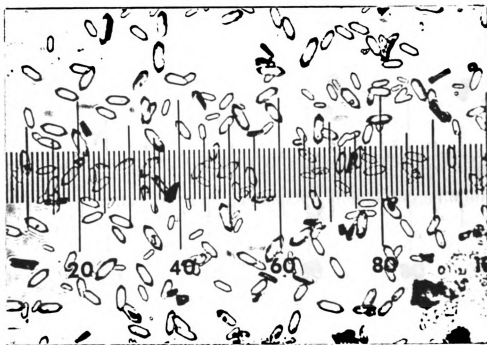


Figure 5-12 COM crystals on glass in an experiment with MDCK cells,
 a spot with cells detached; Run 1102087,
 $T_{Ca} - T_{Ox} = 1.5$ mM, taken after experiment.

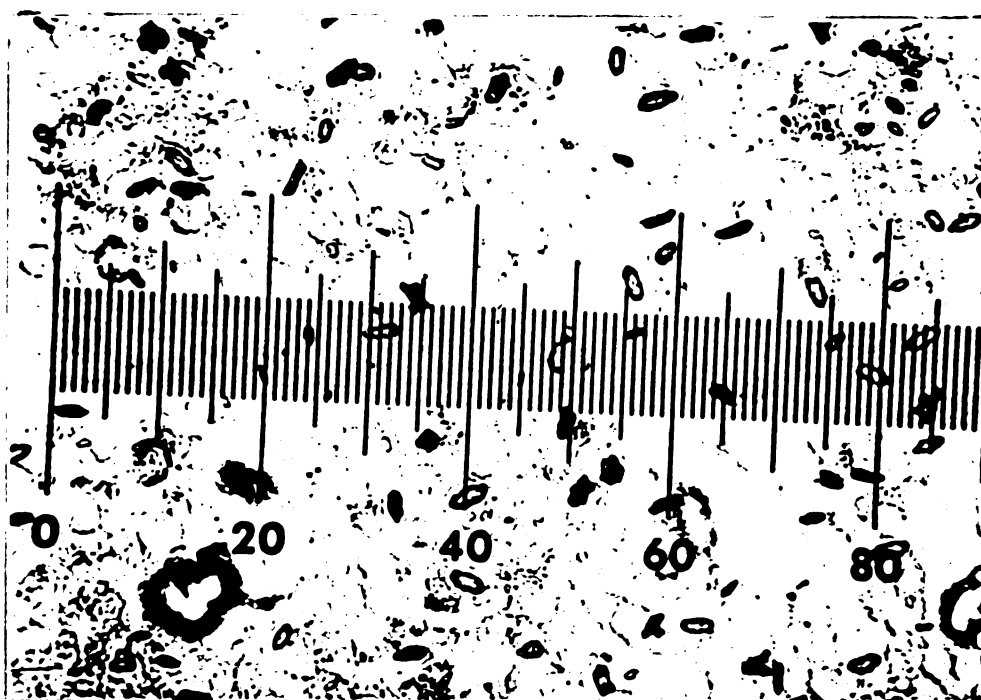


Figure 5-13 COM crystals on MDCK cells treated with papain;
Run 2110487, $T_{Ca} = T_{Ox} = 1.25$ mM, $t = 15$ min.

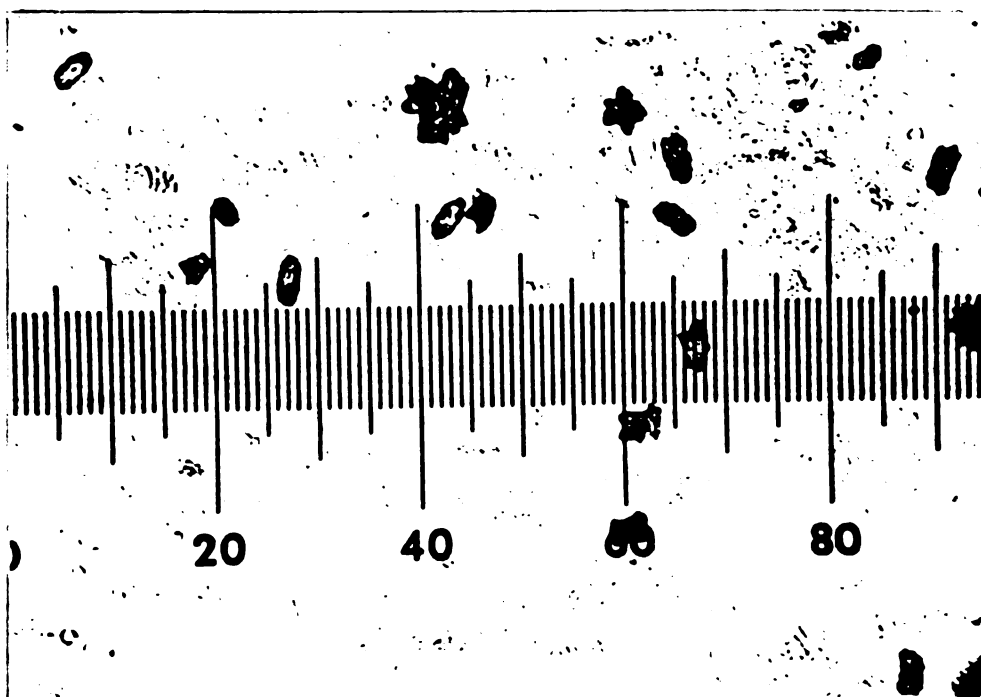


Figure 5-14 COM crystals on MDCK cells treated with HCl;
Run 2102087, $T_{Ca} = T_{Ox} = 1.5$ mM, $t = 27$ min.

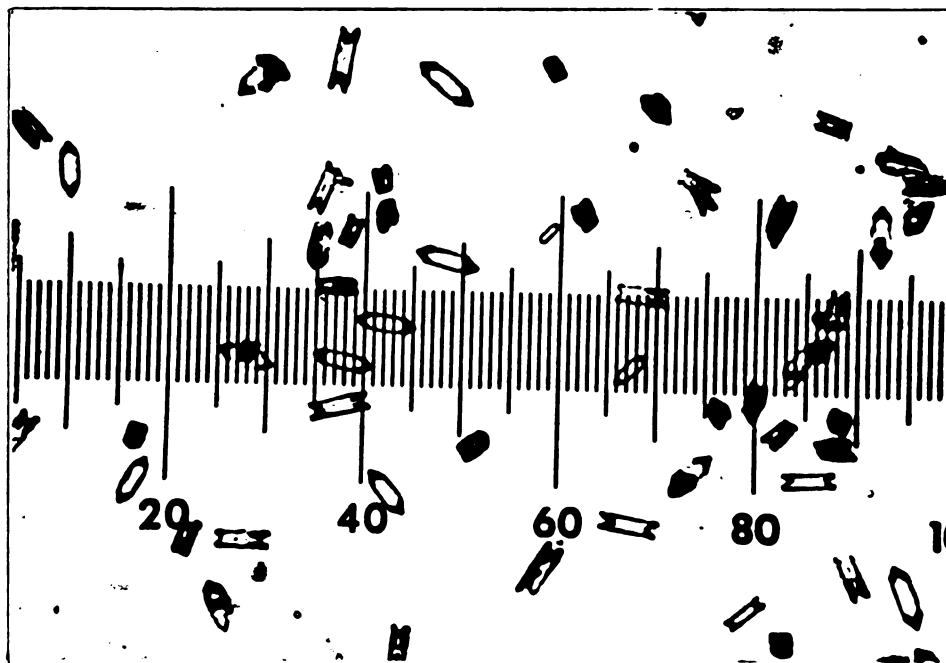


Figure 5-15 COM crystals on glass; Run 2092387,
 $T_{Ca} = T_{Ox} = 1.25$ mM, $t = 35$ min.

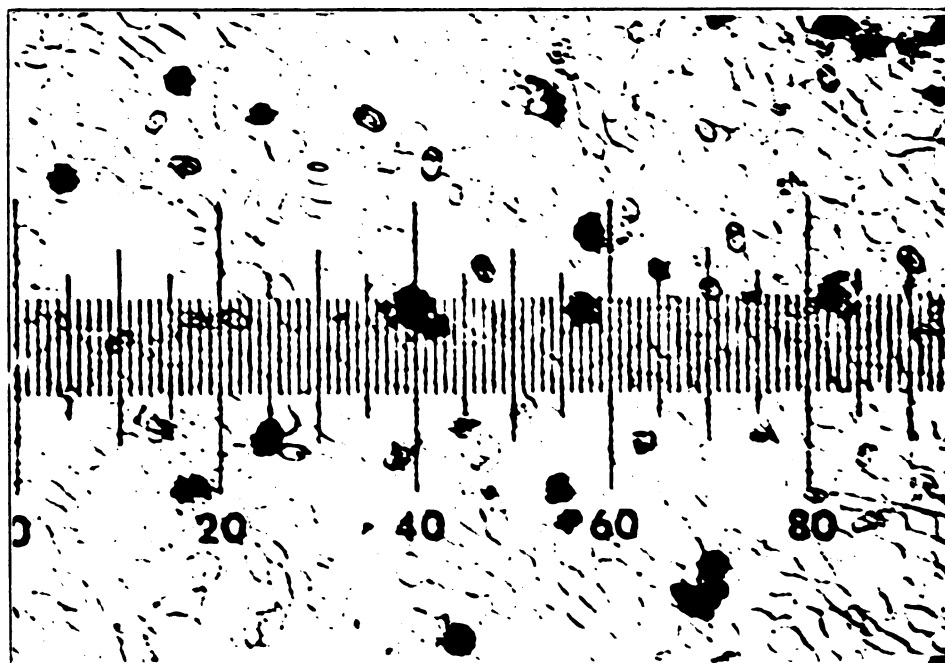
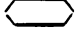
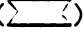


Figure 5-16 COM crystals on MDCK cells with 100 mg/l heparin;
Run 1082587, $T_{Ca} = T_{Ox} = 1.0$ mM, $t = 40$ min.

(Figure 5-13) epithelia, it appeared that nucleation of new crystals occurred around some of the "not-so-healthy" (rounded) cells. The healthy cells seemed to be immune from calcium oxalate nucleation.

For the experiments with HCl injured epithelium cells, there was no further nucleation seen after the nucleation was initiated by enhanced supersaturation and by high flow rates. Only growth of a small number of crystals was observed through a run (Figure 5-14). Because rounded cells were also observed for HCl injured epithelia, the inhibition of post-nucleation (nucleation after initial nucleation activated by elevated supersaturation and by high flowrate) on HCl injured cells may be attributed to the removal of "active sites" for nucleation with HCl treatment.

5-5-2-4. Crystal Habit

Besides the nucleation characteristics, the appearance of growing calcium oxalate crystals was also influenced by the nature of supporting surfaces. Figure 5-15 shows crystals formed on plain glass surface. The single crystals are transparent hexagons with distinct angles and have been identified as calcium oxalate monohydrates (DeLong, 1988). Crystals of both convex () and concave () hexagons were usually seen. When comparing Figure 5-15 (growth on glass without previous MDCK attachment) with Figure 5-12 (growth on glass with previous MDCK attachment), it is surprising to see the convex type of crystals predominating on the glass surface where epithelial cells were detached. Whether it is a coincidence or whether this is an indication of the changes in the properties of the glass surface due to previous epithelial attachment remains unknown at this point.

The crystals growing on untreated and papain injured cells (Figures 5-11 and 5-13) show more convex type of crystals and fewer concave hexagons with two unequal parallel edges. Fewer convex type single crystals were seen on epithelial cells treated with HCl (Figure 5-14). In general, crystals growing on live cells, untreated or injured, exhibited less distinct angles than those on glass surfaces. For all the various conditions, imperfect or distorted crystals were also observed on the epithelial cells. They were darker in comparison to the transparent single crystals.

Addition of heparin to the experimental solution also changed the appearance of crystals growing on MDCK cells. As seen in Figure 5-16 for the crystals formed with the addition of 100 mg/l heparin, the convex hexagons show significant increase in the width to length ratio of the crystals. This aspect ratio increased with increase of heparin concentrations, while the frequency of occurrence of the concave hexagons decreased. These results are consistent with the results of DeLong's work (1988), in which the aspect ratios of crystals grown on glass surface were investigated under the influence of heparin additive.

5-5-3. Supersaturation Level in Flow Chamber

Since supersaturation is required in correlating crystal growth quantitatively with its driving force, an effort was made to estimate solution supersaturation around the observed crystals grown in the flow chamber precipitator.

For some of the experiments performed with KCl as an ionic strength buffer, calcium concentrations of the effluent samples were analyzed with AA and with a calcium selective electrode. $T_{Ca,e}$ denotes

the total calcium concentration measured with AA, and $[Ca^{2+}]_e$ is the concentration of free calcium ions measured with calcium electrode. Table 5-6 shows the results for chamber outlet concentrations in comparison with the total inlet concentration of calcium, $T_{Ca,i}$, prepared for each run. A consistent trend was found among the data, that is, $T_{Ca,i} > T_{Ca,e} > [Ca^{2+}]_e$. The $[Ca^{2+}]_e$ values were lower than $T_{Ca,e}$ due to formation of calcium-complex ions in the 1:10 diluted effluent samples; a decrease in concentrations from the inlet $T_{Ca,i}$ to outlet $T_{Ca,e}$ streams indicates consumption of solute within the flow chamber. Calculation of $(T_{Ca,i} - T_{Ca,e})/T_{Ca,i}$ showed a 4-15% concentration drop. As a result, supersaturation level in solution around the observed single crystals must be lower than that calculated from $T_{Ca,i}$.

Table 5-6 Calcium concentrations of some effluent samples*.

Run No.	$T_{Ca,i}$ (mM)	$T_{Ca,e}$ (mM)	$[Ca^{2+}]_e$ (mM)	$\frac{T_{Ca,i} - T_{Ca,e}}{T_{Ca,i}}$ (%)	Flow Rate (ml/min)
R1020787	0.5	0.4666	---	6.7	40
R1020587	0.75	0.7221	0.583	3.7	40
R1013187	1.0	0.8737	0.809	12.6	40
R1020387	1.5	1.2768	1.121	14.9	40
R1012987	1.0	0.9056	0.823	9.4	99
R1012487	1.0	0.917	0.865	8.3	98
R1012587	1.5	1.335	1.25	11.0	99

* Effluent samples were diluted 1:10 after collection.

The measured calcium concentrations $T_{Ca,e}$ and $[Ca^{2+}]_e$ are shown in Figure 5-17 for the 40 ml/min runs. Linear regression of $T_{Ca,e}$ data

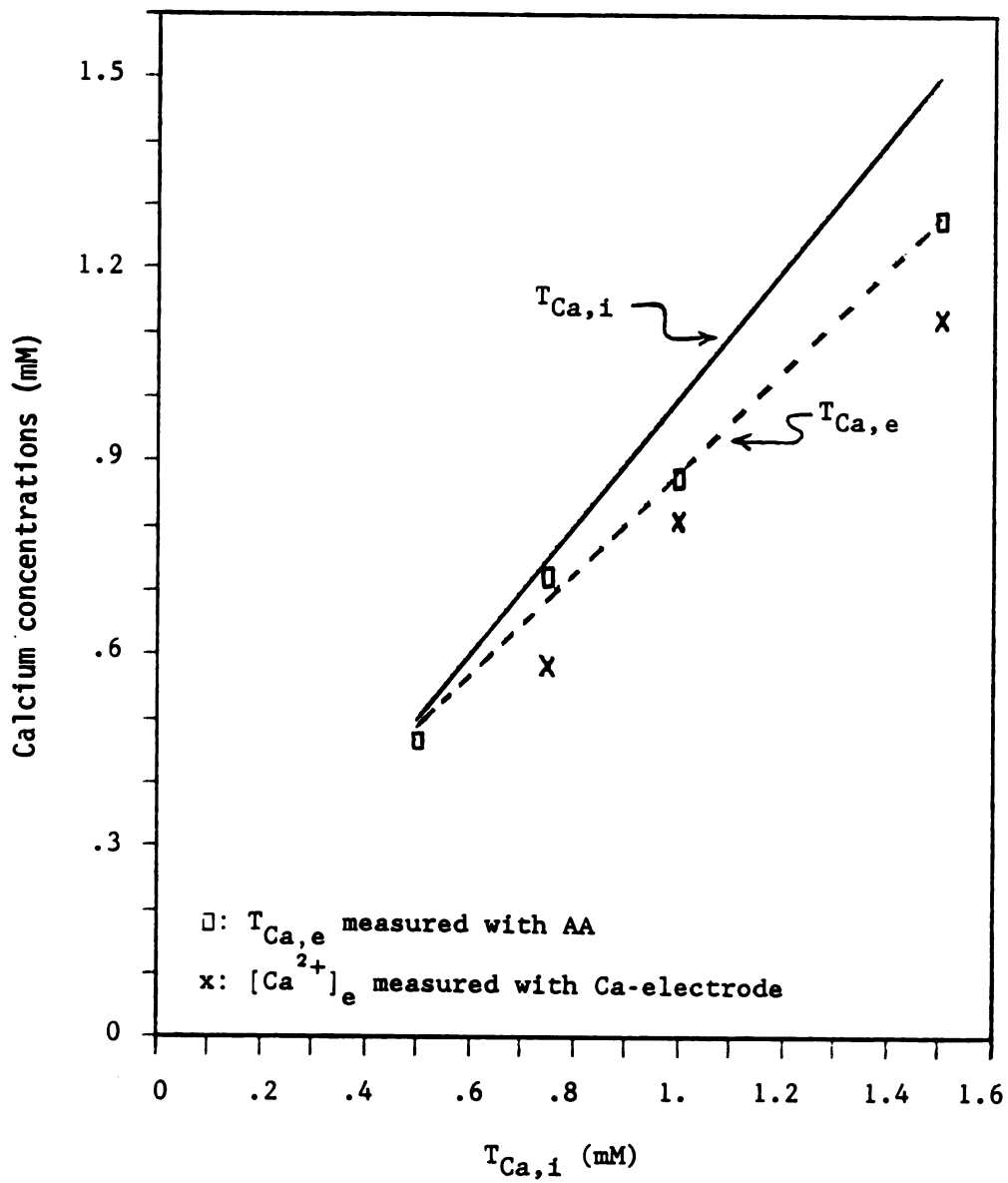


Figure 5-17 Effluent calcium concentrations.

versus $T_{Ca,i}$ is shown as a dashed line. The solid line is $T_{Ca,i}$. The total calcium concentration in the solution around the crystals, $T_{Ca,b}$, must be somewhere between $T_{Ca,i}$ and $T_{Ca,e}$. Since the crystals were located at the downstream end of the flow chamber, it may be logically assumed that $T_{Ca,b}$ was close to but lower than the average value of $T_{Ca,i}$ and $T_{Ca,e}$. It was assumed that $T_{Ca,b} = 0.6T_{Ca,e} + 0.4T_{Ca,i}$. With the substitution of the linear regression result for $T_{Ca,e}$, $T_{Ca,b}$ may be expressed as

$$T_{Ca,b} \text{ (M)} = 0.8754 T_{Ca,i} \text{ (M)} + 5.523 \times 10^{-5} \quad (5-16)$$

Calcium oxalate supersaturations, either $(S_{COM,c})_b$ or $(S_{COM,i})_b$, calculated from the modified EQUIL programs with $T_{Ca,b}$ from Equation (5-16) were used in characterizing the driving force for crystal growth rate discussed in the following section.

5-5-4. Growth Rate under Effects of Additive and Tissue Surfaces

Following the experimental scheme described in Section 5-4-4, experiments were conducted to observe growth rates of single calcium oxalate crystals under the effects of biopolymer additives and epithelial cells. The original crystal growth data obtained from image analysis were equivalent circular diameter of crystals versus time, of which the slopes were used to calculate growth rate as per Equation (5-15). For the discussion that follows, size-independent growth rate was assumed.

5-5-4-1. Effects of Tissue Surfaces

For crystals growing on glass and tissue surfaces, the results show that growth rates, G ($\mu\text{m}/\text{min}$), may be correlated to the supersaturation driving force, $(S_{COM,c})_b$ or $(S_{COM,i})_b$, such that

$$G = k_c (S_{\text{COM},c})_b \quad (5-17)$$

$$\text{or } G = k_i (S_{\text{COM},i})_b^2 \quad (5-18)$$

where the subscript b denotes supersaturations in the bulk solution, and the rate constants, k_c and k_i , were obtained from regression with the appropriate supersaturation. Figures 5-18 and 5-19 show the growth rates and such correlations for four different growth conditions, COM crystal growth on glass, on healthy MDCK cells, on HCl-treated MDCK cells, and on papain-treated MDCK cells. The rate constants of both correlations are also listed in Table 5-7. A consistent decrease of the rate constants for both correlations in the order of crystal growth on glass > MDCK cells treated with HCl > MDCK treated with papain > healthy MDCK cells was observed.

Each of these two correlations (Equations (5-17) and (5-18)) provides a direct comparison of growth rate from the rate constants; i.e., the higher the rate constant, the higher the growth rate for a given supersaturation. Therefore, the rate constants in Table 5-7 indicate fastest crystal growth on glass, followed by HCl-treated cells, and then papain-treated cells. Crystal growth on untreated MDCK cells was slowest.

Table 5-7 Rate constants of COM growth.

Correlation	rate constant	Growth conditions			
		Glass	MDCK/HCl	MDCK/papain	MDCK
$\propto (S_{\text{COM},c})_b$	k_c	0.0137	0.0090	0.0081	0.0071
$\propto (S_{\text{COM},i})_b^2$	k_i	0.0201	0.0134	0.0119	0.0105

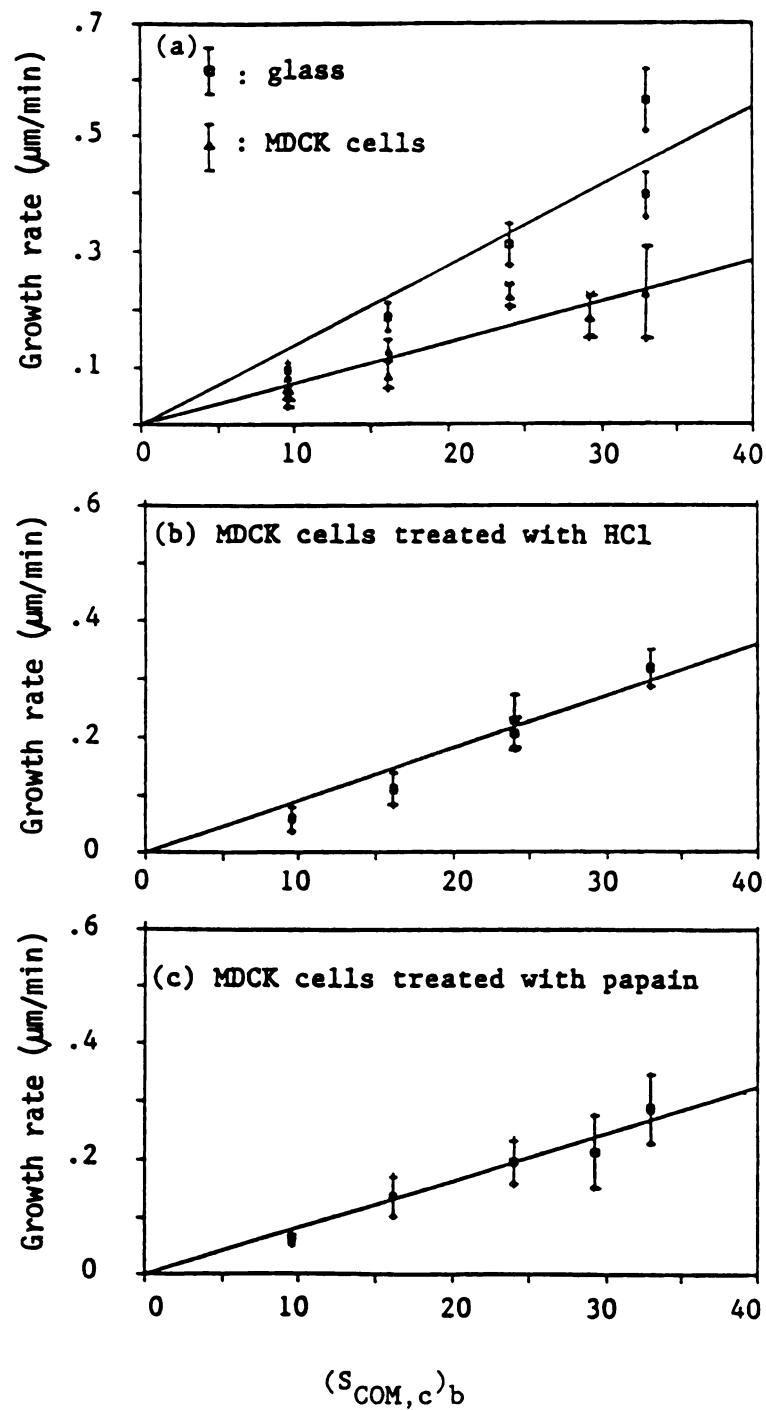


Figure 5-18 Growth rate versus $(S_{\text{COM},c})_b$;
 (a) crystal growth on glass and on healthy MDCK cells,
 (b) crystal growth on HCl treated MDCK cells,
 (c) crystal growth on papain treated MDCK cells.

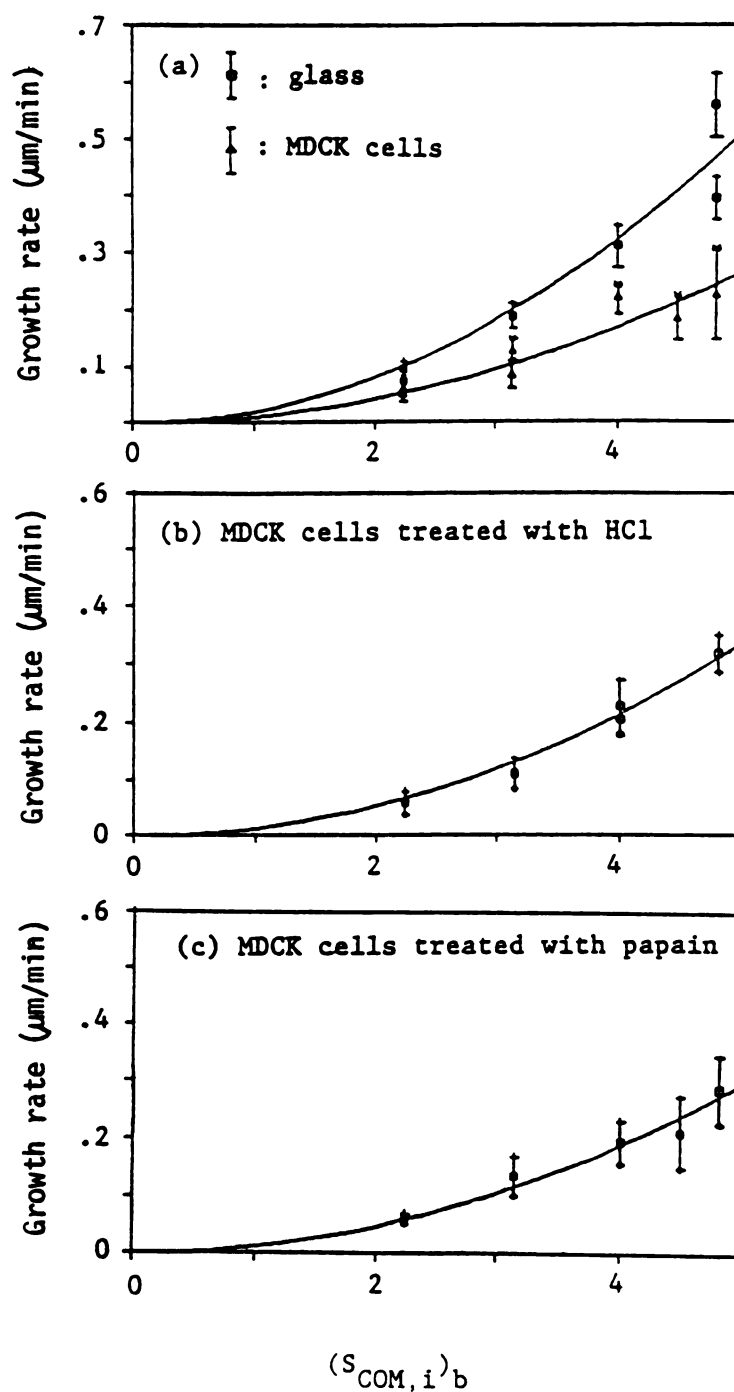


Figure 5-19 Growth rate versus $(S_{\text{COM},i})_b$;
 (a) crystal growth on glass and on healthy MDCK cells,
 (b) crystal growth on HCl treated MDCK cells,
 (c) crystal growth on papain treated MDCK cells.

Confidence in the above results was tested according to the Student's-t test described by Steel and Torrie (1960). The rate constants of crystal growth correlated with $(S_{COM,c})_b$ along with the upper and lower bounds of a 90% confidence interval are shown in Figure 5-20. The growth rate inhibition from healthy MDCK cells over that from HCl-treated or papain-treated cells was not dramatic. However, inhibition of growth by healthy MDCK cells over growth on glass was significant.

The growth rate result for crystals growing on glass may be compared with previous work. DeLong (1988) reported growth rate constants for three faces of COM growth using the second order growth rate correlation as per Equation (5-18). The rate constants were 0.0238, 0.00777, and 0.0109 for 110, 010, and 101 crystal faces. The rate constant (0.0201) obtained in this work for crystals growing on a glass surface (Table 5-7) is consistent with DeLong's result.

5-5-4-2. Effects of Heparin

The addition of heparin, a model urinary biopolymer, had a distinct inhibitory effect on COM growth. Figure 5-21 shows the inhibition of COM crystal growth on untreated MDCK cells by heparin. This result is the same as that found by DeLong (ibid) for COM growth on glass surfaces.

Since the concentration of heparin added in the experimental solution was not in a great enough amount to cause significant complexation with calcium or oxalate ions, the marked inhibitory effect of heparin on COM growth rate may not be explained by the decrease of calcium oxalate supersaturation due to the addition of heparin. The inhibition of crystal growth rate is likely due to the adsorption of heparin on crystal surface which retards calcium oxalate ion

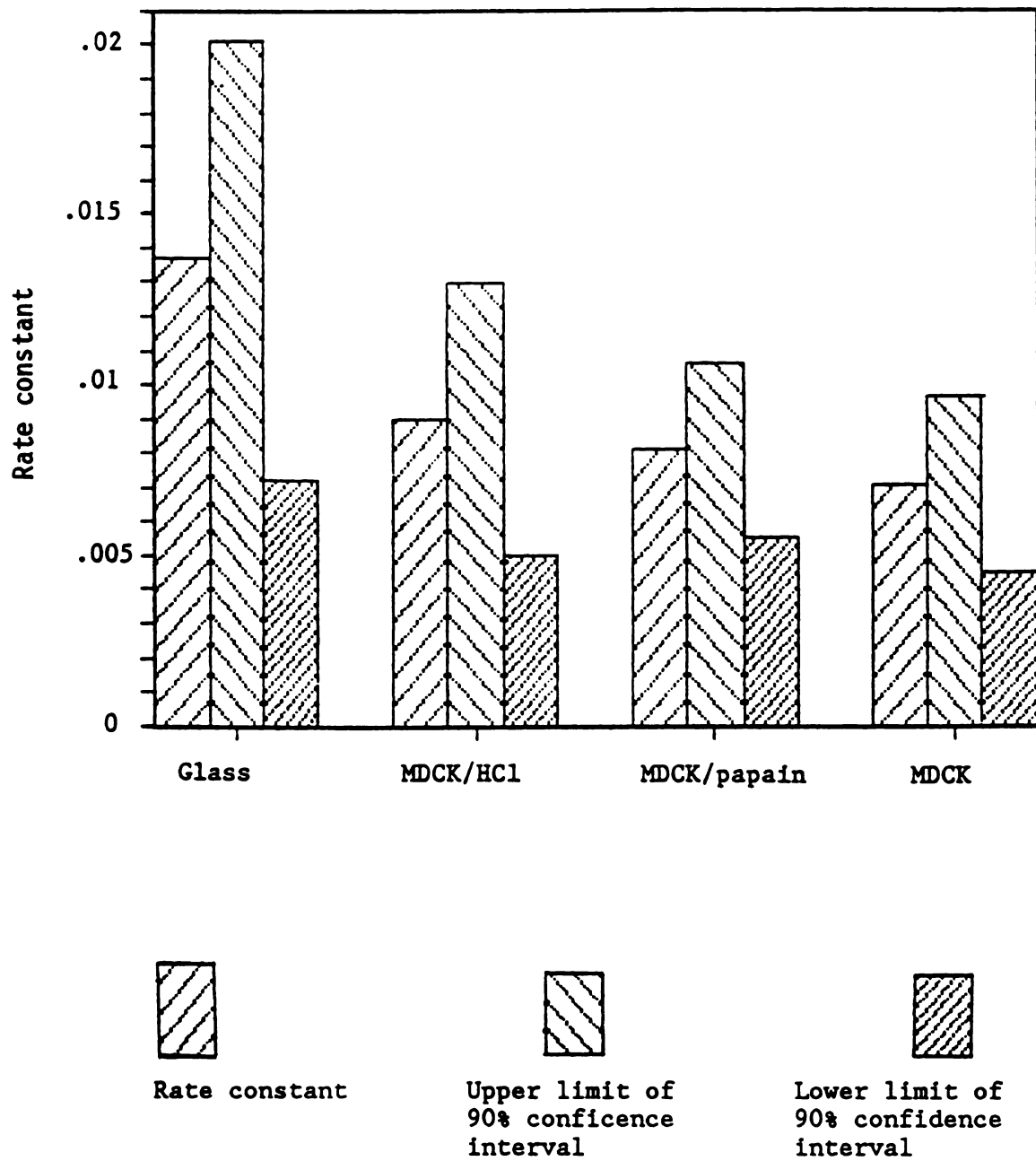


Figure 5-20 Comparison of growth rates at any constant ($S_{COM,c}$)_b.

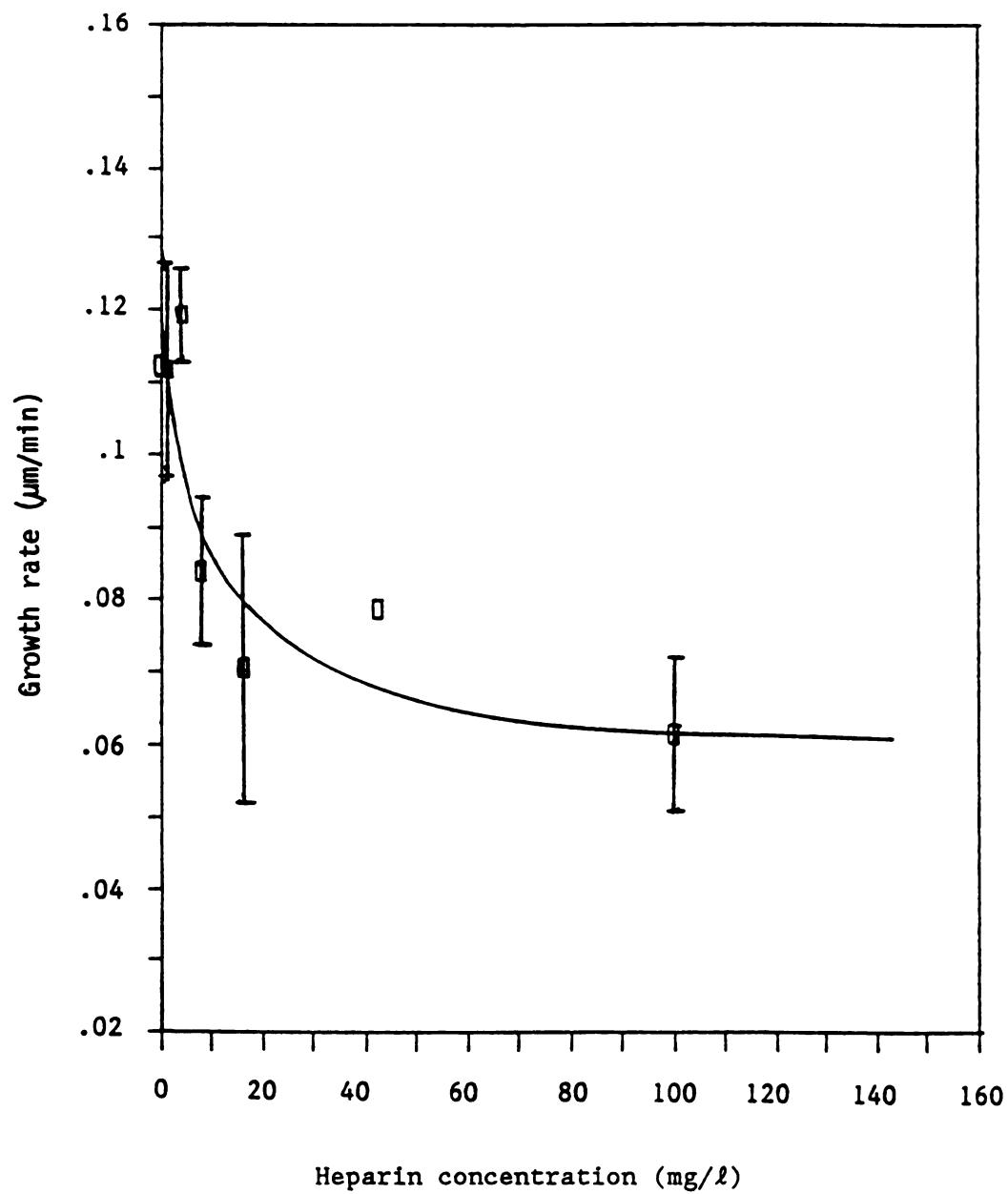


Figure 5-21 Inhibition of COM crystal growth on MDCK cells by heparin;
 $T_{Ca} = T_{Ox} = 1.0$ mM.

incorporation into the crystal lattice. If the growth rate of COM crystals, G , is proportional to the total crystal surface uncovered by heparin and the total crystal surface on which heparin is adsorbed is proportional to the concentration of heparin, $[\text{heparin}]$, then

$$G = G_0 (1 - k_{\text{ads}}[\text{heparin}]) \quad (5-19)$$

where G_0 is the crystal growth rate in the absence of heparin additive, G is the growth rate in the presence of heparin, and k_{ads} is the proportionality constant relating the fractional coverage of crystal surface to the concentration of heparin. Equation (5-19) may be rearranged to give

$$\frac{G_0}{G_0 - G} = \frac{1}{k_{\text{ads}}[\text{heparin}]} \quad (5-20)$$

The growth rate data read from the solid line in Figure 5-21 were replotted in Figure 5-22 in the form of $G_0/(G_0 - G)$ versus $1/[\text{heparin}]$. The linear relationship between $G_0/(G_0 - G)$ and $1/[\text{heparin}]$ in Figure 5-22 indicates that the inhibitory effect of heparin on calcium oxalate crystals is due to a saturation or adsorption-like phenomenon on the crystal surface; the adsorption of heparin follows a Langmuir adsorption isotherm mode.

5-5-5. Experimental Results and Stone Formation Hypothesis

Observations of calcium oxalate crystal formation and growth rate results from above suggest a biopolymer-inhibition hypothesis for urinary stone formation in vivo. For the growth inhibition in the presence of MDCK cells, a biopolymeric inhibitor of the type similar to sulfated glycosaminoglycans such as heparin that consists of negatively charged carboxylate and/or sulfate groups may be present on the surface

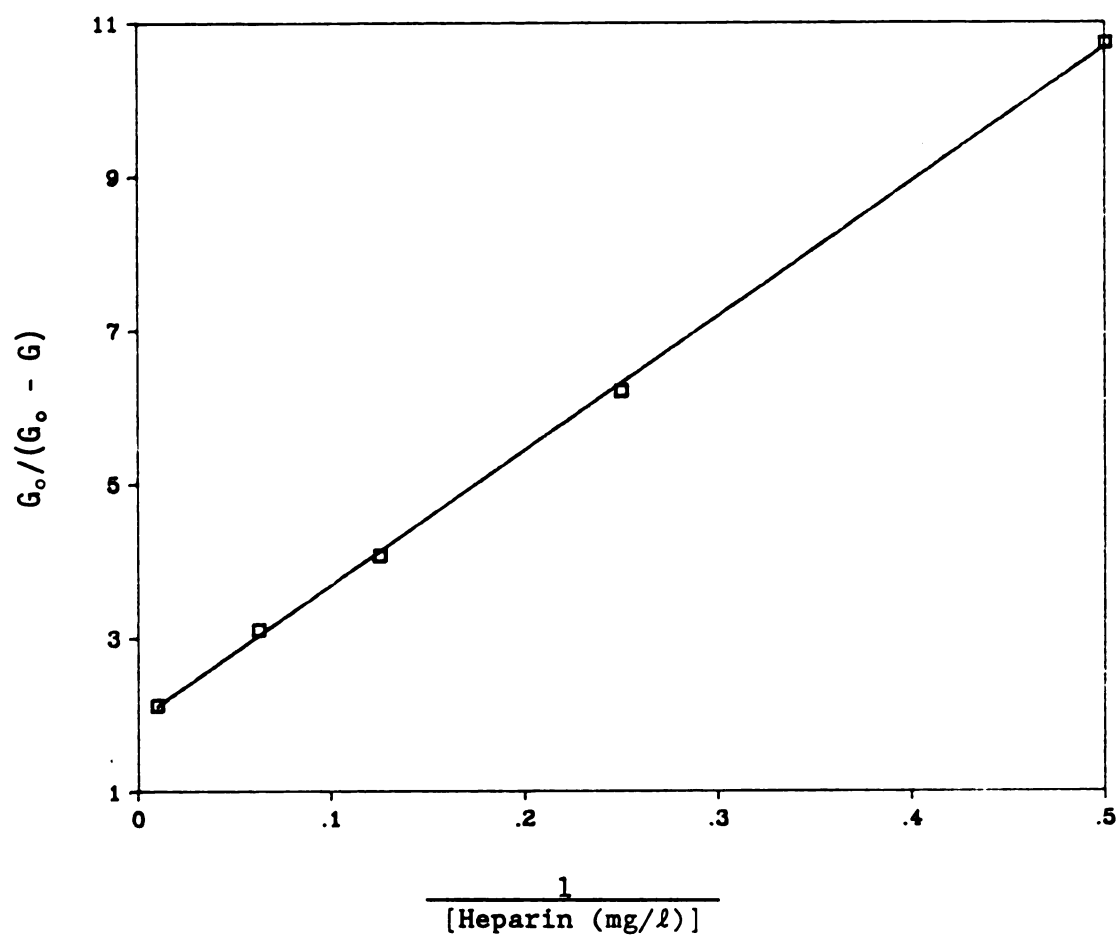


Figure 5-22 Inhibitory effect of heparin on COM crystal growth follows Langmuir adsorption isotherm.

of MDCK epithelial cells; this may interfere with the growth process. Biopolymer molecules may incorporate in the crystal lattice and change the crystal habit so that crystals become less transparent (see Figure 5-11). This biopolymer may be part of a structural protein on the MDCK cell membrane or a substance secreted from the cells. Chemical treatment of the MDCK cells may either destroy the active inhibitor structure on cell surface or close or disturb secretion of the active inhibition substance from the cell so that crystal growth on HCl- or papain-treated cells is less inhibited than growth on healthy cells. The inhibitor present in the solution, e.g., heparin, affects crystal growth more dramatically but in a similar fashion probably because the effective biopolymer concentrations in solution are greater than those on the tissue surfaces.

Nucleation on epithelial surfaces may also be affected by a biopolymeric substance. The absence or presence of the biopolymer around the rounded, unhealthy cells may be the cause of more nucleation around these cells. At the present time, the exact effect of HCl on epithelial cells is not understood; however, the distinct inhibition of nucleation on HCl-treated cells is not likely to be due to the presence of an excess of biopolymer. Nucleation inhibition would probably be caused by the removal of nucleation sites on epithelial surfaces by HCl. Dr. Robert Roth, a pharmacologist in the Department of Veterinary Medicine, has suggested that HCl might completely strip the cell surface of all proteins, glycoproteins, or other biopolymers. The cell appearance in the photomicrographs and the lower degree of inhibition of crystal growth rate on HCl-treated cells than by papain-treated or untreated cells are strong evidence for this hypothesis.

From the above results and discussions, it appears that both tissue surface and solution composition play important roles in nucleation and growth of COM crystals. Since crystal nucleation depends greatly upon availability of nucleation sites and biopolymers may actively interfere with both nucleation and crystal growth, kidney tissue injury or the lack of nucleation inhibitors may be the first step in early stages of stone formation. Once the crystal nidus is formed, it may provide sites for crystal growth where crystal growth takes place in a relatively lower supersaturation than crystal nucleation. The nidus on a tissue surface may also be available for attachment of other small crystals formed from upstream in the urinary tubule due to crystal affinity for aggregation or due to clogging of the urinary tract from the existing nidus. The absence of protection from biopolymer inhibitors in urinary fluid or on tissue surfaces may result in the growth of kidney stones to sizes that become physiological problem.

CHAPTER 6

SUMMARY, CONCLUSIONS, AND RECOMMENDATIONS

6-1. Summary and Conclusions

This study of calcium oxalate crystallization was undertaken to develop a fundamental understanding of the physical and chemical mechanisms of kidney stone formation. The important aspects of this work are summarized and conclusions from the work are presented in this section.

The driving force for the crystallization process was quantified by the calculation of supersaturation of calcium oxalate in solution. The supersaturation was defined in two forms: in terms of the concentrations of calcium and oxalate ions and in terms of the concentration of calcium oxalate complex species for each hydrate phase. The concentrations of calcium and oxalate ion species and of the associated calcium oxalate complex were calculated with computer programs by assuming an equilibrium state among all the free ions and the associated species in the solution.

Calcium oxalate crystallization was studied with a MSMPR crystallizer and with a flow chamber crystallizer. The MSMPR crystallizer allowed determination of free-solution phenomenon of calcium oxalate crystallization and the flow chamber crystallizer allowed study of crystal-tissue interactions. For the work conducted with the MSMPR crystallizer, particle size distribution (PSD) of the suspension sample was one of the major properties characterizing calcium oxalate crystallization. A particle sizing instrument, the ELZONE^(R) particle data analyzer (Particle Data, Inc.), was used to size the particles for the determination of PSD. The instrument counted data were correlated to PSD; limitations of the ELZONE^(R)

system were found. Because of these limitations, the implementation of the ELZONE's data analysis was modified for obtaining reliable PSD data. A modified calibration procedure was also developed for an improved understanding of the basis for the calibration procedure. This modified calibration procedure offers a more straightforward determination of the calibration constants than the original technique provided by the ELZONE^(R) manufacturer. Calibrations of the ELZONE^(R) system were conducted to show the validity of the modified calibration procedure and the "Normalize" function of the instrument's operation.

Calcium oxalate crystallization in the MSMPR crystallizer was characterized by the determination of particle size distributions and the total calcium concentration in the suspension and in the filtrate. Crystal hydrates and crystal phases were identified with x-ray diffractometry and optical microscopy. The results show that calcium oxalate trihydrate was the major hydrate formed in the reactor for the calcium and oxalate feed concentrations above 2 mM. Calcium oxalate monohydrate formed at 1 mM calcium and oxalate concentrations. Addition of PGA (with calcium and oxalate concentrations 2 mM) favored the formation of calcium oxalate dihydrate and monohydrate.

From the measurement of PSD and calcium concentrations with time, the crystallization process in the MSMPR was characterized by unsteady state, quasi-steady state, and steady state periods. Crystal aggregation, nucleation, and crystal growth occurred in the unsteady state region. Crystal aggregation and nucleation decreased as crystallization progressed with time. At steady state, crystal growth was the only significant mechanism in the crystallizer. The unsteady state MSMPR crystallizer operation was of interest because of the

ultimate goal of understanding crystal aggregation mechanism as well as the crystal growth mechanism.

For the unsteady state period in which crystal aggregation and crystal growth were superimposed, an isolation approach for determining crystal growth rate was developed based on shifts of PSDs along the x-axis (particle size) with time. The growth rate for the entire MSMPR crystallizer operation, including unsteady state and steady state, were obtained. The growth rate results were compared with other growth rate data and with other MSMPR crystallizer work modeled with linear population density analysis. A good correlation was observed. The growth rate for the process was correlated linearly with supersaturation calculated from the calcium concentration in the filtrate. The correlation is written in the form:

$$G_L = k \times \text{supersaturation} \quad (4-3)$$

where G_L is the linear growth rate and k is the growth rate constant.

The addition of PGA, a model urinary biopolymer, in the MSMPR crystallizer experiments increased the total crystal retention and supersaturation in the reactor, and reduced crystal growth rate. The biopolymer PGA was thought to affect the calcium oxalate crystallization by adsorbing on the crystals and inhibit crystal growth units from integrating into the crystal lattice. Low crystal growth rate in the crystallizer in the case of PGA addition results in higher supersaturation, which may generate bursts of nucleation and be the reason for the wave-like appearance observed in the PSD data. The inhibitory PGA adsorption on crystal surface may also prevent crystal deposition on the wall of crystallizer; as a result, the total crystal retention in the reactor is higher.

The flow chamber crystallizer experiments were conducted to investigate the effects of both healthy and injured cultured epithelium (Maden Darby Canine Kidney (MDCK) cells) on the growth of calcium oxalate single crystals in the presence of flow shear. Chemical injury by HCl and by papain was used to simulate histological damage. The healthy MDCK cells was found to inhibit crystal nucleation. The calcium oxalate monohydrate (COM) crystal growth rates decreased in the following order: crystal growth on glass > MDCK cells treated with HCl > MDCK cells treated with papain > healthy MDCK cells. The biopolymer additive, heparin, exhibited inhibition on COM crystal growth in the presence of healthy MDCK cells. Inhibition may also be due to the adsorption of the negatively charged biopolymer on the crystal surface.

The growth rate obtained from the MSMPR crystallizer experiment is approximately twice of the growth rate resulted from the flow chamber crystallizer experiment. The growth rate constants resulting from these two experimental systems for the uninhibited COM crystal growth are 0.037 (Table 4-4, $[Ca^{2+}] = [C_2O_4^{2-}] = 1 \text{ mM}$) and 0.0137 (Table 5-8, crystal growth on glass surface) for the correlations with $S_{COM,c}$. The lower growth rate constant for the flow chamber crystallizer may be due to a certain degree of mass transfer resistance in the laminar flow, while the MSMPR crystallizer was substantially turbulent. The supersaturation in the MSMPR crystallizer was calculated from the calcium concentration in the filtrate. Because of the unavoidable time delay in filtration, the calcium concentration and supersaturation may be underestimated, which also results in a higher rate constant observed for the crystal growth in the MSMPR crystallizer.

From this study, the paucity of kidney stone formation in healthy individuals may be understood as follows: inhibitory effect of healthy

MDCK cells on crystal nucleation and crystal growth and the inhibitory effect of PGA and heparin on crystal growth suggest a membrane-crystal interaction via some biopolymers on the epithelial surface or in solution that prevent stone formation. Since stone-formers seem to be lacking these biopolymers, they also lack the stone formation inhibitors. A crystal-membrane interaction with damaged kidney epithelium may also be the precursor to stone formation.

6-2. Recommendations for Future Research

Suggestions for the future research are:

1. Using the growth rates obtained in the MSMPR crystallizer experiments in the study of crystal aggregation with numerical analysis.
2. Testing of other biopolymers on crystal growth and crystal aggregation model to understand kidney stone formation.
3. Finding the mass transfer coefficients for calcium oxalate, so that the growth rate in the flow chamber crystallizer may be characterized with known mass transfer resistance. In this case, the growth rate correlations with the two supersaturation definitions may be discerned one from the other.

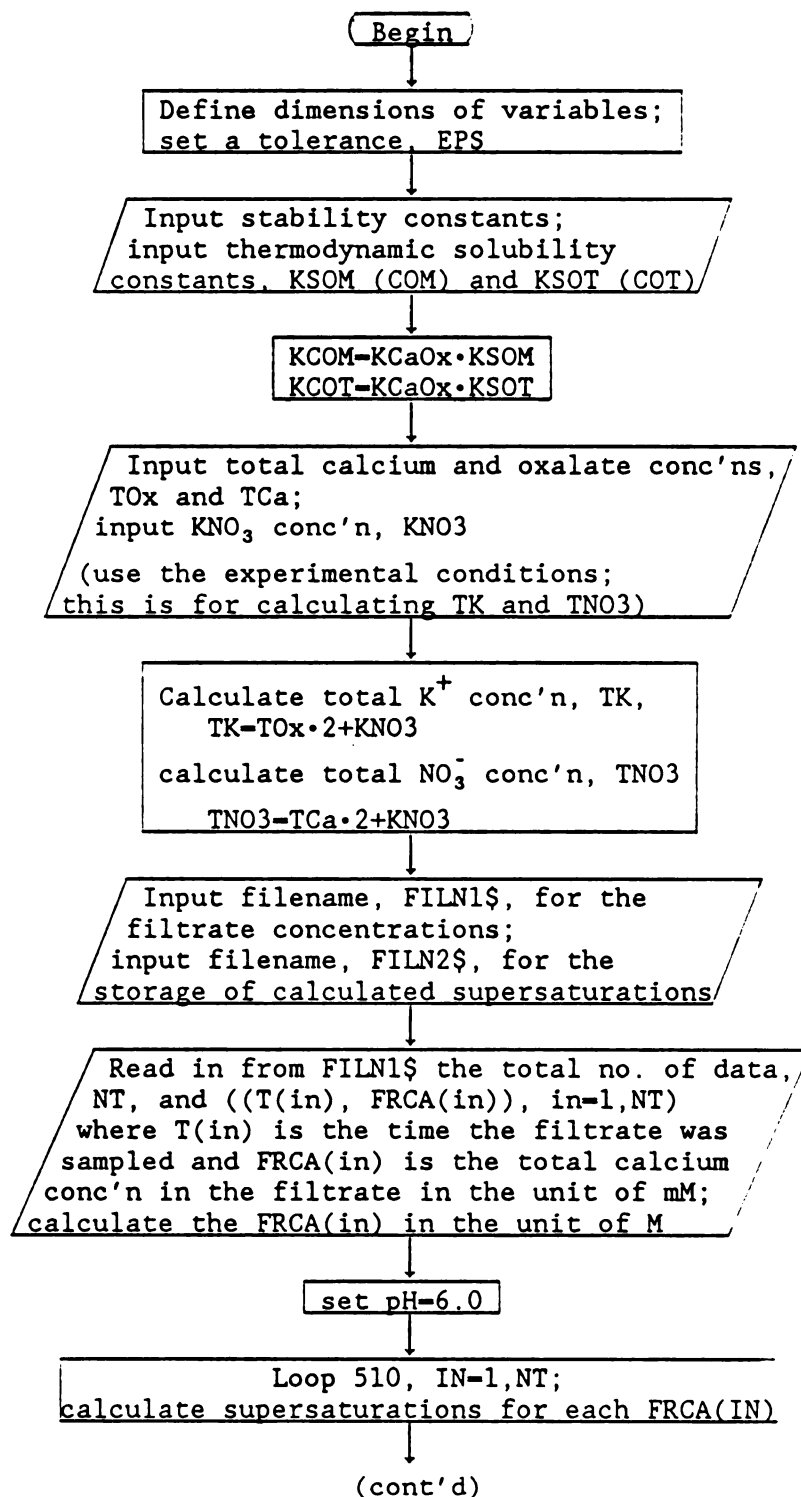
APPENDICES

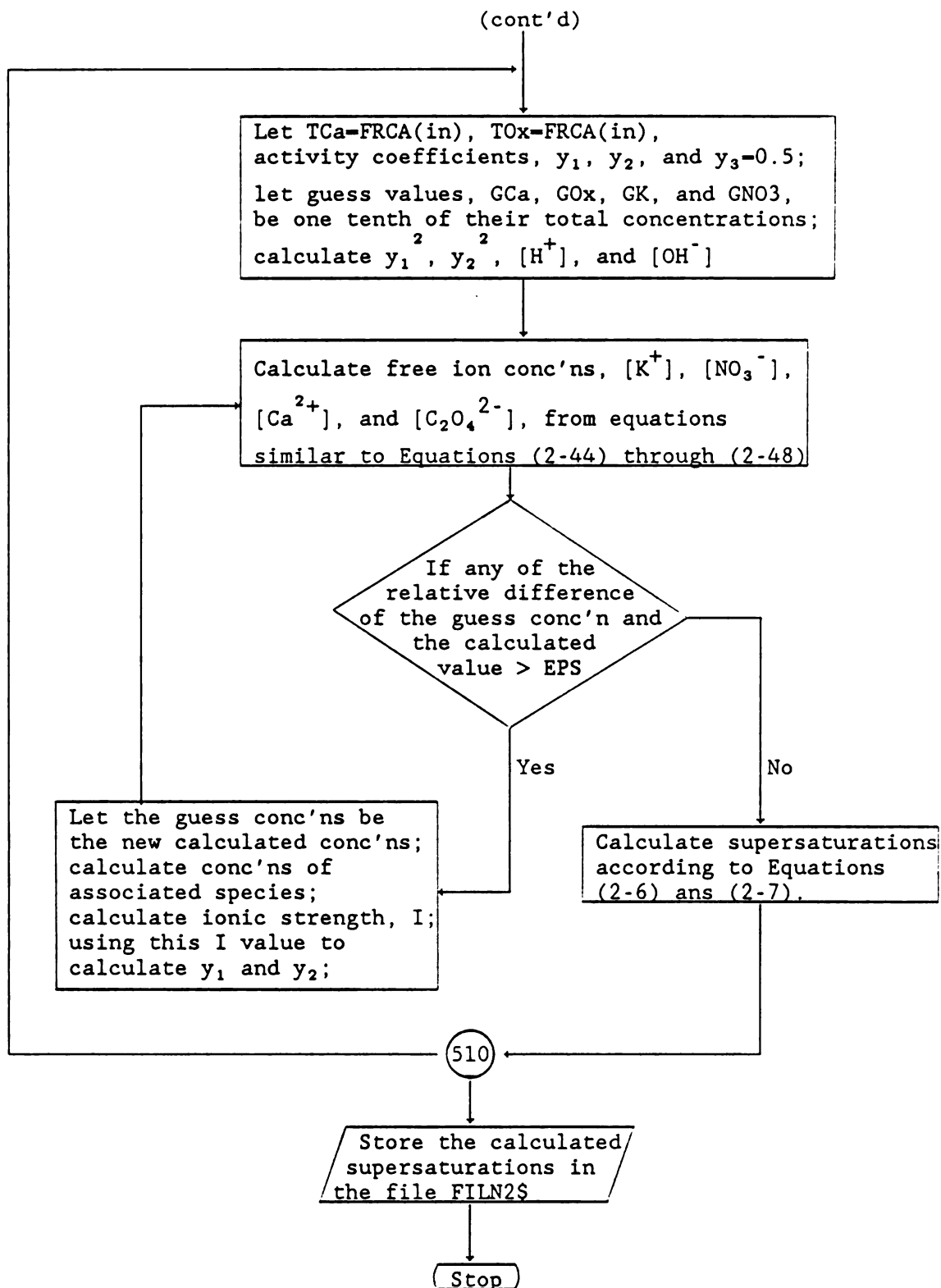
APPENDIX A

EQUIL COMPUTER PROGRAMS

Two EQUIL computer programs were written in BASICA to calculate calcium oxalate supersaturations for the experimental conditions in this work as described in Chapter 2. Program EQUIL-NA.BAS was written for the solutions used in the MSMPR crystallizer experiments (Chapter 4), which contain $\text{Ca}(\text{NO}_3)_2$, $\text{K}_2\text{C}_2\text{O}_4$, and the ionic strength buffer KNO_3 . The other program EQUIL-M7.BAS was written for the modified medium used in the study of crystal growth on MDCK cells (Chapter 5). The modified medium contains CaCl_2 , $\text{Na}_2\text{C}_2\text{O}_4$, KCl , NaCl , and D-glucose. D-glucose was assumed not to affect the solution supersaturation through complexation. The flow diagram of EQUIL-NA.BAS and program listings of EQUIL-NA.BAS and EQUIL-M7.BAS are shown in the following. The flow diagram of EQUIL-M7.BAS is similar to the flow diagram of EQUIL-NA.BAS. The latter is shown as an example.

Flow Diagram of EQUIL-NA.BAS





Listing of EQUIL-NA.BAS

```

10 CLS:PRINT "PROGRAM: EQUIL-NA, (EQUIL-KNO3 SYSTEM)":PRINT SPC(10)
"Calculate SCOM and SCOT for the filtrates from MSMPR":PRINT:PRINT
STRING$(50,61):PRINT
20 DIM T(20),FRCA(20),SCOMC(20),SCOTC(20),SCOMI(20),SCOTI(20)
30 EPS=.0001
40 KHOX=21008.74
50 KKOX=10!
60 KCAOX=1869
70 KCA2OX=71.6
80 KCAOX2=17.3
90 KH2O=1/3.8905E+13
100 KH2OX=19.12
110 KCAOH=29.5
120 KCAHOX=64.592
130 KCAHOX2=312.8
140 KHNO3=4.938556E-02
150 KCANO3=4.7863
160 KKNO3=.47863
170 KSOM=2.514E-09
180 KSOT=7.88E-09
190 KCOM=KCAOX*KSOM
200 KCOT=KCAOX*KSOT
210 INPUT "Ca(NO3)2 (M) = ";TCA
220 INPUT "K2Ox (M) = ";TOX
230 INPUT "KNO3 (M) = ";KNO3
240 TK=TOX*2+KNO3
250 TNO3=TCA*2+KNO3
260 INPUT "Filename for filtrate concentrations";FILN1$
270 INPUT "Filename for output results";FILN2$
280 OPEN FILN1$ FOR INPUT AS #1
290 INPUT #1,NT:FOR IN=1 TO NT:INPUT
#1,T(IN),FRCA(IN):FRCA(IN)=FRCA(IN)*.001:NEXT:CLOSE
300 PH =6!
320 FOR IN=1 TO NT:TCA=FRCA(IN):TOX=FRCA(IN)

```

```

330 F1=.5:F2=.5:F3=.5
340 GCA=TCA*.1:GOX=TOX*.1:GK=TK*.1:GNO3=TNO3*.1
350 IT=1
360 F11=F1*F1
370 F22=F2*F2
375 FH=10^(-PH)/F1:FOH=10^(LOG(KH2O)/LOG(10)+PH)/F1
380 FK=TK/(1+KKN03*GNO3*F11+KKOX*GOX*F2)
390 FRNO3=TNO3/(1+KHNO3*FH*F11+KKN03*GK*F11+KCAN03*GCA*F2)
400 FCA=TCA/(1+KCAOX*GOX*F22+KCAOH*FOH*F2+KCAHOX*KHOX*FH*GOX*F22+KCAHOX
2*(KHOX*FH*GOX*F2*F1)^2*F2+2*KCAOX*KCA2OX*GCA*GOX*F22+KCAOX2*KCAOX*GOX^
2*F22+KCAN03*GNO3*F2)
410 FOX=TOX/(1+KHOX*FH*F2+KCAOX*GCA*F22+KCAHOX*KHOX*GCA*FH*F22+2*KCAHOX
2*(KHOX*FH*F1*F2)^2*GCA*GOX*F2+KCAOX*KCA2OX*GCA^2*F22+2*KCAOX2*KCAOX*GC
A*GOX*F22+KHOX*KH2OX*FH
420 IF ABS((GCA-FCA)/FCA)>EPS GOTO 550
430 IF ABS((GOX-FOX)/FOX)>EPS GOTO 550
440 IF ABS((GK-FK)/FK)>EPS GOTO 550
450 IF ABS((GNO3-FRNO3)/FRNO3)>EPS GOTO 550
460 CAOX=KCAOX*FCA*FOX*F22
470 SCOMC(IN)=CAOX/KCOM-1
480 SCOTC(IN)=CAOX/KCOT-1
490 SCOMI(IN)=(SQR(FCA*FOX*F22)-SQR(KSOM))/SQR(KSOM)
500 SCOTI(IN)=(SQR(FCA*FOX*F22)-SQR(KSOT))/SQR(KSOT)
510 NEXT IN
520 OPEN FILN2$ FOR OUTPUT AS #2
530 FOR I=1 TO NT:PRINT #2,T(I),FRCA(I),SCOMC(I),SCOTC(I),SCOMI(I),
SCOTI(I):NEXT:CLOSE
540 END
550 HOX=KHOX*FH*FOX*F2
560 CAOH=KCAOH*FCA*FOH*F2
570 CAOX=KCAOX*FCA*FOX*F22
580 CAHOX=KCAHOX*FCA*HOX*F2
590 CAOX2=KCAOX2*CAOX*FOX
600 CA2OX=KCA2OX*CAOX*FCA
610 KOX=KKOX*FK*FOX*F2
620 CANO3=KCANO3*FCA*FRNO3*F2
630 IS=(FH+FOH+FK+FRNO3+HOX+CAOH+CAHOX+KOX+CANO3+(FCA+FOX+CAOX2+CA2OX)

```

```

*4)/2
640 FOR I=0 TO 1:FF(I)=10^(-.523*(I+1)^2*(SQR(IS)/(1+SQR(IS))-.3*IS)):
NEXT
650 F1=FF(0):F2=FF(1):GCA=FCA:GOX=FOX:GK=FK:GNO3=FRNO3:IT=IT+1:GOTO 360

```

Listing of EQUIL-M7.BAS

```

10 CLS:PRINT "PROGRAM: EQUIL-M7, (EQUIL-MEDIUM7, MODIFIED EARLE'S
MEDIUM, Version 7)":PRINT "(TCA=TOX, with varied TCA)":PRINT:PRINT
STRING$(70,61):PRINT
20 DEFDBL A-G,K,P,S,T:DEFINT I,N
30 DIM ATCA(400),ACA(400),AOX(400),SCOMC(400),SCOTC(400),SCOMI(400),
SCOTI(400),AF2(400),IIT(400)
40 EPS=.0001
50 KHOX=21008.74
60 KKOX=10#
70 KCAOX=1869
80 KCA2OX=71.6
90 KCAOX2=17.3
100 KH2O=1/3.8905E+13
110 KH2OX=19.12
120 KCAOH=29.5
130 KCAHOX=64.592
140 KCAHOX2=312.8
150 KNAOX=13.3
160 KNACL=.3981072
170 KKCL=.1737801
180 KSOM=2.514E-09
190 KSOT=7.88E-09
200 KCOM=KCAOX*KSOM
210 KCOT=KCAOX*KSOT
220 INPUT "Concentrations of CaCl2 and Na2Ox (M) vary from";TCAI
230 INPUT "How many values of concentrations to be calculated
(<=401)";NC
240 INPUT "Constant concentration difference=";DC
250 INPUT "Filename for data storage (Maxmium 7 letters)";FILEN$

```

```

260 PRINT:PRINT "Program is running.  Please wait!"
270 TK=5.88331E-03:PH=7.2
280 FOR N=0 TO NC-1:TCA=TCAI+DC*N
290 TOX=TCA:TNACL=.15741706#-2*TCA
300 F1=.5:F2=.5:F3=.5
310 TNA=TOX*2+TNACL
320 TCL=TCA*2+TK+TNACL
330 GCA=TCA*.1:GOX=TOX*.1:GK=TK*.1:GNA=TNA*.1:GCL=TCL*.1
340 FH=10^(-PH)/F1
350 FOH=10^(LOG(KH2O)/LOG(10)+PH)/F1
360 IT=1
370 F11=F1*F1
380 F22=F2*F2
390 FK=TK/(1+KKCL*GCL*F11+KKOX*GOX*F2)
400 FRNA=TNA/(1+KNACL*GCL*F11+KNAOX*GOX*F2)
410 FCL=TCL/(1+KNACL*GNA*F11+KKCL*GK*F11)
420 FCA=TCA/(1+KCAOX*GOX*F22+KCAOH*FOH*F2+KCAHOX*KHOX*FH*GOX*F22+KCAHOX
2*(KHOX*FH*GOX*F2*F1)^2*F2+2*KCAOX*KCA2OX*GCA*GOX*F22+KCAOX2*KCAOX*GOX^
2*F22)
430 FOX=TOX/(1+KHOX*FH*F2+KCAOX*GCA*F22+KCAHOX*KHOX*GCA*FH*F22+2*KCAHOX
2*(KHOX*FH*F1*F2)^2*GCA*GOX*F2+KCAOX*KCA2OX*GCA^2*F22+2*KCAOX2*KCAOX*GC
A*GOX*F22+KHOX*KH2OX*FH
440 IF ABS((GCA-FCA)/FCA)>EPS GOTO 620
450 IF ABS((GOX-FOX)/FOX)>EPS GOTO 620
460 IF ABS((GK-FK)/FK)>EPS GOTO 620
470 IF ABS((GNA-FRNA)/FRNA)>EPS GOTO 620
480 IF ABS((GCL-FCL)/FCL)>EPS GOTO 620
490 ATCA(N)=TCA
500 CAOX=KCAOX*FCA*FOX*F22
510 SCOMC(N)=CAOX/KCOM-1
520 SCOTC(N)=CAOX/KCOT-1
530 SCOMI(N)=(SQR(FCA*FOX*F22)-SQR(KSOM))/SQR(KSOM)
540 SCOTI(N)=(SQR(FCA*FOX*F22)-SQR(KSOT))/SQR(KSOT)
542 ACA(N)=FCA:AOX(N)=FOX
550 AF2(N)=F2:IIT(N)=IT:NEXT N
560 OPEN FILEN$+"a.csv" FOR OUTPUT AS #2:FOR I=0 TO NC-1:PRINT
#2,ATCA(I) ", " SCOMC(I):NEXT:PRINT #2,"END,DATA":CLOSE

```

```

570 OPEN FILEN$+"b.csv" FOR OUTPUT AS #2:FOR I=0 TO NC-1:PRINT
#2,ATCA(I) "," SCOTC(I):NEXT:PRINT #2,"END,DATA":CLOSE
580 OPEN FILEN$+"c.csv" FOR OUTPUT AS #2:FOR I=0 TO NC-1:PRINT
#2,ATCA(I) "," SCOMI(I):NEXT:PRINT #2,"END,DATA":CLOSE
590 OPEN FILEN$+"d.csv" FOR OUTPUT AS #2:FOR I=0 TO NC-1:PRINT
#2,ATCA(I) "," SCOTI(I):NEXT:PRINT #2,"END,DATA":CLOSE
600 OPEN FILEN$+"e.csv" FOR OUTPUT AS #2:FOR I=0 TO NC-1:PRINT
#2,ATCA(I) "," AF2(I):NEXT:PRINT #2,"END,DATA":CLOSE
610 OPEN FILEN$+"f.csv" FOR OUTPUT AS #2:FOR I=0 TO NC-1:PRINT
#2,ATCA(I) "," IIT(I):NEXT:PRINT #2,"END,DATA":CLOSE
612 OPEN FILEN$+"g.csv" FOR OUTPUT AS #2:FOR I=0 TO NC-1:PRINT
#2,ATCA(I) "," ACA(I):NEXT:PRINT #2,"END,DATA":CLOSE
614 OPEN FILEN$+"h.csv" FOR OUTPUT AS #2:FOR I=0 TO NC-1:PRINT
#2,ATCA(I) "," AOX(I):NEXT:PRINT #2,"END,DATA":CLOSE:END
620 CHOX=KHOX*FH*FOX*F2
630 CAO=KCAO*FCA*FOH*F2
640 CAOX=KCAOX*FCA*FOX*F22
650 CAHOX=KCAHOX*FCA*CHOX*F2
660 CAOX2=KCAOX2*CAOX*FOX
670 CA2OX=KCA2OX*CAOX*FCA
680 KOX=KKOX*FK*FOX*F2
690 CNAOX=KNAX*FRNA*FOX*F2
700 SI=(FH+FOH+FK+FRNA+FCL+CHOX+CAOH+CAHOX+KOX+CNAOX+(FCA+FOX+CAOX2
+CA2OX)*4)/2
710 FOR I=0 TO 1:FF(I)=10^(-.523*(I+1)^2*(SQR(SI)/(1+SQR(SI))-.3*SI)):
NEXT I
720 F1=FF(0):F2=FF(1):GCA=FCA:GOX=FOX:GK=FK:GNA=FRNA:GCL=FCL:IT=IT+1:
GOTO 370

```

APPENDIX B

CALIBRATION DATA OF THE ELZONE^(R) SYSTEM AND THEIR APPLICATIONS

This appendix consists of the calibration data of the ELZONE^(R) particle data analyzer and will briefly review the applications of these calibration data to the practical operation of the instrument.

The calibration and particle size measurement of the ELZONE^(R) system are strongly influenced by the current-trim control setting. Since changing the current-trim control setting requires a new calibration for the instrument (Particle Data, (a)), the current trim setting was set at 52 for all the calibrations and sample measurements in this work. Calibrations of the ELZONE^(R) system for several aperture tubes and some log span settings were conducted following the modified calibration procedure described in Chapter 3. The data obtained directly from calibration are the slope and intercept of the regression line of the (I+G) values versus the recorded median channels (Equation (3-32)) for the calibration particles of size D_{std} . From the slope and intercept, the (I+G) value at channel 128, $(I+G)_{128}$, and the true log span, L_s , may be calculated from Equations (3-32) and (3-35), respectively. The L_s and $(I+G)_{128}$ values thus obtained are listed in Table B-1.

To obtain the sizes of each counting channel for a specific aperture tube and log span setting used in particle size measurement, the appropriate L_s and $(I+G)_{128}$ values may be chosen from Table B-1. With known (I+G) value, the particle size of each counting channel may be calculated from Equation (3-36).

In the operation of the instrument, the choice of proper log span, current, and gain settings was found to be difficult. Tables B-2

through B-6 were prepared to gain a broad view of the variation of size ranges with respect to the I and G settings for a particular aperture tube and log span setting. The lower and upper size (equivalent spherical diameter) limits, D_z and D_f , of the counted particles were calculated according to Eq. (3-36) with the channel number, ch , equal to 1 and 128.

Small debris in the electrolyte solution or the electronic interference may also be counted as particles, called noise, in particle size measurement. The noise usually overwhelms the first few channels in the small size range. Therefore, the actual lower size limit is larger than the particle size of the first channel, D_z . The D_z and D_f values shown in Tables B-2 through B-6 may serve as ideal maximum sizing windows for particle counting.

The measuring range for a selected aperture tube as provided by the instrument's manufacturer is 1.5-3% to 40-50% of the diameter of the orifice on the aperture tube, D_{ap} . On the other hand, 5% to 20% of the aperture diameter is the suggested range for standard particles used in calibration. Therefore, 2%, 5%, 20%, 40%, and 50% of the diameter of the aperture tubes are also included in Tables B-2 through B-6.

Table B-1 Calibration constants with current-trim
control setting = 52.

Aperture:	76 μm (D_{ap})		
D_{std} :	10 μm (13.6% D_{ap})		
Log span setting:	10	12	14
Ls:	10.018558	11.94107	13.645753
(ItG) ₁₂₈ :	11.835012	11.888911	11.837729
Aperture:	95 μm (D_{ap})		
D_{std} :	10 μm (10.53% D_{ap})		
Log span setting:	8	10	12
Ls:	7.9995131	9.9590889	11.972443
(ItG) ₁₂₈ :	9.7976095	12.856577	12.894593
Aperture:	150 μm (D_{ap})		
D_{std} :	20.27 μm (13.51% D_{ap})		
Log span setting:	10	12	14
Ls:	10.070323	11.973205	13.741679
(ItG) ₁₂₈ :	11.993836	12.029075	11.956434
Aperture:	300 μm (D_{ap})		
D_{std} :	44.66 μm (14.89% D_{ap})		
Log span setting:	8	10	12
Ls:	8.0204586	10.105556	12.092228
(ItG) ₁₂₈ :	8.9026537	11.991407	12.029926
Aperture:	480 μm (D_{ap})		
D_{std} :	91.2 μm (19.0% D_{ap})		
Log span setting:	10	12	
Ls:	10.204376	12.174651	
(ItG) ₁₂₈ :	12.137953	12.163773	

Table B-2 Maximum sizing windows for 76 μ m aperture tube;
current-trim control setting = 52.

Aperture tube:		76 μm			
D _{std} :		10 μm (= 13.16% D _{ap})			

2% D _{ap} :		1.52 μm			
5% D _{ap} :		3.8 μm			
20% D _{ap} :		15.2 μm			
40% D _{ap} :		30.4 μm			
50% D _{ap} :		38.0 μm			

Log span setting:		10	12	14	
L _s :		10.018558	11.94107	13.645753	
(I+G) ₁₂₈ :		11.835012	11.888911	11.837729	

I+G	D _z	D _f	D _z	D _f	D _z D _f

3	7.61	77.01	4.94	77.97	3.29 77.06
3.5	6.78	68.61	4.40	69.47	2.93 68.65
4	6.04	61.12	3.92	61.89	2.61 61.16
4.5	5.38	54.45	3.49	55.14	2.33 54.49
5	4.79	48.51	3.11	49.12	2.07 48.54
5.5	4.27	43.22	2.77	43.76	1.85 43.25
6	3.80	38.50	2.47	38.99	1.65 38.53
6.5	3.39	34.30	2.20	34.73	1.47 34.32
7	3.02	30.56	1.96	30.94	1.31 30.58
7.5	2.69	27.23	1.75	27.57	1.16 27.24
8	2.40	24.26	1.56	24.56	1.04 24.27
8.5	2.13	21.61	1.39	21.88	.92 21.62
9	1.90	19.25	1.24	19.49	.82 19.26
9.5	1.69	17.15	1.10	17.37	.73 17.16
10	1.51	15.28	.98	15.47	.65 15.29
10.5	1.34	13.61	.87	13.78	--- ---
11	1.20	12.13	.78	12.28	--- ---
11.5	1.07	10.80	.69	10.94	--- ---

Table B-3 Maximum sizing windows for 95 μm aperture tube;
current-trim control setting = 52.

Aperture tube: 95 μm								
D _{std} : 10 μm (= 10.53% D _{ap})								

2% D _{ap} : 1.9 μm								
5% D _{ap} : 4.75 μm								
20% D _{ap} : 19.0 μm								
40% D _{ap} : 38.0 μm								
50% D _{ap} : 47.5 μm								

Log span setting: 8 10 12 14								
L _s : 7.9995131 9.9590889 11.972443 13.643723								
(I+G) ₁₂₈ : 9.7976095 12.856577 12.894593 12.870295								

I+G	Dz	Df	Dz	Df	Dz	Df	Dz	Df

2	9.54	60.60	---	---	---	---	---	---
2.5	8.50	53.98	---	---	---	---	---	---
3	7.58	48.09	---	---	---	---	---	---
3.5	6.75	42.85	8.70	86.87	5.51	87.64	3.73	87.15
4	6.01	38.17	7.75	77.39	4.91	78.08	3.32	77.64
4.5	5.36	34.01	6.91	68.95	4.38	69.56	2.96	69.17
5	4.77	30.30	6.15	61.43	3.90	61.97	2.63	61.62
5.5	4.25	26.99	5.48	54.72	3.47	55.21	2.35	54.90
6	3.79	24.05	4.88	48.75	3.09	49.18	2.09	48.91
6.5	3.37	21.42	4.35	43.44	2.76	43.82	1.86	43.57
7	3.01	19.09	3.88	38.70	2.46	39.04	1.66	38.82
7.5	2.68	17.00	3.45	34.47	2.19	34.78	1.48	34.58
8	2.39	15.15	3.08	30.71	1.95	30.98	1.32	30.81
8.5	2.13	13.50	2.74	27.36	1.74	27.60	1.17	27.45
9	1.89	12.02	2.44	24.38	1.55	24.59	1.05	24.45
9.5	1.69	10.71	2.18	21.72	1.38	21.91	.93	21.79
10	1.50	9.54	1.94	19.35	1.23	19.52	---	---
10.5	1.34	8.50	1.73	17.24	1.09	17.39	---	---
11	1.19	7.57	1.54	15.36	.97	15.49	---	---

Table B-4 Maximum sizing windows for 150 μm aperture tube;
current-trim control setting = 52.

Aperture tube:		150 μm					
D _{std} :		20.27 μm (= 13.51% D _{ap})					
<hr/>							
2% D _{ap} :		3.0 μm					
5% D _{ap} :		7.5 μm					
20% D _{ap} :		30.0 μm					
40% D _{ap} :		60.0 μm					
50% D _{ap} :		75.0 μm					
<hr/>							
Log span setting:		10		12		14	
L _s :		10.070323		11.973205		13.741679	
(I+G) ₁₂₈ :		11.993836		12.029075		11.956434	
<hr/>							
I+G	D _z	D _f	D _z	D _f	D _z	D _f	
<hr/>							
3	15.81	161.93	10.27	163.25	6.71	160.54	
3.5	14.08	144.26	9.15	145.44	5.98	143.02	
4	12.55	128.52	8.15	129.57	5.33	127.42	
4.5	11.18	114.50	7.26	115.44	4.74	113.52	
5	9.96	102.01	6.47	102.84	4.23	101.13	
5.5	8.87	90.88	5.76	91.62	3.77	90.10	
6	7.90	80.96	5.13	81.63	3.35	80.27	
6.5	7.04	72.13	4.57	72.72	2.99	71.51	
7	6.27	64.26	4.07	64.79	2.66	63.71	
7.5	5.59	57.25	3.63	57.72	2.37	56.76	
8	4.98	51.00	3.23	51.42	2.11	50.57	
8.5	4.44	45.44	2.88	45.81	1.88	45.05	
9	3.95	40.48	2.57	40.81	1.68	40.13	
9.5	3.52	36.07	2.29	36.36	1.49	35.76	
10	3.14	32.13	2.04	32.39	1.33	31.85	
10.5	2.79	28.63	1.81	28.86	---	---	
11	2.49	25.50	1.62	25.71	---	---	
11.5	2.22	22.72	1.44	22.91	---	---	

Table B-5 Maximum sizing windows for 300 μm aperture tube;
current-trim control setting = 52.

Aperture tube: 300 μm						
D _{std} : 44.66 μm (= 14.89% D _{ap})						

2% D _{ap} : 6.0 μm						
5% D _{ap} : 15.0 μm						
20% D _{ap} : 60.0 μm						
40% D _{ap} : 120.0 μm						
50% D _{ap} : 150.0 μm						

Log span setting: 8 10 12						
L _s : 8.0204586 10.105556 12.092228						
(I+G) ₁₂₈ : 8.9026537 11.991407 12.029926						

I+G	D _z	D _f	D _z	D _f	D _z	D _f

3	27.38	174.67	34.52	356.57	22.01	359.76
3.5	24.39	155.61	30.76	317.67	19.61	320.51
4	21.73	138.63	27.40	283.01	17.47	285.54
4.5	19.36	123.51	24.41	252.13	15.56	254.39
5	17.25	110.03	21.75	224.63	13.87	226.63
5.5	15.37	98.03	19.38	200.12	12.35	201.91
6	13.69	87.33	17.26	178.29	11.01	179.88
6.5	12.20	77.81	15.38	158.83	9.80	160.25
7	10.87	69.32	13.70	141.51	8.74	142.77
7.5	9.68	61.75	12.21	126.07	7.78	127.19
8	8.62	55.02	10.87	112.31	6.93	113.32
8.5	7.68	49.01	9.69	100.06	6.18	100.95
9	6.84	43.67	8.63	89.14	5.50	89.94
9.5	6.10	38.90	7.69	79.42	4.90	80.13
10	5.43	34.66	6.85	70.75	4.37	71.39
10.5	4.84	30.88	6.10	63.03	3.89	63.60
11	4.31	27.51	5.44	56.16	3.47	56.66
11.5	3.84	24.51	4.84	50.03	3.09	50.48

Table B-6 Maximum sizing windows for 480 μm aperture tube;
current-trim control setting = 52.

Aperture tube: 480 μm				
D_{std} : 91.2 μm (- 19.0% D_{ap})				

2% D_{ap} :		9.6 μm		
5% D_{ap} :		24.0 μm		
20% D_{ap} :		96.0 μm		
40% D_{ap} :		192.0 μm		
50% D_{ap} :		240.0 μm		

Log span setting:		10	12	
L_s :		10.204376	12.174651	
$(I+G)_{128}$:		12.137953	12.163773	

$I+G$	D_z	D_f	D_z	D_f

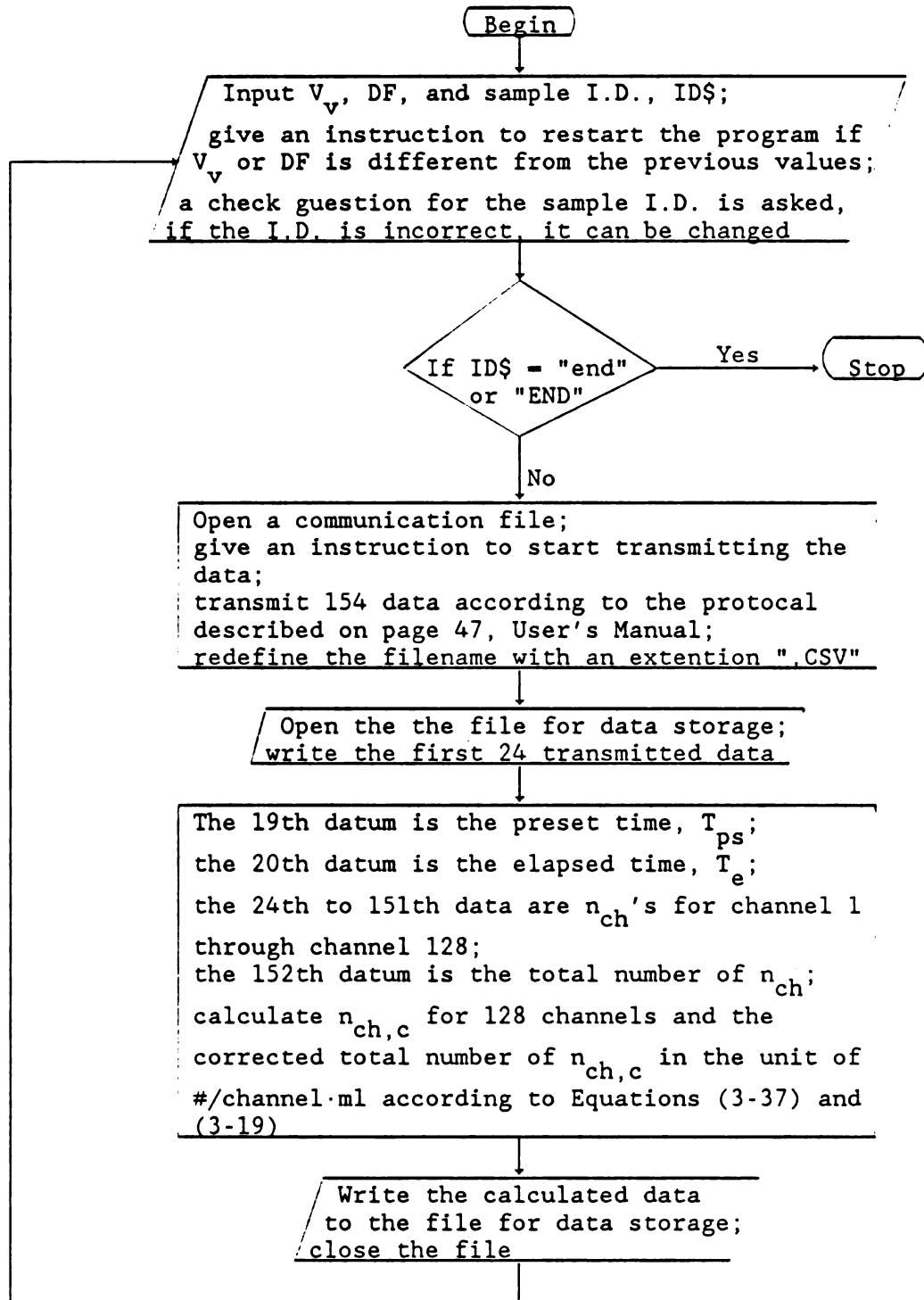
5	44.91	474.51	28.65	477.34
5.5	40.01	422.74	25.53	425.27
6	35.64	376.61	22.74	378.87
6.5	31.75	335.53	20.26	337.53
7	28.29	298.92	18.05	300.71
7.5	25.20	266.31	16.08	267.90
8	22.45	237.25	14.33	238.67
8.5	20.00	211.37	12.76	212.63
9	17.82	188.31	11.37	189.43
9.5	15.88	167.76	10.13	168.77
10	14.14	149.46	9.03	150.35
10.5	12.60	133.15	8.04	133.95
11	11.23	118.63	7.16	119.34
11.5	10.00	105.68	6.38	106.32
12	8.91	94.15	5.69	94.72
12.5	7.94	83.88	5.07	84.38
13	7.07	74.73	4.51	75.18

APPENDIX C

COMPUTER PROGRAM 80XYABCV.BAS

The computer program 80XYABCV.BAS was written in BASICA to transmit the particle data counted by the ELZONE^(R) particle data analyzer to IBM PC as described in Chapter 3. The data transmitted are the n_{ch} 's of 128 channels. In program execution, 80XYABCV.BAS requires inputs of the calibrated volume of the mercury volumetric siphon, V_v , the dilution factor in sample preparation, DF, and the sample I.D. for the filename for data storage. The program stores the $n_{ch,c}$ data calculated from Equation (3-19) to the diskette, for which the drive is specified with the input filename, e.g., C:filename or A:filename.

Flow Diagram of 80XYABCV.BAS



Listing of 80XYABCV.BAS

```

10 DIM V$(153)
20 CLS:PRINT SPC(20)"80XYABCV: 80XYAB ----> CSV DATA FILES.":PRINT:
PRINT "---- Transmit the data from area A or B in 80XY to IBM and store
them as          Comma Separated Value files."`
25 PRINT:INPUT "Volume of mercury volumetric siphon in ml; VV";VV
27 PRINT:INPUT "Dilution factor (>=1); DF";DF
30 PRINT:PRINT "Restart the program whenever VV or DF is changed.":
PRINT:PRINT "VV = ";VV,;";";";DF = ";DF
31 PRINT:INPUT "Sample I.D.";ID$:PRINT:INPUT "Is above I.D. correct
<y/n>";A$:IF A$<>"Y" AND A$<>"y" GOTO 31
40 IF ID$="end" OR ID$="END" THEN PRINT:PRINT "End of program." :END
50 OPEN "COM1:2400,E,7,1,CS,DS,CD" AS #1
60 PRINT:PRINT "Press (<CTRL-T> then) <XMIT> on TP50 when ready to
transmit the data."
70 FOR I=0 TO 153:INPUT #1,V$(I):NEXT:CLOSE
80 IE$=ID$+".CSV":DM$=" "
90 OPEN IE$ FOR OUTPUT AS #2
100 FOR I=0 TO 23 STEP 6
110 FOR J=I TO I+4:PRINT #2,V$(J)",,":NEXT:PRINT #2,V$(J):NEXT
120 TPS=VAL(V$(18)):TE=VAL(V$(19))
130 PRINT #2,DM$ ", " DM$ ", " DM$ ", " DM$ ", " "Differential Population
[#/channel.ml], "
140 FOR I=24 TO 152:DP=VAL(V$(I))*TPS*DF/(TE*VV):PRINT #2,DM$ ", " DM$
", " DM$ ", " DM$ ", " STR$(DP) ", ":NEXT
150 PRINT #2,V$(153)
160 CLOSE:PRINT:PRINT "Finish with " ID$;".":PRINT:PRINT STRING$(79,45)
:GOTO 30

```

APPENDIX D **PHYSICAL PROPERTIES OF SOLUTIONS**

The solutions used in the MSMPR experiments contain the ionic buffer KNO_3 to maintain solution ionic strength at 0.15 M. The physical properties of 0.15 M KNO_3 ($\approx 1.517\%$ KNO_3) were used to estimate the physical properties of the experimental solutions. For the study of the effects of MDCK cells, the modified media used contain approximately 0.0059 M KCl and 0.1574 M NaCl in addition to equal molar of CaCl_2 and NaC_2O_4 (varied from 0.00075 to 0.0015 M) and D-glucose (0.00555 M). The physical properties of 0.165 M NaCl ($\approx 0.9644\%$ NaCl) were used. The property data for both systems are shown in Table D-1.

Table D-1 Physical properties of solutions at 37°C.

Physical properties	Solutions containing 1.517% KNO_3 0.9644% NaCl		Reference
Density, ρ (g/cm^3)	1.00223	0.99984	a
Viscosity, μ ($10^{-3} \text{ g}/\text{cm}\cdot\text{s}$)	6.897	7.039	b

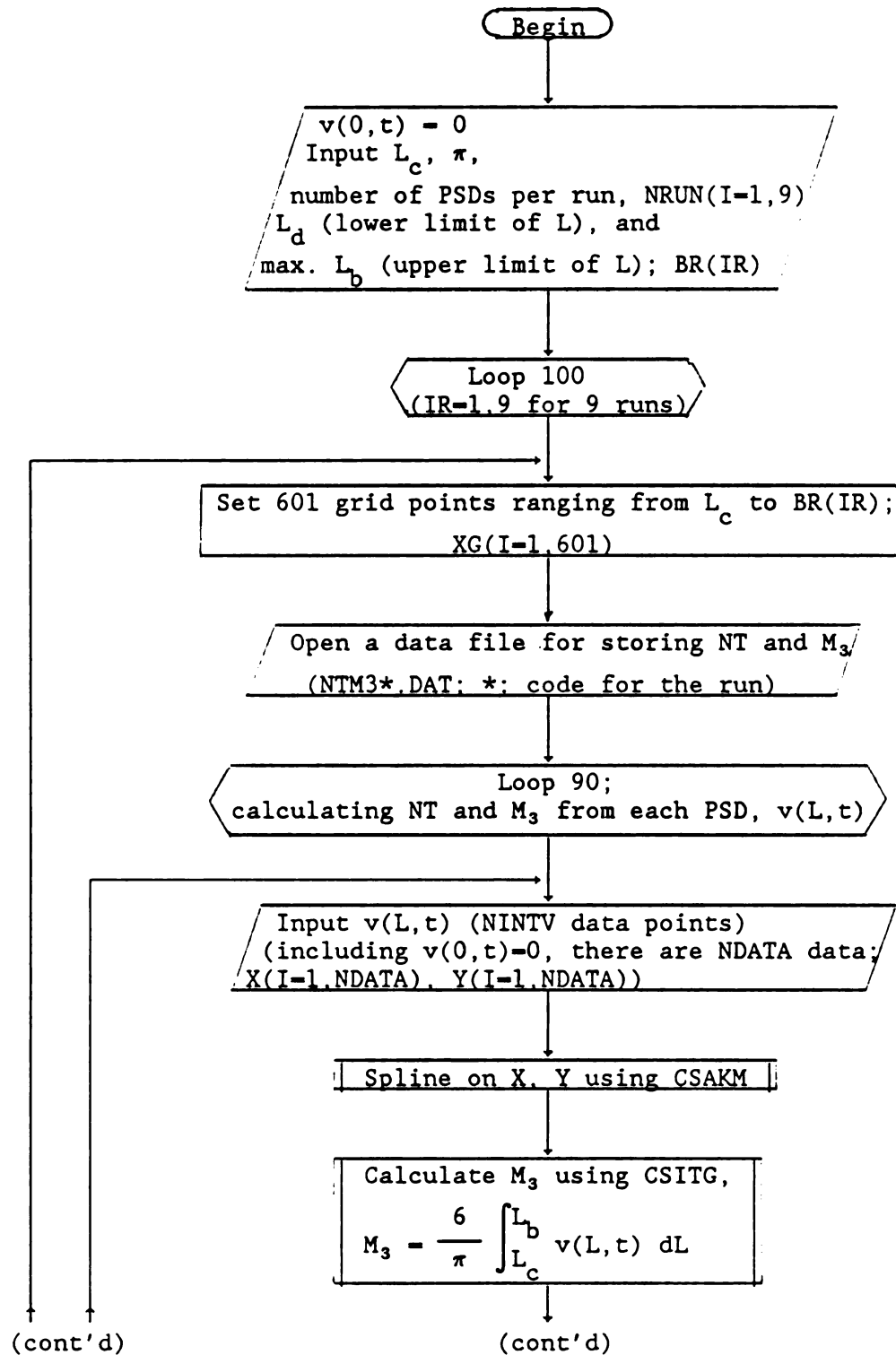
a: Perry and Chilton, 1973.

b: International Critical Tables, Washburn et al., 1930.

APPENDIX E
COMPUTER PROGRAM NTM3.FOR

The FORTRAN program NTM3.FOR was written to calculate the total particle number, N_T , and the third moment, M_3 , for calcium oxalate crystallization in the MSMPR system as discussed in Chapter 4. The input data are $v(L,t)$ PSDs, L_c , π , and number of sets of PSDs, lower particle size limit, and maximum upper particle size of each experiment. CSAKM, CSITG, and CSVAL are the IMSL subroutines used to manipulate data with a spline-fit approximation and to calculate integrals and the approximated values.

Flow Diagram of NTM3.FOR



(cont'd)

(cont'd)

Find the $XG(J)$ immediately below L_b :

if $XG(J) = L_b$, then $NSPL = J$, $N_{switch} = 0$

if $XG(J) < L_b$, then $NSPL = J+1$, $N_{switch} = 1$

$XG(J+1) = L_b$,

(store the original $XG(J+1)$ as $XGJPl$)

where $NSPL$ is the total number of $n(L,t)$ data
calculated from $v(L,t)$ and to be used to calculate NT .

Calculate $NSPL$ values of
$$n(L,t) = \frac{6}{\pi L^3} v(L,t) \text{ using CSVAL}$$

Spline on $n(L,t)$ using CSAKM

Calculate NT using CSITG,

$$NT = \int_{L_c}^{L_b} n(L,t) dL$$

Write NT , M_3 in $NTM3*.DAT$,
where $*$ is the code identifying the run

If $N_{switch} = 1$

Yes

Restore $XG(NSPL) = XGJPl$
and set $N_{switch} = 0$

No

90

100

Stop

Listing of NTM3.FOR

```

C*****
C      PROGRAM NTM3.FOR
C
C *** Calculate total number of particles (NT) and the third moment C
*** (M3) from v(L,t) data.
C
C SYMBOLS:
C      X(i);  L (micron)
C      Y(i);  v(L,t)
C      XG(i); grid points on L
C      YN(i); n(L,t)
C      C;     Lc= .0013 microns
C      BR(i); max. Lb of each experimental run
C              (Lb= upper limit of L for a PSD)
C      D(i);  Ld= lower limit of L for an experimental run
C      TM3;   M3= third moment
C      PNT;   NT
C      N1;    grids between Lc and Ld
C      N2;    grids between Ld and BR(i)
C      WD;    w at Ld
C      DW;    delta w
C      NRUN(i); number of PSD data per experimental run

      DIMENSION X(101),Y(101),XG(601),YN(601),BREAK(601),CSCOEF(4,601),
+          NRUN(9),D(9),BR(9)
      CHARACTER NMCODE*19,FILDAT*9,FILENM*7
      DATA PI,X(1),Y(1),C/3.141593,0.,0.,.0013/
      DATA NMCODE/'ABCDEFGHIJKLMNOPSRS'/
      DATA (NRUN(I),I=1,9)/17,15,15,16,14,13,16,19,15/
      DATA (D(I),I=1,9)/3.,10.,6.,6.,6.,12.,6.5,6.5,6.2/
      DATA (BR(I),I=1,9)/38.5,78.8,74.3,71.2,69.6,89.5,74.8,35.3,68.3/

      DO 100 IR=1,9
C -repeating for 9 experimental runs

C -----
C -----
C *SET 600 GRID POINTS BETWEEN Lc AND BR(IR)*
C -----
      N2=INT(.5+600./(1.+(D(IR)-C)/2./(BR(IR)-D(IR))))
      N1=600-N2
      BDC=BR(IR)/C
      WD=LOG(D(IR)/C)/LOG(BDC)
      DW=WD/N1

      DO 12 J=0,N1
          XG(J+1)=C*BDC**(DW*J)
12      CONTINUE

      DW=(1.-WD)/N2

```

```

      DO 14 J=1,N2
        XG(J+N1+1)=C*BDC**(WD+DW*J)
14      CONTINUE

C-----
C *OPEN A FILE FOR DATA STORAGE*
C-----
      FILDAT='NTM3'//NMCODE(IR:IR)//'.DAT'
      OPEN(UNIT=5,FILE=FILDAT,STATUS='NEW')
      WRITE(5,20)
20      FORMAT(' ',6X,'NT',13X,'M3')

      DO 90 I=1,NRUN(IR)
        FILENM='A'//NMCODE(IR:IR)//NMCODE(I:I)//'.DAT'

C-----
C *INPUT PSD; v(L,t)*
C-----
      OPEN(UNIT=6,FILE=FILENM,STATUS='OLD')
      READ(6,30)NINTV
30      FORMAT(I4)
        NDATA=NINTV+1
        DO 50 J=2,NDATA
          READ(6,40)X(J),Y(J)
40          FORMAT(2E16.0)
50          CONTINUE
        CLOSE(6)

C-----
        B=X(NDATA)
        CALL CSAKM(NDATA,X,Y,BREAK,CSCOE)
C -spline v(L,t)
        TM3=CSITG(C,B,NINTV,BREAK,CSCOE)*6./PI

C-----
C *CALCULATE NT AND n(L,t) FROM SPLINED v(L,t) DATA*
C-----
      DO 52 J=601,N1,-1
        IF (XG(J) .LT. B) THEN
          NSPL=J+1
          XGJPl=XG(J+1)
          XG(J+1)=B
          NSWCH=1
          GO TO 60
        ELSE
          IF (XG(J) .EQ. B) THEN
            NSPL=J
            NSWCH=0
            GO TO 60
          END IF
        END IF
52      CONTINUE

60      DO 70 J=1,NSPL
        YN(J)=CSVAL(XG(J),NINTV,BREAK,CSCOE)*6./PI/XG(J)/XG(J)/XG(J)
70      CONTINUE

```

```
      CALL CSAKM(NSPL,XG,YN,BREAK,CSCOE)  
      NINTV=NSPL-1  
      PNT=CSITG(C,XG(NSPL),NINTV,BREAK,CSCOE)  
C-----  
  
      WRITE(UNIT=5,FMT=80)PNT, TM3  
80     FORMAT(2E16.7)  
  
      IF (NSWCH .EQ. 1) THEN  
        XG(NSPL)=XGJP1  
        NSWCH=0  
      END IF  
  
90     CONTINUE  
      CLOSE(5)  
C-----  
  
100    CONTINUE  
      STOP  
      END
```


APPENDIX F

SHIFTS OF THE $v(L,t)$ CURVES

Examples of the $v(L,t)$ shifts due to crystal growth as described in Approach A for finding crystal growth rate (Chapter 4) are shown in Figures F-1 through F-6. In these figures, the origin (zero size) of each PSD is marked. The scales show the relative magnitudes of particle size and particle volume, $v(L,t)$. For each curve, the PSD below the lower particle counting limit are neglected and shown as zero values (a straight line on the x-axis). The matches of the characteristic shapes of the curves are shown with arrows on these figures.

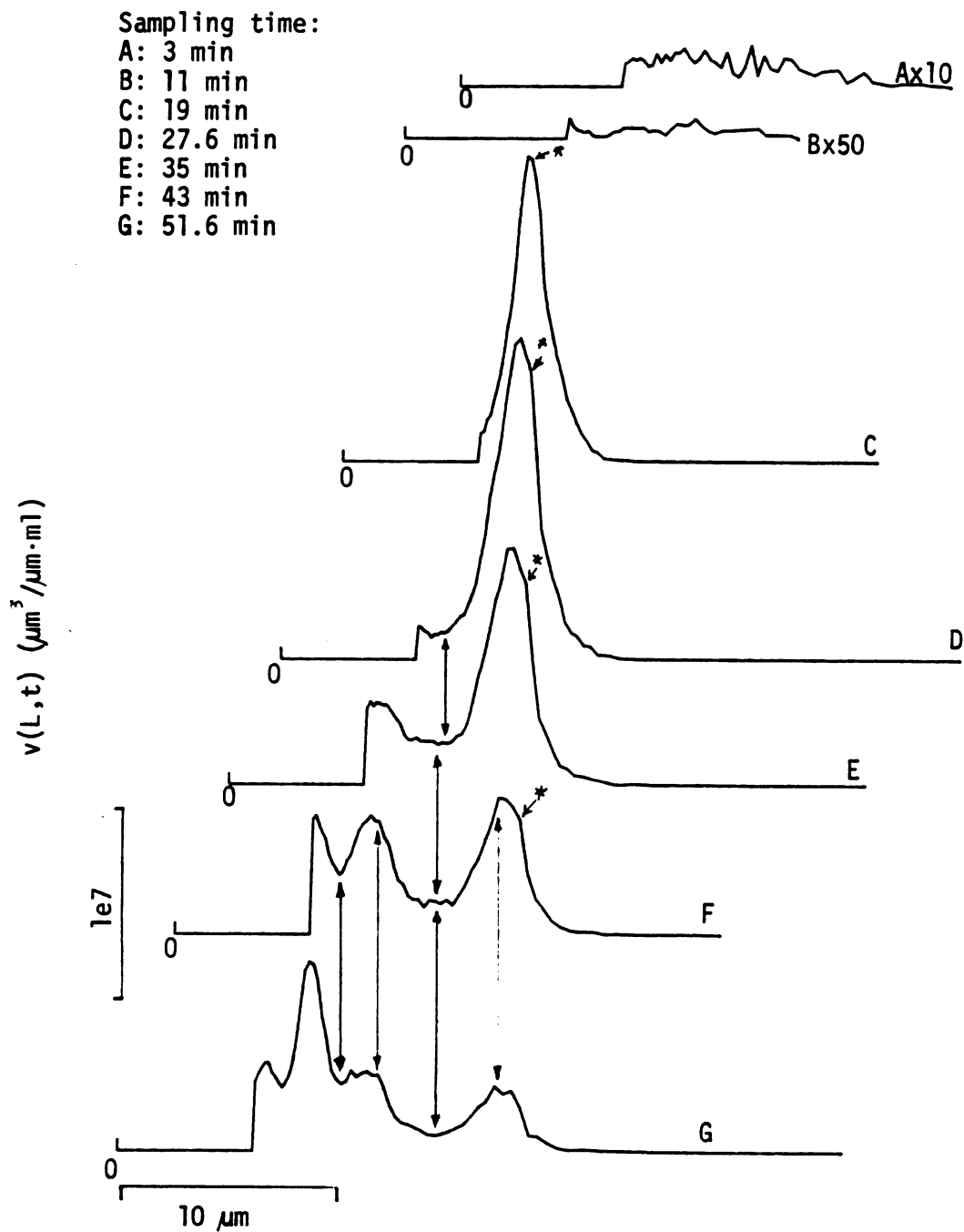


Figure F-1 Shifts of $v(L,t)$ for the experiment with PGA = 100 ppm; sampling time: 3 to 51.6 min. Arrows and "*" identify points compared among the PSD curves.

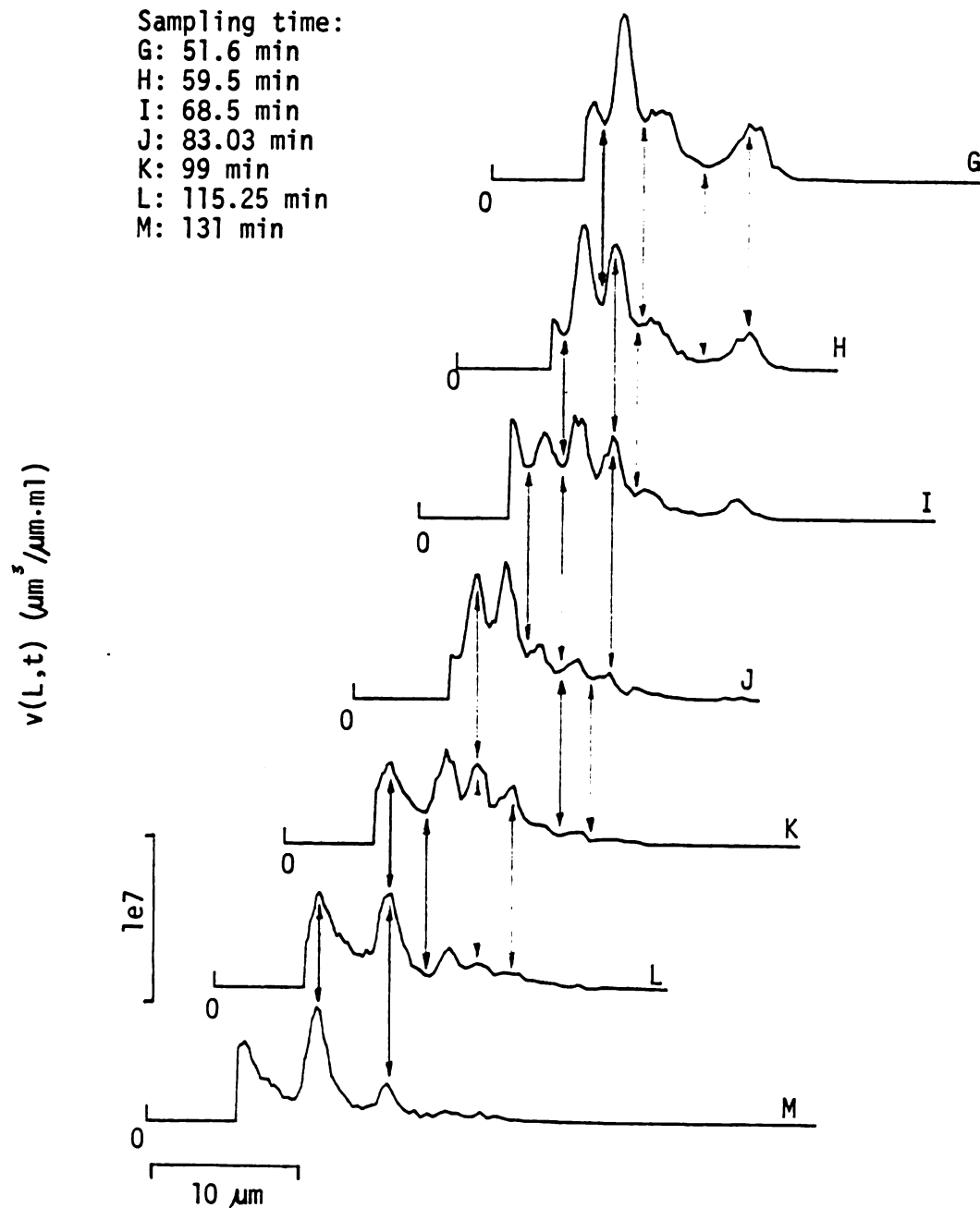


Figure F-2 Shifts of $v(L,t)$ for the experiment with PGA
 = 100 ppm; sampling time: 51.6 to 131 min.

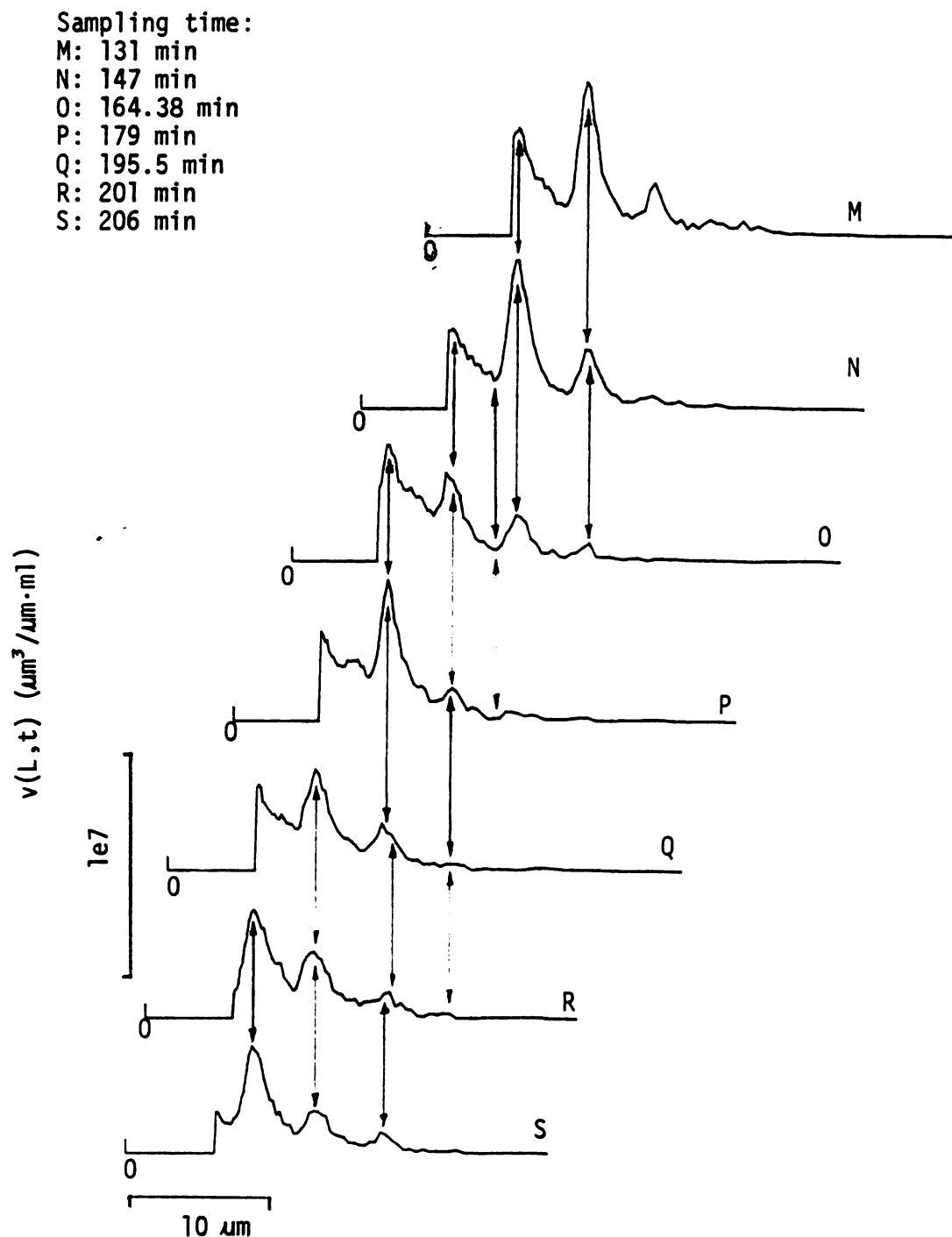


Figure F-3 Shifts of $v(L, t)$ for the experiment with PGA
 - 100 ppm; sampling time: 131 to 206 min.

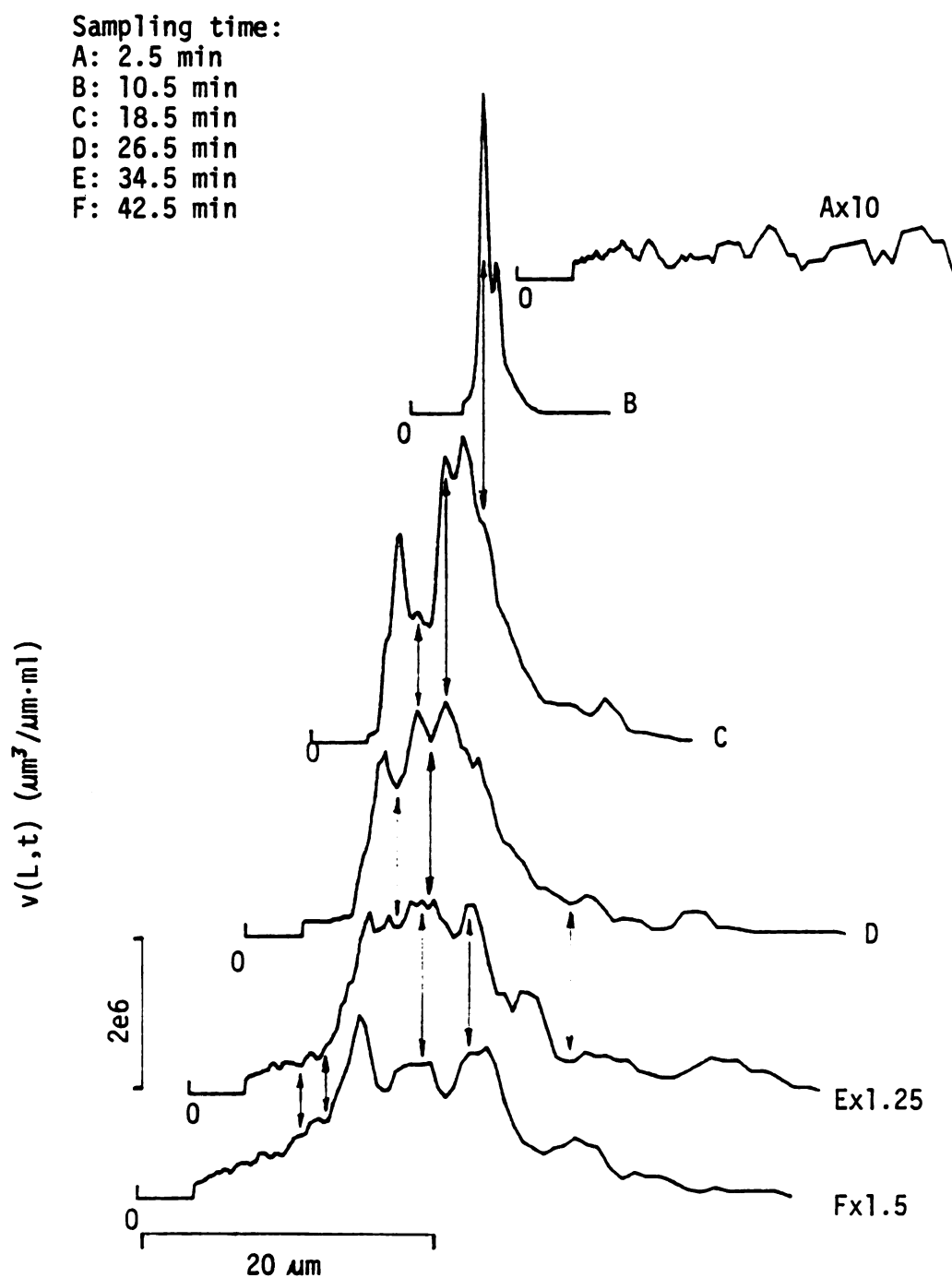


Figure F-4 Shifts of $v(L,t)$ for the base run;
 sampling time: 2.5 to 42.5 min.

Sampling time:

F: 42.5 min

G: 50.5 min

H: 58.5 min

I: 70.5 min

J: 82.5 min

K: 98.5 min

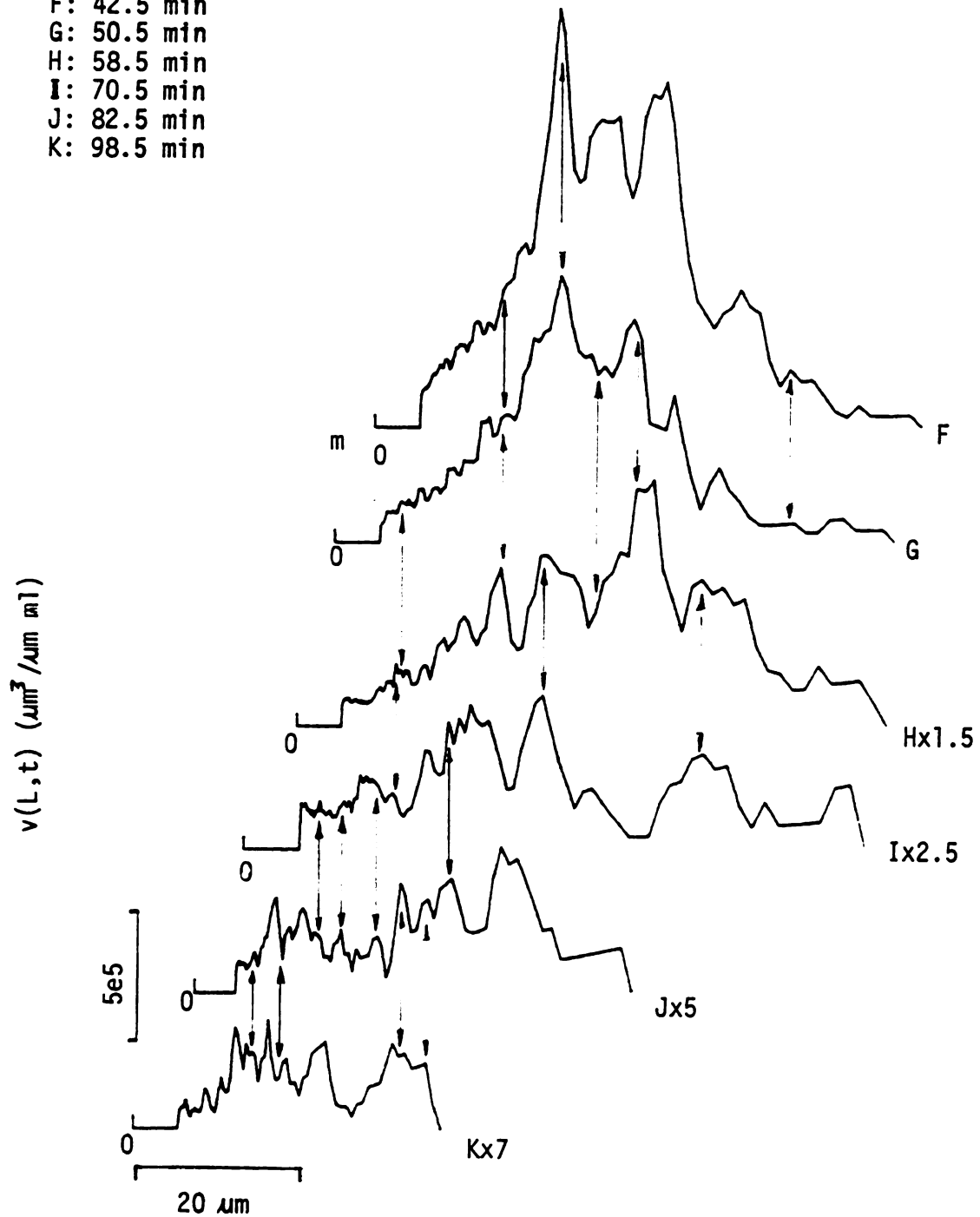


Figure F-5 Shifts of $v(L,t)$ for the base run;
sampling time: 42.5 to 98.5 min.

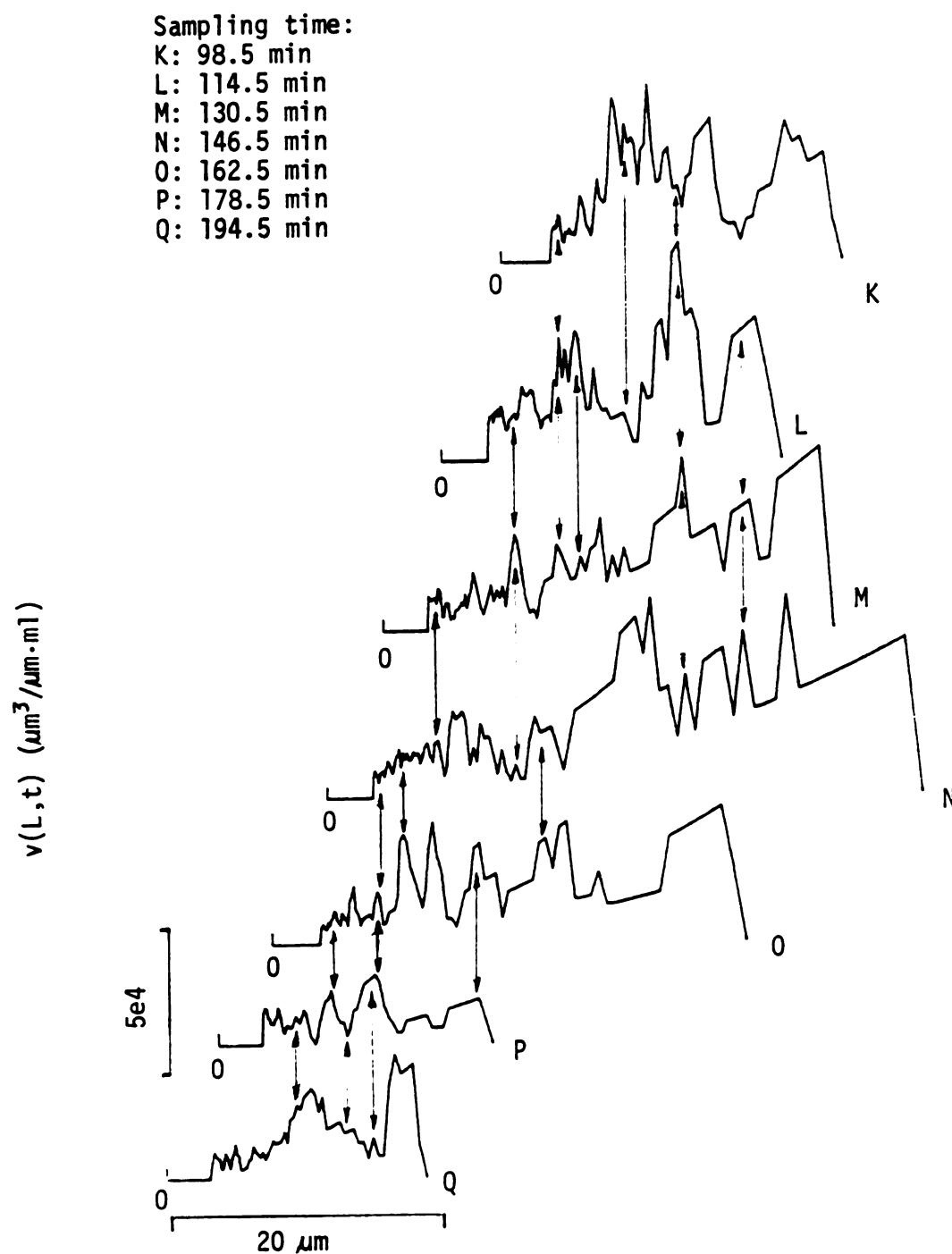


Figure F-6 Shifts of $v(L,t)$ for the base run;
 sampling time: 98.5 to 194.5 min.

APPENDIX G

COMPUTER PROGRAM GMSMPR

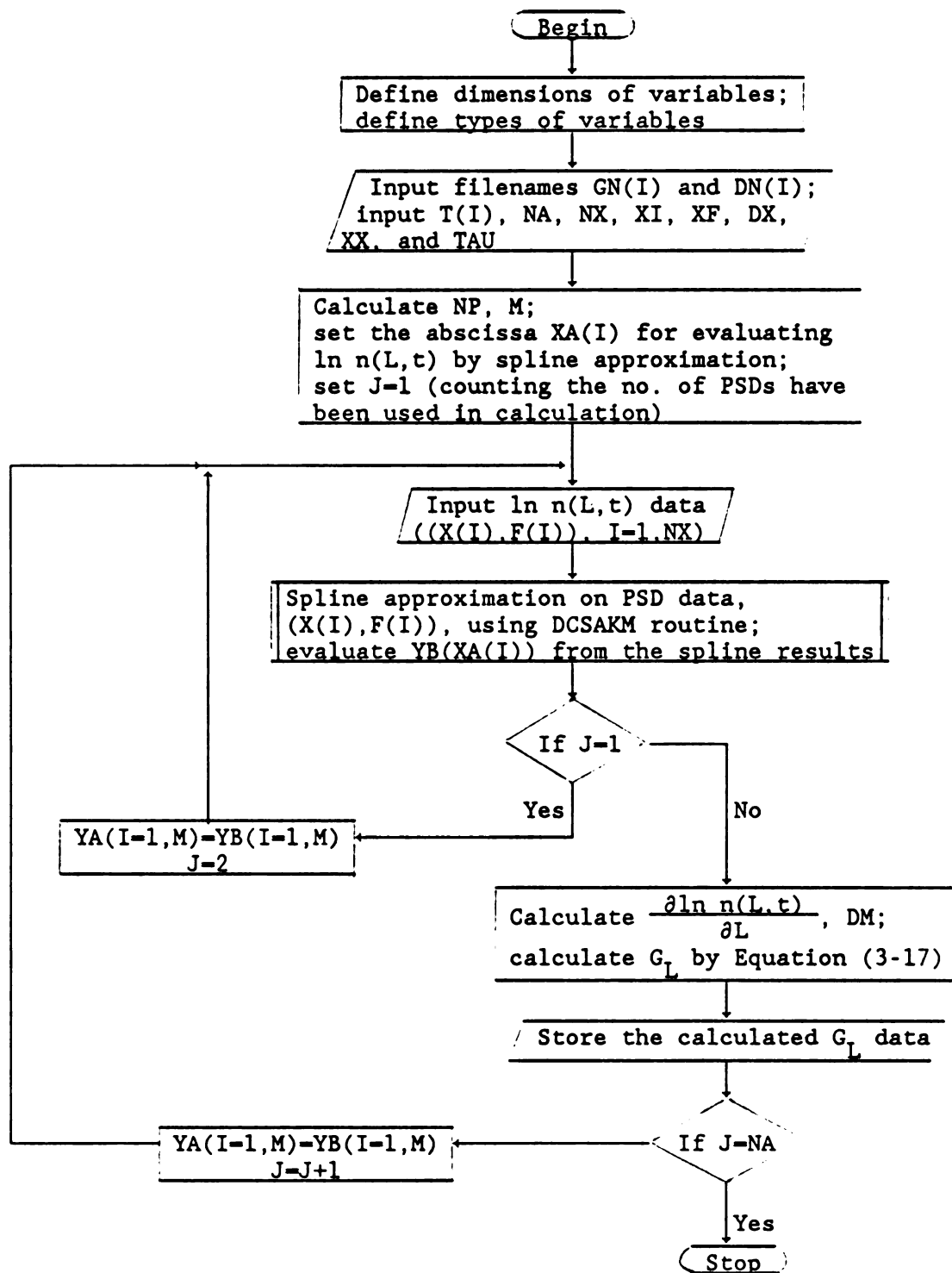
The computer program GMSMPR was written in FORTRAN to calculate the linear growth rate, G_L , for the MSMPR crystallizer operating at quasi-steady state as discussed in Chapter 4. Equation (3-17) was used in the calculation. The required input data are the digitized PSD ($\ln n(L,t)$), sampling time, filenames of these PSD data, filenames for storing the calculated growth rates, residence time, total number of PSD data being used in the calculation (NA), and the lower and upper size limits of the PSD data (XI and XF).

The list of principal variables, flow diagram, and the program listing for the experiment with calcium and oxalate concentrations equal to 1 mM are shown in the following.

List of Principal Variables

<u>Program Symbol</u>	<u>Definition</u>
X(I)	x-value of the input $\ln n(L,t)$ distribution.
F(I)	y-value of the input $\ln n(L,t)$ distribution.
XA(I)	x-value of the grid points on L.
YB(I)	y-value evaluated by an IMSL subroutine, DCSVAL, for $x = XA(I)$.
YA(I)	YB(I-1), I is the index counting the sequence of sampling time of the PSD data.
C(4,30) and BREAK(30)	Spline coefficients of DCSAKM, the IMSL spline subroutine.
G(167)	Calculated growth rate.
T(20)	Sampling time, t (min).
TAU	Residence time, τ (min).
DN(20)	Filenames for the digitized $\ln n(L,t)$.
GN(20)	Filenames for the calculated growth rate.
DX	Increment of L of the points growth rates are to be calculated.
XX	Difference of length L in calculating $\partial(\ln n(L,t))/\partial L$.
XI	Lower limit of L.
XF	Upper limit of L.
NA	Number of sets of PSDs in each experimental run planned for growth rate calculation.
NX	Number of digitized points of each PSD.
NP	Total number of points at which the growth rates are calculated.
M	$NP \cdot 3$.
DM	$\partial(\ln n(L,t))/\partial L$.
IM	A dummy variable.

Flow Diagram of GSMMPR



Listing of GMSMPR

```

      DIMENSION X(30),F(30),XA(501),YA(501),YB(501),C(4,30),G(167),
&          T(20),BREAK(30)

      DOUBLE PRECISION X,F,C,XA,YA,YB,TAU,DM,XX,T,G,XI,XF,DX,BREAK
      INTEGER NA,NX,IC,M,I,J,IM,NP
      CHARACTER DN(20)*11,GN(20)*12

      DATA NA,NX,IC,XI,XF,DX,TAU,XX/10,30,29,2.5,24.5,.5,8.,1.E-4/
      DATA GN(1),GN(2),GN(3),GN(4),GN(5),GN(6),GN(7),GN(8),GN(9)/
+ 'G408T409.DAT','G409T410.DAT','G410T411.DAT','G411T412.DAT',
+ 'G412T413.DAT','G413T414.DAT','G414T415.DAT','G415T416.DAT',
+ 'G416T417.DAT'/
      DATA DN(1),DN(2),DN(3),DN(4),DN(5),DN(6),DN(7),DN(8),DN(9),
+ DN(10),'DGT4080.DAT','DGT4090.DAT','DGT4100.DAT','DGT4110.DAT',
+ 'DGT4120.DAT','DGT4130.DAT','DGT4140.DAT','DGT4150.DAT',
+ 'DGT4160.DAT','DGT4170.DAT'/
      DATA T(1),T(2),T(3),T(4),T(5),T(6),T(7),T(8),T(9),T(10)/
+ 56.,64.,80.,96.,112.,128.,144.,160.,176.,192./

      NP=INT((XF-XI)/DX+1.1)
      M=NP*3
      DO 10 I=0,NP-1
      IM=3*I+2
      XA(IM)=XI+DX*I
      XA(IM-1)=XA(IM)-XX
      XA(IM+1)=XA(IM)+XX
10    CONTINUE

      J=1

30    OPEN(UNIT=11,FILE=DN(J),STATUS='OLD')
      DO 45 I=1,NX
      READ(UNIT=11,FMT=40)X(I),F(I),IM
40    FORMAT(F13.0,2X,F13.0,2X,I2)
45    CONTINUE
      CLOSE(11)

      CALL DCSAKM (NX,X,F,BREAK,C)

      DO 48 I=1,M
      YB(I)=DCSVAL (XA(I),IC,BREAK,C)
48    CONTINUE

      IF(J.EQ. 1) THEN
      DO 50 I=1,M
      YA(I)=YB(I)
50    YA(I)=YB(I)
      J=2
      GO TO 30
      END IF

      DO 60 I=0,NP-1
      IM=3*I+2

```

```

DM=(YA(IM+1)-YA(IM-1)+YB(IM+1)-YB(IM-1))/XX/4
IF (ABS(DM) .LT. 1.E-25) THEN
  G(I+1)=0
  GO TO 60
END IF

60  G(I+1)--((YB(IM)-YA(IM))/(T(J)-T(J-1))+1/TAU)/DM
    CONTINUE

    OPEN(UNIT=11,FILE=GN(J-1),STATUS='NEW',
&ACCESS='SEQUENTIAL',FORM='FORMATTED')
    WRITE(UNIT=11,FMT=65)XX
65  FORMAT('  XA(I)',10X,'G(I) (XX= ',E8.1,')')
    DO 80 I=1,NP
    WRITE(UNIT=11,FMT=70)XA(3*I-1),G(I)
70  FORMAT(F8.3,5X,E13.6)
80  CONTINUE
    ENDFILE(UNIT=11)
    CLOSE(UNIT=11,STATUS='KEEP')

    IF(J .EQ. NA) THEN
    GO TO 100
    END IF

    DO 90 I=1,M
    YA(I)=YB(I)
90  CONTINUE
    J=J+1
    GO TO 30

100  STOP
    END

```

BIBLIOGRAPHY

- Adair, J. H., Coagulation of Calcium Oxalate Monohydrate Suspensions, PhD dissertation, University of Florida, 1981.
- Allen, T. A., Particle Size Measurement, 3rd ed., Chapman and Hall, New York, 1981.
- Barman, T. E., Enzyme Handbook. II, p. 625, Springer-Verlag Berlin Heidelberg, New York, 1969.
- Beal, S. K., Aerosol Sci., **3**, 113 (1972).
- Berglund, K. A., PhD Thesis, Iowa State University, University Microfilms International (1981).
- Berne, R. M. and Levy, M. N., eds., Physiology, Mosby, St. Louis, 1983.
- Bird, R. B., Steward, W. Z., and Lightfoot, E. N., Transport Phenomena, Wiley, New York, 1960.
- Bowyer, R. C., Brockis, J. G., and McCulloch, R. K., Clin. Chim. Acta, **95**, 23 (1979).
- Boyce, W. H., in Renal Stone Research Symposium, Hodgkinson, A. and Nordin, B. E. C., eds., p. 93, Churchill, London, 1969.
- Boyce, W. H., in Urinary Calculi International Symposium. Renal Stone Research, Madrid, 1972, p. 247, Basel, Karger, 1973.
- Brecevic, L. and Garside, J., Chem. Eng. Sci., **36**, 867 (1981).
- Brindley, G. W., Index to the X-ray Powder Data File, Special Technical Publication 48-F, American Society For Testing Materials, Philadelphia, 1957.
- Burns, J. R., Finlayson, B., and Smith, A., in Urolithiasis. Clinical and Basic Research, Smith, L. H., Robertson, W. G., and Finlayson, B., eds., Plenum Press, 1981.
- Camp, T. R. and Stein, P. C., J. Boston Soc. Civil Engrs., **30**, 219 (1943). Reference in Abrahamson, J., Chem. Eng. Sci., **30**, 1371 (1975).
- Chudacek, M. W., Chem. Eng., Oct. 1, 79 (1984).
- Coe, F. L., Nephrolithiasis. Pathogenesis and Treatment, Year Book Medical Publishers, Inc., Chicago, 1978.

Cooney, D. O., Biomedical Engineering Principles, Marcel Dekker, Inc., New York, 1976.

CRC Handbook of Chemistry and Physics, p. B-88., 63rd ed., CRC Press, Boca Raton, Florida.

Curreri, P., Onoda, G. Y., Jr., and Finlayson, B., J. Colloid & Interface Sci., **69**, 1, 170 (1979).

Davies, C. W., Ion Association, Butterworths, London, 1962.

Delichatsios, M. A. and Probstein, R. F., J. Colloid Interface Sci., **51**, 394 (1975).

DeLong, J. D., Single Crystal Growth of Calcium Oxalate Monohydrate in Various Aqueous Ionic Media, PhD dissertation, Michigan State University, 1988.

DeLong, J. D. and Briedis, D., J. Crystal Growth, **71**, 689 (1985).

Drach, G. W., Kraljevich, A., and Randolph, A. D., J. Urol., **127**, 805 (1982).

Drach, G. W., Randolph, A. D., and Miller, J. D., J. Urol., **119**, 99 (1978).

Drach, G. W., Sarig, S., Randolph, A. D., and Thorson, S., Urol. Res., **10**, 165 (1982).

Drach, G. W., Thorson, S., and Randolph, A., J. Urol., **123**, 519 (1980).

Drake, R. L., in Topics in Current Aerosol Research, Hidy, G. M. and Brock, J. R., eds., Part 2, pp. 201-383, Pergamon Press, New York, 1972.

Eigen, M., Pure Appl. Chem., **6**, 97 (1963).

Felix, R., Monod, A., Broge, L., Hansen, N. M., and Fleisch, H., Urol. Res., **5**, 21 (1977).

Finlayson, B., Urol. Clin. North. Amer., **1**, 2, 181 (1974).

Finlayson, B., in Calcium Metabolism in Renal Failure and Nephrolithiasis, Davis D. S., ed., John Wiley & Sons, New York, 1977.

Finlayson, B., Roth, R., and Dubois, L., in Urinary Calculi. Recent Advances in Aetiology. Stone Structure and Treatment, Delatte, L. C., Rapado, A., and Hodgkinson, A., eds., S. Karger, Basel, 1972.

Gardner, G. L., J. Crystal Growth, **30**, 158 (1975).

Gardner, G. L., J. Colloid Interface Sci., **54**, 298 (1976).

Gardner, G. L., J. of Phys. Chem., **82**, 8, 864 (1978).

Gardner, G. L. and Doremus, R. H., Invest. Urol., **15**, 478 (1978).

- Garside, J., Brecevic, L., and Mullin, J. W., *J. Crystal Growth*, **57**, 233 (1982).
- Garside, J. and Larson, M. A., *J. Crystal Growth*, **43**, 694 (1978).
- Gelbard, F., Seinfeld, J. H., *J. Comput. Phys.*, **28**, 357 (1978).
- Gibco Laboratories, Catalog, Grand Island, New York.
- Gill, W. B., Jones, K. W., Ruggiero, K. J., and Fromes, M. C., in Urolithiasis. Clinical and Basic Research, Smith, L. H., Robertson W. G., and Finlayson, B., eds., p. 497, Plenum Press, New York, 1980.
- Gill, W. B., Jones, K. W., and Ruggiero, K. J., *J. Urol.*, **127**, 152 (1982).
- Gjaldbaek, J. C., *Clin. Chim. Acta*, **120**, 363 (1982).
- Hansen, R. S., in Physical Chemistry: Enriching Topics from Colloid and Surface Chemistry, van Olphen, H. and Meyers, K. J., eds., pp. 201-218, Theorex, La Jolla, California, 1975.
- Halfon, A. and Kaliaguine, S., *Can. J. Chem. Eng.*, **54**, 168 (1976).
- Harnby, N., Edwards, M. F., and Nienow, A. W., Mixing in the Process Industries, Butterworths, London, 1985.
- Hartel, R. W. and Randolph, A. D., *AIChE J.*, **32**, 1, 1186 (1986).
- Heijnen, W., Jellinghaus, W., and Klee, W. E., *Urol. Res.*, **13**, 281 (1985).
- Hiemenz, P. C., Principles of Colloid and Surface Chemistry, 2nd ed., Marcel Dekker, Inc., New York, 1986.
- Hirtzel, C. S. and Rajagopalan, R., Colloidal Phenomena. Advanced Topics, Noyes Publications, New Jersey, 1985.
- Hogfeldt, E., Stability Constants of Metal-Ion Complexes: Part A: Inorganic Ligands, IUPAC Chemical Data Series, No. 21, Pergamon Press, New York, 1982.
- Hunter, R. J., Foundations of Colloid Science, vol. 1, Oxford University Press, New York, 1987.
- Ito, H. and Coe, F. L., *Am. J. Physiol.*, **233**, f455 (1977).
- Kachel, V., in Flow Cytometry and Sorting, Melamed, M. R., Mullaney, P. R., and Mendelsohn, M. L., eds., Wiley, New York, 1979.
- Karuhn, R. F. and Berg, R. H., "Practical Aspects of Electrozone Size Analysis", in Particle Characterization in Technology, Vol. 1, CRC Press, 1984, pp. 157-181.
- Knudsen, J. G. and Katz, D. L., Fluid Dynamics and Heat Transfer, McGraw-Hill, New York, 1958.

Kraljevich, Z. I., Effect of Urinary Macromolecules on Crystallization of Calcium Oxalate in Synthetic Urine Solution, PhD dissertation, University of Arizona, 1981.

Lanzalaco, A. C., Singh, R. P., Smesko, S. A., Nancollas, G. H., Sufrin, G., Binette, M., and Binette, J. P., *J. Urol.*, **139**, 190 (1988).

Leal, J. J. and Finlayson, B., *Invest. Urol.*, **14**, 278 (1977).

Levenspiel, O., Chemical Reaction Engineering, 2nd ed., John Wiley & Sons, 1972.

Lin, S. H. and Briedis, D. M., *Rev. Sci. Instrum.*, **59**, 383 (1988a).

Lin, S. H. and Briedis, D. M., *Rev. Sci. Instrum.*, **59**, 386 (1988b).

Mandel, N. S., Mandel, S. S., and Hasegawa, A. T., *J. Urol.*, **138**, 557, (1987).

McCabe, W. L., Smith, J. C., and Harriott, P., Unit Operation of Chemical Engineering, 4th ed., McGraw-Hill, 1985.

Meyer, J. and Smith, L., *Invest. Urol.*, **13**, 31 (1975).

Nakagawa, Y., Abram, V., Kézdy, F. J., Kaiser, E. T., and Coe, F. L., *J. Biol. Chem.*, **258**, 20, 12594 (1983).

Nancollas, G. H. and Gardner, G. L., *J. of Crystal Growth*, **21**, 267 (1974).

Nielsen, A. E., *J. Colloid Science*, **10**, 576 (1955).

Nielsen, A. E., Kinetics of Precipitation, The Macmillan Company, New York, 1964.

Ohara, M. and Reid, R. C., Modeling Crystal Growth Rates from Solution, Prentice-Hall, Inc., Englewood Cliffs, N. J., 1973.

Pak, C. Y. C., ed., Renal Stone Disease. Pathogenesis. Prevention. and Treatment, Martinus Nijhoff Publishing, Boston, 1987.

Particle Data, Inc.,(a), Electrozone/Celloscope Instruction Manual. Operator's Manual for 81603. Model: 112LSGD/ADC/SSA-SGD/80XY/VM5/TP50, Elmhurst, Illinois.

Particle Data, Inc.,(b), OXY007.R01 80XY User's Manual - REX 710, Elmhurst, Illinois.

Perrin, D. D., Stability Constants Of Metal-Ion Complexes: Part B: Organic Ligands, IUPAC Chemical Data Series, No. 22, Pergamon Press, New York, 1979.

Perry, R. H. and Chilton, C. H., eds., Chemical Engineer's Handbook, 5th ed., McGraw-Hill, New York, 1973.

Pyrah, L. N., Renal Calculus, Springer-Verlag, New York, 1979.

- Randolph, A. D. and Drach, G. W., in Urolithiasis. Clinical and Basic Research, Smith, L. H., Robertson, W. G., and Finlayson, B., eds., p. 383, Plenum Press, New York, 1980.
- Randolph, A. D. and Drach, G. W., *J. Crystal Growth*, **53**, 195 (1981).
- Randolph, A. D. and Larson, M. A., Theory of Particulate Processes. Analysis and Techniques of Continuous Crystallization, Academic Press, New York, 1971.
- Robertson, W. G. and Peacock, M., *Clinical Sci.*, **43**, 499 (1972).
- Robertson, W. G. and Scurr, D. S., *J. Urol.*, **135**, 1322 (1986).
- Robertson, W. G., Scurr, D. S., and Bridge, C. M., *J. Crystal Growth*, **53**, 182 (1981).
- Rose, G. A., Urinary Stones: Clinical and Laboratory Aspects, MTP Press Limited, 1982.
- Saffman, P. G. and Turner, J. S., *J. Fluid Mech.*, **1**, 16 (1956).
- Schwartz, L. M. and Azar, M. M., Advanced Cell Biology, p. 29, Van Nostrand Reinhold, New York, 1981.
- Shaw, D. J., Introduction to Colloid and Surface Chemistry, 3rd ed., Butterworths, Boston, 1980.
- Sheehan, M. E. and Nancollas G. H., *Invest. Urol.*, **17**, 446 (1980).
- Sherwood, T. K., Pigford, R. L., and Wilke, C. R., Mass Transfer, McGraw-Hill, New York, 1975.
- Shiau, L. D. and Berglund, K. A., *AIChE J.*, **33**, 1028 (1987).
- Shinnar, R., *J. Fluid Mech.*, **10**, 259 (1961).
- Sillén, L. G. and Martell, A. E., Solubility Constants of Metal-ion Complexes, Special Publication No. 17, Chemical Society, London, 1964.
- Sillén, L. G. and Martell, A. E., Solubility Constants of Metal-ion Complexes, Special Publication No. 25, Chemical Society, London, 1971.
- Skoog, D. A., West, D. M., Analytical Chemistry, 3rd ed., Holt, Rinehart and Winston, 1979.
- Skrtic, D., Markovic, M., Komunjer L., and Furedi-Milhofer, H., *J. Crystal Growth*, **66**, 431 (1984).
- Sonntag, H. and Streng, K., Coagulation and Stability of Disperse Systems, John Wiley & Sons, Inc., New York, 1972.
- Stathopoulos, N. A. and Hellums, J. D., *Biotechnology and Bioengineering*, **27**, 1021 (1985).

Steel, R. G. D. and Torrie, J. M., Principles and Procedures of Statistics, pp. 170-171., McGraw-Hill, New York, 1960.

Sutor, D. J., Scheidt, S., British J. Urol, **40**, **1**, 22 (1968).

Swift, D. L. and Friedlander, S. K., J. Colloid Sci., **19**, 621 (1964).

Taub, M. and Suier, M. H., Jr., Methods in Enzymology, **58**, 552 (1979).

Tomazic B. and Nancollas, G. H. , J. of Crystal Growth, **46**, 355 (1979).

Tomazic, B. and Nancollas, G., J. Colloid Interface Sci., **75**, 149 (1980).

Valcic, A. V., J. Crystal Growth, **30**, 129 (1975).

Vermooten, V., in Etiologic Factors in Renal Lithiasis, Butt, A. J., ed., Charles C. Thomas, Springfield, 1956.

Voigt, J. A., An Integrated Study of the Ceramic Processing of Yttria, PhD dissertation, Iowa State Univ., 1986.

Vold, M. J., J. Colloid Science, **9**, 451 (1954).

Vold, R. D. and Vold, M. J., Colloid and Interface Chemistry, Addison-Wesley Publishing Company, Inc., 1983.

Walton, A. G., The Formation and Properties of Precipitates, Chemical Analysis, vol. 23, Editors, Elving, P. J., Kolthoff, I. M., Interscience Publishers, New York, 1967.

Washburn, E. W., West, C. J., Dorsey, N. E., and Ring, M. D., eds., International Critical Tables of Numerical Data, Physics, Chemistry and Technology, McGraw-Hill, published for the National Science Council, New York, 1930.

Wiessner, J. H., Kleinman, J., G., Blumenthal, S. S., Garancis, J. C., Mandel, G. S., and Mandel, N. S., J. Urol., **138**, 640 (1987).

Yuu, S., AIChE J., **30**, 802 (1984).

MICHIGAN STATE UNIV. LIBRARIES



31293006201069